



JOHANNES GUTENBERG
UNIVERSITÄT MAINZ

Comprehensive characterization of cardiovascular protection by the GLP-1 (Glucagon-like peptide-1) analog liraglutide in experimental arterial hypertension

Dissertation

zur Erlangung des Grades

Doktor der Naturwissenschaften

am Fachbereich Biologie

der Johannes Gutenberg-Universität Mainz

Johanna Helmstädter

geb. am 28.11.1989 in Worms

Mainz, September 2021

Dekan: xxx

1. Berichterstatter: xxx

2. Berichterstatter: xxx

3. Berichterstatter: xxx

Tag der mündlichen Prüfung: 29.03.2022

*In Dankbarkeit
meiner Familie
gewidmet.*

Table of contents

List of figures	5
List of tables	8
List of abbreviations	9
1 Introduction	18
1.1 Cardiovascular disease	18
1.1.1 Atherosclerosis	18
1.1.2 Arterial hypertension	20
1.2 The renin-angiotensin-aldosterone system (RAAS)	22
1.2.1 Systemic and local RAAS	22
1.2.2 ATII signal transduction in the cardiovascular system	25
1.3 The endothelium as major regulator of vascular tone	27
1.3.1 Nitric oxide (*NO) synthases	28
1.3.2 *NO/sGC/cGMP signaling pathway	32
1.3.3 Endothelial dysfunction	33
1.4 Oxidative stress	35
1.4.1 NADPH oxidase	35
1.4.2 Uncoupled eNOS	37
1.4.3 Peroxynitrite	39
1.5 Inflammation as a mediator of arterial hypertension	40
1.5.1 Immune cells and mechanisms of hypertensive damage	41
1.5.2 Interplay of inflammation and oxidative stress in ATII-induced arterial hypertension	42
1.6 Glucagon-like peptide-1	44
1.6.1 Gut-derived GLP-1 controls glucose homeostasis	45
1.6.2 GLP-1R agonists as antidiabetic drugs and cardiovascular outcome trials (CVOTs)	48
1.6.3 Cardiovascular targets for GLP-1	53
1.7 GLP-1 and cardiovascular protection in arterial hypertension	55
2 Aim	57
3 Materials	58
3.1 Chemicals	58
3.2 Consumables	60

3.3	Technical Devices	61
3.4	Surgical instruments	63
3.5	Reagents and Kits	63
3.6	Media and Buffer	64
3.7	Enzymes and Standards	65
3.8	Antibodies	65
3.8.1	Primary antibodies	66
3.8.2	Fluorescent-labeled antibodies and dyes	66
3.8.3	Secondary antibodies	67
3.9	Oligonucleotides	67
3.9.1	<i>TaqMan</i> probe-and-primer sets for quantitative real-time PCR	67
3.9.2	Oligonucleotide sequences for genotyping of transgenic mice	68
3.10	Laboratory Animals	68
3.11	Software	69
4	Methods	70
4.1	<i>In vivo</i> animal studies	70
4.1.1	Cre/loxP mediated generation of <i>Glp1r</i> conditional knockout mice	70
4.1.2	Implantation of osmotic pumps	72
4.1.3	Treatment with GLP-1 receptor agonist (GLP-1RA) liraglutide	73
4.1.4	Non-invasive blood pressure (NIBP) recordings	74
4.1.5	Oral glucose tolerance test (OGTT) and measurement of glucose levels in whole blood	75
4.1.6	Intravital fluorescence microscopy (IVM)	75
4.2	<i>Ex vivo</i> animal studies	76
4.2.1	Harvest of blood, organs, and tissue from mice	76
4.2.2	Red blood cells (RBCs) lysis for pan-leukocyte enrichment	77
4.2.3	Isolation of primary mouse lung endothelial cells (MLECs)	77
4.2.4	Isolation of primary mouse bone marrow-derived macrophages (BMDMs)	79
4.2.5	Determination of the heart/body weight ratio	79
4.2.6	Vascular isometric tension recordings	79
4.2.7	Dihydroethidium (DHE)-dependent fluorescence oxidative microtopography in aortic and cardiac cryosections	80
4.2.8	Quantification of aortic superoxide formation by HPLC analysis	81
4.2.9	Quantification of NADPH oxidase activity in cardiac membrane fractions by lucigenin-enhanced chemiluminescence (ECL)	82
4.2.10	Quantification of whole blood oxidative stress by L-012-enhanced chemiluminescence (ECL)	84

4.2.11	Quantification of aortic nitric oxide by electron paramagnetic resonance spectroscopy (EPR)	84
4.2.12	Quantification of nitrite and nitrate from plasma by HPLC analysis	85
4.2.13	Histological and immunohistochemical staining of aortic rings	86
4.2.14	Flow cytometric quantification of aortic immune cell infiltration	88
4.3	Molecular biological methods	91
4.3.1	DNA extraction from murine tissue	91
4.3.2	Genotyping of transgenic mice by polymerase chain reaction (PCR)	91
4.3.3	Agarose gel electrophoresis	94
4.3.4	RNA extraction from murine tissue and primary cells	94
4.3.5	RNA quantitation	95
4.3.6	Quantitative real-time PCR (qRT-PCR)	95
4.4	Protein biochemical methods	98
4.4.1	Total protein extraction from murine tissue	98
4.4.2	Protein quantitation by Bradford assay	98
4.4.3	SDS polyacrylamide gel electrophoresis	99
4.4.4	Immunological detection of proteins by Western blot	100
4.4.5	Immunological detection of proteins by Dot blot	101
4.4.6	Immunoprecipitation with magnetic beads	102
4.4.7	ELISA (enzyme-linked immunosorbent assay)	103
4.4.8	Coating of <i>Dynabeads Sheep Anti-Rat IgG</i> with anti-mouse CD102 antibody from rat	103
4.5	Statistics	104
5	Results	105
5.1	Liraglutide exerts cardio- and vasoprotective properties in experimental arterial hypertension without altering glucose and insulin metabolism	105
5.1.1	Liraglutide improves ATII-induced arterial hypertension and hypertensive heart disease	105
5.1.2	Liraglutide ameliorates ATII-induced endothelial dysfunction and vascular fibrosis	106
5.1.3	Liraglutide does not affect glucose and insulin metabolism in murine arterial hypertension	108
5.2	Liraglutide diminishes oxidative stress and inflammation in murine arterial hypertension	110
5.2.1	Liraglutide reduces ATII-induced oxidative stress and inflammation of whole blood and the heart	111
5.2.2	Liraglutide attenuates ATII-induced oxidative stress and inflammation of the vasculature	113
5.3	Liraglutide modulates the interplay of inflammation, oxidative stress, and eNOS uncoupling in murine arterial hypertension	117

5.3.1	Liraglutide suppresses an NF- κ B-mediated proinflammatory cascade responsible for leukocyte adhesion and migration in murine arterial hypertension	118
5.3.2	Liraglutide avoids uncoupling of eNOS and maintains \bullet NO bioavailability in murine arterial hypertension	120
5.4	The cardiovascular protective effects of liraglutide are abrogated in ATII-infused <i>Glp1r</i> ^{-/-} mice	121
5.5	The cardiovascular protective effects of liraglutide persist in ATII-infused <i>Glp1r my</i> ^{-/-} mice	124
5.5.1	Verification of GLP-1R deficiency in <i>Glp1r my</i> ^{-/-} mice and determination of metabolic parameters	124
5.5.2	Liraglutide alleviates endothelial dysfunction, vascular fibrosis, and cardiac hypertrophy in ATII-infused <i>Glp1r my</i> ^{-/-} mice	127
5.5.3	Liraglutide diminishes vascular inflammation in ATII-infused <i>Glp1r my</i> ^{-/-} mice	128
5.6	The cardiovascular protective effects of liraglutide are abolished in ATII-infused <i>Glp1r ec</i> ^{-/-} mice	130
5.6.1	Verification of GLP-1R deficiency in <i>Glp1r ec</i> ^{-/-} mice and determination of metabolic parameters	130
5.6.2	Liraglutide does not protect from endothelial dysfunction, vascular fibrosis, cardiac hypertrophy, and hypertension in ATII-infused <i>Glp1r ec</i> ^{-/-} mice	133
5.6.3	Liraglutide fails to prevent aortic inflammatory infiltration and vascular oxidative stress in ATII-infused <i>Glp1r ec</i> ^{-/-} mice	134
6	Discussion	138
6.1	GLP-1RA liraglutide controls cardiovascular function in experimental arterial hypertension through anti-inflammatory and antioxidative actions	140
6.2	Cardiovascular protection by liraglutide in experimental arterial hypertension depends on canonical GLP-1R signaling	145
6.3	The GLP-1R on endothelial cells mediates cardiovascular protection in experimental arterial hypertension	147
6.4	Relevance of the results and implication for further use/strategy of GLP-1 therapeutics	151
7	Summary	154
8	Zusammenfassung	155
9	Literature	157
	Appendix	179
	Publications	180
	Curriculum Vitae	183
	Danksagung	186

List of figures

Figure 1-1: Molecular processes involved in the initiation and progression of atherosclerosis.	19
Figure 1-2: Control of blood pressure by the systemic (circulating) renin-angiotensin-aldosterone system (RAAS).....	24
Figure 1-3: AT ₁ R- and AT ₂ R-mediated effects of ATII in the vessel wall.	26
Figure 1-4: Structure and catalytic mechanism of functional (coupled) *NO synthase.	31
Figure 1-5: *NO/sGC/cGMP pathway of VSMC relaxation.	33
Figure 1-6: Composition and cellular distribution of NADPH oxidase (Nox) enzyme complexes in the vasculature.	37
Figure 1-7: Redox regulation of eNOS.....	38
Figure 1-8: Proton-catalyzed decay of peroxyntirite.....	40
Figure 1-9: Redox regulation of ATII-mediated inflammatory actions.....	43
Figure 1-10: Structure of mammalian proglucagon and proglucagon-derived peptides (PGDPs).....	45
Figure 1-11: Pancreatic actions of GLP-1.....	47
Figure 1-12: GLP-1 actions in peripheral tissues.....	48
Figure 1-13: Structure and molecular mass of native human GLP-1 in comparison with approved GLP-1R agonists (GLP-1RAs) liraglutide and exenatide.....	50
Figure 1-14: Cardiovascular Outcomes for the GLP-1RA liraglutide in the LEADER trial.....	51
Figure 1-15: Direct and indirect actions of GLP-1 in the heart and vasculature.	54
Figure 4-1: Cre/loxP strategy for the generation of <i>Glp1r</i> conditional knockout mice in endothelial and myeloid cells.	71
Figure 4-2: Breeding schemes for the generation and maintenance of the <i>Glp1r^{fllox/fllox}Cdh5^{cre+}</i> (<i>Glp1r^{ec-/-}</i>) and <i>Glp1r^{fllox/fllox}LysM^{cre+/-}</i> (<i>Glp1r^{my-/-}</i>) mouse line.	72
Figure 4-3: Treatment scheme for the investigation of GLP-1RA liraglutide in experimental hypertension.	74
Figure 4-4: Scheme of the mouse holder used in tail-cuff plethysmography.	75
Figure 4-5: Isolation of primary endothelial cells from murine lung tissue.	78
Figure 4-6: Isolation of bone marrow-derived macrophages (BMDMs) from murine femur and tibia.	79
Figure 4-7: Oxidation products of dihydroethidium (DHE) with corresponding fluorescence spectra.....	81
Figure 4-8: Lucigenin-enhanced chemiluminescence.	83
Figure 4-9: Molecular interactions of the ABC-based detection method.....	86
Figure 4-10: The principle of flow cytometry.....	89

Figure 4-11: Gating strategy for identification of immune cell subtypes in aortic tissue.....	91
Figure 4-12: The principle of RNA isolation by acid guanidinium thiocyanate–phenol–chloroform extraction.....	94
Figure 4-13: The principle of one-step reverse transcription-quantitative PCR.....	96
Figure 4-14: Principle of the <i>TaqMan</i> MGB probe-based assay chemistry.....	97
Figure 4-15: One-dimensional SDS-polyacrylamide gel electrophoresis (SDS-PAGE).....	99
Figure 5-1: Liraglutide (Lira) normalizes elevated blood pressure levels and cardiac hypertrophy caused by angiotensin II (ATII) in wild-type (C57BL/6J) mice.....	106
Figure 5-2: Liraglutide (Lira) improves angiotensin II (ATII)-induced endothelial dysfunction and vascular fibrosis in wild-type (C57BL/6J) mice.....	108
Figure 5-3: Liraglutide (Lira) does not alter glucose and insulin metabolism of wild-type (C57BL/6J) mice with arterial hypertension.....	110
Figure 5-4: Liraglutide (Lira) lowers the angiotensin II (ATII)-induced oxidative burden of whole blood and heart in wild-type (C57BL/6J) mice.....	112
Figure 5-5: Liraglutide (Lira) reduces angiotensin II (ATII)-induced oxidative stress, dysregulation of eNOS, and immune cell infiltration in cardiac tissue of wild-type (C57BL/6J) mice.....	113
Figure 5-6: Liraglutide (Lira) reduces angiotensin II (ATII)-induced vascular oxidative stress in wild-type (C57BL/6J) mice.....	115
Figure 5-7: Liraglutide (Lira) mitigates angiotensin II (ATII)-induced infiltration of inflammatory cells into the vasculature of wild-type (C57BL/6J) mice.....	117
Figure 5-8: Liraglutide (Lira) attenuates angiotensin II (ATII)-triggered leukocyte migration (rolling, adhesion) and moderates proinflammatory signals in the vasculature of wild-type (C57BL/6J) mice with arterial hypertension.....	119
Figure 5-9: Liraglutide (Lira) avoids endothelial •NO synthase (eNOS) uncoupling and improves nitric oxide (•NO) bioavailability in wild-type (C57BL/6J) mice with arterial hypertension.....	121
Figure 5-10: Liraglutide (Lira) causes increased vascular inflammation and oxidative stress in hypertensive <i>Glp1r</i> ^{-/-} mice and fails to prevent endothelial dysfunction.....	123
Figure 5-11: <i>Glp1r</i> gene deficiency in bone marrow-derived macrophages (BMDMs), vascular and metabolic phenotyping of myelomonocytic cell-specific <i>Glp1r</i> knockout mice (<i>Glp1r</i> my ^{-/-}).....	126
Figure 5-12: Liraglutide (Lira) amends angiotensin II (ATII)-induced endothelial dysfunction, vascular fibrosis and cardiac hypertrophy in myelomonocytic cell-specific <i>Glp1r</i> knockout mice (<i>Glp1r</i> my ^{-/-}) mice.....	128

Figure 5-13: Liraglutide (Lira) mitigates angiotensin II (ATII)-induced infiltration of inflammatory cells into the vasculature of myelomonocytic cell-specific <i>Glp1r</i> knockout mice (<i>Glp1r my^{-/-}</i>) mice.....	129
Figure 5-14: <i>Glp1r</i> gene deficiency in mouse lung endothelial cells (MLECs), vascular and metabolic phenotyping of endothelial cell-specific <i>Glp1r</i> knockout mice (<i>Glp1r ec^{-/-}</i>).	132
Figure 5-15: Liraglutide (Lira) does not eradicate angiotensin II (ATII)-induced endothelial dysfunction, vascular fibrosis, cardiac hypertrophy, and hypertension in endothelial cell-specific <i>Glp1r</i> knockout mice (<i>Glp1r ec^{-/-}</i>) mice.	134
Figure 5-16: Liraglutide (Lira) fails to mitigate angiotensin II (ATII)-induced infiltration of inflammatory cells into the vasculature of endothelial cell-specific <i>Glp1r</i> knockout mice (<i>Glp1r ec^{-/-}</i>) mice.	136
Figure 5-17: Liraglutide (Lira) fails to reduce angiotensin II (ATII)-induced oxidative stress and proinflammatory mediators in the vasculature of endothelial cell-specific <i>Glp1r</i> knockout mice (<i>Glp1r ec^{-/-}</i>) mice.	137
Figure 6-1: Schematic illustration of the proposed mechanism of cardiovascular protection by GLP-1RA liraglutide in experimental arterial hypertension.	139

List of tables

Table 1-1: Comparison of European and American Society Definitions of hypertension for adults.....	21
Table 1-2: *NO synthase (NOS) isoforms.	29
Table 1-3: Pharmacokinetic properties of approved GLP-1RAs and their results in cardiovascular outcome trials (CVOTs).	52
Table 3-1: Chemicals.....	58
Table 3-2: Consumables.....	60
Table 3-3: Technical Devices.	61
Table 3-4: Surgical instruments.....	63
Table 3-5: Reagents and Kits.....	63
Table 3-6: Media and Buffer.....	64
Table 3-7: Enzymes and Standards.....	65
Table 3-8: Primary antibodies.	66
Table 3-9: Fluorescent-labeled antibodies and dyes.....	66
Table 3-10: Secondary antibodies.	67
Table 3-11: Taqman® assays for qRT-PCR.....	67
Table 3-12: Primer sequences for genotyping PCR.....	68
Table 3-13: Overview of used mouse strains including description and source.	68
Table 3-14: Software.	69
Table 4-1: Antibodies and dyes used for the assessment of aortic immune cell infiltration. ..	90
Table 4-2: Reaction mix and program for the genotyping PCR of <i>Glpr1rlfox</i>	92
Table 4-3: Reaction mix and program for the genotyping PCR of <i>Cdh5cre</i>	93
Table 4-4: Reaction mix and program for the genotyping PCR of <i>LysMcre</i>	93
Table 4-5: Reaction mix and profile for the <i>TaqMan</i> qRT-PCR.	98
Table 4-6: Recipes for stacking and resolving gels used in the SDS-PAGE.....	100

List of abbreviations

2-HE	2-hydroxyethidium, also 2-OH-E ⁺
2-OH-E ⁺	2-hydroxyethidium, also 2-HE
3-NT	3-nitrotyrosine
6-FAM	6-carboxyfluorescein
ABC	avidin-biotin-peroxidase complex
AC	adenylyl cyclase
ACC/AHA	American College of Cardiology / American Heart Association
ACE	angiotensin-converting enzyme
ACh	acetylcholine
ACS	acute coronary syndrome
ADA/EASD	American Diabetes Association and European Association for the Study of Diabetes
ADH	antidiuretic hormone
ADMA	asymmetric dimethylarginine
AMPK	AMP-activated protein kinase
ANP	atrial natriuretic peptide
AP-1	activator protein-1
APC	allophycocyanin
Apo E	apolipoprotein E
approx.	approximately
AT ₁ R	angiotensin II receptor type 1
AT ₂ R	angiotensin II receptor type 2
ATI	angiotensin I
ATII	angiotensin II
ATP	adenosine-5'-triphosphate
B6	C57BL/6J
BH ₂	7,8-dihydrobiopterin
BH ₄	(6 <i>R</i>)-5,6,7,8-tetrahydro-L-biopterin
BMDM	bone marrow-derived macrophage

BMI	body mass index
bp	base pair
BP	blood pressure
BSA	bovine serum albumin
CaM	calmodulin
cAMP	cyclic adenosine 3',5'-monophosphate
CANTOS	Canakinumab Antiinflammatory Thrombosis Outcome Study (Clinical Trial)
CD	cluster of differentiation
Cdh5	cadherin 5
cDNA	complementary DNA
cGK-I	cGMP-dependent kinase I, also PKG1
cGMP	cyclic guanosine 3',5'-monophosphate
CI	confidence interval
CICR	calcium-induced calcium release
CKD	chronic kidney disease
CNS	central nervous system
Cre	cyclization recombination
CRP	C-reactive protein
Ct	cycle threshold
CTGF	connective tissue growth factor
CVD	cardiovascular disease
CVOT	cardiovascular outcome trial
Cy	cyanine
DAB	3,3'-diaminobenzidine
DAG	diacylglycerol
DALY	disability-adjusted life year
DBP	diastolic blood pressure
DC	dendritic cells
DDAH	dimethylarginine dimethylaminohydrolase
ddH ₂ O	double distilled water
DHE	dihydroethidium

DHFR	dihydrofolate reductase
DMP	dimethyl pimelimidate
DNA	deoxyribonucleic acid
DOCA	deoxycorticosterone acetate
DPP-4	dipeptidylpeptidase-4
DPP-4I	dipeptidylpeptidase-4 inhibitor
Duox	dual oxidase
e.g.	<i>exempli gratia</i> (for example)
EC	endothelial cell
ECL	enhanced chemiluminescence
ECM	extracellular matrix
EDHF	endothelium-derived hyperpolarizing factor
EDRF	endothelium-derived relaxing factor
EDTA	ethylene diamine tetraacetic acid
ELISA	enzyme-linked immunosorbent assay
ELIXA	Evaluation of Lixisenatide in Acute Coronary Syndrome (Clinical Trial)
Em	emission
EMA	European Medicines Agency
EMPA-REG OUTCOME	Empagliflozin Cardiovascular Outcome Event Trial in Type 2 Diabetes Mellitus Patients (Clinical trial)
eNOS	endothelial •NO synthase
Epac	exchange protein activated by cAMP
EPR	electron paramagnetic resonance spectroscopy
ERK	extracellular signal-regulated kinase
ESC/ESH	European Society of Cardiology / European Society of Hypertension
ET-1	endothelin-1
Ex	excitation
EXSCEL	Exenatide Study of Cardiovascular Event Lowering (Clinical Trial)
FACS	fluorescence-activated cell sorting
FAD	flavin adenine dinucleotide
FCS	fetal calf serum

FDA	U.S. Food and Drug Administration
FITC	fluorescein isothiocyanate
FMD	flow-mediated dilation
FMN	flavin mononucleotide
FRET	Förster resonance energy transfer
FRT	flippase recognition target
FSC	forward scatter
GBD	Global Burden of Disease Study
GCH1	GTP-cyclohydrolase-1
GIP	glucose-dependent insulintropic polypeptide
GLP-1	glucagon-like peptide-1
GLP-1R	glucagon-like peptide-1 receptor
GLP-1RA	glucagon-like peptide-1 receptor agonist
<i>Glp1r</i>	gene coding for glucagon-like peptide-1
<i>Glp1r^{ec}-/-</i>	<i>Glp1r^{flox/flox}Cdh5^{cre+}</i> , endothelial-specific <i>Glp1r</i> knockout mice
<i>Glp1r^{my}-/-</i>	<i>Glp1r^{flox/flox}LysM^{cre+/-}</i> , myeloid-specific <i>Glp1r</i> knockout mice
<i>Glp1r^r-/-</i>	<i>Glp1r</i> deficient mice
<i>Glp1r^{flox/flox}</i>	floxed <i>Glp1r</i> mice
GPCR	G protein-coupled receptor
GPx	glutathione peroxidase
GSH	glutathione
GSSG	glutathione disulfide
GTP	guanosine-5'-triphosphate
GTPCH1	GTP cyclohydrolase 1
HAEC	human aortic endothelial cell
HARMONY	Albiglutide and Cardiovascular Outcomes in Patients With Type 2 Diabetes and Cardiovascular Disease (Clinical Trial)
HbA _{1c}	hemoglobin A1c, glycated hemoglobin
HBSS	Hanks' Balanced Salt Solution
HFD	high-fat diet
HFSSD	diet high in fat, sugar, and sodium

HIER	heat-induced epitope retrieval
HIF-1	hypoxia-inducible factor 1
HPLC	high-performance liquid chromatography
HR	hazard ratio
HRP	horseradish peroxidase
HUVEC	human umbilical vein endothelial cell
i.e.	<i>id est</i> (that is)
i.p.	intraperitoneal
ICAM-1	intercellular adhesion molecule 1
IE	international unit
IEL	intraepithelial lymphocyte
IGCT	Intensive Glycemic Control Trial
IHC	immunohistochemistry
IHD	ischemic heart disease
IL	interleukin
INF- γ	interferon γ
iNOS	inducible *NO synthase
IOD	integrated optical density
IP ₃	inositol trisphosphate
IRAG	IP ₃ R-associated cGMP kinase substrate
IRI	ischemia-reperfusion injury
JAK/STAT	Janus kinase/signal transducers and activators of transcription
JNK	c-Jun N terminal kinase
KH	Krebs-Hepes
K _v channel	voltage-gated potassium channel
L-012	8-amino-5-chloro-7-phenylpyrido[3,4-d]pyridazine-1,4-(2H,3H)dione sodium salt
L-NAME	L-N ^G -nitroarginine methyl ester
LDL	low-density lipoprotein
LEADER	Liraglutide Effect and Action in Diabetes Evaluation of Cardiovascular Outcome Results (Clinical Trial)
Lira	liraglutide

loxP	locus of X-over of P1
LPS	lipopolysaccharide
LVH	left ventricular hypertrophy
Ly6C	lymphocyte antigen 6 complex, locus C1
Ly6G	lymphocyte antigen 6 complex, locus G
LysM	lysozyme M
M-CSF	macrophage colony-stimulating factor
MACE	major adverse cardiovascular event
mAChR	muscarinic acetylcholine receptor
MACS	magnetic activated cell sorting
MAPK	mitogen-activated protein kinase
MCP-1	monocyte chemoattractant protein 1
MGB	minor groove binder
MHC	major histocompatibility complex
MIP-1a	macrophage inflammatory protein 1 alpha
MLC	myosin light chain
MLCK	myosin light chain kinase
MLCP	myosin light chain phosphatase
MLEC	mouse lung endothelial cell
MMP	matrix metalloproteinase
MR	mineralocorticoid receptor
mRNA	messenger RNA
MTP α	mitochondrial trifunctional protein- α
MW	molecular weight
NADPH	nicotinamide adenine dinucleotide phosphate
NASH	nonalcoholic steatohepatitis
NEP	neutral endopeptidase
NF-kB	nuclear factor-kB, nuclear factor kappa-light-chain-enhancer of activated B cells
NFQ	non-fluorescent quencher
NHS	normal horse serum

NIBP	non-invasive blood pressure
NK cell	natural killer cell
NMR	nuclear magnetic resonance
nNOS	neuronal •NO synthase
•NO	nitric oxide
•NO ₂	nitrogen dioxide
Nox	NADPH oxidase
Nrf2	nuclear factor erythroid 2-related factor 2
NTG	nitroglycerine
O ₂ ^{•-}	superoxide
OGTT	oral glucose tolerance test
•OH	hydroxyl radical
ONOO ⁻	peroxynitrite
oxLDL	oxidized low-density lipoprotein
Pam	peptidyl-glycine alpha-amidating monooxygenase
PBS	phosphate buffered saline
PCR	polymerase chain reaction
PCSK	proprotein convertase subtilisin-kexin
PDE	phosphodiesterase
PDGF	platelet-derived growth factor
PE	phycoerythrin
PerCP	peridinin-chlorophyll-protein
PGI ₂	prostacyclin
phox	phagocyte oxidase
PIONEER 6	Peptide Innovation for Early Diabetes Treatment (Clinical Trial)
PIP ₂	phosphatidylinositol 4,5-bisphosphate
PKA	protein kinase A
PKC	protein kinase C
PKG1	protein kinase G type 1, also cGK-I
PLC	phospholipase C
PNS	peripheral nervous system

pp.	pages
pps	percentage points
PRMT	protein arginine N-methyltransferase
pVAT	perivascular adipose tissue
PYK-2	protein tyrosine kinase-2
qRT-PCR	quantitative reverse transcription polymerase chain reaction
RAAS	renin–angiotensin–aldosterone system
RANTES	Regulated upon Activation, Normal T cell Expressed and Secreted
RBC	red blood cell
REWIND	Researching Cardiovascular Events with a Weekly Incretin in Diabetes (Clinical Trial)
RhoA	Ras homolog family member A
RNA	ribonucleic acid
RNS	reactive nitrogen species
RONS	reactive oxygen and nitrogen species
ROS	reactive oxygen species
RT	reverse transcription
s.c.	subcutaneous
SAN	sinoatrial node
SBP	systolic blood pressure
SDS-PAGE	sodium dodecyl sulfate polyacrylamide gel electrophoresis
SELECT	Semaglutide effects on cardiovascular outcomes in people with overweight or obesity (Clinical Trial)
SEM	standard error of the mean
sGC	soluble guanylate cyclase
SGLT-2	sodium-glucose cotransporter-2
SGLT-2I	sodium-glucose cotransporter-2 inhibitors
SHR	spontaneous hypertensive rat
SMC	smooth muscle cell
SNS	sympathetic nervous system
SOD	superoxide dismutase
SSC	side scatter

SSTR2	somatostatin-2 receptor
SUSTAIN-6	Trial to Evaluate Cardiovascular and Other Long Term Outcomes with Semaglutide in Subjects with Type 2 Diabetes (Clinical Trial)
T2DM	type 2 diabetes mellitus
Taq	<i>Thermus aquaticus</i>
TBP	TATA-box binding protein
TCR β	T-cell receptor beta chain
tg	transgene
TGF- β	transforming growth factor β
TNF- α	tumor necrosis factor alpha
TXA ₂	thromboxane
UV/Vis spectroscopy	ultraviolet and visible spectroscopy
v/v	volume fraction
VASP	vasodilator-stimulated phosphoprotein
VCAM-1	vascular cell adhesion molecule 1
VDCC	voltage-dependent calcium channel
VEGF	vascular endothelial growth factor
VPR	volume-pressure recording
vs.	versus
VSMC	vascular smooth muscle cell
w/v	mass concentration
WBC	white blood cell

1 Introduction

1.1 Cardiovascular disease

For the last 20 years, cardiovascular diseases (CVDs) (ischemic heart disease, stroke) have remained the leading cause of death globally, with a nowadays especial increase in low- and middle-income countries ¹.

According to the Global Burden of Disease (GBD), ischemic heart disease (IHD) and stroke were the world's leading causes of disability-adjusted life years (DALYs, equivalent to a lost year of full health) in both the 50–74-year and 75-years-and-older age groups in 2019, with 197 million prevalent cases of IHD worldwide ^{2,3}. The top-ranked global risk factor for attributable deaths was thereby identified as arterial hypertension ⁴. Most of the cardiovascular deaths can be ascribed to atherosclerotic changes in the vasculature and its complications like acute myocardial infarction, stable angina pectoris, stroke, or peripheral artery disease ⁵.

Glucagon-like peptide-1 receptor agonists (GLP-1RAs) are a relatively new class of drugs that are approved for the treatment of type 2 diabetes mellitus (T2DM). T2DM has epidemically increased over the last three decades, with the number of diabetic adults in the world risen from 108 million in 1980 to 463 million in 2019 ⁶⁻⁸. Diabetic patients often suffer from chronic comorbidities like obesity and hypertension, and CVD is their most prevalent cause of morbidity and mortality ⁹. Hence, new preventive and treatment strategies that not only attenuate hyperglycemia but also target cardiovascular impairment have gained special attention.

In this regard, GLP-1RAs have entered the spotlight as they reduce cardiac events in T2DM patients and accumulating evidence links them to cardiovascular protection beyond glycemic control ¹⁰, yet with limited knowledge about their mode of action. This thesis characterizes the cardioprotective effects and mechanisms of GLP-1RA liraglutide in an experimental (non-diabetic) model of angiotensin II (ATII)-induced arterial hypertension.

1.1.1 Atherosclerosis

Atherosclerosis describes a chronic vascular disease, in which fatty and/or fibrous material accumulates in the intima, the innermost layer of arteries ⁵. As these atherosclerotic plaques build up in the arteries, the artery walls become thickened and stiff, narrowing the arterial lumen, which can eventually impede blood flow and lead to tissue ischemia ^{5,11}. Even though low-density lipoprotein (LDL) cholesterol is known to be a principal determinant of disease

initiation and progression, atherosclerosis is no longer considered a simple fatty degeneration of the vasculature but rather a slowly progressing, chronic inflammatory condition of the artery wall^{5,12}. Figure 1-1 depicts the molecular processes involved in the pathogenesis of atherosclerosis.

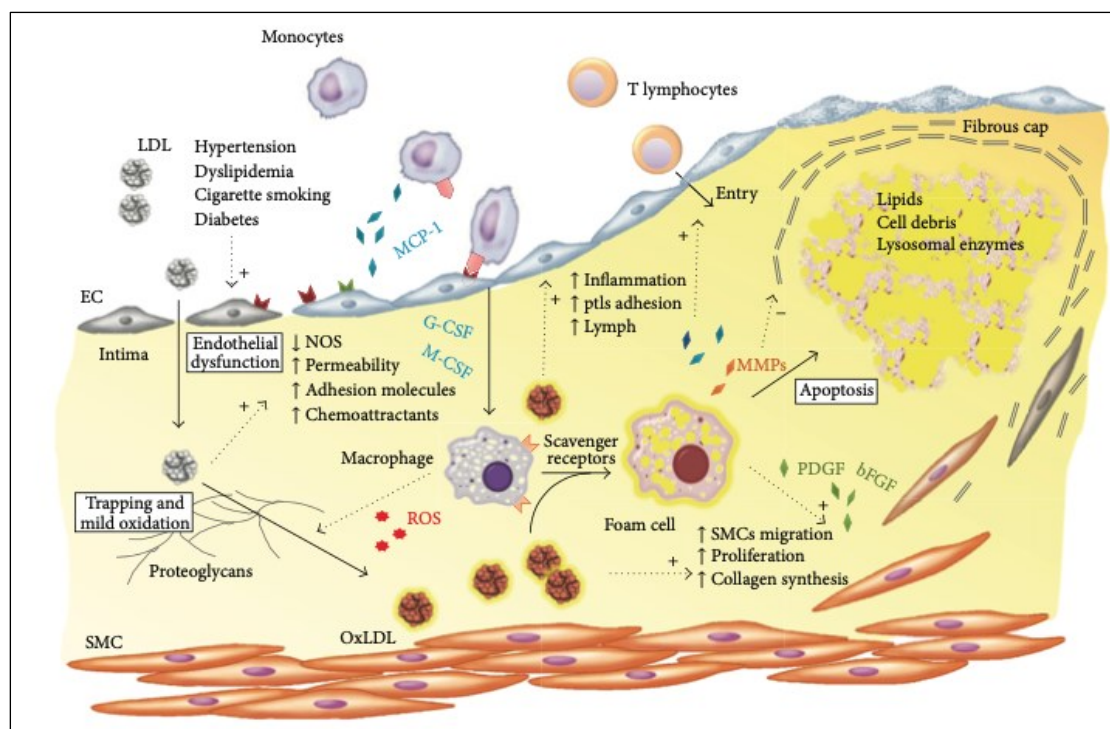


Figure 1-1: Molecular processes involved in the initiation and progression of atherosclerosis. As a consequence of endothelial dysfunction, evoked by cardiovascular risk factors such as arterial hypertension, low-density lipoproteins (LDLs) enter the subendothelial space, where they are partially oxidized to oxLDLs. Scavenger receptor-bearing macrophages bind oxLDL, turning them into foam cells that build fatty streaks. As a result of further migration of immune cells into the intima, proliferation of smooth muscle cells (SMCs), and excessive production of extracellular matrix, complex lesions are formed over the course of time. MCP-1: monocyte chemoattractant protein 1; G-CSF: granulocyte colony-stimulating factor; M-CSF: macrophage colony-stimulating factor; PDGF: platelet-derived growth factor; bFGF: basic fibroblast growth factor; MMPs: Matrix metalloproteinases. Taken from¹³ with permission. © 2013 Giuseppe Maiolino et al.

Due to endothelial lesions (impaired barrier function of the endothelium), LDL particles enter the subendothelial space, where they accumulate, trapped by intimal proteoglycans. In the absence of plasma antioxidants, a part of the LDL particles is oxidized by reactive oxygen species (ROS, see 1.4) in the intima. These oxidized LDL (oxLDL) particles are pro-inflammatory and immunogenic. Furthermore, the increased expression of surface adhesion molecules by activated endothelial cells promotes circulating monocytes to bind and migrate into the intimal space. In response to different growth factors and cytokines, the monocytes differentiate into macrophages. Via their scavenger receptors, they phagocytose particularly oxLDL, turning them into so-called foam cells. Together with T lymphocytes, that also enter the intima (even though less abundantly than monocytes), and extracellularly deposited LDL cholesterol, the foam cells build fatty streaks, the first grossly visible fatty lesion in the artery wall. Over the course of years, these fatty streaks form the lipid core of atherosclerotic plaques. Additionally, mediators released from platelets, endothelial cells, and accumulating

macrophages initiate smooth muscle cells (SMCs) to migrate from the tunica media into the subintimal space and proliferate. The recruited SMCs produce extracellular matrix molecules, especially collagen, that build a fibrous cap overlying the plaque. The stability of these fibrous caps is very critical, as its thinning and structural weakening enhance the susceptibility of a plaque to rupture. The latter is the most detrimental complication of atherosclerosis, as it causes acute thrombosis at the site of the ruptured plaque, leading in most cases to complete occlusion of the blood vessel, and hence to an infarction (i.e., acute myocardial infarction) ^{5,11}.

As mentioned above, the atherogenic process is initiated by alterations in the endothelial monolayer lining the inner wall of the vasculature. Already in 1973, Russel Ross and John A. Glomset formulated in their “response to injury” hypothesis that endothelial denudation represents the first step in atherosclerosis ¹⁴⁻¹⁶. A more modern, modified approach defines so-called 'endothelial dysfunction' as an early precursor of atherosclerosis. Endothelial dysfunction functionally describes an impairment in vascular reactivity due to a shortage of bioavailable endothelial-derived nitric oxide but also encompasses a proinflammatory, proliferative, and procoagulatory milieu that promotes all stages of atherogenesis ^{17,18}. The molecular mechanisms of endothelial dysfunction are described in more detail in 1.3.3, as well as oxidative stress and inflammation, which both play a pivotal role in the alteration of endothelial function (see 1.4 and 1.5). Classical cardiovascular risk factors that lead to the development of endothelial dysfunction (and atherosclerosis) are hypercholesterolemia, diabetes mellitus, cigarette smoking, a familial predisposition, and most of all arterial hypertension.

1.1.2 Arterial hypertension

Arterial hypertension characterizes a chronically high blood pressure (BP) in the systemic arteries. Hypertension is the leading preventable risk factor for CVD (including coronary heart disease, heart failure, stroke, myocardial infarction, atrial fibrillation, and peripheral artery disease), chronic kidney disease (CKD), and cognitive impairment and represents the foremost contributor to all-cause mortality and disability in the world. In 2019, nearly 11 million deaths were attributable to high systolic BP (SBP) ⁴.

In an estimate from 2015, 3.5 billion people worldwide have non-optimal SBP levels (> 110–115 mmHg) and one in four adults suffers from hypertension (SBP \geq 140 mmHg, ca. 874 million adults) ¹⁹. Globally, the prevalence of hypertension is rising, with an emerging burden especially in low- and middle-income countries ^{19,20}. Hence, to reduce cardiovascular morbidity and mortality, adequate management of hypertension is very important, and clinical guidelines have been established that allow the diagnosis and treatment of hypertension.

The following table gives an overview of the current European and American definitions of hypertension.

Table 1-1: Comparison of European and American Society Definitions of hypertension for adults. Modified from ²¹.

	European Society of Cardiology / European Society of Hypertension (ESC/ESH) ²² (2018)	American College of Cardiology / American Heart Association (ACC/AHA) ²³ (2017)
Normal blood pressure ranges [mmHg]	Optimal: < 120/80 Normal: 120–129/80–84 High normal: 130–139/85–89	Normal: < 120/80 Elevated: 120–129/<80
Definition of hypertension [mmHg]	≥ 140/90	≥ 130/80
Hypertension stages [mmHg]	Grade 1: 140–159/90–99 Grade 2: 160–179/100–109 Grade 3: ≥ 180/110	Stage 1: 130–139/80–89 Stage 2: ≥ 140/90
Age-specific blood pressure targets [mmHg]	< 65 years: < 120–129/70–79 ≥ 65 years: < 130–139/70–79	< 65 years: < 130/80 ≥ 65 years: < 130/80

When comparing the guidelines, it is apparent that the American definition of normal and high BP is stricter than the European one. According to the ACC/AHA (American College of Cardiology / American Heart Association), normal BP should be < 120 mmHg (for SBP) and < 80 mmHg (for diastolic blood pressure, DBP), whereas in the ESC/ESH (European Society of Cardiology / European Society of Hypertension) guidelines BP ranges of 120–129 mmHg (SBP) and 80–84 mmHg (DBP) are still considered normal, and ranges of 130–139/85–89 mmHg high normal. However, they acknowledge that optimal BP is < 120/80 mmHg. Furthermore, the American cut-off for the definition of hypertension (requiring treatment) has been lowered to ≥ 130/80 mmHg in 2017, with stage 1 hypertension defined as a BP range from 130–139/80–89 mmHg and BP values ≥ 140/90 mmHg classified as stage 2 hypertension. In the European guidelines, hypertension is defined as a BP ≥ 140/90 mmHg, with BP ranges of 140–159/90–99 mmHg rated as grade 1, 160–179/100–109 mmHg as grade 2 and BP values ≥ 180/110 mmHg as grade 3 hypertension. However, the European guidelines recommend a more aggressive reduction of BP (< 130/80 mmHg) in hypertensive patients with established CVD, CKD, or diabetes mellitus (not shown) and in older patients (≥ 65 years) given their higher risk for CVD ²¹⁻²⁴.

Among the reasons for lowering the threshold for the diagnosis of hypertension in the American guidelines were clinical trial data that associated intensive SBP targets < 120 mmHg with lower rates of fatal and nonfatal major cardiovascular events (myocardial

infarction, acute coronary syndrome, stroke, heart failure or death from cardiovascular causes) in patients without diabetes mellitus but with increased CVD risk compared to the standard-treatment group with a targeted SBP of < 140 mmHg (Systolic Blood Pressure Intervention Trial, SPRINT)²⁵. Furthermore, a prospective observational study by Lewington et al. has demonstrated a strong and direct correlation between BP and CVD, with the relationship being continuous and no evidence of a threshold down to at least 115/75 mm Hg²⁶.

Two types of arterial hypertension can be distinguished: primary (or essential) hypertension and secondary hypertension. Primary hypertension is a heterogeneous, complex, and multifactorial disorder, that accounts for the vast majority of cases (> 90 %). Causes include classical risk factors such as overweight, obesity, smoking, and age, as well as dietary factors (excess alcohol consumption, high sodium chloride, and low potassium intake). Furthermore, a sedentary lifestyle, high mental stress, and a genetic predisposition contribute to the development of hypertension^{11,27,28}. In addition, in the last years, environmental pollutants (noise, particulate matter) have emerged as potent, modern risk factors for arterial hypertension^{29,30}. Secondary hypertension refers to high BP that is caused by another condition/disease (i.e., primary aldosteronism or renal artery stenosis) and accounts for 5–10 % of human hypertension^{27,28}.

1.2 The renin-angiotensin-aldosterone system (RAAS)

Several factors of the cardiovascular system determine BP, including cardiac output, blood volume, and the vascular tone. The regulation of physiological BP levels involves complex interactions of neurohumoral and local control systems like the renin–angiotensin–aldosterone system (RAAS), the sympathetic nervous system (SNS), natriuretic peptides, as well as the endothelium and the immune system. Any malfunction or dysregulation in one of these components can increase BP and promote the development of hypertension^{27,28}. The RAAS plays an important part in the pathogenesis of arterial hypertension, as it regulates sodium balance (and thus blood volume) and systemic vascular resistance.

1.2.1 Systemic and local RAAS

Classically, the RAAS is considered a circulating endocrine system, composed of angiotensinogen, renin, angiotensin-converting enzyme (ACE), angiotensin II (ATII), and the two ATII receptors (AT₁ and AT₂ receptors) (Figure 1-2)³¹.

At the beginning of the cascade stands renin, which cleaves hepatocyte-derived angiotensinogen to produce angiotensin I (ATI). Renin is synthesized and stored in the juxtaglomerular cells of the kidney, and is released into the circulation upon various stimuli

such as vasodilatation, activation of renal sympathetic nerves, a drop in renal sodium (Na^+) delivery, and decreased renal afferent arteriolar perfusion pressure^{27,28,32}. ATI is a decapeptide, which is subsequently cleaved by ACE, a membrane-bound dipeptidyl-carboxypeptidase, to form ATII. ACE is abundant on the surface of endothelial cells (ECs), particularly on those of the lung^{33,34}. ATII, an octapeptide, is the major bioactive component of the RAAS, that exerts its function primarily via two receptors, the angiotensin II receptor type 1 (AT_1R) and angiotensin II receptor type 2 (AT_2R), which have opposing functions³⁵. The main receptor for ATII is the AT_1R , which regulates most of the physiological but also pathophysiological functions, and is thus central to the pathogenetic role of the RAAS in hypertension (see also 1.2.2)³⁶. First of all, ATII-mediated stimulation of the AT_1R causes vasoconstriction of blood vessels, which directly leads to an increase in BP. Furthermore, ATII causes salt and water retention through direct actions on the kidneys by stimulating sodium reabsorption in the proximal tubule and indirectly by inducing the adrenal glands to release the mineralocorticoid aldosterone^{27,37,38}. Aldosterone enhances renal sodium reabsorption and potassium secretion by binding to nuclear mineralocorticoid receptors (MRs), whose activation leads to the synthesis and insertion of ionic transport systems into the distal tubules and collecting ducts of the nephron³⁹. In addition, ATII reduces renal blood flow through constriction of renal efferent arterioles, promotes the sensation of thirst in the central nervous system (CNS), and stimulates the secretion of vasopressin (also antidiuretic hormone, ADH) from the posterior lobe of the pituitary gland. The release of the latter increases the amount of reabsorbed water from the filtrate in the kidney tubules, thereby elevating the blood volume^{11,40}. Hence, all of the ATII-caused effects mediated by the AT_1R intertwine to ultimately lead to an increase in BP (Figure 1-2).

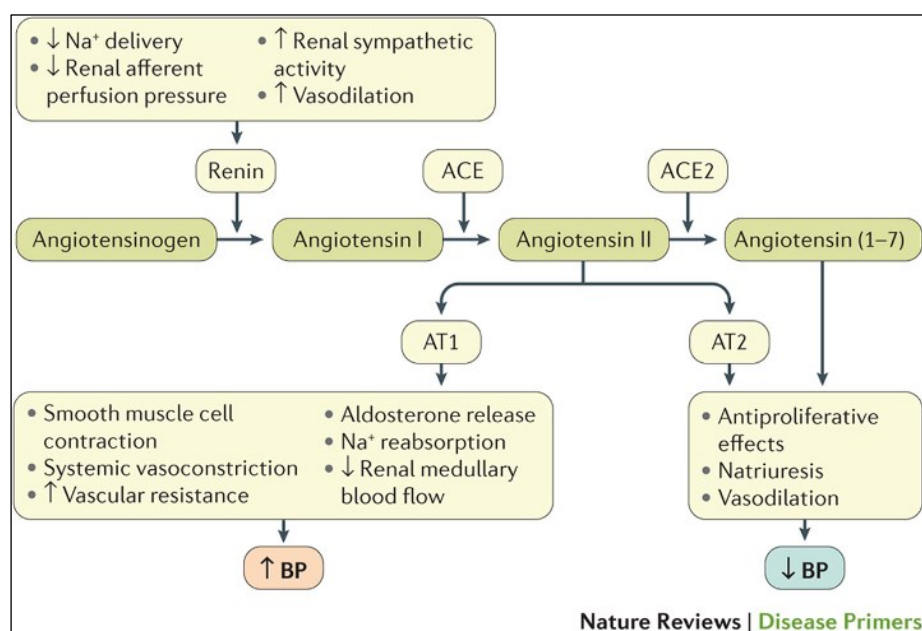


Figure 1-2: Control of blood pressure by the systemic (circulating) renin-angiotensin-aldosterone system (RAAS). Angiotensin II, the major bioactive peptide of the RAAS, is the product of sequential enzymatic cleavages of angiotensinogen. Main stimuli for the cascade-initiating protease Renin are a drop in BP, reduced renal perfusion, and catecholamines. ATII exerts its BP increasing effects via the predominant AT₁ receptor, whose activation culminates in vasoconstriction, water, and salt retention. Taken from ²⁸ with permission. © 2018, Macmillan Publishers Limited.

In contrast, activation of the AT₂R by ATII has opposite effects, causing vasodilatation, natriuresis, and inhibition of cell proliferation. Thus, the AT₂R seems to play a counterregulatory protective role in the regulation of sodium excretion and BP (Figure 1-2) ³⁵. However, the expression of the AT₂R is relatively low in comparison to the AT₁R, with a predominant role during fetal development ^{41,42}.

ACE2, a homologue of ACE, has been discovered as a relatively new component of the RAAS ⁴³. It metabolizes ATII into angiotensin(1-7) (and ATI into angiotensin(1-9)). Unlike ATII, angiotensin(1-7) exerts cardiorenal protective effects like vasodilatation, natriuresis, antiproliferative and antigrowth effects on vascular SMCs (VSMCs), cardiac myocytes, fibroblasts, and glomerular and proximal tubular cells. It predominantly acts through Mas1, the main receptor for angiotensin(1-7) ^{28,44}.

Since the medical approval of the ACE inhibitor captopril in 1980, the RAAS has been a therapeutic target for CVD ⁴⁵. Together with the later discovered AT₁R antagonists (sartans), ACE inhibitors are still used as first-line antihypertensives. Other drugs targeting the RAAS are renin inhibitors (e.g., aliskiren) and MR antagonists (e.g., spironolactone for the treatment of resistant hypertension) ^{22,23}.

The discovery that components of the RAAS (including enzymes, ATII, and ATII receptors) are formed and released from peripheral tissues that do not belong to the classical RAAS expanded the traditional concept of a solely circulating RAAS by the presence of an additional local or tissue RAAS ⁴⁶. A local RAAS exists in diverse tissues and organs,

including the heart, vasculature, brain, kidney, macrophages, and adipose tissue, as well as in the reproductive system⁴⁷⁻⁵³. In contrast to the systemic RAAS, which provides immediate hemodynamic stability through rapid changes in fluid balance, blood flow, and BP, the tissue RAAS is involved in chronic modulation of BP through functional and structural changes. Locally synthesized ATII exerts paracrine and autocrine effects mediating cell-specific effects on cell growth, apoptosis, cell migration and differentiation, ROS production, as well as extracellular matrix remodeling^{46,54}.

1.2.2 ATII signal transduction in the cardiovascular system

ATII exerts its biological effects via two receptors, the AT₁R and AT₂R, which belong to the 7-transmembrane G protein-coupled receptors (GPCRs) superfamily⁵⁵. The AT₁R predominates over the AT₂R and is abundantly expressed in various tissues of the cardiovascular system including the heart, kidney, vascular smooth muscle, and endothelium. Only in rodents, the AT₁R exists in two isoforms, AT_{1a}R and AT_{1b}R, which share over 90 % sequence homology but are products of distinct genes (*Agtr1a* and *Agtr1b*) that are differentially expressed and regulated⁵⁶⁻⁵⁸. The AT_{1a}R is the closest homologue to the human AT₁R and prevails in most tissues, except for the anterior pituitary gland and adrenal zona glomerulosa, where AT_{1b}R expression dominates⁵⁹. In the cardiovascular system, the AT_{1a}R regulates BP and contributes to the development of atherosclerosis and aortic aneurysms, whereas the AT_{1b}R seems to regulate BP in the absence of the AT_{1a}R^{36,59-61}.

Nowadays, ATII is no longer considered a pure vasoconstrictor but a "growth-factor" like hormone that employs multiple signaling pathways to influence numerous processes that contribute to the development and progression of CVD, ranging from hypertrophy, endothelial dysfunction, cardiac remodeling, fibrosis, inflammation to oxidative stress⁶².

Figure 1-3 gives an overview of the AT₁R- and AT₂R-mediated effects of ATII in the vessel wall.

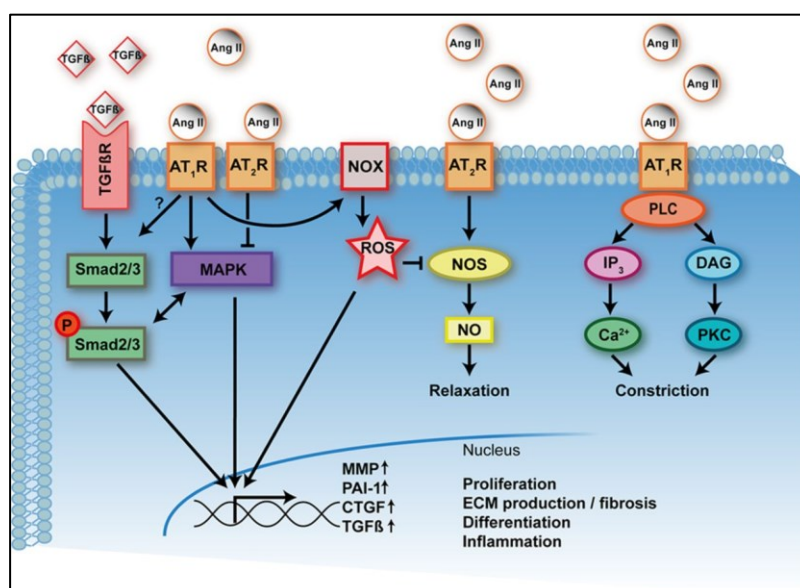


Figure 1-3: AT₁R- and AT₂R-mediated effects of ATII in the vessel wall. AT₁R-mediated signaling is complex and involves various intracellular signaling pathways as well as crosstalk with other signaling cascades, all ultimately inducing vasoconstriction, endothelial dysfunction, inflammation, growth, and vascular remodeling. A key pathway activated through the AT₁R is NADPH (nicotinamide adenine dinucleotide phosphate) oxidase-dependent ROS generation in VSMCs and ECs. Via redox signaling in the vasculature, ROS contribute to the transcriptional regulation of target genes (e.g., MMP: matrix metalloproteinase; PAI-1: plasminogen-activator inhibitor-1; CTGF: connective tissue growth factor; TGF- β : transforming growth factor β) and thus to the development of CVD and end-organ damage. Taken from ⁶³ with permission. © 2015, Wolters Kluwer Health.

ATII-induced vasoconstriction is mainly mediated by AT₁R-coupled G_q proteins that activate phospholipase C (PLC), leading to the generation of inositol trisphosphate (IP₃) and diacylglycerol (DAG) from membrane phosphatidylinositol 4,5-bisphosphate (PIP₂). These second messengers in turn release calcium (Ca²⁺) from internal stores (i.e., sarcoplasmic reticulum) and activate protein kinase C (PKC). Both stimuli lead to the contraction of VSMCs by triggering the phosphorylation of myosin light chains (MLCs), a prerequisite for the formation of cross-bridges between myosin heads and actin filaments ⁶⁴⁻⁶⁶.

Furthermore, the cardiovascular AT₁R activates intracellular protein kinases, including the mitogen-activated protein kinase (MAPK) family (consisting of extracellular signal-regulated kinase (ERK), c-Jun N terminal kinase (JNK), and p38MAPK). MAPKs are associated with the ATII-induced hypertrophic response of VSMCs, as their activation induces transcription factors that initiate the expression of proliferation and cell growth-promoting genes (e.g., transforming growth factor β , TGF- β) ^{67,68}. In addition to that, ATII has been shown to activate the Smad pathway via AT₁Rs in VSMCs, independently of TGF- β , leading to the upregulation of connective tissue growth factor (CTGF) and extracellular matrix (ECM) proteins, thereby contributing to the profibrogenic effects of ATII in vascular diseases ⁶⁹.

Besides, the AT₁R has been shown to directly stimulate the Janus kinase/signal transducers and activators of transcription (JAK/STAT) pathway, which has been implicated in ATII-induced nuclear transcriptional changes leading to VSMC growth and modulated immune

effector mechanisms^{70,71}. Importantly, ATII also induces nuclear factor- κ B (NF- κ B) activity and NF- κ B-related genes, enhancing inflammatory and proliferative processes^{72,73}.

Another crucial signaling pathway through the AT₁R in the cardiovascular system is activation of nicotinamide adenine dinucleotide phosphate (NADPH) oxidase in VSMCs and ECs, leading to the formation of ROS (see 1.4)⁷⁴⁻⁷⁶. ATII uses ROS as specific second messengers to influence many of its downstream signaling targets. Activation of these redox-sensitive pathways regulates vascular cell growth, proinflammatory genes, and the production of ECM proteins. In case of hyperactivation of NADPH oxidases, excessive ROS are generated, contributing to vascular damage and the development of CVD⁷⁷. Besides, the reduction of bioavailable nitric oxide (\bullet NO) by ROS results in vasoconstriction. The interplay of ATII, oxidative stress, and inflammation will be explained in more detail in section 1.5.2.

As mentioned above, the AT₂R counteracts the actions of the AT₁R and promotes vasorelaxation through protein kinase A (PKA)-dependent endothelial nitric oxide synthase (eNOS) activation^{35,78}.

1.3 The endothelium as major regulator of vascular tone

The artery wall of larger blood vessels is made up of three layers: the tunica interna (short *intima*, inner layer), the tunica media (short *media*, middle layer), and the tunica externa (short *adventitia*, outer layer)⁷⁹. The intima contains a single layer of flat endothelial cells (the endothelium) resting on a basal lamina, which is surrounded by fine collagen fibers and a fenestrated elastic membrane, the elastica interna. The media is a dense layer of smooth muscle cells and elastic fibers and the adventitia is comprised of connective tissue, mostly elastic and collagen fibers, that attaches the vessel to its environment¹¹. Lining the entire vascular system, the endothelium makes up 6×10^{13} of the body's cell count, amounts to 1.5 kg in mass and 1000 m² in surface area, and can be thus regarded as an autonomous organ⁸⁰. However, for a long time, the endothelium was only considered a passive barrier for blood cells and macromolecules to prevent their diffusion into the interstitial space. This view tremendously changed with the discovery that endothelial cells themselves release a host of vasoactive substances that modulate the contractile activity of adjacent smooth muscle cells, leading to the current view of the endothelium as a highly dynamic endocrine organ of its own⁸¹. Endothelial cells produce both vasodilatory (nitric oxide (\bullet NO), prostacyclin (PGI₂), endothelium-derived hyperpolarizing factor (EDHF)) and vasoconstrictive substances (Endothelin-1 (ET-1), locally generated ATII, thromboxane (TXA₂), prostaglandin A₂ (PGA₂)), and the proportion of these factors determines the final effect of the endothelium on vascular tone^{28,79}. (Aside from this local regulation, the vascular tone is also modulated by the autonomic innervation of blood vessels. Neural mechanisms mainly include sympathetic

fibers which innervate the adventitia of (nearly) all arteries, arterioles and veins in the body^{82,83}. Using noradrenaline as neurotransmitter, activation of these nerves causes vasoconstriction due to α -adrenoreceptor-mediated contraction of adjacent VSMCs. This neural control of the circulation is especially important in situations wherever a rapid adaption of regional blood flow is needed, e.g., the transition from a supine to standing position^{82,84}. By contrast, the influence of parasympathetic neurons on vascular tone is minor as most blood vessels have no or little vagal innervation^{82,85}.)

From all the endothelial substances mentioned above, none plays such an outstanding role in the maintenance of basal vasodilator tone of the blood vessel and BP regulation as $\bullet\text{NO}$ ^{79,86,87}. The existence of such an *endothelium-derived relaxing factor* (EDRF) was first described by Furchgott and Zawadzki in 1980, who discovered that the vasodilating substance acetylcholine (ACh) loses its relaxing potential on preparations of isolated rabbit aorta once the endothelium has been destroyed through rubbing of the intimal surface⁸⁸. Later, EDRF has been revealed to be identical with the gaseous free radical $\bullet\text{NO}$ ^{89,90}. For their discoveries, the three pharmacologists Robert F. Furchgott, Louis J. Ignarro, and Ferid Murad have been awarded the 1998's Nobel Prize for Physiology or Medicine⁹¹.

$\bullet\text{NO}$ is formed via five-electron oxidation of a terminal guanidino nitrogen atom of L-arginine, catalyzed by the enzyme $\bullet\text{NO}$ synthase (NOS, see 1.3.1)⁹². Once released from healthy endothelial cells, $\bullet\text{NO}$ diffuses to neighboring VSMCs, where it causes relaxation through activation of soluble guanylate cyclase (sGC) and generation of intracellular cyclic guanosine 3',5'-monophosphate (cGMP) (see 1.3.2)⁸⁰. Patients with essential hypertension show impaired endothelium-dependent vasodilation compared with normotensive controls, which has been attributed to a deficit in the endothelium-derived nitric oxide system^{93,94}.

Importantly, $\bullet\text{NO}$ not only acts as a potent vasodilator but also exerts several other athero-protective effects, including inhibition of VSMC proliferation, anti-aggregatory effects on platelets, inhibition of leukocyte adhesion to the endothelium, as well as reduction of cytokine-induced endothelial activation and LDL oxidation⁹⁵⁻¹⁰⁰. Thus, any deficit in bioavailable $\bullet\text{NO}$ is associated with the initiation or acceleration of the atherosclerotic process, for which endothelial dysfunction is an early predictor (see 1.3.3).

1.3.1 Nitric oxide ($\bullet\text{NO}$) synthases

$\bullet\text{NO}$ synthases (NOS) are the biological catalysts for $\bullet\text{NO}$ production. In mammals, three isoforms of NOS exist: neuronal NOS (nNOS), inducible NOS (iNOS), and endothelial NOS (eNOS). All isoforms use L-arginine as substrate, and molecular oxygen (O_2) as well as reduced nicotinamide-adenine-dinucleotide phosphate (NADPH) as co-substrates. They all require the cofactors flavin adenine dinucleotide (FAD), flavin mononucleotide (FMN), and

(6*R*)-5,6,7,8-tetrahydro-L-biopterin (BH₄), bind calmodulin (CaM), and contain heme. All NOS proteins share structural homology, but differ in tissue localization, function, and regulation (Table 1-2) ^{101,102}.

Table 1-2: •NO synthase (NOS) isoforms. Created with information derived from ¹⁰¹⁻¹⁰⁵.

Isoform	Tissue	Function	Cofactors	Regulation
nNos (NOS I)	Central and peripheral neurons Non-neuronal cells (VSMCs, cardiomyocytes)	Synaptic plasticity in the CNS Central regulation of BP Atypical neurotransmitter in the PNS	NADPH FAD FMN BH ₄ Zn ²⁺	Constitutive Ca ²⁺ CaM Phosphorylation
iNOS (NOS II)	Macrophages, neutrophils and many other cell types	Non-specific immune defense Mediation of inflammation Main mediator of drop in BP in septic shock	NADPH FAD FMN BH ₄ Zn ²⁺	Inducible, in response to LPS and cytokines Mainly regulated on the level of expression
eNOS (NOS III)	Endothelial cells Cardiomyocytes Epithelial cells Certain neurons of the brain	Vasodilation BP regulation Vasoprotection Anti-atherosclerotic effects	NADPH FAD FMN BH ₄ Zn ²⁺	Constitutive Ca ²⁺ CaM Phosphorylation

Neuronal NOS (nNOS or NOSI)

Neuronal NOS is constitutively and abundantly expressed in neuronal and skeletal muscle tissue. In the central nervous system (CNS), nNOS is involved in synaptic plasticity (learning and memory formation) and contributes to the central regulation of BP. In the peripheral nervous system (PNS), nNOS-derived •NO from nitrenergic nerves acts as an atypical neurotransmitter, mediating SMC relaxation and vasodilation. The latter mechanism is known to be of particular importance in the relaxation of corpus cavernosum and penile erection. Enzyme activity of nNOS is controlled by an increase in intracellular free Ca²⁺ and CaM binding ¹⁰².

Inducible NOS (iNOS or NOSII)

In contrast, inducible NOS is not expressed in the cell under basal conditions, but is strongly upregulated in response to bacterial lipopolysaccharide (LPS) and cytokines (e.g., interferon γ (INF- γ), tumor necrosis factor alpha (TNF- α), interleukin 1 beta (IL-1 β)) – independently of intracellular Ca²⁺ concentrations ^{102,104}. Activated immune cells, in particular monocytes/macrophages, are a major source of iNOS-derived •NO, generating 100–1000-fold more •NO than constitutive eNOS. In conjunction with their endogenous Nox2 activity to produce superoxide (O₂^{•-}, see 1.4.1), they exploit these large amounts of •NO to exert cytostatic and cytotoxic actions on parasitic target cells (e.g., viruses, bacteria, fungi, protozoa) ^{106,107}. This antimicrobial activity is mostly attributable to the formation of peroxynitrite (ONOO⁻), the highly reactive reaction product of •NO and O₂^{•-} (see 1.4.3) ¹⁰⁸.

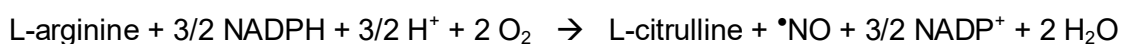
Besides immune cells, iNOS expression is also inducible in various other cell types (e.g., endothelial cells, hepatocytes, astrocytes). It is important to mention that iNOS – once induced at the wrong site and time – has detrimental consequences, including the mediation of inflammation or severe hypotension during septic shock ^{102,104}.

Endothelial NOS (eNOS or NOSIII)

Endothelial NOS, like nNOS, is a Ca²⁺-dependent constitutive enzyme that is mainly expressed in endothelial cells but is also present in cardiomyocytes, epithelial cells, and some other cell types ¹⁰². Given that eNOS is the predominant NOS isoform in the vasculature and produces most of the vascular •NO ¹⁰⁹, its structure, catalytic mechanism, and regulation will be presented in more detail in the following.

Like the other isoforms, intact eNOS is a homodimer, a modular enzyme consisting of two identical subunits (Figure 1-4). Every monomer consists of a C-terminal reductase domain, which serves as binding site for NADPH, FMN and FAD, and an N-terminal oxygenase domain, which binds the prosthetic heme group, the essential cofactor BH₄, O₂, and the substrate L-arginine. Furthermore, all NOS isoforms contain a zinc ion (Zn²⁺) at the NOS dimer interface, which is coordinated in a tetrahedral conformation as zinc tetrathiolate (Zn[S-cysteine]₄) from two CysXXXXCys motifs, one contributed by each monomer. Zinc in NOS serves a structural purpose, whereas the cysteine residues are crucially implicated in the binding site of BH₄ and L-arginine ^{102,109,110}.

A functional NOS catalyzes the electron transfer from NADPH via the flavins FAD and FMN in the C-terminal reductase domain to heme in the N-terminal oxygenase domain, where the electrons are employed to reduce and activate O₂, and to oxidize L-arginine to L-citrulline under the release of •NO:



Importantly, the electrons from the reductase domain of one monomer are transferred to the oxygenase domain of the *other* monomer (Figure 1-4). Thus, a correct enzyme dimerization is a prerequisite for proper eNOS activity and explains its "error-proneness" under conditions of oxidative stress (see 1.4.2). The electron transfer in the reductase domain is stimulated whenever the intracellular Ca²⁺ concentration strongly rises, as this enhances binding of CaM to eNOS which in turn induces a conformational change in the enzyme, displacing an auto-inhibitory loop ¹⁰². However, this mechanism also occurs in monomers and even in isolated reductase domains. The critical cofactor for the formation of active NOS dimers is heme, and it is also indispensable for the interdomain electron transfer from the flavins of one monomer to the heme of the opposite monomer. In the presence of sufficient substrate L-arginine and

cofactor BH_4 , intact NOS dimers couple their heme and O_2 reduction to the synthesis of $\bullet\text{NO}$ ^{102,109}.

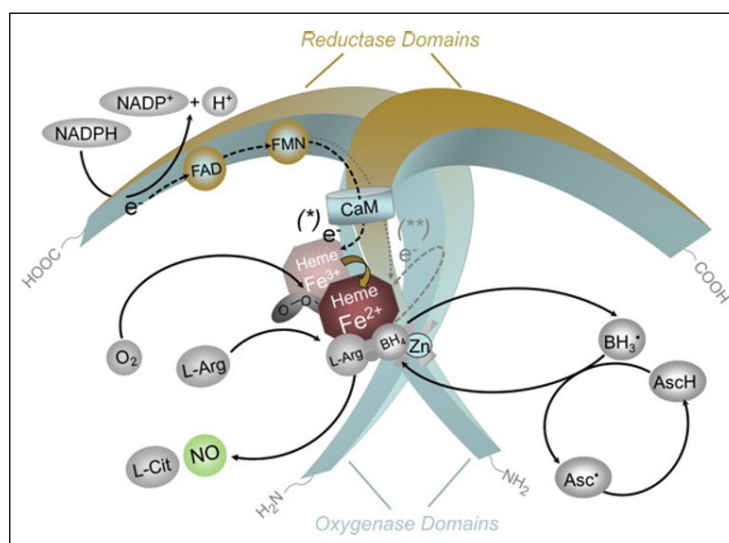


Figure 1-4: Structure and catalytic mechanism of functional (coupled) $\bullet\text{NO}$ synthase. NOS are homodimers, with each monomer containing a reductase and oxygenase domain on the C- and N-terminus, respectively. The binding of a Ca^{2+} /CaM-complex to the enzyme stimulates flavin (FAD, FMN)-mediated electron transfer from NADPH of one monomer to the heme of the opposite monomer, where the electrons are used to reduce molecular oxygen. Binding of O_2 to the catalytic heme iron is enabled by the reduction of Fe^{3+} to Fe^{2+} (formation of Fe(II)O_2). The reduced oxygen reacts with the guanidino group of the substrate L-arginine, which, via the formation of the intermediate N^{ω} -hydroxy-L-arginine, leads to the release of $\bullet\text{NO}$ with L-citrulline as byproduct. BH_4 is an essential cofactor for NOS coupled catalysis, as it acts as an electron donor to the oxyferrous complex. The oxidized BH_4 either exists as a trihydrobiopterin radical (BH_3^{\bullet}) or in its protonated form (BH_4^{+}) and is most likely recycled by a flavin-derived electron from NOS itself. Alternatively, ascorbic acid (AscH, vitamin c) could act as a reducing agent for BH_3^{\bullet} . For clarity reasons, the electron flow is only shown for one monomer. Taken from ¹⁰² with permission. © 2011, Oxford University Press.

Activity of eNOS is induced by both chemical (receptor-dependent agonists) and physical (flow-induced shear stress) stimuli. Agonists such as acetylcholine, bradykinin, and ATP (adenosine-5'-triphosphate) act on specific receptors that increase intracellular Ca^{2+} concentrations and thus promote the binding of CaM to eNOS ¹¹¹. For instance, acetylcholine binds to the endothelial muscarinic receptor mAChR₃, a G_q -coupled receptor, whose activation leads, via phospholipase C signaling, to the release of Ca^{2+} from the endoplasmic reticulum ^{112,113}. However, eNOS can be also activated in a calcium-independent manner, i.e., by phosphorylation on serine (Ser), threonine (Thr), and tyrosine (Tyr) residues. In human eNOS, important regulatory phosphorylation sites are Ser1177 and Thr495. Ser1177 is an activation site of eNOS enzyme activity, as its phosphorylation stimulates electron flow in the reductase domain and increases eNOS Ca^{2+} sensitivity. Phosphorylation of Ser1177 is mainly induced by fluid shear-stress, hormones, and growth factors (e.g., estrogen, vascular endothelial growth factor (VEGF), insulin). Depending on the primary stimulus, different downstream kinases have been identified to mediate Ser1177 phosphorylation (Estrogen, VEGF: Akt; insulin: Akt, AMP-activated protein kinase (AMPK)). On the other hand, Thr495 serves as an eNOS inactivation site and its phosphorylation reduces enzymatic activity and electron flux in the reductase domain, likely due to a

decreased affinity of CaM to the enzyme. The kinase responsible for Thr495 phosphorylation under non-stimulated conditions has been proposed to be PKC^{102,111,114,115}.

1.3.2 •NO/sGC/cGMP signaling pathway

Vascular •NO mediates its vasodilatory effect via the •NO/sGC/cGMP signaling pathway in VSMCs. Even though •NO is a free radical, its inability to react towards organic target molecules (due to radical stabilization) and its hydrophobicity allows the diffusion across cell membranes, from endothelial cells to adjacent VSMCs. On the contrary, •NO readily reacts with other radicals in a diffusion-controlled process as well as with transition metals to form stable •NO-complexes^{116,117}.

One of the most important ones is the heme-containing soluble guanylate cyclase (sGC) in VSMCs, which serves as an intracellular receptor for •NO. Upon binding of •NO, sGC catalyzes the conversion of guanosine-5'-triphosphate (GTP) to cGMP. A prerequisite for this •NO-induced activation of sGC is the presence of the heme iron in the reduced ferrous (Fe^{2+}) state^{80,118}. The main cGMP effector responsible for SMC relaxation is the cGMP-dependent kinase I (cGK-I or protein kinase G type 1 (PKG1), Figure 1-5).

The contractile state of VSMCs is majorly regulated by the amount of intracellular free Ca^{2+} . When intracellular Ca^{2+} levels rise, free Ca^{2+} binds to CaM, which in turn activates an enzyme called myosin light chain kinase (MLCK). MLCK phosphorylates MLCs in the presence of ATP. As mentioned above (see 1.2.2), phosphorylation of MLCs enables the formation of cross-bridges between myosin heads and actin filaments and thus leads to VSMC contraction and vasoconstriction.

cGK-I mediates VSMC relaxation by phosphorylation of a number of target proteins (e.g., IRAG: IP_3R -associated cGMP kinase substrate, Ca^{2+} -activated K^+ -channels, RhoA: Ras homolog family member A), culminating in pathways that reduce intracellular Ca^{2+} and promote the dephosphorylation of MLCs (via activation of myosin light chain phosphatase (MLCP))¹¹⁹. Another cGK-I substrate in VSMCs is vasodilator-stimulated phosphoprotein (VASP), which is phosphorylated at serin 239. Analysis of P-VASP can be used as a reporter of cGK-I activity to monitor endothelial integrity and activity of the •NO-cGMP pathway¹²⁰.

The actions of cGMP are rapidly terminated by phosphodiesterases (PDEs), which hydrolyze cGMP to guanosine monophosphate (GMP). In VSMCs, the predominant isoform is PDE5¹²¹.

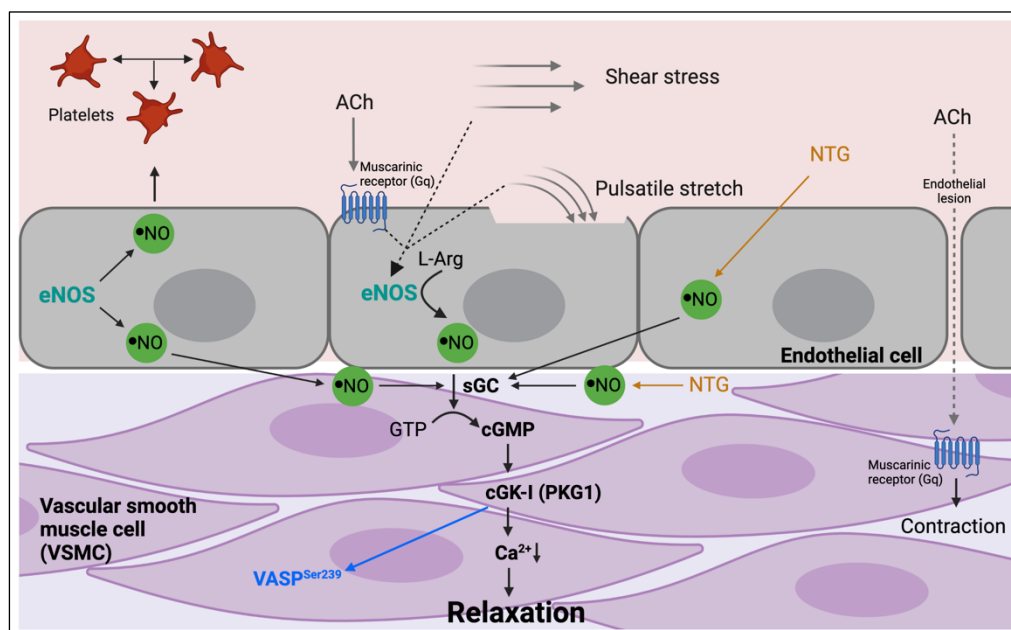


Figure 1-5: •NO/sGC/cGMP pathway of VSMC relaxation. •NO is synthesized by eNOS in endothelial cells upon physical stimuli (fluid shear stress, pulsatile stretch) or by receptor-dependent agonists such as acetylcholine (ACh). •NO is released into the bloodstream (where it inhibits platelet aggregation) and diffuses abluminally into the media, where it activates the soluble guanylate cyclase (sGC) of VSMCs. sGC forms cyclic guanosine 3',5'-monophosphate (cGMP), which in turn stimulates the cGMP-dependent kinase I (cGK-I or PKG1). cGK-I activates pathways that reduce intracellular Ca^{2+} concentrations, leading to VSMC relaxation and vasodilation. cGK-I also directly phosphorylates vasodilator-stimulated phosphoprotein (VASP) at serine 239, which serves as a biochemical marker for the integrity and activity of the •NO-cGMP pathway. The described mechanism represents the "endothelium-dependent relaxation" of blood vessels by •NO. However, vasodilation can also be induced by nitroglycerin (NTG), an organic nitrate, that serves as a •NO donor and causes vasorelaxation via the same signaling mechanism as eNOS-derived •NO, except for bypassing the endothelium ("endothelium-independent relaxation")¹²². Intra-arterial infusion of acetylcholine is used in clinical endothelial function testing, because – depending on the functional integrity of the endothelium – acetylcholine either causes VSMC relaxation or contraction (so-called *paradoxical vasoconstriction*)¹²³. The latter can be explained by direct stimulation of muscarinic receptors in the media. Created with [BioRender.com](https://www.biorender.com).

1.3.3 Endothelial dysfunction

In case of an endothelial dysfunction, the endothelium loses its functional integrity due to an imbalance of vasoactive substances in favor of vasoconstrictors such as ATII or ET-1. Hemodynamically, endothelial dysfunction is an impairment of endothelium-dependent vasodilation, in contrast to normal vascular relaxation in response to endothelium-independent nitrovasodilators such as nitroglycerin (NTG, Figure 1-5)¹¹⁹. Mostly, it is caused by an inability of the endothelium to generate adequate amounts of bioactive •NO¹⁰². As •NO also reduces platelet aggregation and mediates anti-proliferative actions on VSMCs as well as anti-adhesive effects on endothelial cells, an endothelial dysfunction not only results in vasoconstriction but is also associated with a pro-inflammatory and pro-atherothrombotic phenotype. Endothelial dysfunction is a hall-mark of most cardiovascular risk factors (e.g., arterial hypertension, diabetes mellitus, hypercholesterolemia, smoking) and serves as an early indicator of atherosclerosis and future cardiovascular events¹²⁴.

In vivo, endothelial function can be assessed by both invasive and non-invasive techniques. For example, the relaxation potential of coronary vessels can be tested by quantitative

coronary angiography upon infusion of acetylcholine^{80,124}. Alternatively, endothelial function can be measured non-invasively by flow-mediated dilation (FMD) of peripheral resistance vessels (e.g., in the forearm), which has been demonstrated to closely correlate with coronary artery endothelial function¹²⁵. The FMD procedure involves the recording of a baseline diameter of the brachial artery by ultrasound, followed by an interruption of blood flow by inflation of a BP cuff for 5 min. Upon release of the cuff, a sudden increase in blood flow (reactive hyperemia) causes shear stress on the endothelial cells, leading to the release of •NO. Thus, the degree of vasodilation (detected by ultrasound) is a marker of •NO bioavailability^{79,124}. An established technique to assess endothelial function *ex vivo* is the isometric tension method, where isolated blood vessels are subjected to cumulative doses of acetylcholine (see 4.2.6). An endothelial dysfunction manifests through a right-shift of the relaxation curve (i.e., plotting the percentage of relaxation against the dose of acetylcholine)¹²⁴.

Several mechanisms come into question for reductions in bioavailable •NO, including attenuated activity and/or expression of eNOS or a decreased sensitivity of VSMCs for •NO. However, a dominant role in the development of endothelial dysfunction plays the direct inactivation of •NO by the radical superoxide ($O_2^{\bullet-}$)^{80,126,127}. Indeed, a multitude of studies has demonstrated that endothelial dysfunction, encompassed by CVD such as atherosclerosis, hypertension, or heart failure, is associated with a significantly enhanced production of vascular ROS, particularly $O_2^{\bullet-}$ ¹²⁸⁻¹³⁰. The phenomenon that increased degradation of endogenous, vasoprotective •NO by vascular $O_2^{\bullet-}$ contributes to abnormal vascular reactivity resulted in the formulation of the "oxidative stress hypothesis" of endothelial dysfunction¹²⁶. This concept is substantiated by results from studies demonstrating that acute administration of antioxidants such as vitamin c improves endothelial dysfunction in patients suffering from classical cardiovascular risk factors like smoking, diabetes mellitus, or hypertension¹³¹⁻¹³³. In addition, vitamin c deficiency has been shown to correlate with cardiovascular outcomes in patients with coronary artery disease. In a study from 2001, patients who showed a strong improvement of endothelial dysfunction in response to vitamin c more often sustained an adverse cardiovascular event (e.g., cardiovascular death, myocardial infarction, ischemic stroke, coronary angioplasty, and coronary or peripheral bypass operation) within the next 4.5 years compared to individuals with only a low vitamin c effect¹³⁴. This finding shows that endothelial dysfunction possesses also a prognostic value for cardiovascular events and emphasizes that oxidative stress plays a causative role in its development¹³⁵.

1.4 Oxidative stress

ROS are a family of oxygen-derived free radicals and related oxidants that are ubiquitously found in all aerobic organisms¹¹⁷. Common ROS include molecules such as superoxide radical anion ($O_2^{\bullet-}$), hydroxyl radical ($\bullet OH$), peroxy radical ($ROO\bullet$), hydrogen peroxide (H_2O_2), organic peroxides ($ROOH$), and hypochlorite (ClO^-). Similarly, reactive nitrogen species (RNS) are short-lived nitric oxide-derived compounds, including $\bullet NO$, nitrogen dioxide radicals ($\bullet NO_2$), or peroxynitrite ($ONOO^-$)^{136,137}. Together, ROS and RNS are often referred to as reactive oxygen and nitrogen species (RONS).

Importantly, ROS are not per se harmful. Depending on their local concentration, they exert different actions. At moderate concentrations, they act as signaling molecules in redox-sensitive processes involving reversible oxidative protein modifications ("redox signaling", e.g., altered activity of protein kinases or transcription factors through oxidation of critical thiol residues¹³⁸). However, at higher concentrations they cause irreversible oxidative damage to biological macromolecules such as proteins, lipids, and DNA, impairing normal cellular function¹¹⁷. Thus, under physiological conditions, ROS production needs to be tightly controlled to maintain a redox homeostasis, the healthy physiological balance between reduced and oxidized biomolecules in a cell^{139,140}. For this purpose, the body possesses endogenous antioxidant defense mechanisms (e.g., superoxide dismutase (SOD), glutathione peroxidase (GPx), catalase, and non-enzymatic compounds like vitamin c, α -tocopherol, and glutathione) counteracting the potential harmful effects of ROS¹⁴¹.

The term "oxidative stress" refers to a state of imbalance between antioxidants and ROS in favor of the latter, caused by either antioxidant depletion and/or excess cellular ROS production and accumulation¹³⁶. Oxidative stress is a known molecular trigger for neurodegenerative and many CVDs such as hypercholesterolemia, atherosclerosis, hypertension, diabetes, and heart failure¹⁴²⁻¹⁴⁴.

The main sources of ROS in the vasculature are the NADPH oxidase (Nox), xanthine oxidase, the mitochondrial electron transport chain, and an uncoupled endothelial $\bullet NO$ synthase, of which the first and the latter will be presented in more detail in the following (see 1.4.1 and 1.4.2). Due to its ability to directly inactivate $\bullet NO$, $O_2^{\bullet-}$ plays a predominant role among all vascular-derived ROS. In fact, $\bullet NO$ and $O_2^{\bullet-}$ react with each other at (almost) diffusion-controlled rates to form $ONOO^-$, one of the most potent biological oxidizing agents (see 1.4.3).

1.4.1 NADPH oxidase

NADPH oxidases (Nox) are enzymes that catalyze the electron transfer from NADPH to molecular oxygen, thus generating superoxide:



They are the only enzyme family, whose sole physiological purpose is the production of ROS¹⁴⁵. Historically, Nox2 was the first Nox isoform to be identified, as part of the bacterial defense of neutrophils and macrophages mediating the respiratory burst^{146,147}. Hence, Nox2 is often referred to as 'phagocyte Nox' and was initially described as gp91phox (glycosylated protein of 91 kDa phagocyte oxidase).

Nowadays, seven catalytic homologues are known within mammals (Nox1-5, Duox 1-2). Four of them, Nox1, Nox2, Nox4, and Nox5, are found in the vasculature, named after the largest transmembrane catalytic subunit (Figure 1-6). Structurally, this core region is highly conserved between all Nox enzymes, comprising an intracellular NADPH and FAD (flavin adenine dinucleotide) binding sites, six transmembrane domains, and four heme-binding histidines^{145,148}.

Despite their similar structure and enzymatic function, Nox family members differ in their mechanism of activation, subunit assembly, and cellular distribution. Nox1 is predominantly expressed in VSMCs, and to a lower extent in ECs. Nox2 mainly shows a phagocyte-specific tissue expression but has been also detected in ECs and adventitial fibroblasts. Nox4 is present in all layers of the vascular wall (intimal ECs, medial VSMCs, and adventitial fibroblasts), being the predominant isoforms in ECs. Nox5 is expressed in healthy ECs and VSMCs of atherosclerotic vessels^{145,149,150}.

Active Nox enzymes are multi-protein enzyme complexes, composed of several membrane-bound and cytosolic subunits. When present alone, the transmembrane catalytic subunit is not active. Only after activation by an isoform-specific assembly of different subunits, Nox enzymes become active and catalyze the electron transfer across biological membranes, from NADPH, via FAD and the two Fe-hemes to O₂¹⁵¹. For example, Nox2 activity requires the membrane-associated protein p22phox (phox: phagocyte oxidase) and the cytosolic activators p47phox, p67phox, and rac-GTPase. A key role in the translocation of the cytosolic subunits to the membrane plays the PKC-dependent phosphorylation of p47phox (Figure 1-6)¹⁵². Active p47phox is able to bind both p67phox and p22phox, enabling a steady association between p67phox and Nox2, which is needed for initiation of the Nox2 catalytic activity^{153,154}. Furthermore, Nox2 oxidase activity also depends on membrane binding of the small GTPase rac, which occurs upon cellular activation, yet separately from p47phox^{155,156}. Similarly, the activation of Nox1 relies on p22phox, two cytosolic factors (p47phox and Noxa1) as well as rac. An exemption is Nox4, which is constitutively active and only associates with the membrane-bound p22phox subunit¹⁵⁷. The Nox5 isoform functions independent of any maturation factors with its activity is regulated by calcium (Ca²⁺)¹⁵⁸. The

physiological functions of Nox5 are less well characterized than the other isoforms due to the lack of the *Nox5* gene in rodents.

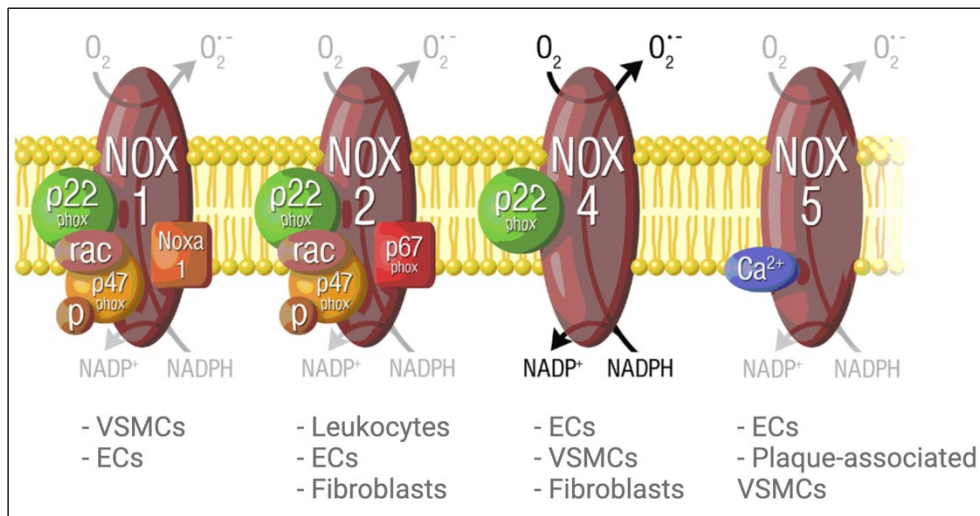


Figure 1-6: Composition and cellular distribution of NADPH oxidase (Nox) enzyme complexes in the vasculature. All Nox isoforms produce superoxide by electron transfer from NADPH to molecular oxygen. The isoforms Nox1, Nox2 (also termed gp91phox), and Nox4 are permanently associated with p22phox. Yet, only Nox1 and Nox2 depend on cytosolic factors (Nox1: p47phox, Noxa1, rac; Nox2: p47phox, p67phox, rac) for full activation, in contrast to Nox4, which is constitutively active. Nox5 is functional without any membrane-bound or cytosolic components but requires Ca²⁺ for activation. Nox enzymes can be located either within cells (e.g., vesicles, endosomes, caveolae) or at the plasma membrane, leading to intracellular or extracellular O₂^{•-} release, respectively^{148,159}. Taken from¹⁵⁰ with permission. © 2008 American College of Cardiology Foundation. Published by Elsevier Inc.

Various external stimuli regulate cellular Nox activity, including vasoactive substances like ATII or ET-1, growth factors, cytokines, and physical stimuli such as shear stress on the endothelium. As briefly mentioned in 1.2.2, ATII-mediated increase in NADPH oxidase activity significantly contributes to oxidative stress and vascular damage in arterial hypertension^{77,160}. Functionally, ATII has been associated with all vascular Nox isoforms, Nox1¹⁶¹⁻¹⁶³, Nox2^{164,165}, Nox4¹⁶⁶, and Nox5¹⁶⁷.

1.4.2 Uncoupled eNOS

Under conditions of oxidative stress, eNOS can become a ROS source itself, converting from a •NO to an O₂^{•-} producing enzyme. This phenomenon is known as 'NOS uncoupling', because, molecularly, the electron flow from the reductase domain is no longer coupled with the NOS substrate L-arginine and cofactor BH₄ to form •NO, but is diverted to reduce molecular oxygen, resulting in the production of O₂^{•-}^{102,109}.

Uncoupling of eNOS has been associated with endothelial dysfunction from patients with T2DM¹⁶⁸, hypercholesterolemia¹⁶⁹, chronic smoking¹⁷⁰, and essential hypertension¹⁷¹. Particularly concerning the latter, eNOS uncoupling has been also demonstrated in several animal models of increased BP, including genetically¹⁷², DOCA (deoxycorticosterone acetate)-salt¹⁷³, and ATII-induced hypertension¹⁷⁴.

Pathophysiological factors leading to eNOS uncoupling mainly imply insufficient cellular levels of L-arginine and BH₄, accumulation of asymmetric dimethylarginine (ADMA), and S-glutathionylation of eNOS. In this regard, *redox switches* in eNOS play a key role, as they confer alterations in enzymatic eNOS activity and thereby substantially contribute to eNOS uncoupling (Figure 1-7)^{175,176}.

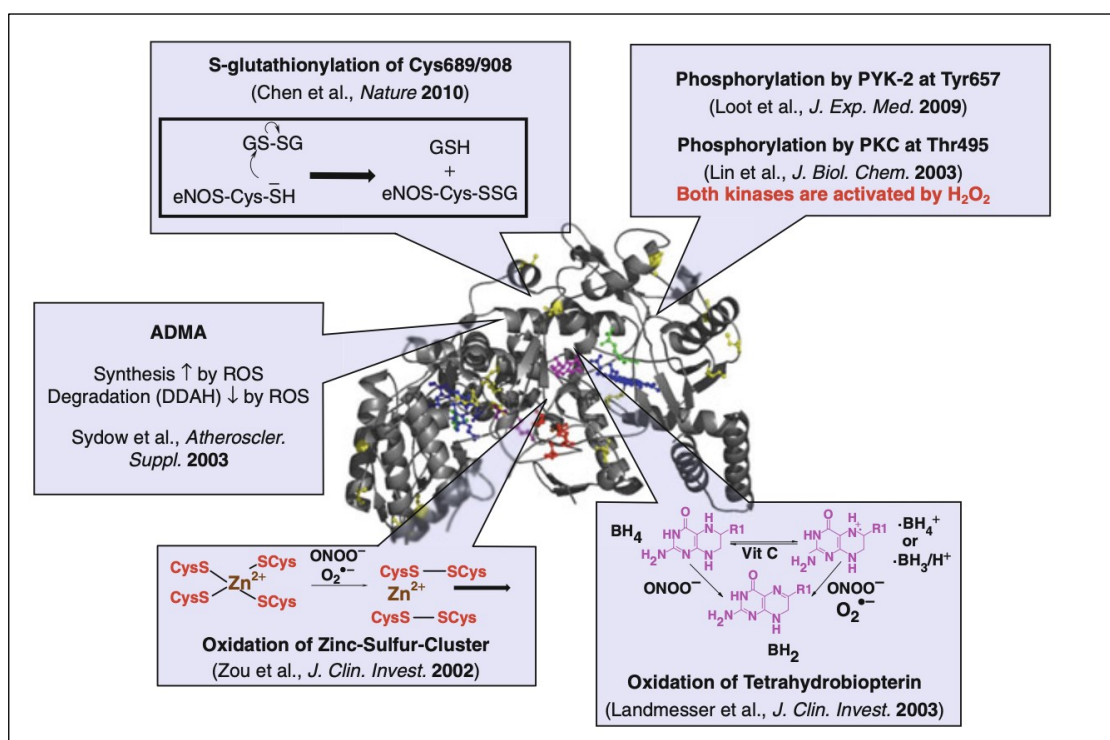


Figure 1-7: Redox regulation of eNOS. Five main *redox switches* exist in eNOS, which significantly contribute to enzyme activity during oxidative stress. Oxidative depletion of the cofactor BH₄, oxidative disruption of the zinc-thiolate complex involved in BH₄ and L-arginine binding, and S-glutathionylation of essential cysteine residues have been causally associated with eNOS uncoupling, a process where eNOS reduces O₂ instead of L-arginine, switching it from •NO to O₂^{•-} production. Asymmetric dimethylarginine (ADMA) as well as PKC- and protein tyrosine kinase-2 (PYK-2)-dependent phosphorylation cause inhibition/inactivation of eNOS. PKC and PYK-2 are both induced by ROS. Taken from¹³⁶ with permission. © 2014, Springer-Verlag Berlin Heidelberg.

One of the most important pathways causing eNOS uncoupling, and representing a fundamental redox switch, is the oxidative depletion of the essential cofactor BH₄^{102,109,175}. Of particular importance is hereby ONOO⁻, which can oxidize BH₄ to both the BH₃[•]/BH₄^{•+} radical and BH₂ (7,8-dihydrobiopterin)^{177,178}. Oxidative degradation not only reduces BH₄ bioavailability, but BH₂ additionally competes with BH₄ for binding to the enzyme¹⁷⁹. In contrast to BH₂, which can be only recycled by energy-consuming enzymatic reactions, the BH₃[•]/BH₄^{•+} radical can be re-reduced by vitamin c^{178,180}, providing an explanation for the beneficial effect of the latter in CVD patients with endothelial dysfunction (see 1.3.3). Furthermore, insufficient vascular BH₄ bioavailability and eNOS uncoupling may also result from decreased levels of the BH₄ recycling enzyme dihydrofolate reductase (DHFR) or BH₄ synthesizing enzyme GTP-cyclohydrolase-1 (GCH1), whereby the expression of the latter itself is redox-sensitive^{175,176,181,182}.

Related to this, another redox regulatory pathway and cause of eNOS uncoupling is the oxidative disruption of the zinc-thiolate cluster ($\text{Zn}[\text{S-cysteine}]_4$), which is crucially involved in the binding site of BH_4 and L-arginine (see 1.3.1). Again, ONOO^- seems to play a dominant role as oxidizing agent^{176,183}.

ADMA is an endogenous L-arginine methyl derivative that competes with L-arginine for the substrate-binding site, thereby inhibiting eNOS enzymatic activity. High ADMA levels have been associated with eNOS uncoupling, however final proof for a causal interaction between eNOS and ADMA beyond inhibition is pending¹⁸⁴. Nevertheless, vascular oxidative stress leads to significantly increased ADMA, as both the activity of the ADMA producing key enzyme protein arginine N-methyltransferase (PRMT) and degrading enzyme dimethylarginine dimethylaminohydrolase (DDAH) are redox-sensitive (and are enhanced and reduced, respectively)^{176,185,186}.

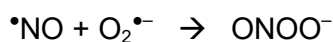
Another major redox switch in control of eNOS uncoupling is S-glutathionylation of the enzyme at cysteine residues that are important for a proper eNOS function. Mechanistically, glutathione disulfide (GSSG), built under conditions of oxidative stress, reacts with one or more cysteine residues of the reductase domain, forming glutathione (GSH) and S-glutathionylated eNOS in a redox reaction. With this oxidative modification, eNOS no longer produces $\bullet\text{NO}$ but switches to $\text{O}_2^{\bullet-}$ generation^{175,187}.

As mentioned in 1.3.1, eNOS activity is modulated by phosphorylation. Protein tyrosine kinase-2 (PYK-2) and PKC are kinases mediating inhibitory phosphorylations of eNOS (at Tyr657 and Thr495, respectively). Both kinases are activated by oxidative stress, thus representing another redox regulatory mechanism in eNOS activity. However, regarding eNOS uncoupling, only PKC has been associated with eNOS-derived superoxide production^{188,189}.

In summary, all of the redox switches in eNOS markedly contribute to the uncoupling of the enzyme. However, their activity depends on oxidants and reductants – under conditions of oxidative stress, they favor eNOS uncoupling due to the formation of ROS and RONS from other sources. Indeed, several studies demonstrated improved eNOS function and recoupling of eNOS, when primary sources are either genetically deleted (e.g., *p47phox*^{-/-} and *gp91phox*^{-/-} mice^{173,190,191}) or pharmacologically inhibited (e.g., AT_1R antagonists, PKC inhibitors¹⁹²⁻¹⁹⁴).

1.4.3 Peroxynitrite

ONOO^- is formed in a nearly diffusion-controlled reaction between $\bullet\text{NO}$ and $\text{O}_2^{\bullet-}$ ($\sim 10^{10} \text{ M}^{-1}\text{s}^{-1}$) that even outcompetes the detoxification of $\text{O}_2^{\bullet-}$ by SOD ($\sim 2 \times 10^9 \text{ M}^{-1}\text{s}^{-1}$)^{136,195}.



Even though ONOO^- is no radical, it is one of the most potent biological oxidizing agents (100–1000-fold more potent than H_2O_2) and is thus highly cytotoxic. A substantial part of ONOO^- 's cytotoxicity can be explained by homolysis of its protonated form, peroxyntrous acid (ONOOH). Importantly, this is even relevant under physiological pH conditions, at which ONOO^- and ONOOH coexist ($\text{pK}_a=6.8$ at 37°C). The reaction yields $\bullet\text{OH}$ and $\bullet\text{NO}_2$ in a solvent cage from which the two radicals can either recombine to form NO_3^- or diffuse into the bulk solution as free radicals (Figure 1-8) ^{116,117,196}.

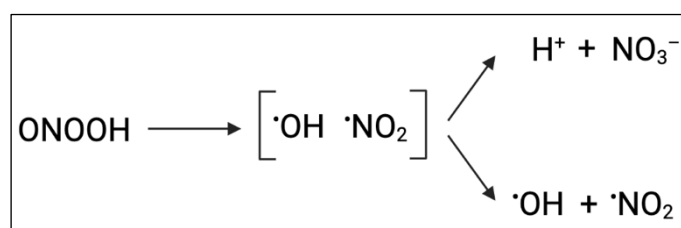


Figure 1-8: Proton-catalyzed decay of peroxyntrite. Homolytic cleavage of ONOOH (peroxyntrous acid) generates the radical cage pair [$\bullet\text{OH}$ (hydroxyl radical) $\bullet\text{NO}_2$ (nitrogen dioxide)], which can either recombine to form nitrate (right upper reaction) or diffuse out of the solvent cage (right lower reaction). Created with BioRender.com.

The yield of $\bullet\text{OH}$ and $\bullet\text{NO}_2$ in solution is still a matter of debate but has been suggested to be $\leq 30\%$, yet significantly contribute to the cytotoxicity of ONOO^- . ¹⁹⁵ Peroxyntrite can cause oxidative damage to a variety of biomolecules including proteins, lipids, and DNA. Of particular importance are the lipid peroxidation, fragmentation/oxidation of DNA to form 8-oxoguanine, and protein modifications such as (sulf-)oxidation of methionine or cysteine residues and nitration of tyrosine residues. The latter leads to the formation of (protein-bound) 3-nitrotyrosine (3-NT), which is commonly used as a biomarker for nitro-oxidative stress ¹⁹⁷. All these reactions have a direct impact on the cell and trigger responses that can range from impaired cell signaling (e.g., due to altered enzymatic activities) to apoptosis or necrosis (e.g., due to overwhelming oxidative injury) ¹⁰⁸.

Equipped with both iNOS and Nox2 (see 1.3.1 and 1.4.1), this mechanism is particularly exploited by phagocytes such as macrophages and neutrophils that produce ONOO^- to damage or kill microorganisms ¹⁰⁸. However, extensive peroxyntrite formation has been also associated with inflammatory conditions such as systemic lupus erythematoses, rheumatoid arthritis, neurodegenerative disorders, and CVD ^{142,198-200}.

1.5 Inflammation as a mediator of arterial hypertension

Over the last years, it has become clear that inflammation is a major molecular trigger for arterial hypertension and CVD in general ¹⁴³. The close association between inflammation and CVD is underlined by the fact that patients with chronic autoimmune diseases like

rheumatoid arthritis, systemic lupus erythematoses, and psoriasis have increased cardiovascular risk²⁰¹⁻²⁰⁴, with the latter even being recognized as an independent cardiovascular risk factor^{176,205}. Strikingly, immunosuppressive treatment with mycophenolate mofetil in hypertensive patients with rheumatoid arthritis or psoriasis significantly reduced BP²⁰⁶. Conversely, high levels of inflammatory markers such as C-reactive protein (CRP), TNF- α , or IL-1 β have been associated with hypertension²⁰⁷.

Importantly, inflammation not only contributes to the pathophysiology but also to the end-organ damage of arterial hypertension (see 1.5.1). One relevant mechanism is hereby the exertion of oxidative stress and injury by immune cells. Yet, oxidative stress has been shown to initiate and/or enhance inflammatory responses itself, illustrating that oxidative stress and inflammation are inextricably linked with each other (see 1.5.2).

1.5.1 Immune cells and mechanisms of hypertensive damage

Nowadays, hypertension is regarded as an inflammatory process, which is characterized by the infiltration and accumulation of immune cells in the vasculature²⁰⁸. Interestingly, immune cells of both the innate and adaptive immune system have been implicated in hypertension: myelomonocytic cells such as monocytes/macrophages²⁰⁹ and neutrophils²¹⁰, natural killer (NK) cells²¹¹, dendritic cells (DC)²¹² as well as T²¹³ and B cells²¹⁴.

Particularly noteworthy is a 2011 study from Wenzel et al., in which the authors showed that ATII-induced hypertension increases the number of monocytes/macrophages in the artery wall of mice and that selective ablation of these cells prevented increased BP, endothelial dysfunction, and vascular superoxide production. Reconstitution of depleted mice with proinflammatory monocytes re-established the hypertensive response to ATII, thus identifying a fundamental role of this cell type in arterial hypertension²⁰⁹. Yet, there is also substantial evidence for an essential role of T cells in the genesis of hypertension. In a study from Guzik et al., *Rag1*^{-/-} mice, that lack both B and T cells, were protected from high BP pressure, vascular dysfunction and hypertrophy caused by ATII or DOCA-salt challenge. Importantly, only adoptive transfer of functional T, but not B cells, restored these abnormalities²¹³.

Even though it is still debated which particular cell type is causative to the development of hypertension, it is generally accepted that all immune cells can confer alterations to the function and structure of the blood vessel^{207,208}. One important mechanism is by exerting oxidative injury²⁰⁷. As mentioned in 1.4.1, myelomonocytic cells provide functional NADPH oxidases (Nox2) as part of their innate immunity and are thus capable to produce high amounts of ROS. However, also other immune cells such as T cells and DCs possess Nox2 activity^{215,216}. ROS directly inactivate •NO and promote vasoconstriction through

mechanisms that have been explained in detail in subchapter 1.4. The concept that immune-cell derived ROS is necessary for full development of ATII-induced hypertension was again substantiated by experiments from Wenzel and Guzik et al. (as part of their studies mentioned above): when they re-transferred monocytes from *gp91phox* (=Nox2) knockout or T cells from *p47phox* knockout mice in myelomonocytic-depleted (*LysM^{iDTR}*) or *Rag1^{-/-}* mice, respectively, ATII-hypertension was significantly blunted. Moreover, in both studies, immune Nox2 activation was dependent on the AT₁R^{209,213}.

Another pre-dominant mechanism of how immune cells contribute to hypertensive damage is by releasing cytokines²⁰⁷. Cytokines are small regulatory proteins that can exert powerful proatherogenic effects in the vasculature. For example, they promote the production of chemokines, thereby attracting other immune cells. Activated monocytes/macrophages, neutrophils and mast cells in turn are major sources of matrix metalloproteinases (MMPs)²¹⁷ that reorganize the ECM and initiate vascular remodeling. Furthermore, cytokines can activate Nox expression in various cell types including VSMCs, thus increasing the vascular oxidative stress burden²¹⁸⁻²²⁰. As briefly mentioned in 1.2.2, excessive Nox-derived ROS not only promotes vasoconstriction but also contributes to VSMC hypertrophy and collagen deposition through activation of redox-sensitive proliferative and pro-fibrotic pathways (Figure 1-3). Additionally, one cytokine always stimulates the release of other cytokines, in fact, a whole cascade, that act in concert to mediate inflammation and target organ damage, thus exacerbating hypertension.

The main cytokines involved in arterial hypertension have been identified as interleukin 17 (IL-17), interleukin 6 (IL-6), TNF- α , and INF- γ , produced by T cells, macrophages, and DCs^{207,208}. The importance of IL-17 and IL-6 in the development of hypertension is highlighted by studies using *Il17^{-/-}* and *Il6^{-/-}* mice, that were protected from vascular superoxide production and endothelial dysfunction in response to chronic ATII infusion^{221,222}.

1.5.2 Interplay of inflammation and oxidative stress in ATII-induced arterial hypertension

Inflammation and oxidative stress are closely intertwined and effect each other²²³. This is underlined by the fact that inflammatory cells markedly contribute to vascular oxidative stress in arterial hypertension (see 1.5.1) and conversely, oxidative stress itself promotes immune cell infiltration into the hypertensive vasculature.

For example, ROS, derived from AT₁R-mediated stimulation of Nox (see 1.2.2), can activate redox-sensitive pro-inflammatory transduction pathways (e.g., JNK, p38MAPK) or transcription factors (e.g., activator protein-1 (AP-1), nuclear factor erythroid 2-related factor 2 (Nrf2), hypoxia-inducible factor-1 (HIF-1), NF- κ B) (Figure 1-9)^{143,223}. Of particular

importance is NF- κ B which is known to regulate a multitude of genes involved in both inflammation development and progression²²⁴. In ECs, NF- κ B has been shown to induce the surface expression of adhesion molecules (e.g., intercellular adhesion molecule 1 (ICAM-1), vascular cell adhesion molecule 1 (VCAM-1)) and the secretion of pro-inflammatory cytokines (e.g., TNF- α , IL-1 β , IL-6) and chemokines (e.g., monocyte chemoattractant protein 1 (MCP-1), macrophage inflammatory protein 1 alpha (MIP-1 α or CCL3), Regulated upon Activation, Normal T cell Expressed and Secreted (RANTES or CCL5)), thereby promoting inflammatory cell recruitment and transmigration into the vasculature²²⁵⁻²²⁸.

Furthermore, ROS-activated signaling cascades stimulate the synthesis and secretion of prostaglandins and VEGF, which enhance vascular permeability and thus, facilitate vascular immune cell infiltration²²⁹.

As already mentioned, ROS also modulate signaling cascades involved in tissue remodeling, and may hence trigger vascular cell proliferation, hypertrophy, apoptosis, as well as ECM alterations.

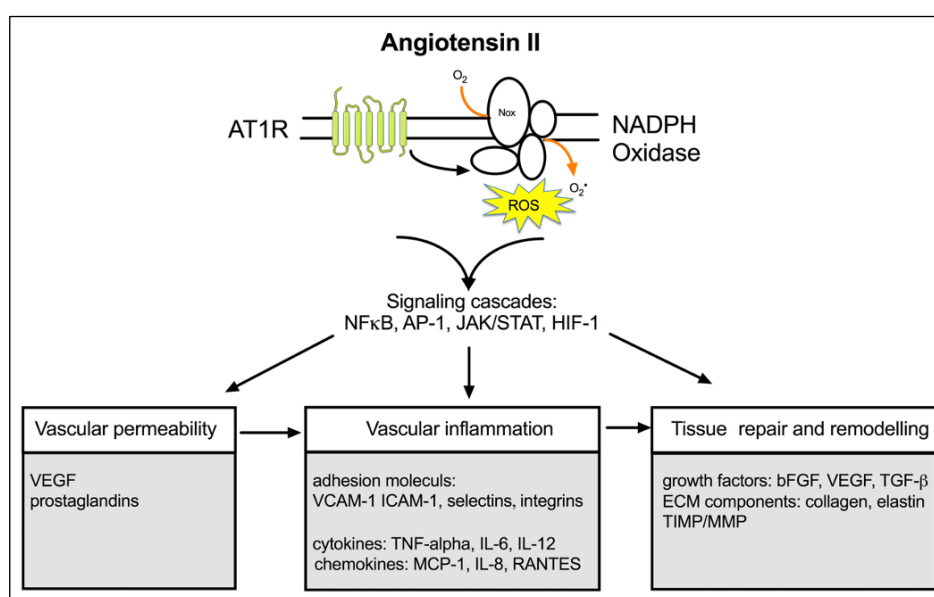


Figure 1-9: Redox regulation of ATII-mediated inflammatory actions. Nox-derived oxidative stress triggers vascular inflammation by coupling to redox-sensitive signaling molecules that in turn induce various mediators that promote vascular permeability, chemotaxis, and tissue remodeling. VEGF: vascular endothelial growth factor; VCAM-1: vascular cell adhesion molecule 1; ICAM-1: intercellular adhesion molecule 1; TNF- α : tumor necrosis factor alpha; MCP-1: monocyte chemoattractant protein 1; IL: interleukin; RANTES: Regulated upon Activation, Normal T cell Expressed and Secreted; bFGF: basic fibroblast growth factor; TGF- β : transforming growth factor beta; MMP: matrix metalloproteinase; ECM: extracellular matrix; TIMP: tissue inhibitor of MMP. Taken from²²⁹ with permission. © 2017 Elsevier Inc.

Another, relatively new mechanism linking oxidative stress, inflammation, and the genesis of hypertension is the ROS-triggered formation of 'neoantigens' on the surface in DCs. This process includes ATII-mediated Nox2 activation and thus $O_2^{\bullet-}$ production in DCs, which leads to intracellular oxidation of arachidonic acid and formation of isoketals (γ -ketoaldehydes). Isoketals are highly reactive compounds, which rapidly ligate to protein

lysines in DCs. They recognize the oxidatively modified proteins as non-self and present peptide fragments in major histocompatibility complexes (MHC) to T cells, which in turn proliferate, infiltrate the vasculature and promote hypertension^{208,212}.

1.6 Glucagon-like peptide-1

Glucagon-like peptide-1 (GLP-1), which is the focus of this PhD studies, belongs, together with GIP (glucose-dependent insulintropic polypeptide), to a class of gut hormones called incretins. The latter are released upon meal ingestion from the gastrointestinal tract into the circulation and stimulate glucose-dependent insulin secretion²³⁰⁻²³². The phenomenon of an endocrine communication between the intestine and pancreas in control of postprandial glucose levels has been referred to as 'incretin effect', deriving from the observation that intravenous injection of glucose leads to significantly less secretion of insulin compared with the same amount of glucose given orally²³⁰.

GLP-1 is a product of post-translational processing of proglucagon and, thus, counts as a proglucagon-derived peptide (PGDP) (Figure 1-10)²³³. Mammalian species transcribe a single conserved proglucagon mRNA transcript. However, depending on tissue-specific posttranslational modification by prohormone convertases, different profiles of PGDPs in the brain, pancreas, and intestine are produced. In the gut, predominance of PCSK1 (proprotein convertase subtilisin-kexin type 1) and PCSK3 generates GLP-1, which is secreted by enteroendocrine L cells (see 1.6.1)^{232,234}. Native GLP-1 exists in two equally bioactive forms, GLP-1(7-37) and GLP-1(7-36)amide, whereby the latter is produced from GLP-1(7-37) through removal of the C-terminal glycine and amidation of the penultimate arginine, catalyzed by the peptidyl-glycine alpha-amidating monooxygenase (PAM)²³⁰. The biological reason for the amidation is unclear but has been suggested to improve stability towards plasma enzymes. In humans, almost all of GLP-1 secreted from the intestinal L cells is amidated (80 %), whereas in rodents the GLP-1(7-37) form is predominant (50–60 %)^{235,236}.

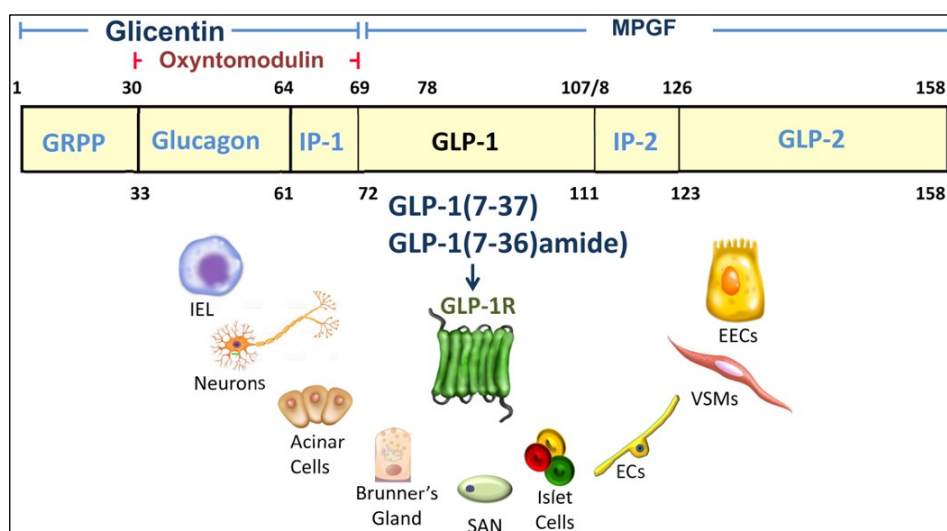


Figure 1-10: Structure of mammalian proglucagon and proglucagon-derived peptides (PGDPs). Tissue-specific post-translational processing of proglucagon generates different PGDPs. The gut-derived incretin hormone GLP-1 is synthesized in and secreted from enteroendocrine L cells in two bioactive forms, GLP-1(7-37) and GLP-1(7-36)amide. Both peptides equally bind the GLP-1 receptor (GLP-1R), e.g., the pancreatic β -cell GLP-1R promoting insulin secretion after meal ingestion. Also depicted are principal cell types that have been validated to express the canonical GLP-1R, which is discussed in more detail within sections 1.6.1–1.6.3. Taken from ²³⁷ with permission. © 2018 Elsevier Inc.

The discovery that GLP-1 not only promotes insulin release via activation of the β -cell GLP-1 receptor but also diminishes glucagon secretion, reduces food intake, and delays gastric emptying (see 1.6.1), led to the development of GLP-1 receptor agonists (GLP-1RAs) for the treatment of type 2 diabetes mellitus (T2DM) (see 1.6.2) ²³⁷. Surprisingly, cardiovascular outcome trials (CVOTs) revealed that long-acting GLP-1RAs possess positive effects on cardiovascular outcome in diabetic patients (see 1.6.2). This finding fueled the search for tissues expressing the canonical GLP-1 receptor (GLP-1R) and attempts to understand GLP-1R-dependent actions in the cardiovascular system (see 1.6.3). In the last decade, substantial advances have been made describing the pleiotropic salutary actions of GLP-1 and GLP-1RAs in multiple tissue and organs. Yet, current knowledge about precise cell type expression of the GLP-1R and their location is limited (Figure 1-10), which is discussed in the following chapters with special emphasis on GLP-1R activity within the heart, vasculature, and inflammatory cells (see 1.6.3).

1.6.1 Gut-derived GLP-1 controls glucose homeostasis

GLP-1 is secreted from enteroendocrine L cells, which are found throughout the entire gut, although the majority of L cells is located in the ileum and colon. L cells are in direct contact with the gut lumen through their apical surface, which enables them – upon nutrient stimulus – to secrete GLP-1 into the local circulation via their basolateral surface ^{230,238}.

In the pancreas, GLP-1 exerts several endocrine and exocrine effects, through actions on islet and acinar cells (Figure 1-11 A) ^{237,238}. For glucose homeostasis, the control of both

insulin and glucagon by GLP-1 is important. The insulinotropic actions of GLP-1 are known to be mediated by GLP-1R activation on β -cells in a glucose-dependent manner, yet the inhibitory effect on glucagon secretion from α -cells is less well understood. It has been proposed to be indirect, through GLP-1R activation on δ -cells, leading to the secretion of somatostatin, which in turn paracrinally stimulates the SSTR2 (somatostatin-2 receptor) on α -cells, resulting in lowered glucagon secretion²³⁷. Furthermore, despite low expression, the GLP-1R is present in the exocrine pancreas, more accurately in acinar cells, where GLP-1 promotes the secretion of pancreatic enzymes (lipase, amylase), assisting in the digestion of food^{237,238}. Clinically, GLP-1R activation on acinar cells has been associated with increased pancreatic mass possibly promoting the development of pancreatitis or pancreatitis, which has been observed upon GLP-1RA administration²³⁸.

It exists only a single known GLP-1R that is highly conserved across species. In a comparative study of different mammalian GLP-1R, the human GLP-1R was shown to share 92 % homology on amino acid level and 87 % homology on DNA level with the murine GLP-1R, with the essential residues and motifs for structural integrity, ligand selectivity and binding being conserved²³⁹. Together with the identical GLP-1 peptide sequence across mammals, this emphasizes the importance of the GLP-1/GLP-1R physiology. The GLP-1R belongs to the class B family of GPCRs and is predominantly coupled to the Gs alpha subunit ($G_s\alpha$). Hence, the signaling cascade includes adenylyl cyclase (AC)-mediated upregulating of intracellular cyclic AMP (cAMP), followed by protein kinase A (PKA) and/or Epac (exchange protein activated by cAMP) activation, which induces cell-specific downstream targets^{240,241}.

GLP-1R signaling is exemplarily shown for GLP-1-mediated insulin secretion in the β -cell (Figure 1-11 B). Binding of GLP-1 to the pancreatic β -cell GLP-1R induces AC, leading to an increase in cAMP, which directly activates PKA and Epac. PKA and Epac subsequently act together to generate downstream signals that yield in enhanced insulin secretion, including the closure of ATP-sensitive K^+ channels, facilitated opening of voltage-dependent calcium channels (VDCCs), inhibition of membrane repolarization via voltage-gated K^+ channels (K_v), and Ca^{2+} -induced Ca^{2+} release (CICR) from cytoplasmic storage sites²⁴². As already mentioned, GLP-1-derived insulin secretion only occurs in a glucose-dependent manner, i.e., when plasma glucose levels are above fasting levels (key signal: ATP generation). Furthermore, activation of GLP-1R signaling inhibits β -cell death, promotes β -cell proliferation, and induces insulin biosynthesis, partly through transcriptional mechanisms (Figure 1-11 A-B)²³⁷.

In addition, GLP-1 exerts extra-pancreatic effects, which are also involved in the regulation of glucose homeostasis. First, GLP-1 suppresses gastric and small bowel motility, which delays gastric emptying and nutrient uptake, an effect known as 'the ileal brake'. As a result,

postprandial peaks in glucose levels are reduced²³². This effect is GLP-1R dependent, however, it remains unclear whether it is mediated via direct activation of (non-vascular) intestinal smooth muscle cells (SMCs) or indirectly through neural mechanisms²³⁸. Second, GLP-1R signaling induces satiety, which reduces food intake and promoting body weight loss, an action associated with the activation of the GLP-1R in the hypothalamus and brainstem²³². Importantly, the gluoregulatory effects of GLP-1 are maintained in diabetic patients, which encouraged the development of GLP-1RAs as diabetic medication (see 1.6.2).

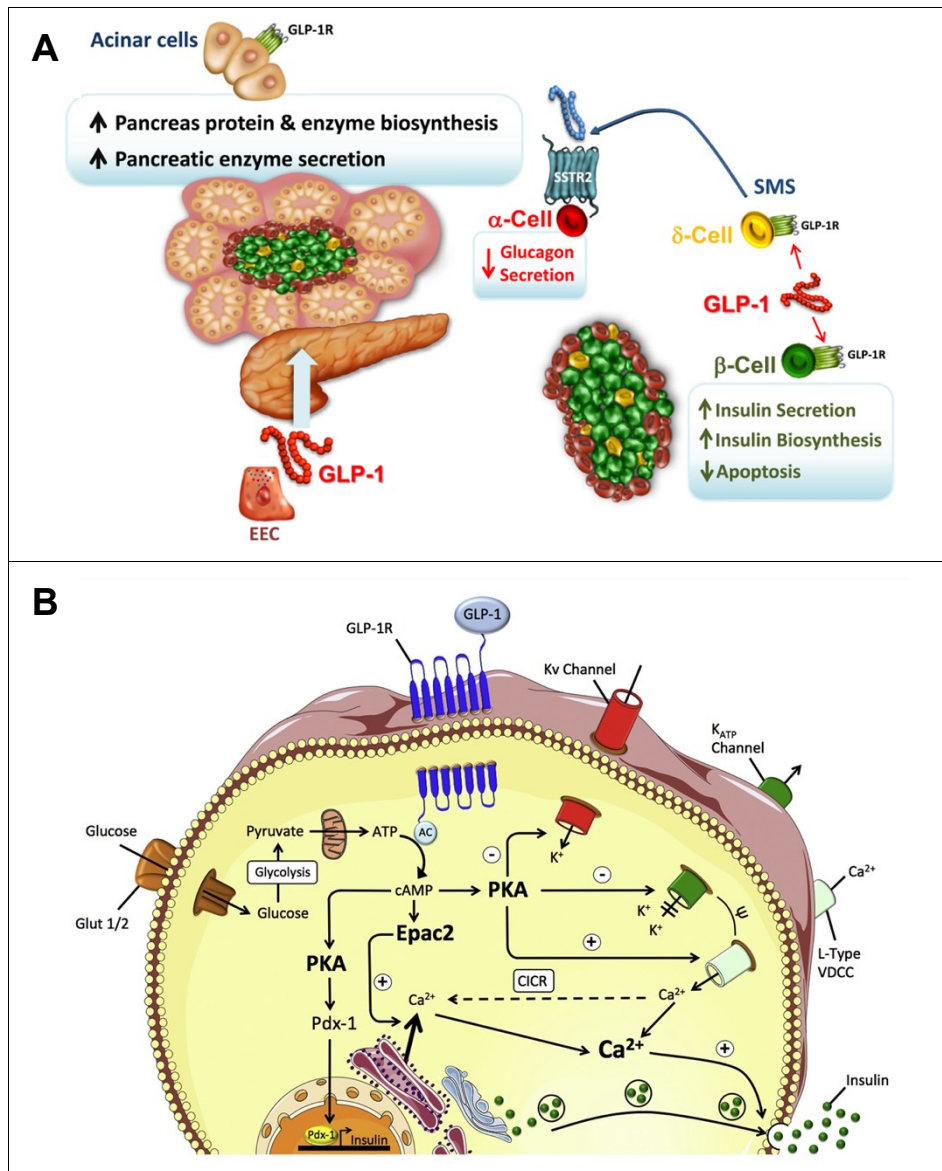


Figure 1-11: Pancreatic actions of GLP-1. (A) Direct activation of the GLP-1R on pancreatic β -cells leads to increased insulin secretion, whereas glucagon secretion from α -cells is indirectly suppressed by somatostatin (SMS), which is released upon GLP-1 binding to the GLP-1R on δ -cells. GLP-1R activation on acinar cells stimulates the release of pancreatic digestive enzymes. Taken from²³⁷ with permission. © 2018 Elsevier Inc. **(B)** The GLP-1R is a stimulatory Gs-coupled (Gs-coupled) receptor, whose activation on pancreatic β -cells leads to PKA and Epac-mediated insulin secretion in a glucose-dependent manner. Glut 1/2: glucose transporter 1/2; AC: adenylate cyclase; PKA: protein kinase A; Epac2: exchange protein activated by cAMP; Pdx-1: pancreatic and duodenal homeobox 1; CICR: calcium-induced calcium release. Taken from²⁴³ with permission. © 2019 The Authors. Published by Elsevier GmbH.

The described effects on gastric emptying, satiety and islet hormone secretion are by far the best characterized metabolic actions of GLP-1 relevant for improved glycemic control. However, several other actions of GLP-1 on peripheral tissue are described that contribute to glucose control, even though they are less well understood. These actions include inhibited hepatic glucose production, enhanced glucose uptake in muscle and adipose tissue, and lipolytic effects in adipocytes (Figure 1-12)^{230,231}. As there is no conclusive evidence on GLP-1R expression in hepatocytes, skeletal myocytes, or adipocytes, these actions seem to be indirect, possibly involving central GLP-1R activation²³⁷. The multiple metabolic actions of GLP-1 are not the focus of this study but should be kept in mind when interpreting studies or results reporting systemic GLP-1/GLP-1RA treatment.

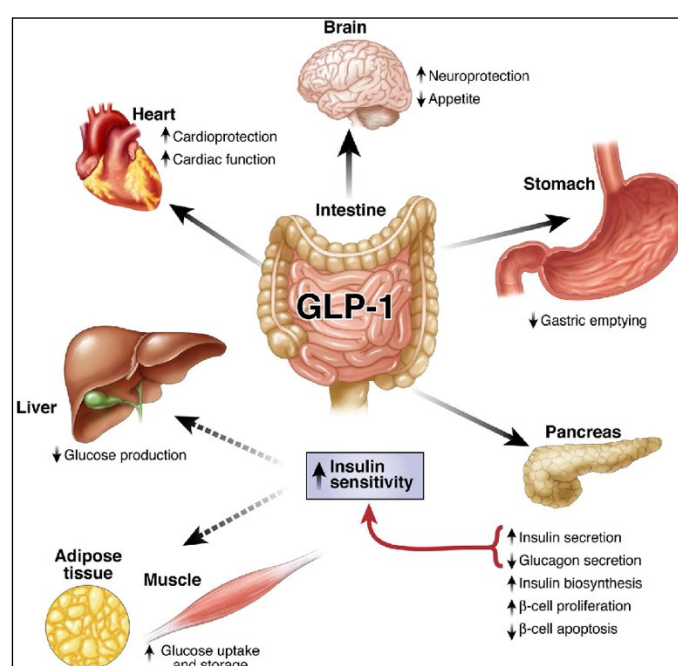


Figure 1-12: GLP-1 actions in peripheral tissues. GLP-1 controls glucose levels through regulatory actions on gastrointestinal motility, islet hormone secretion, and food intake via GLP-1R-dependent mechanisms, whereas the actions in liver, fat, and muscle are likely to be indirect. Taken from²³⁰ with permission. © 2007 AGA Institute. Published by Elsevier Inc.

1.6.2 GLP-1R agonists as antidiabetic drugs and cardiovascular outcome trials (CVOTs)

Native GLP-1 possesses a very short plasma half-life of only 1–2 min, as it is promptly degraded by the ubiquitously expressed exopeptidase dipeptidylpeptidase-4 (DPP-4). DPP-4 cleaves GLP-1(7-37) and GLP-1(7-36)amide at the N-terminal dipeptide, yielding the truncated forms GLP-1(9-37) and GLP-1(9-36)amide, both of which are unable to activate the canonical GLP-1R^{243,244}. These truncated forms, and native GLP-1 itself, are further cleaved by neutral endopeptidase (NEP24.11), generating multiple carboxyterminal fragments, including GLP-1(28-37) and GLP-1(28-36)amide^{243,245}. As a result, only 10–15 % of endogenously released GLP-1 reaches the general circulation, whereas the intact form as

wells as the GLP-1 metabolites are also rapidly eliminated from the blood through the kidneys²⁴³.

Consequently, two classes of drugs were developed for the treatment of hyperglycemia in patients with T2DM: GLP-1R agonists (GLP-1RAs, "glutide") and DPP-4 inhibitors (DPP-4Is, "gliptide")²³². DPP-4Is produce their glucose-lowering actions through increased levels of intact GLP-1. However, the interpretation of the physiological activities of DPP-4I is complicated by the fact that DPP-4 cleaves multiple other substrates besides GLP-1 (e.g., chemokines, peptide hormones) that exert pleiotropic biological activities²⁴⁶. This study focuses on the actions of GLP-1RAs, with DPP-4I effects only mentioned if relevant.

Two principal strategies have been exploited to make GLP-1RAs (mostly) resistant to proteolysis by DPP-4, thereby providing them with a longer half-life than natural GLP-1. One strategy uses GLP-1RAs which are based on the native GLP-1 structure but that have been chemically modified by different techniques to avoid degradation by DPP-4 and delay renal clearance²³². For example, liraglutide, the GLP-1RA central to this study, is an acylated derivative of natural GLP-1. Sharing 97 % amino acid sequence identity with GLP-1, a C16 fatty acid chain [*N*-ε-(γ-L-glutamyl-(*N*-α-palmitoyl))], which has been attached to lysin 26 through a glutamate spacer, enables reversible (non-covalent) binding to albumin and/or protection from proteolytic inactivation by direct steric hindrance. These structural properties provide liraglutide with a half-life of 13 hours, which is thus considered a long-acting GLP-1RA that requires subcutaneous administration once daily at a dose of 0.6–1.8 mg^{232,247,248}. The second strategy is based upon the use of exendin-4, a naturally occurring peptide isolated from saliva of the lizard *Heloderma suspectum*. Exenatide, a synthetic version of exendin-4, shares only 53 % amino acid sequence identity and is resistant to degradation by DPP-4 due to a changed DPP-4 recognition site (His-Gly N terminal) and an extended nine-residue C-terminal (Figure 1-13). Exenatide is a short-acting GLP-1RA with a plasma half-life of about 2.4 hours and is administered subcutaneously at 5–10 µg twice per day²³².

Currently, six structurally distinct GLP-1RAs exist that have been approved for the treatment of T2DM (Table 1-3), whereas exenatide also exists in a long-acting form ("exenatide once weekly") through dispersion of exenatide twice daily in injectable microspheres for extended release²³². Furthermore, the long-acting, once weekly GLP-1RA semaglutide has been developed for both subcutaneous and oral administration^{249,250}. (Subcutaneous) Semaglutide and liraglutideⁱ are the only GLP-1RAs additionally approved for the treatment of obesity

ⁱ Semaglutide for chronic weight management has been approved by the U.S. Food and Drug Administration (FDA) in June 2021 and is currently (as of July 23, 2021) under regulatory review by the European Medicines Agency (EMA). Liraglutide for obesity treatment is both FDA (2014) and EMA (2015) approved.

(Body Mass Index (BMI) of $\geq 30 \text{ kg/m}^2$)²⁵¹⁻²⁵⁴, with the latter being approved as the first drug in the United States (US) and European Union (EU) for the obesity management also in adolescents (≥ 12 years)^{253,255,256}.

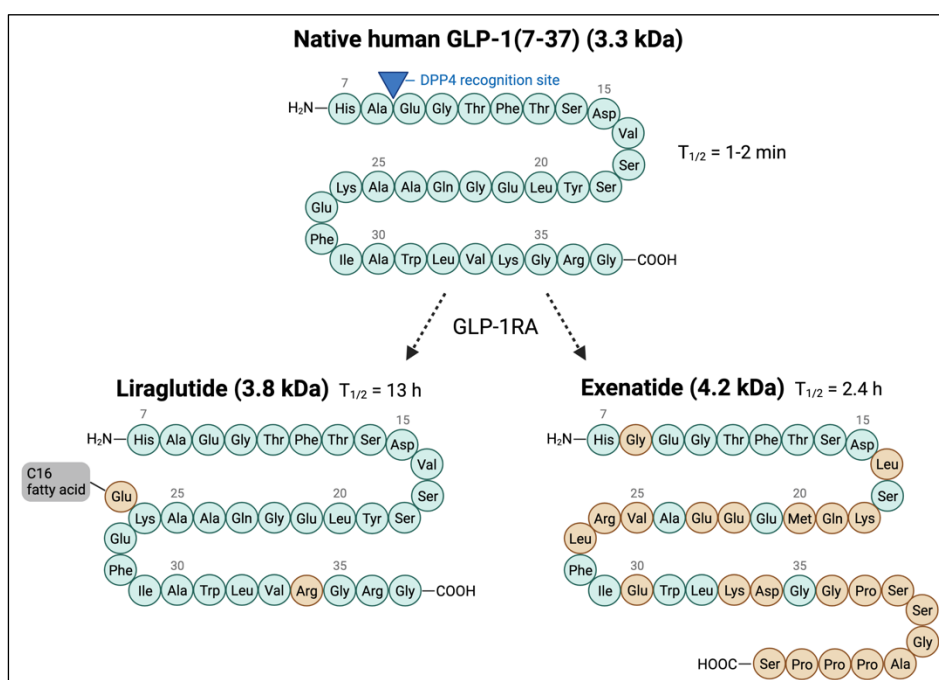


Figure 1-13: Structure and molecular mass of native human GLP-1 in comparison with approved GLP-1R agonists (GLP-1RAs) liraglutide and exenatide. Liraglutide differs from GLP-1 only by replacing Lys34 with Arg and attachment of a C16 fatty acid [*N*- ϵ -(γ -L-glutamyl-(*N*- α -palmitoyl))] to Lys26 through a glutamate spacer. Accordingly, liraglutide shares 97 % structural homology with native GLP-1 and is considered a "true" GLP-1 homologue. Exenatide, on the other hand, is a synthetic version of exenin-4, a Glia monster salivary hormone. Exenatide is equipotent with GLP-1 to activate the GLP-1R, yet only shares 53 % structural homology with native GLP-1. Created with [BioRender.com](https://www.biorender.com).

In 2008, the FDA issued the requirement to evaluate all new antihyperglycemic drugs for their cardiovascular safety, motivated by the high prevalence of CVD in diabetic patients and uncertainty of the cardiovascular safety of existing antidiabetic medication at that time (sulfonylureas, the thiazolidinedione rosiglitazone)^{257,258}. This resulted in several cardiovascular outcome trials (CVOTs), in which T2DM patients, at high risk or with established CVD, were treated with a standard therapy (blood-sugar-, blood-pressure- and lipid-lowering medication) and either received the testing GLP-1RA or placebo. The patients were monitored in a time-to-event analysis, with the typical primary composite outcome defined as the first occurrence of a major adverse cardiovascular event (MACE: death from cardiovascular causes, nonfatal myocardial infarction, or nonfatal stroke)²⁵⁹. Interestingly, all GLP-1RAs proved cardiovascular safety and some (liraglutide, semaglutide, albiglutide, dulaglutide) even demonstrated an additional cardiovascular benefit (Table 1-3).

Figure 1-14 shows the results of the LEADER trial (Liraglutide Effect and Action in Diabetes: Evaluation of Cardiovascular Outcome Results), an international, randomized, double-blinded, placebo-controlled study with 9340 diabetic patients, designed to test the

cardiovascular outcome of the GLP-1RA liraglutide. The primary null hypothesis was that liraglutide would be non-inferior to placebo with regard to the primary outcome. Yet, the study goal was even overachieved, demonstrated by a risk reduction of MACE by 13 % with liraglutide compared to placebo treatment (hazard ratio (HR) 0.87, 95 % confidence interval (CI) 0.78–0.97, $P < 0.001$ for noninferiority and $P = 0.01$ for superiority) (Figure 1-14 A). Furthermore, fewer patients died from cardiovascular causes in the liraglutide group than in the placebo group (HR 0.78, 95 % CI 0.66–0.93; $P = 0.007$, Figure 1-14 B) and the rate of death from any cause was lower upon liraglutide than placebo treatment (HR 0.85, 95 % CI 0.74–0.97, $P = 0.02$, not shown)²⁶⁰.

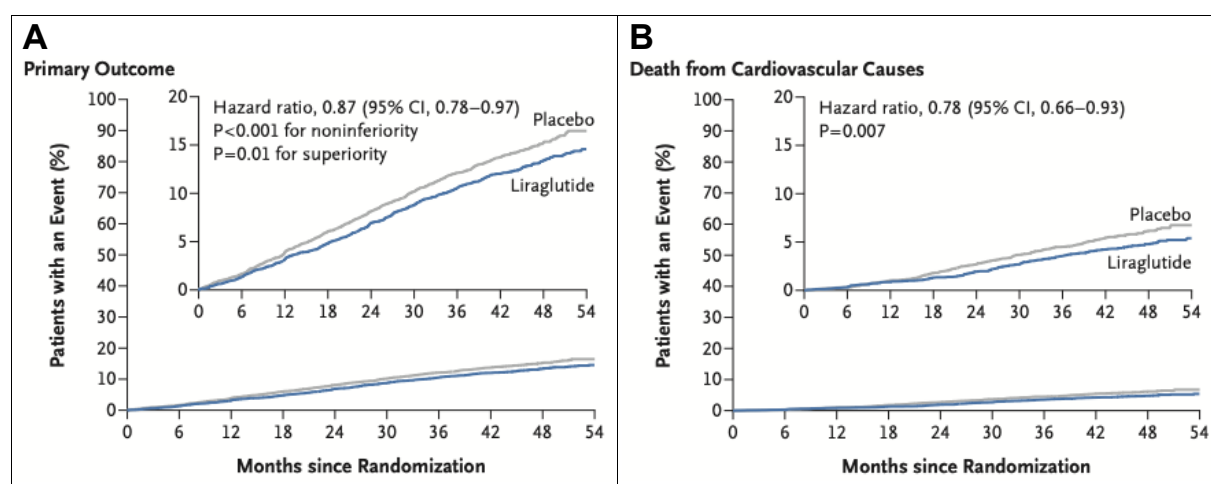


Figure 1-14: Cardiovascular Outcomes for the GLP-1RA liraglutide in the LEADER trial. Patients with T2DM, of whom 72.5 % had an established atherosclerotic CVD, were either treated with placebo or liraglutide added to standard care. The study was started in September 2010 and last up to 54 months, in which patients were monitored in a time-to-event analysis. Patients treated in the liraglutide group had a lower risk of the primary composite outcome (first occurrence of cardiovascular death, nonfatal myocardial infarction, or non-fatal stroke, **A**) and death from cardiovascular causes (**B**). Taken from²⁶⁰ with permission. © 2016, Massachusetts Medical Society.

Concomitant to this pattern of improved cardiovascular outcome, liraglutide-treated patients in the LEADER trial were reported to have a higher weight loss (-2.3 kg) compared to the placebo group and to have reduced systolic and diastolic BP (-1.2 mmHg and -0.6 mmHg, respectively), despite only a moderate difference in glycated hemoglobin (HbA_{1c}) of -0.40 percentage points (Table 1-3) and a slightly increased heart rate (+3.0 beats per minute)²⁶⁰. Together with the late separation of the Kaplan-Meier curve after 12–18 months (Figure 1-14 A-B), the cardiovascular benefit of liraglutide, and GLP-1RAs in general, has been associated with the modified progression of atherosclerotic vascular disease²⁶⁰⁻²⁶². The salutary results of GLP-1RAs in CVOTs fueled both pre-clinical and clinical studies, aimed to better understand how GLP-1 and GLP-1RAs modify cardiovascular risk factors. Indeed, multiple direct and indirect actions of GLP-1 and GLP-1RAs on the cardiovascular system have been described since then, which will be summarized in the next subchapter with a focus on heart, vessel, and inflammatory cells, and particular regard to the respective tissue-specific GLP-1R expression.

Table 1-3: Pharmacokinetic properties of approved GLP-1RAs and their results in cardiovascular outcome trials (CVOTs). Currently available GLP-1RAs are either based on the structure of native GLP-1 or exendin-4, and can be divided into short- vs. long-acting GLP-1RAs. All GLP-1RAs proved cardiovascular safety in CVOTs, with the ones highlighted in green even demonstrating a beneficial effect on the reduction of major adverse cardiovascular events (MACE) compared to placebo. Data derived from ^{232,246,262-264}, and original CVOT studies.

Compound, brand name (Approval Year, EMA)	Structure based on	Administration, Half-life	Trial, Year of Completion	Population	Follow-up Time, y	Primary Cardiovascular Outcome [‡] (Hazard Ratio)	HbA _{1c} Reduction
Lixisenatide Lyxumia® (2013)	Exendin-4	Once-daily, s.c., T _{1/2} = 3 h short-acting	ELIXA ²⁶⁵ , 2015	T2DM + recent ACS	2.1	1.02 (0.89–1.17) P<0.001 for noninferiority; P=0.81 for superiority	-0.27 pps (-0.31 to -0.22)
Liraglutide Victoza® (2009)	GLP-1	Once-daily, s.c., T _{1/2} = 13 h long-acting	LEADER ²⁶⁰ , 2016	T2DM + CVD or high risk	3.8	0.87 (0.78–0.97) P<0.001 for noninferiority; P=0.01 for superiority	-0.40 pps (-0.45 to -0.34)
Semaglutide Ozempic® (2018)	GLP-1	Once-weekly, s.c., T _{1/2} = 165 h long-acting	SUSTAIN-6 ²⁶⁶ , 2016	T2DM + CVD or high risk	2.1	0.74 (0.58–0.95) P<0.001 for noninferiority P=0.02 for superiority	0.5 mg: -0.7 pps 1 mg: -1.0 pps
Exenatide QW Bydureon® (2011)	Exendin-4	Once-weekly, s.c., T _{1/2} = NA long-acting	EXSCEL ²⁶⁷ , 2017	T2DM + CVD and non-CVD	3.2	0.91 (0.83–1.00) P<0.001 for noninferiority P=0.06 for superiority	-0.53 % (-0.57 to -0.50)
Albiglutide Eperzan® (2014)	GLP-1	Once-weekly, s.c., T _{1/2} = 5 d long-acting	HARMONY ²⁶⁸ , 2018	T2DM + CVD	1.5	0.78 (0.68–0.90) P<0.0001 for noninferiority P=0.0006 for superiority	-0.52 % (-0.58 to -0.45)
Dulaglutide Trulicity® (2014)	GLP-1	Once-weekly, s.c., T _{1/2} = 4.7 d long-acting	REWIND ²⁶⁹ , 2019	T2DM + CVD and non-CVD	5.4	0.88 (0.79–0.99) P=0.026 for superiority	-0.61 % (-0.65 to -0.58)
Semaglutide Rybelsus® (2020)	GLP-1	Once-weekly, oral, T _{1/2} = 165 h long-acting	PIONEER 6 ²⁷⁰ , 2019	T2DM + CVD or high risk	1.3	0.79 (0.57–1.11) P<0.001 for noninferiority P=0.17 for superiority	
Semaglutide Wegovy® (under review)	GLP-1	Once-weekly, s.c., T _{1/2} =165 h long-acting	SELECT ²⁷¹ (expected 2023)	Overweight or obese patients + CVD	NA	NA	

ACS: Acute coronary syndrome; CVD: Cardiovascular disease; ELIXA: Evaluation of Lixisenatide in Acute Coronary Syndrome; EMA: European Medicines Agency; EXSCEL: Exenatide Study of Cardiovascular Event Lowering; HARMONY: Albiglutide and Cardiovascular Outcomes in Patients With Type 2 Diabetes and Cardiovascular Disease; HbA_{1c}: glycated hemoglobin; HF: Heart Failure; LEADER: Liraglutide Effect and Action in Diabetes: Evaluation of Cardiovascular Outcome Results; NA: Not available; PIONEER-6: Peptide Innovation for Early Diabetes Treatment; pps: percentage points; REWIND: Researching Cardiovascular Events with a Weekly Incretin in Diabetes; s.c.: subcutaneous; SELECT: Semaglutide effects on cardiovascular outcomes in people with overweight or obesity; SUSTAIN-6: Trial to Evaluate Cardiovascular and Other Long Term Outcomes with Semaglutide in Subjects with Type 2 Diabetes, QW: once weekly.

[‡] In all trials, primary composite outcome included cardiovascular death, myocardial infarction, and stroke; only ELIXA also counted hospitalization for unstable angina.

1.6.3 Cardiovascular targets for GLP-1

GLP-1 and GLP-1RAs produce robust cardioprotection in experimental models of acute myocardial infarction^{272,273} and ventricular dysfunction/heart failure^{274,275}, actions that are associated with improved survival, reduced area of necrosis, and improved left ventricular (LV) performance^{10,245}. Yet, ventricular cardiomyocytes do not express the canonical GLP-1R but only the cardiac atrium (rodents: atrial cardiomyocytes, humans: sinoatrial node (SAN), Figure 1-10)^{276,277}. However, also the atrial GLP-1R is not needed for cardioprotection, as liraglutide persisted to potently reduce adverse LV remodeling in mice with a selective knockdown of the endogenous atrial GLP-1R (*Glp1r^{CM-/-}*) following occlusion of the left anterior descending coronary artery²⁷⁸. Thus, even though atrial GLP-1R activation has been implicated in the control of heart rate in mice²⁷⁹ and is supposedly responsible for the positive chronotropic effect upon GLP-1RA treatment in humans and mice²⁸⁰, GLP-1R-dependent cardioprotection is likely to be indirect²⁸¹.

In experimental models of acute (*ex vivo*) ischemia-reperfusion injury (IRI) and pacing-induced dilated cardiomyopathy, native GLP-1 administration improved myocardial glucose uptake and was associated with coronary artery vasodilation, enhanced coronary flow, reduced ischemic damage, and improved LV performance, respectively. Interestingly, the effects were mimicked by the truncated GLP-1(9-36)amide in both models, indicating an active role for GLP-1 metabolites²⁸¹⁻²⁸³. Furthermore, adenoviral overexpression of GLP-1(9-37) or GLP-1(28-37) promoted plaque stability in atherosclerotic apolipoprotein E-deficient (*ApoE^{-/-}*) mice, which was attributed to mitigated plaque macrophage infiltration and reduced matrix metalloproteinase 9 (MMP-9) expression.²⁸⁴ The cardioprotective mechanisms of GLP-1 metabolites are not fully understood but seem to target mitochondrial pathways²⁴⁶. The metabolite GLP-1(28-36) was recently shown to enter coronary artery endothelial and smooth muscle cells via macropinocytosis, where it inhibited the mitochondrial trifunctional protein- α (MTP α), a protein regulating fatty acid oxidation. This induced an energetic shift towards more efficient, oxygen-sparing glucose oxidation, resulting in the protection of vascular cells from metabolic oxidative stress, thereby reducing infarct size and preventing cardiac dysfunction in a model of IRI²⁸⁵.

Anti-inflammatory actions of GLP-1RAs are well documented, in both humans and animal models. In T2DM patients, liraglutide therapy reduced levels of circulating cytokines TNF- α , IL-1 β , and IL-6 independently of changes in body weight and HbA_{1c}²⁸⁶, and a single injection of exenatide exerted immediate antioxidant and anti-inflammatory effects in human blood mononuclear cells by mitigation of ROS, NF- κ B activity and *Tnfa* and *Il1b* gene expression²⁸⁷. In murine lipopolysaccharide-induced sepsis, liraglutide attenuated vascular and systemic inflammation, which improved the survival of the animals^{288,289}. In models of

experimental atherosclerosis using *Apoe*^{-/-} mice, GLP-1 and GLP-1RAs robustly reduce plaque lesion development, even at doses that do not produce weight loss¹⁰. These anti-atherogenic actions are associated with reduced monocyte/macrophage accumulation in the vascular wall and have been suggested to be caused by GLP-1RA-mediated down-regulation of inflammatory pathways (leukocyte recruitment, rolling, adhesion/extravasation, lipid-mediated signaling, extracellular matrix protein turnover, plaque hemorrhage)²⁹⁰ or direct anti-inflammatory actions in monocytes/macrophages reducing the gene expression of inflammatory mediators *Tnfa* and *Mcp1*²⁹¹. However, it remains unclear whether macrophages express the canonical GLP-1R²⁸¹. So far, the GLP-1R on circulating immune cells has been limited to very low expression on lymphocytes isolated from thymus, spleen, or bone marrow^{246,292}. Within the immune system, only intraepithelial lymphocytes (IELs) have been validated to show enriched GLP-1R expression, whose stimulation with exendin-4 suppressed the production of proinflammatory cytokines (IL-2, IL-17a, INF- γ , and TNF- α), thereby improving the gut barrier function²⁹³. Similarly, liraglutide-mediated activation of the GLP-1R on Brunner glands (exocrine glands of the duodenum) induced the production of barrier-protective molecules such as mucin 5b, which reduced murine inflammatory bowel disease²⁹⁴.

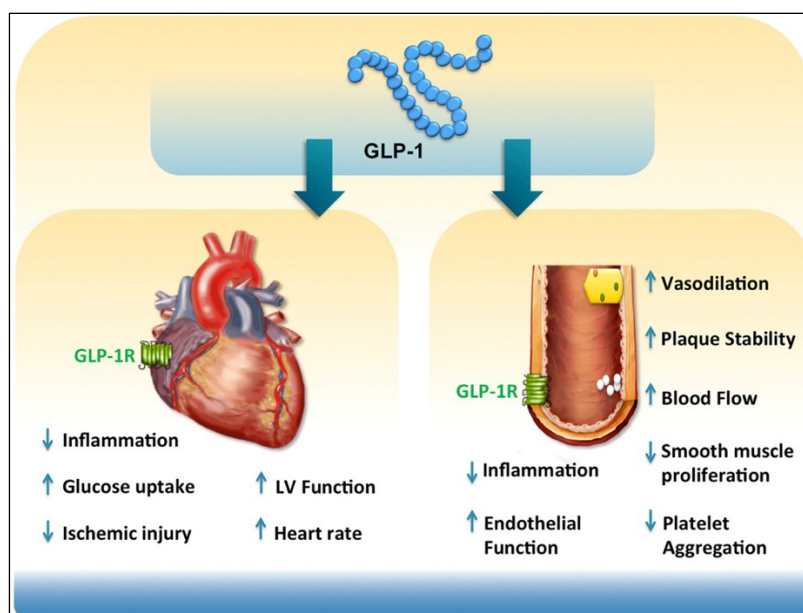


Figure 1-15: Direct and indirect actions of GLP-1 in the heart and vasculature. Direct actions of GLP-1 on the cardiovascular system may be mediated by activation of the GLP-1R on atrial cardiomyocytes, endothelial or vascular smooth muscle cells. However, some of the beneficial effects may be also caused through indirect GLP-1R activity on other cell types bearing the GLP-1R, or involve GLP-1 metabolite actions. Taken from¹⁰ with permission. © 2016 Elsevier Inc.

Despite the mentioned effects on the vasculature, no direct vasodilatory effect of GLP-1RAs has been described *in vivo* and *ex vivo*, and conclusive evidence on GLP-1R expression from intact blood vessels is lacking until today^{238,246}. Neither in rodents nor humans, GLP-1R expression has been demonstrated in endothelial cells (ECs) within major blood vessel, and

only limited evidence exists for vascular smooth muscle cell (VSMC) GLP-1R expression within ventricular blood vessels in mice^{277,280}. Hence, the majority of data on GLP-1/GLP-1RA action in the vascular endothelium is derived from *in vitro* studies employing human endothelial cells (ECs), mainly HUVECs (human umbilical vein ECs) and HCAECs (human coronary artery ECs), for which GLP-1R protein expression has been demonstrated. The numerous *in vitro* studies uniformly report improved endothelial function, actions that are mostly attributed to antioxidant and anti-inflammatory effects of native GLP-1 and GLP-1RAs²⁹⁵. For example, treatment of HUVECs with GLP-1 reduced advanced glycation end products (AGE)-induced ROS generation and subsequent up-regulation of *Vcam1* gene expression²⁹⁶. Besides, GLP-1 attenuated cell apoptosis and Nox-derived oxidative stress in HUVECs induced by high levels of glucose. Interestingly, the antioxidative effect of GLP-1 was abolished by co-treatment with the GLP-1R antagonist exendin(9-39)²⁹⁷. Furthermore, GLP-1RA liraglutide inhibited TNF- α and LPS-induced endothelial cell inflammation in human aortic ECs (HAECs), as demonstrated by attenuated protein expression of the adhesion molecules VCAM-1 and E-cadherin as well as reduced THP-1 (Tohoku hospital pediatrics-1) monocytes to HAECs. These anti-inflammatory effects were suggested to be mediated through a calcium and AMPK-dependent mechanism²⁹⁸. In HUVECs treated with exendin-4, *NO production, eNOS phosphorylation at serine 1177, and GTP cyclohydrolase 1 (GTPCH1) levels were increased, actions that were antagonized by exendin(9-39) or *Glp1r* siRNA treatment. These direct protective effects were proposed to be mediated through activation of the AMPK/PI3K-Akt/eNOS pathway²⁹⁹. Similarly, despite the lack of rigorous information on GLP-1R expression in VSMCs *in vivo*, antiproliferative and antioxidative actions of GLP-1RAs have been demonstrated *in vitro*. For example, exendin-4 treatment of rat aortic SMCs reduced platelet-derived growth factor (PDGF)-induced smooth muscle cell proliferation, which was reversed by pre-incubation with a PKA inhibitor, suggesting a cAMP-PKA-dependent pathway³⁰⁰. Furthermore, liraglutide treatment *in vivo*, in high-cholesterol fed *Apoe*^{-/-} mice for 4 weeks, suppressed atherosclerotic lesions, which was attributed to an AMPK-mediated reduction of VSMC proliferation³⁰¹.

Figure 1-15 summarizes major direct and indirect actions of GLP-1 and GLP-1RAs on the cardiovascular system.

1.7 GLP-1 and cardiovascular protection in arterial hypertension

Arterial hypertension is a major risk factor for atherosclerosis (see 1.1.2) and inflammation has been shown to play a crucial role in the development and progression of arterial hypertension (see 1.5.1). Anti-inflammatory therapy has the potential to significantly lower rates of recurrent cardiovascular events, which has been highlighted by the CANTOS

(Canakinumab Antiinflammatory Thrombosis Outcome Study) trial in 2017. In this CVOT, treatment of post-myocardial infarction patients every 3 months with 150 mg of the monoclonal antibody canakinumab, targeting IL-1 β , significantly reduced the occurrence of nonfatal myocardial infarction, nonfatal stroke, or cardiovascular death by 15 % compared with the placebo group (HR= 0.85, 95 % CI 0.74 to 0.98, P=0.021)³⁰². Interestingly, the risk reduction of MACE was of similar magnitude as the one observed in the LEADER trial with GLP-1RA liraglutide in T2DM patients (see 1.6.2)³⁰³. GLP-1 and GLP-1RAs robustly reduce cardiac and vascular inflammation (see 1.6.3), which has been suggested to occur independently of their metabolic actions, thus making a beneficiary role of GLP-1 in arterial hypertension likely.

Besides, the involvement of endothelial activation together with eNOS impairment in the pathogenesis of arterial hypertension is well established (see 1.4.2) and GLP-1/GLP-1RA treatment improves endothelial function, which has been connected to the reduction of ROS and improvement of •NO production (see 1.6.3). This interplay also hints at a possible role of GLP-1 in arterial hypertension.

Thus, the numerous interactions of GLP-1/GLP-1RAs with parts of the cardiovascular system, including the heart, vasculature, and inflammation, strongly suggest a modulating effect of GLP-1 in arterial hypertension.

2 Aim

The LEADER trial has demonstrated a reduced risk for cardiovascular events in diabetic patients with established CVD by treatment with the GLP-1RA liraglutide. Even though these cardiovascular benefits have been associated with anti-atherogenic actions, the precise mechanism and cellular origin of cardio- and vasoprotection by liraglutide remain incompletely understood.

This thesis aimed to characterize the actions of GLP-1RA liraglutide on the heart and vessels in an experimental (non-diabetic) model of arterial hypertension, a major risk factor for atherosclerosis and ensuing CVD. Most importantly, subsequent goals were to delineate underlying mechanisms for cardiovascular protection and to identify the involved cellular components. Functional studies were at first conducted in C57BL/6J wild-type mice subjected to chronic angiotensin II (ATII) infusion for induction of arterial hypertension. *In vivo* measurements of blood pressure and *ex vivo* studies of cardiac hypertrophy, vasorelaxation, and vascular fibrosis were employed to analyze the effect of additional liraglutide treatment on the cardiovascular system. Furthermore, glucose and insulin levels were determined regarding a possible metabolic contribution of GLP-1R activation to cardiovascular benefits. As vascular inflammation, vascular oxidative stress, and eNOS uncoupling are known key components in the development of arterial hypertension, the modulation of these detrimental factors by liraglutide was investigated in mechanistic analyses. For this purpose, chemiluminescence- and fluorescence-based methods were used to measure the production of reactive oxygen species (ROS) in the heart and aorta, and intravital microscopy (IVM), immunohistochemical (IHC) as well as flow cytometric experiments applied to determine vascular inflammatory cell infiltration. Complementary gene expression and immunological detection methods were used to study inflammatory markers and eNOS integrity.

To verify if the identified cardio- and vasoprotective effects of liraglutide are mediated by the canonical GLP-1R, key experiments were repeated in *Glp1r*^{-/-}. As the analyses revealed a GLP-1R-dependent mechanism, the particular contribution of the myeloid vs. the endothelial GLP-1R for the anti-inflammatory and antioxidative effects of liraglutide was investigated by exploiting myelomonocytic and endothelial-specific knockout mice of the GLP-1R (*Glp1r my*^{-/-} and *Glp1r ec*^{-/-} mice).

The findings of this work contribute to the understanding of clinical observations linking GLP-1R agonists to the reduction of major adverse cardiovascular events and could help refine the therapeutic strategies of GLP-1RAs.

3 Materials

3.1 Chemicals

All other chemicals that are not listed below were of analytical grade and obtained from Sigma-Aldrich, Fluka or Merck.

Table 3-1: Chemicals.

Product	Company	Prod. No.
2-Mercaptoethanol (β -ME)	Sigma	M6250
Acetic acid (glacial) 100%	AppliChem	A2354
Acetylcholine chloride	Sigma	A6625
Acridine Orange hydrochloride solution	Sigma	A8097
Acrylamide/Bis solution 40%, 29:1	Bio-Rad	1610146
Agarose	Invitrogen	16500-100
Albumin Fraction V (BSA)	Roth	8076.3
Ammonium persulfate (APS)	Sigma	A3678
Angiotensin II acetate salt	Bachem	4006473
Aprotinin	Sigma	A6279
Aqua-Phenol	Roth	A980.4
Braunol	B.Braun	3864065
Bromophenol Blue sodium salt	Sigma	B8026
Calcium ionophore A23187	Sigma	C5149
Chloroform – isoamyl alcohol mixture, 49:1	Sigma	25668
Cytoseal™ XYL mounting medium	Thermo Scientific	8312-4
DEPC (diethylpyrocarbonate)-treated water, nuclease-free and autoclaved	Roth	T143.3
Dihydroethidium 95% (DHE)	Sigma	37291
Dimethyl pimelimidate (DMP)	Thermo Scientific	21667
Dithiothreitol (DTT)	Sigma	D0632
DMEM (1x) + GlutaMAX™	Gibco	21885-025
EDTA-free Protease Inhibitor Cocktail, cOmplete™	Roche	11873580001
Ethanol, absolute	Sigma	32205

Ethylene glycol-bis(2-aminoethylether)- <i>N,N,N',N'</i> -tetraacetic acid (EGTA)	Sigma	E4378
Ethylenediaminetetraacetic acid (EDTA)	Sigma	E9884
Ethylenediaminetetraacetic acid tripotassium salt dihydrate (K ₃ EDTA • 2 H ₂ O)	Sigma	03664
Fetal calf serum (FCS)	Thermo Scientific	10270106
Glycerol	Roth	3783.1
Guanidine thiocyanate	AppliChem	A1107
HBSS (1x), Hanks' Balanced Salt Solution with calcium and magnesium	Sigma	55037C
Hematoxylin	Dako	S3309
Heparin-Natrium-25000	Ratiopharm	
HEPES sodium salt hydrate	Sigma	H2393
Histofix 4 %	Roth	P087.1
Iron(II) sulfate heptahydrate	Sigma	F7002
Isofluran	Abbott	B506
Isopropanol	AppliChem	A3465
Ketamine hydrochloride/xylazine hydrochloride solution	Sigma	K113
L-012 (8-amino-5-chloro-7-phenylpyridol [3,4-d]pyridazine-1,4-(2H,3H)dione sodium salt	WAKO Chemicals	120-04891
L-Glutamine	Sigma	G3126
L-N ^G -nitroarginine methyl ester-hydrochlorid (L-NAME)	Sigma	N5751
Leupeptin hydrochloride	Sigma	L0649
Liraglutide (Victoza®)	Novo Nordisk	
Lucigenin (<i>N,N'</i> -dimethyl-9,9'-biacridinium dinitrate)	Sigma	M8010
Methanol, 99.8 %	Sigma	322415
Midori Green Advance	NIPPON Genetics	MG04
Milk powder	Roth	T145.2
<i>N</i> -lauryl sarcosine sodium salt	Merck	814715
<i>N,N,N',N'</i> -Tetramethylethylenediamine	Sigma	T9281
NADPH tetrasodium salt	AppliChem	A1395
Nitroglycerin (NTG), NITRO Carino Infus	Carinopharm	
Normal Horse Serum (NHS) Blocking Solution	Vector lab	S201250
OCT (Optimal Cutting Temperature)-resin Tissue-Tek®	Sakura	4583

PBS (1x), Dulbecco's Phosphate Buffered Saline without calcium and magnesium	Sigma	D8537
Penicillin-Streptomycin (PenStrep)	Sigma	P0781
Pepstatin A	Sigma	P5318
Phenylmethanesulfonyl fluoride (PMSF)	Sigma	P7626
Phosphatase Inhibitor Cocktail	Sigma	P2850
Picric acid solution (saturated aqueous)	Sigma	80456
Ponceau S / Ponceau Red	Sigma	P5288
Prostaglandin F2 α	Cayman Chemicals	16010
Protease Inhibitor Cocktail	Sigma	P8340
RNase AWAY™	Thermo Scientific	7002
Roti®-Quant	Roth	K015.1
RPMI-1640	Sigma	R8758
Sirius Red	Sigma	43665
Sodium DETC (diethyldithiocarbamate) trihydrate	Sigma	D3506
Sodium dodecyl sulfate	Merck	822050
Triethanolamine	Sigma	T1502
Tris-hydrochlorid (Tris-HCl)	Roth	9090.2
Tris(hydroxymethyl)-aminomethane (Tris-base)	Sigma	252859
TritonX-100	Sigma	93420
Tween 20	Sigma	P2287
Wash buffer (IHC), 10x	Dako	S3006
Zymosan A from <i>S. cerevisiae</i>	Sigma	Z4250

3.2 Consumables

Table 3-2: Consumables.

Product	Company	Prod. No
Blood glucose test strips	Roche	6114963
C-Chip Disposable Hemocytometer, Neubauer Improved	NanoEnTek	DHC-N01
Cell Strainer 100 μ m	Falcon®, Corning	352360
Cell Strainer 40 μ m	Falcon®, Corning	352340
Cell Strainer 70 μ m	Falcon®, Corning	352350

Centrifuge tube, 15 mL	Greiner	188271
Centrifuge tube, 50 mL	Greiner	227261
Coverslips 24 x 50 mm	DIAGONAL	LD2450
Eppendorf® Safe-Lock microcentrifuge tubes volume 0.5 mL	Eppendorf	0030121023
Eppendorf® Safe-Lock microcentrifuge tubes volume 1.5 mL	Eppendorf	0030120086
Eppendorf® Safe-Lock microcentrifuge tubes volume 2.0 mL	Eppendorf	0030120094
FACS tubes	Falcon®, Corning	352052
Glass petri dish	Duran	237554805
LS Columns	Miltenyi Biotec	130-042-401
Micro-osmotic pump	Alzet	1007D
Microlance™ 3 24 G cannula	Becton Dickinson	304100
Microlance™ 3 26 G cannula	Becton Dickinson	303800
Microplate, 24 well, F-bottom, transparent	Greiner	662160
Microplate, 96 well, F-bottom, transparent	Greiner	655101
Microplate, 96 well, U-bottom, transparent	Greiner	650101
Microscope slides Superfrost plus	Thermo Scientific	J1800AMNZ
Nitrocellulose Blotting membrane Amersham™ Protran® 0.45µm	GE Healthcare	GE10600002
PCR tubes, 0.2 mL	Kisker Biotech	G003-A
Petri dish, sterile	Greiner	632181
Pre-Seperation Filters 30 µm	Miltenyi Biotec	130-041-407
Suture clip Michel 7.5 X 1.75mm	B.Braun	BN507R
Vasofix® Safety 14 G cannula	B.Braun	4268210S-01

3.3 Technical Devices

Table 3-3: Technical Devices.

Device	Company
Benchtop centrifuge ROTOFIX 32	Hettich
BioPhotometer	Eppendorf
Bridge amplifier	CB Sciences / ADInstruments
Chemiluminescence plate reader Mithras ² LB 943	Berthold Technologies

ChemiLux Imager (CsX-1400 M)	Intas
Cold light lamp KL1500	Schott
Cryostat CM3050 S	Leica Biosystems
DynaMag™-15	Life Technologies
DynaMag™-2	Life Technologies
EPR spectrometer MiniScope MS400	Magnettech
FACSCanto™ II Flow Cytometer with FACSDiva software	BD Biosciences
Fluorescence microscope Axiovert 40CFL with AxioCam MRm	Zeiss
Force transducer	Kent Scientific / ADInstruments
Glucometer Accu-Chek® Aviva	Roche
Hematology analyzer KX-21N	Sysmex
Heraeus Megafuge 16R	Thermo Fisher
HPLC-column C18-Nucleosil	Macherey & Nagel
HPLC-System	Jasco
Inverted bright-field / fluorescence microscope IX71 with ColorView II camera	Olympus
Luminometer Lumat LB 9507	Berthold Technologies
Mini Trans-Blot Electrophoretic Transfer Cell (Blotting apparatus)	Bio-Rad
Mini-Protean 3 Cell (Electrophoresis apparatus)	Bio-Rad
Minifold I vacuum dot-blot system device	Whatman® Schleicher&Schuell
MiniSpin® Centrifuge	Eppendorf
MRX II microplate reader	Dynex Technologies
NeoLab-Sunlab Rotator	NeoLab
Non-invasive Blood Pressure (NIBP) System CODA®	Kent Scientific
Organ bath chambers	Radnoti
Paraffin dispenser EG 1120	Leica Biosystems
PowerPac™ Basic power supply	Bio-Rad
QuadroMACS™ Separator	Miltenyi Biotec
Refrigerated benchtop centrifuge Mikro 22R	Hettich
Rotary microtome RM2145	Leica Biosystems
SimpliAmp Thermal Cycler	Thermo Fisher
StepOnePlus™ Real-Time PCR Systems	Applied Biosystems

Stereomicroscope MSZ 5400	Krüss
Thermomixer comfort	Eppendorf
Tilt/roller mixer RS-TR05	Phoenix Instrument
Tissue Processor TP 1020	Leica Biosystems
TissueLyser LT	Qiagen
UV transilluminators iX	Intas
Vortex-Genie™ 2	Scientific Industries
Wide Mini-Sub Cell GT Cell (DNA electrophoresis apparatus)	Bio-Rad

3.4 Surgical instruments

Table 3-4: Surgical instruments.

Product	Company	Prod. No
Extra Fine Bonn Scissors Straight, 8.5 cm	Fine Science Tools	14084-08
Extra Fine Graefe Forceps Curved 10 cm	Fine Science Tools	11152-10
Graefe Forceps Straight, 10 cm	Fine Science Tools	11050-10
Michel Suture Clip Applying Forceps, 12.5 cm	Fine Science Tools	12018-12
Noyes Spring Scissors Curved 12 cm	Fine Science Tools	15011-12
Scissors Curved BluntBlunt 12 cm	Fine Science Tools	14003-12
Strabismus Scissors Tungsten Carbide Curved 9 cm	Fine Science Tools	14575-09

3.5 Reagents and Kits

Table 3-5: Reagents and Kits.

Product	Company	Prod. No
Dynabeads® Sheep anti-Rat IgG	Invitrogen	11035
ABC reagent VECTASTAIN® Elite®	Vector lab	PK-6100
CD31 MicroBeads, mouse	Miltenyi Biotec	130-097-418
DAB substrate	Vector lab	SK-4105
dNTP Mix	Thermo Scientific	R0242
Dynabeads® M-280 Sheep anti-Mouse IgG	Invitrogen	11201D
Gel Loading Buffer	Sigma	G2526
Pierce™ ECL Western Blotting Substrate	Thermo Scientific	32106

QuantiTect® Probe RT-PCR Kit	Qiagen	204445
SuperSignal™ West Femto Maximum Sensitivity Substrate	Thermo Scientific	34095
Ultra Sensitive Mouse Insulin ELISA Kit	Crystal Chem	90080

3.6 Media and Buffer

Table 3-6: Media and Buffer.

Media / Buffer	Composition
ACK (Ammonium-Chloride-Potassium) lysis buffer	150 mM NH ₄ Cl, 10 mM KHCO ₃ , 0.1 mM EDTA, pH 7.2
Alkaline lysis buffer (DNA extraction)	25 mM NaOH, 0.2 mM EDTA, pH 12
BMDM growth medium, day 1	RPMI 1640, 25 mM HEPES and L-glutamine, 1 % (v/v) PenStrep, 20 % (v/v) FCS, 30 % (v/v) L929 cell-conditioned media
BMDM growth medium, day 4	RPMI 1640, 25 mM HEPES and L-glutamine, 1 % (v/v) PenStrep, 20 % (v/v) FCS, 15 % (v/v) L929 cell-conditioned media
FACS buffer	PBS, 2% (v/v) FCS, 1 mM EDTA
GIT (guanidinium thiocyanate) buffer	4 M guanidinium thiocyanate, 25 mM sodium citrate (pH 7.0), 0.5 % (w/v) <i>N</i> -lauryl sarcosine, 0.1 M 2-mercaptoethanol
Homogenization buffer	20 mM Tris-HCl, 250 mM sucrose, 3 mM EGTA, 20 mM EDTA, 0.5 mM PMSF, 1 % (v/v) protease inhibitor cocktail, 1 % (v/v) phosphatase inhibitor cocktail, 1 % (v/v) TritonX-100
KH (Krebs-Hepes) buffer	99 mM NaCl, 4.7 mM KCl, 2.5 mM CaCl ₂ , 1.2 mM MgSO ₄ , 25 mM NaHCO ₃ , 1 mM K ₂ HPO ₄ , 20 mM HEPES, 11.1 mM D-glucose, pH 7.35
KH buffer including protease inhibitors	KH buffer, 1 % (v/v) aprotinin, 5 µg/ml leupeptin, 8 µg/ml pepstatin
L929 cell-conditioned media	with courtesy of PD Dr. med. Markus Bosmann, Center for Thrombosis and Hemostasis (CTH), Mainz
Laemmli buffer, 3x	188 mM Tris-HCl (pH 6.8), 6 % (w/v) SDS, 30 % (v/v) glycerol, 0.01 % (w/v) bromophenol blue, 15 % (v/v) 2-mercaptoethanol
MACS buffer	PBS, 0.5 % (w/v) BSA, 2 mM EDTA, 1 % (v/v) PenStrep
MLEC digestion solution	DMEM GlutaMAX, 1.5 mg/ml collagenase A
MLEC isolation buffer	DMEM GlutaMAX, 20 % (v/v) FCS
Neutralization buffer (DNA extraction)	50 mM Tris-HCl, pH 5
PBS, 10x	1.37 M NaCl, 100 mM Na ₂ HPO ₄ , 27 mM KCl, 17.6 mM KH ₂ PO ₄ , pH 7.4
PBS-T, 1x	1x PBS, 1 % (v/v) Tween 20

SDS-PAGE resolving gel buffer	1.5 M Tris-HCl, pH 8.8
SDS-PAGE running buffer, 10x	250 mM Tris-base, 192 mM glycine, 35 mM SDS
SDS-PAGE stacking gel buffer	0.5 M Tris-HCl, pH 6.8
TAE (Tris-Acetate-EDTA) buffer, 50x	2 M Tris-base, 1 M acetic acid (glacial), 50 mM EDTA, pH 8.5
TBS, 10x	200 mM Tris-base, 1.5 M NaCl, pH 7.6
TBS-T, 1x	1x TBS, 1 % (v/v) Tween 20
Tris DTT buffer	Tris Mem, 2 mM DTT
Tris Mem buffer	50 mM Tris-HCl, 1 tablet EDTA-free Protease Inhibitor Cocktail (per 50 ml buffer), pH 7.4
Western blot transfer buffer, 10x	250 mM Tris-base, 192 mM glycine, 25 % (v/v) methanol

3.7 Enzymes and Standards

Table 3-7: Enzymes and Standards.

Product	Company	Prod. No
100 bp DNA ladder	New England Biolabs	N3231L
BenchMark™ Unstained Protein Ladder	Invitrogen	10747012
Bovine Serum Albumin Standard Ampules	Thermo Scientific	23209
Collagenase Type A	Worthington	LS004154
DreamTaq™ Hot Start Green DNA Polymerase	Thermo Scientific	EP1712
Liberase™ (Thermolysin Medium)	Roche	5401127001
Precision Plus Protein™ WesternC™ Blotting Standard	Bio-Rad	1610376

3.8 Antibodies

The antibody dilutions that were applied for Dot blot and Western blot, immunohistochemical stainings as well as flow cytometric analyses are marked in parentheses.

3.8.1 Primary antibodies

Table 3-8: Primary antibodies.

Product	Company	Prod. No
monoclonal anti-CD102 (<i>rat</i>)	BD Biosciences	553326
monoclonal anti-Asymmetric dimethylarginine (ADMA) (<i>mouse</i> , 1:2000 in 3 % BSA/PBS-T)	Covalab	mab0004-P
monoclonal anti-CD16/CD32 (<i>rat</i> , 1:100 in FACS buffer), Mouse BD Fc Block™	BD Biosciences	553142
monoclonal anti-eNOS (<i>mouse</i> , 1:1000 in 3 % BSA/TBS-T)	BD Biosciences	610297
monoclonal anti-F4/80 (<i>rat</i> , 1:250 in 3 % milk/PBS)	eBioscience	14-4801-82
monoclonal anti-Glutathione (<i>mouse</i> , 1:1000 in 3 % BSA/PBS-T)	Virogen	101-A
polyclonal anti-Galectin 3 (Mac-2) (<i>rabbit</i> , 1:100 in 2.5 % NHS/PBS)	LSBio	LS-C357474
polyclonal anti-IL-1 β (<i>rabbit</i> , 1:1000 in 3 % BSA/PBS-T)	Abcam	ab9722
polyclonal anti-Nitrotyrosine (<i>rabbit</i> , 1:1000 in 3 % milk/PBS)	Millipore	06-284
polyclonal anti-Nox2 (<i>rabbit</i> , 1:200 in 2.5 % NHS/PBS)	LSBio	LS-B12365
polyclonal anti- β -actin (<i>rabbit</i> , 1:2500 in 5 % BSA/TBS-T)	Sigma	A5060

3.8.2 Fluorescent-labeled antibodies and dyes

Table 3-9: Fluorescent-labeled antibodies and dyes.

Product	Company	Prod. No
Fixable Viability Dye (1:1000 in FACS buffer), eFluor506	BD Biosciences	65-0866
monoclonal anti-CD11b (<i>rat</i> , 1:100 in FACS buffer), PE conjugated	BD Biosciences	553311
monoclonal anti-CD45 (<i>rat</i> , 1:100 in FACS buffer), APC-eFluor 780 conjugated	eBioscience	47-0451-82
monoclonal anti-CD8a (<i>rat</i> , 1:50 in FACS buffer), APC conjugated	eBioscience	17-0081-82
monoclonal anti-F4/80 (<i>rat</i> , 1:50 in FACS buffer), APC conjugated	eBioscience	17-4801-82
monoclonal anti-Ly6C (<i>rat</i> , 1:100 in FACS buffer), PerCP-Cy.5.5 conjugated	BD Biosciences	560525
monoclonal anti-Ly6G (<i>rat</i> , 1:100 in FACS buffer), FITC conjugated	BD Biosciences	551460

monoclonal anti-NK1.1 (<i>mouse</i> , 1:100 in FACS buffer), PE-Cy7 conjugated	eBioscience	25-5941-81
monoclonal anti-TCR β Chain (<i>hamster</i> , 1:100 in FACS buffer), V450 conjugated	BD Biosciences	560706

3.8.3 Secondary antibodies

Table 3-10: Secondary antibodies.

Product	Company	Prod. No
anti-mouse IgG produced in horse, peroxidase-labeled (1:10,000, same conditions as primary antibody)	Vector lab	PI-2000
anti-rabbit IgG produced in goat, biotinylated (1:1000, same conditions as primary antibody)	Invitrogen	B-2770
anti-rabbit IgG produced in goat, peroxidase-labeled (1:10,000, same conditions as primary antibody)	Vector lab	PI-1000
anti-rat IgG produced in goat, peroxidase-labeled (1:10,000, same conditions as primary antibody)	Santa Cruz	sc-2006

3.9 Oligonucleotides

3.9.1 TaqMan probe-and-primer sets for quantitative real-time PCR

TaqMan® gene expression assays were purchased as probe-and-primer sets from Applied Biosystems.

Table 3-11: Taqman® assays for qRT-PCR.

Gene Symbol	Gene Name	Assay ID
<i>Cybb / Nox2</i>	cytochrome b-245, beta polypeptide / NADPH oxidase 2	Mm00432775_m1
<i>Glp1r</i>	glucagon-like peptide-1 receptor	Mm00445292_m1
<i>Icam1</i>	intercellular adhesion molecule 1	Mm00516023_m1
<i>Nfkb2</i>	nuclear factor kappa B subunit 2	Mm00479810_g1
<i>Nos2</i>	inducible nitric oxide synthase 2 (iNOS)	Mm00440485_m1
<i>Selp</i>	P-selectin	Mm01204601_m1
<i>Tbp</i>	TATA box binding protein	Mm00446973_m1
<i>Tnfa</i>	tumor necrosis factor alpha	Mm00443259_g1
<i>Vcam1</i>	vascular cell adhesion molecule 1	Mm00449197_m1

3.9.2 Oligonucleotide sequences for genotyping of transgenic mice

All genotyping primers were purchased from Eurofins Genomics.

Table 3-12: Primer sequences for genotyping PCR.

Name	Sequence	Mer
Cadh5 F (15623)	5'-AGG CAG CTC ACA AAG GAA CAA T-3'	22 mer
Cadh5 R (15625)	5'-TCG TTG CAT CGA CCG GTA A-3'	19 mer
Cre8	5'-CCC AGA AAT GCC AGA TTA CG-3'	20 mer
MLys1	5'-CTT GGG CTG CCA GAA TTT CTC-3'	21 mer
MLys2	5'-TTA CAG TCG GCC AGG CTG AC-3'	20 mer
Glp1r F2	5'-TGA GCC ATC TCC TCA GCT CT-3'	20 mer
Glp1r R2	5'-AGG CAT GTA TCC ACC TCT GG-3'	20 mer

3.10 Laboratory Animals

All animals were used in accordance with §4 Abs. 1 and §6 Abs. 1 Nr. 4 or § 8 Abs. 1 of the German Animal Welfare Act. The study was performed in male mice between 8 and 12 weeks old. All mouse strains that were used are described and summarized in Table 3-13.

Table 3-13: Overview of used mouse strains including description and source.

Mouse strain	Description	Vendor or Source
C57BL/6J	Inbred strain	Charles River
<i>Glp1r</i> ^{-/-}	Inbred strain on C57BL/6 background; <i>Glp1r</i> knockout by replacing two exons of the gene encoding the first and third transmembrane domains and intervening peptide sequence with a neomycin cassette ³⁰⁴	Bred in-house (TARC, Translational Animal Research Center Mainz); provided by Daniel Drucker, Mt. Sinai Hospital, Toronto, Canada
<i>Glp1r</i> ^{fllox/fllox}	Inbred strain on C57BL/6 background; <i>Glp1r</i> conditional knockout by introducing a loxP site on either side of exons 6 and 7 of the <i>Glp1r</i> gene ³⁰⁵	Bred in-house (TARC); provided by Randy Seeley, University of Michigan
<i>Cdh5</i> ^{cre+}	B6.FVB-Tg(Cdh5-cre)7Mlia/J strain; Cre recombinase expression under control of the VE (Vascular Endothelium)-Cadherin promoter; used as a tool for generating endothelial cell-specific knockout mice ³⁰⁶	Bred in-house (TARC); purchased from Jackson Laboratory

		(stock no. 006137)
<i>LysM^{cre+/-}</i>	B6.129P2-Lyz2 ^{tm1(cre)lfo} /J strain; Cre recombinase expression under control of the lysozyme M promoter/enhancer; used as a tool for generating myeloid cell (monocytes, mature macrophages, and granulocytes)-specific knockout mice ³⁰⁷	Bred in-house (TARC); purchased from Jackson Laboratory (stock no. 004781)
<i>Glp1r^{fllox/fllox} Cdh5^{cre+} / Glp1r^{ec-/-}</i>	Endothelial cell-specific deletion of the <i>Glp1r</i> .	Bred in-house (TARC)
<i>Glp1r^{fllox/fllox} LysM^{cre+/-} / Glp1r^{my-/-}</i>	Lysozyme M ⁺ myelomonocytic cell-specific deletion of the <i>Glp1r</i> .	Bred in-house (TARC)

For explanations on the generation of *Glp1r* conditional knockout mice via Cre-loxP mediated tissue-specific deletion of the *Glp1r*, see 4.1.1.

3.11 Software

Table 3-14: Software.

Name	Company
Axiovision Rel 4.3	Zeiss
BioRender (Medical illustrations)	BioRender
cellSens Imaging Software	Olympus
ChemSketch (Freeware) 2020.2.1	ACD/Labs
ChromPass Chromatography Software	JASCO
EndNoteX9 (reference management software)	Clarivate Analytics
Gel-Pro Analyzer 6.0	Media Cybernetics
GraphPad Prism 8	GraphPad Software, Inc.
MiniScopeCtrl (EPR operating software)	Magnettech GmbH
Revelation	Dynex Technologies
StepOne Software v2.3	Applied Biosystems

4 Methods

4.1 *In vivo* animal studies

All animal experiments were treated in accordance with the Guide for the Care and Use of Laboratory Animals as adopted by the U.S. National Institutes of Health. Approval was granted by the Ethics Committee of the University Hospital Mainz and the Landesuntersuchungsamt Rheinland-Pfalz (Koblenz, Germany; permit number: 23 177-07/G 17-1-050) in pursuance of §8 Abs. 1 of the German Animal Welfare Act (currently in the version of the publication dated 18 May 2006 (Federal Law Gazette 1 p. 1206, 1313), last amended by Article 1 of the law dated 18 June 2021 (Federal Law Gazette 1 p. 1828).

4.1.1 Cre/loxP mediated generation of *Glp1r* conditional knockout mice

The Cre/loxP system was used as a tool for generating *Glp1r* tissue-specific knockout mice in order to delineate the contribution of the endothelial vs. the myeloid cell GLP-1 receptor for cardioprotection in experimental arterial hypertension.

The Cre/loxP system allows the cell-specific and/or temporally controlled deletion of certain DNA segments within the mouse genome³⁰⁸. It relies on the Cre recombinase (*cyclization recombination*) enzyme that originates from bacteriophage P1 and catalyzes the recombination between two loxP (locus of X-over of P1) recognition sites. They include a 34 bp consensus sequence consisting of two flanking palindromic sequences of 13 bp separated by an 8 bp core spacer sequence. A DNA sequence between two *cis* loxP sites (i.e., located on the same DNA strand) is excised in form of a circular DNA product if the loxP sites are oriented in the same direction, with one loxP site remaining in the chromosome's intron. The circular piece of DNA gets degraded within the cell^{308,309}. To generate mice with a Cre/loxP-mediated gene deletion, two genetically modified mouse lines are needed: one with the to-deleting gene flanked by two loxP sites ("floxed mouse") and one with selective Cre expression in a certain lineage/cell type ("tissue-specific Cre mouse"). The Cre/loxP principle is exemplarily shown for the generation of endothelial and myeloid cell-specific *Glp1r* knockout mice (Figure 4-1). Additional to the generation of tissue-specific knockout mice, the Cre/loxP systems also allow the excision of DNA in a temporally controlled manner (inducible Cre activation, not shown). This can be achieved, for instance, by the use of a ligand-activated Cre recombinase that is primarily inactive and only gets activated in the presence of a synthetic ligand (e.g., tamoxifen)^{308,310}.

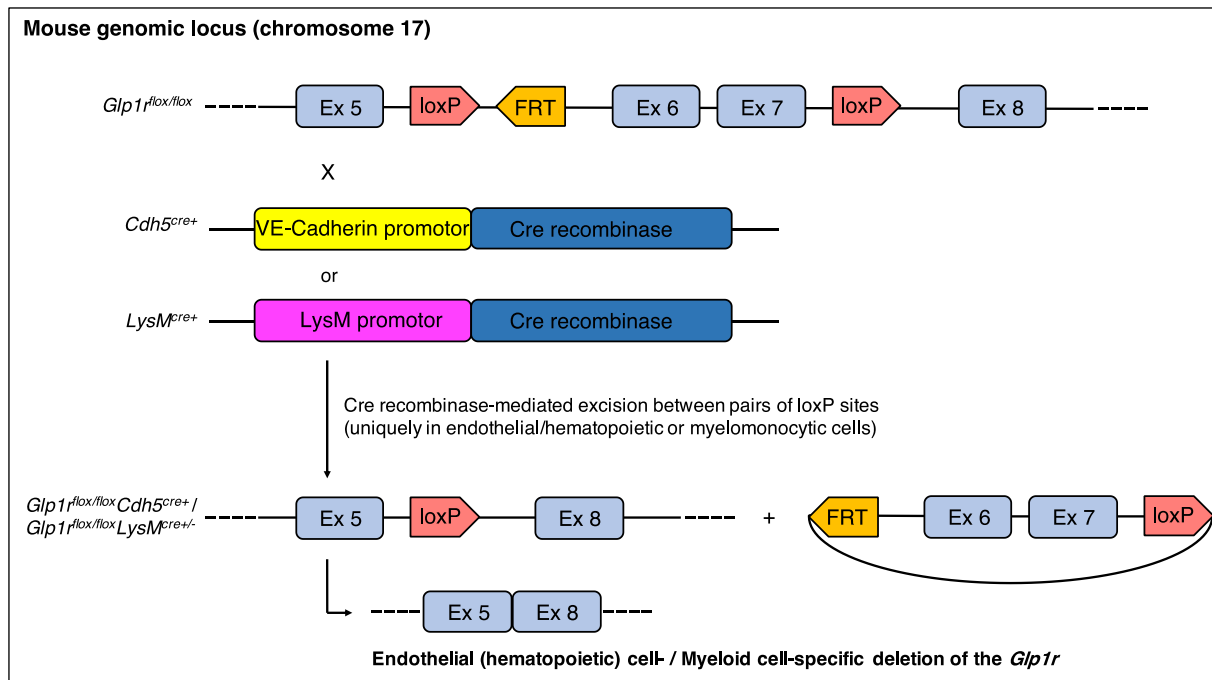


Figure 4-1: Cre/loxP strategy for the generation of *Glp1r* conditional knockout mice in endothelial and myeloid cells. *Glp1r^{lox/flox}* mice ubiquitously express the conditional transgene in which exon 6 and 7 of the *Glp1r* gene are flanked by two loxP sites (facing the same direction)³⁰⁵. Exon 6 and 7 encode transmembrane regions and are therefore indispensable for a functional GLP-1R protein³⁰⁴. Also shown is one residual FRT (flippase recognition target) site that remains in the fifth intron from the removal of the neomycin positive selection marker using the Flp recombinase system during generating of the *Glp1r^{lox/flox}* mice^{309,311}. With absent *Cre* expression, the loxP sites are removed during splicing, thus leaving the full *Glp1r* gene. By crossing *Glp1r^{lox/flox}* mice with mice that express *Cre* under the control of the VE-Cadherin or LysM promoter, endothelial (*Glp1r^{lox/flox}Cdh5^{cre+}*) and myeloid cell-specific (*Glp1r^{lox/flox}LysM^{cre+}*) *Glp1r* knockout were generated, respectively. Figure created with information derived from^{305,311}.

To generate endothelial (*Glp1r^{lox/flox}Cdh5^{cre+}*, *Glp1r^{ec}-/-*) and myeloid (*Glp1r^{lox/flox}LysM^{cre+}*, *Glp1r^{my}-/-*) cell-specific *Glp1r* knockout mice, *Glp1r^{lox/flox}* mice were bred with *Cdh5^{cre+}* and *LysM^{cre+}* mice, respectively. Several crossings are needed to generate mice that are homozygous for the loxP flanked allele and hemizygous (*Cdh5^{cre+}*) or heterozygous (*LysM^{cre+}*) for the *Cre* allele (Figure 4-2 A-B).

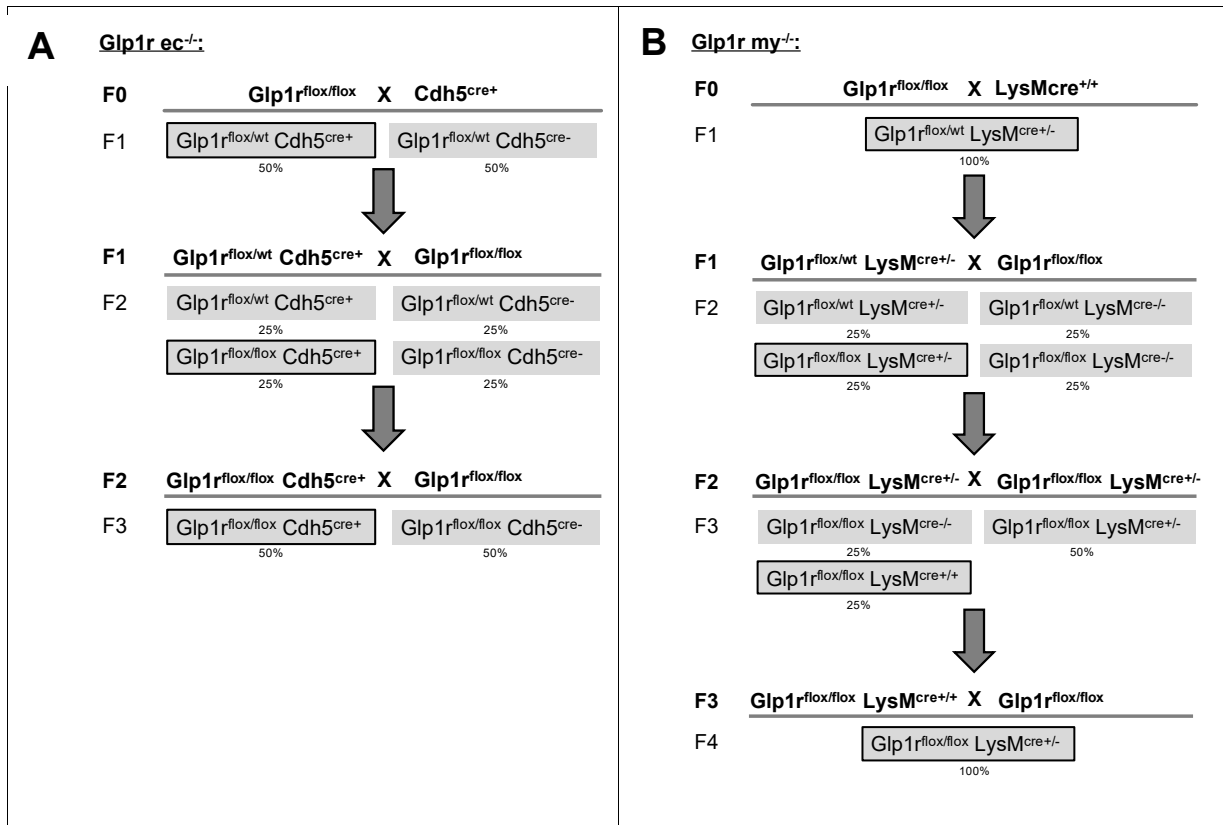


Figure 4-2: Breeding schemes for the generation and maintenance of the $Glp1r^{flox/flox} Cdh5^{cre+}$ ($Glp1r^{ec-/-}$) and $Glp1r^{flox/flox} LysM^{cre+/-}$ ($Glp1r^{my-/-}$) mouse line. Indicated are the genotypes of the mated mice and of the offspring including their average abundance as percentages. F0: parental generation; F1-F4: filial generations.

The offspring of the different breeding steps were genotyped for the presence of the $Glp1r^{flox}$ and $Cdh5^{cre} / LysM^{cre}$ locus (see 4.3.2).

The specificity of a Cre/loxP-mediated gene deletion depends on the expression pattern of the promoter that drives Cre. The VE-Cadherin promoter was shown not to be exclusively active in endothelial but also show expression in a subset of hematopoietic cells^{306,312}. The $Glp1r$ knockdown in $Glp1r^{flox/flox} Cdh5^{cre+}$ and $Glp1r^{flox/flox} LysM^{cre+/-}$ mice was verified by measuring $Glp1r$ mRNA expression in isolated endothelial cells (MLECs, see 4.2.3) and isolated macrophages (BMDMs, see 4.2.4). To assess a possible non-endothelial deletion of the $Glp1r$ in the hematopoietic cell lineage in $Glp1r^{flox/flox} Cdh5^{cre+}$, $Glp1r$ mRNA expression was also analyzed in CD45⁺ cells of these mice. Due to the lack of specific antibodies detecting the GLP-1R^{313,314}, the verification of a tissue-specific GLP-1R deletion on protein level was not conducted. As controls for the analyses, the respective Cre-expressing mice ($Cdh5^{cre+}$ and $LysM^{cre+/-}$) were used.

4.1.2 Implantation of osmotic pumps

Continuous subcutaneous delivery of ATII in unrestrained animals was acquired by the implantation of Alzet[®] osmotic minipumps. The pumps' functional principle is based upon an osmotic difference between an osmotic layer (a compartment within the pump) of high

osmolarity and the tissue of lower osmolarity, causing water influx into the pump through an outer, semipermeable membrane. The incoming water puts pressure on a flexible reservoir within the pump that contains the test agent, releasing it at a continuous rate^{315,316}.

Minipumps were filled with ATII (as angiotensin II acetate salt in 0.9 % NaCl) according to the manufacturer's instructions. The ATII concentration was adjusted considering the manufacturer's specifications of *mean pumping rate* and *fill volume*, to deliver a dose of 0.5 mg/kg/d (for 7 d in total). The implantation procedure was done under sterile conditions. Mice were anesthetized with ketamine/xylazine (120 mg/kg ketamine and 16 mg/kg xylazine in 0.9 % NaCl) and the dorsocaudal area shaved. After disinfection with Braunol, an incision of approximately 1 cm was made on the dorsal flank, a subcutaneous pocket formed and the minipump inserted. The wound was closed by applying metallic clips to the skin and treated with lidocaine ointment for pain management. For consistency and reproducibility, the implantations were carried out at the same time of day (between 10 and 11 am). Control-treated animals underwent the same surgical procedure but a pump filled with 0.9 % NaCl was implanted (sham treatment).

4.1.3 Treatment with GLP-1 receptor agonist (GLP-1RA) liraglutide

GLP-1RA liraglutide ($T_{1/2} = 13$ h, see 1.6.2) was delivered by intraperitoneal injections (i.p.) twice daily, every 12 hours, for 7 d in total. Liraglutide from the injection pen (6 mg/ml) was diluted to a final concentration of 6 ng/ μ l with saline to deliver 30 μ g/kg with every injection. The control and the ATII group were treated with adequate volumes of vehicle only. One week after pump implantation and i.p. injections, animals were either sacrificed and their organs and tissue collected (see 4.2.1) or terminal *in vivo* measurements (oral glucose tolerance tests (OGTTs), see 4.1.5; intravital microscopy (IVM), see 4.1.6) conducted. The treatment scheme is depicted in Figure 4-3.

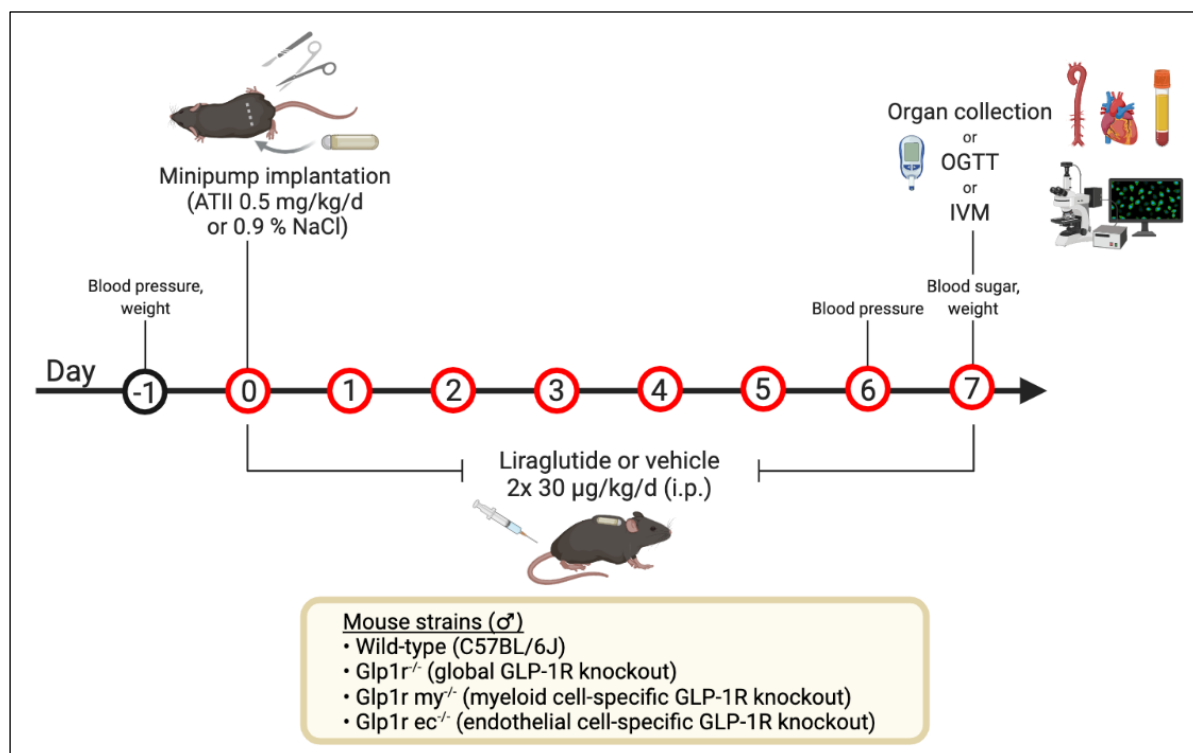


Figure 4-3: Treatment scheme for the investigation of GLP-1RA liraglutide in experimental hypertension. Male mice of each indicated strain were randomly divided into three groups: control, angiotensin II (ATII)- and ATII+liraglutide-treated group (+Lira). In the last two, arterial hypertension was induced by subcutaneous administration of ATII (0.5 mg/kg/d) for 7 days via osmotic minipumps; control mice were sham-infused with 0.9 % NaCl. Additionally, mice were either treated with liraglutide (+Lira) or vehicle (control and ATII group) twice daily, every 12 h, for 7 consecutive days via intraperitoneal injections (i.p.) at a dose of 2x 30 µg/kg/d for Lira or an adequate volume of vehicle (saline). One day prior to treatment start, baseline measurements of blood pressure and body weight were taken. On day 6, blood pressure was measured again. After one week of treatment, mice were weighed as well as their blood sugar levels determined before they were sacrificed for organ collection or final *in vivo* measurements. Created with [BioRender.com](https://www.biorender.com).

4.1.4 Non-invasive blood pressure (NIBP) recordings

Blood pressure in mice was measured non-invasively by tail-cuff plethysmography, which relies on Volume-Pressure Recordings (VPR) to determine the tail blood volume.

For the measurements, mice were placed in a holder on a warming pad (32°C) and the tail threaded through the occlusion tail-cuff and specific VPR sensor cuff (Figure 4-4). The occlusion cuff is inflated and deflated in turns, causing the blood flow alternately to be stopped and to be returned to the tail. The sensor within the VPR cuff measures these tail blood volume changes that are characteristic of the underlying BP³¹⁷. The tail-cuff method has been validated against BP recordings via telemetry if animals are appropriately trained and BP differences are > 10 mmHg³¹⁸. However, as the procedure is based upon measuring tail blood volume changes with the initial increase in tail volume being more distinct than the 'tail volume equalization point' after occlusion, tail-cuff recordings only reliably report systolic BP and are thus only mentioned as such.

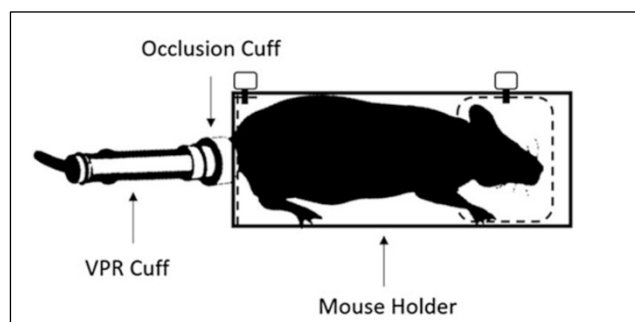


Figure 4-4: Scheme of the mouse holder used in tail-cuff plethysmography. Blood pressure was measured by assessing tail blood volume changes in Volume-Pressure Recordings (VPR). Taken from ³¹⁹ with permission. © 2017, Springer Science Business Media LLC.

Non-invasive blood pressure (NIBP) recordings were conducted on day -1 and 6 of the treatment regimen (Figure 4-3) using a CODA High Throughput 2 Non-invasive Blood Pressure System (Kent Scientific). Prior to recorded measurements, mice were trained three times in the restraining tubes to allow animal habituation and minimize stress reactions. After the animals were placed in the holders, they were allowed to acclimate for 15 min and finally 15 NIBP measurements taken per animal. The mean values of ten NIBP readings were used for BP calculations (the first five recordings were discarded as acclimation cycles). Blood pressure measurements were performed with the co-operation of Katie Frenis (PhD candidate, Laboratory of Molecular Cardiology, University Medical Center Mainz).

4.1.5 Oral glucose tolerance test (OGTT) and measurement of glucose levels in whole blood

To test a possible influence of GLP-1RA liraglutide on glucose and insulin metabolism in non-diabetic hypertensive mice, oral glucose tolerance tests (OGTTs) were performed according to published protocols ^{320,321}. OGTT is an *in vivo* metabolic test, in which a defined amount of glucose is administered and, over a 2 h period, it is measured how fast the glucose is cleared from the blood ³²¹.

OGTTs were performed 7 days after treatment onset (Figure 4-3). Mice were fasted for 6 h (7 am–1 pm) and a glucose load of 1.5 g/kg (in 10 μ l/g) administered by gavage. Blood glucose levels were measured in tail vein blood samples 0, 15, 30, 60, 90, and 120 min after glucose challenge using a hand-held glucometer. Additional blood samples were collected by puncture of the vena facialis at 0 and 120 min for assessment of insulin levels in plasma.

4.1.6 Intravital fluorescence microscopy (IVM)

Intravital microscopy (IVM) of blood vessels was performed in collaboration with Jun. Prof. Dr. Christoph Reinhardt / Platform Intravital Microscopy / Center for Thrombosis and Hemostasis (CTH), University Medical Center Mainz according to published protocols ^{322,323}

(conducted by Dr. Alexandra Grill). IVM allows to study the rolling and adhesion of circulating blood cells on/to the vascular wall by staining them with fluorescent dyes³²³. In this case, injection of the fluorescent dye acridine orange (that only stains nucleated cells) enabled leukocyte visualization. Under flow conditions, leukocyte rolling represents the first adhesive contact of white blood cells to the endothelium and plays a crucial part in leukocyte recruitment during inflammation *in vivo*³²⁴.

One week after treatment onset (Figure 4-3), mice were anesthetized with a mix of midazolam (5 mg/kg), medetomidine (0.5 mg/kg) and fentanyl (0.05 mg/kg) by intraperitoneal injections (10 µl/g) and fixed on a custom-built stage with heating pad to maintain a physiological body temperature. A jugular catheter (inner diameter 0.28 mm; outer diameter 0.61 mm) was implanted and the femoral vein and artery dissected free for microscopic observation. 50 µl of acridine orange (0.5 mg/ml) were injected with the jugular catheter for leukocyte staining. Leukocyte rolling was visualized using an upright confocal spinning disc microscope with a 25x water immersion objective. For image acquisition and analysis, real-time imaging software (NIS Elements, Nikon) was used with cell recruitment quantified in four fields of view (100 × 150 µm) per femoral artery vein. Cells moving in contact with and/or detaching from the endothelial lining within an observation period of 10 s and a minimum distance of 50 µm were defined as rolling leukocytes and quantified per square millimeter.

4.2 Ex vivo animal studies

4.2.1 Harvest of blood, organs, and tissue from mice

Organs, tissue, and blood from experimental mice were harvested according to §4 Abs. 1 and §6 Abs. 1 Nr. 4 of the German Animal Welfare Act. Mice were anesthetized with ketamine/xylazine (120 mg/kg ketamine and 16 mg/kg xylazine in 0.9 % NaCl). Ensuring deep narcosis, the abdomen and the rib cage were exposed and blood (0.5–1.0 ml) withdrawn by cardiac puncture of the beating heart using a 1 ml syringe with 26 G cannula. After measuring glucose levels using a hand-held glucometer, the blood was immediately anti-coagulated by addition of 0.1 vol K₃EDTA (50 mM). To prevent stasis-induced intravascular coagulation, 200 µl of a diluted heparin solution (200 IE) were injected in the left ventricle pre-transection. Finally, tissue and organs were collected (lung, spleen, aorta, femur/tibia, heart, whereby removal of the latter ensured the animal's death). All harvested tissue was instantly put in ice-cold Krebs-HEPES buffer (see 3.6) and either snap-frozen in liquid nitrogen or immediately processed in subsequent experiments. Aortas were very carefully cleaned of any perivascular adipose tissue (pVAT) on ice to ensure an intact

endothelium. Anti-coagulated blood was centrifuged for 10 min at 3600 rpm at room temperature to collect plasma, which was frozen and stored at -80°C for further analyses.

4.2.2 Red blood cells (RBCs) lysis for pan-leukocyte enrichment

EDTA-blood samples (see 4.2.1) were incubated with 10x volume of room-temperature ACK lysis buffer (see 3.6) for 3–5 min until lysis of the red blood cells (RBCs) was evident. White blood cells (WBCs) were collected by centrifugation at 300 g for 5 min at room temperature and washed twice with cold PBS (300 g, 5 min, 4°C). An automated hematology analyzer (Sysmex KX-21N) was used to confirm the removal of RBCs and platelets in the blood samples. Cells were pelleted and resuspended in guanidinium thiocyanate (GIT) denaturing solution (see 3.6) for subsequent RNA isolation (see 4.3.4) and gene expression analysis (see 4.3.6).

4.2.3 Isolation of primary mouse lung endothelial cells (MLECs)

For reasons of abundance, primary endothelial cells were harvested from lung tissue. The isolation procedure of these so-called mouse lung endothelial cells (MLECs) was adapted from published protocols³²⁵⁻³²⁷.

Murine lung lobes without any bronchi or connective tissue from 3–4 animals were pooled and collected in cold DMEM GlutaMAX. The lung tissue was placed in a glass petri dish and minced thoroughly using surgical scissors (Figure 4-5). The disrupted tissue was transferred into a digestion solution containing collagenase A (see 3.6), and incubated for 30 min at 37°C at 600 rpm on a thermomixer. The cell suspension was mixed every 10 min to prevent clumping. The digested tissue was aspirated several times through a 14 G cannula and finally filtered through a 70 µm cell strainer to obtain a single-cell suspension. The digestion was stopped by adding serum-containing medium (MLEC isolation buffer, see 3.6). Cells were pelleted by 1400 rpm for 15 min at 4°C and resuspended in MACS (Magnetic Activated Cell Sorting) buffer (see 3.6). To isolate highly pure endothelial cells, two magnetic-based separation steps were performed: a first one using CD31 *MicroBeads*, followed by a second purification of the magnetically separated CD31⁺ cells with anti-CD102 pre-coated *Dynabeads* (see 4.4.8).

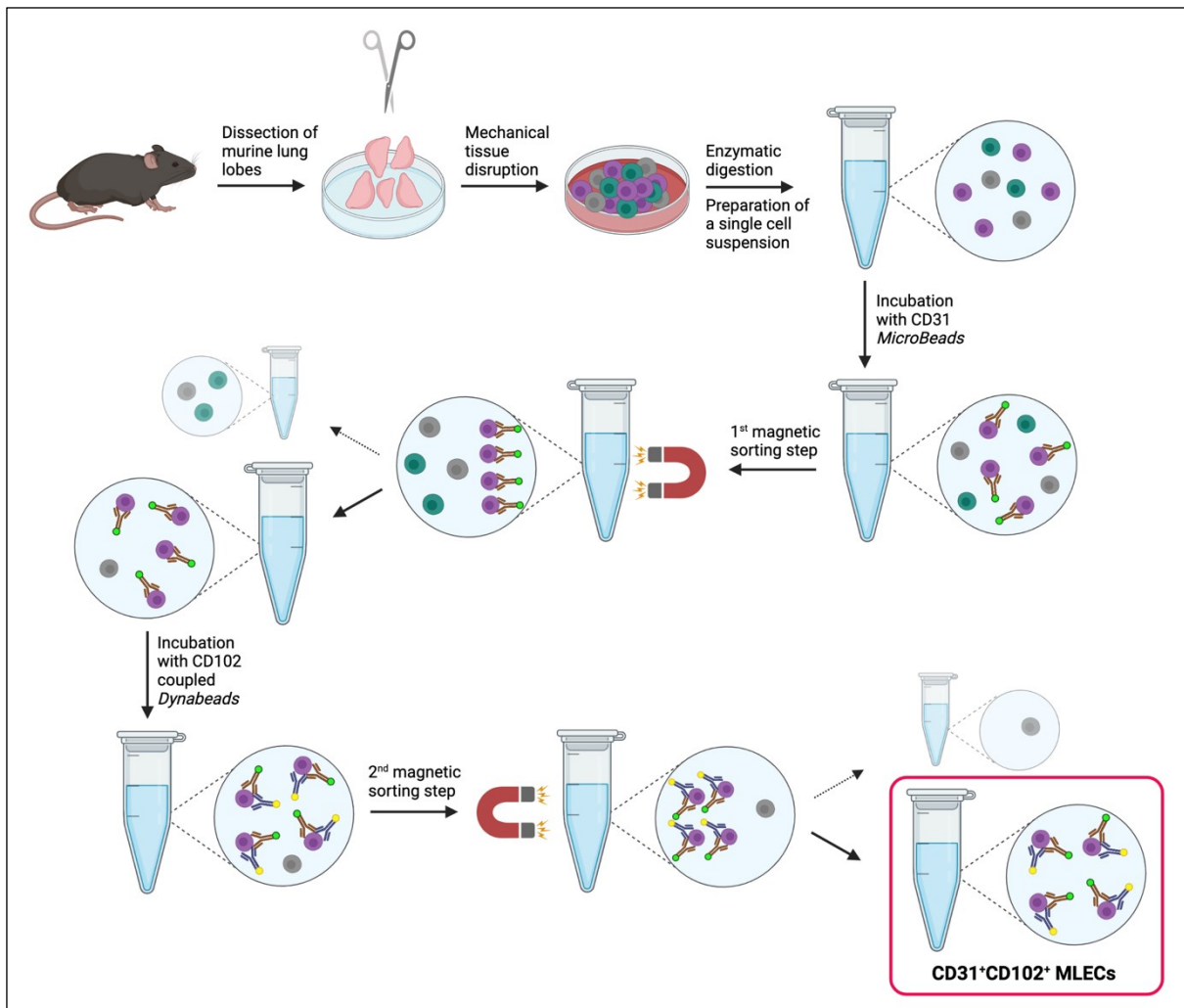


Figure 4-5: Isolation of primary endothelial cells from murine lung tissue. Methodic approach to isolate primary mouse lung endothelial cells (MLECs) via double magnetic selection using CD31 *MicroBeads* and anti-CD102 pre-coated *Dynabeads*. Created with [BioRender.com](https://www.biorender.com/).

50 μ l CD31 *MicroBeads* were added to the resuspended cells and incubated for 15 min at 4°C on a rotor. The MACS® system was used for the separation of magnetically labeled cells in the first step. Cells were loaded over a 30 μ m pre-filter onto LS columns that were attached to a QuadroMACS magnet. The column was washed three times with cold MACS buffer to remove unlabeled cells. The column was removed from the magnet, put in a fresh collection tube and the magnetically labeled (CD31⁺) cells were isolated in 5 ml MACS buffer by flushing the cells from the column using a plunger. Secondly, 50 μ l anti-CD102 conjugated *Dynabeads* were added to the cell suspension and incubated for 1h at 4°C on a rotor. Double-positive MLECs (CD31⁺CD102⁺ cells) were separated using a *DynaMag* magnet. The cells were counted, pelleted, resuspended in GIT buffer, and stored at -80°C for subsequent RNA isolation.

4.2.4 Isolation of primary mouse bone marrow-derived macrophages (BMDMs)

The isolation of bone marrow-derived macrophages (BMDMs) was conducted following published protocols^{328,329}. Murine femur and tibia bones were dissected and cleaned of muscles and fat. Under sterile conditions, the bones were cut open and flushed with PBS using a 24 G cannula and 20 ml syringe (Figure 4-6). The cells were passed through a 100 μm cell strainer, counted, pelleted by 1500 rpm for 5 min at 4°C and finally resuspended in BMDM growth medium (including 30 % L929 cell-conditioned media, see 3.6) at $\sim 2 \times 10^6$ cells/ml. L-cells are known to secrete macrophage colony-stimulating factor (M-CSF), a lineage-specific growth factor causing myeloid progenitor cells to differentiate into macrophages³³⁰. The cells were incubated for 7 d (37°C, 5 % CO₂) to allow macrophage differentiation, with refreshing of the medium at day 4 (see 3.6, including 15 % L929 cell-conditioned media). For cell harvest at day 8, BMDMs were segregated from non-adherent cells, pelleted, resuspended in GIT buffer, and stored at -80°C for subsequent RNA isolation. BMDM isolation was performed with technical assistance of Foruzandeh Samangan (junior group "Experimental Research", Center for Thrombosis and Hemostasis (CTH), University Medical Center Mainz).

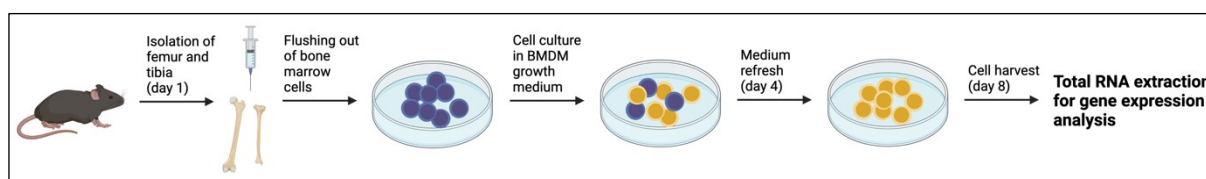


Figure 4-6: Isolation of bone marrow-derived macrophages (BMDMs) from murine femur and tibia. Formation of mature macrophages was achieved by *in vitro* differentiation of bone marrow cells in L-cell-conditioned medium containing macrophage colony-stimulating factor (M-CSF). Created with BioRender.com.

4.2.5 Determination of the heart/body weight ratio

As an indicator of cardiac hypertrophy, the heart/body weight ratio was calculated by dividing the mouse's weight at the day of euthanasia (day 7) by the weight of its isolated heart post-transection.

4.2.6 Vascular isometric tension recordings

To study vascular function and reactivity *ex vivo*, isometric tension recordings of intact aortic segments were conducted. Endothelial dysfunction was evaluated based on the fact that a dysfunctional endothelium loses the ability to properly regulate the vascular tonus in response to endogenously or exogenously added stimuli. This can be measured in relaxation-response curves to acetylcholine. Depending on the functional integrity of the endothelium, aortic rings show different vasomotor responses: with an intact endothelium, acetylcholine administration induces aortic vasodilation due to activation of endothelial

muscarinic receptors leading to eNOS-derived \bullet NO formation, whereas it causes vasoconstriction if the endothelium is damaged, resulting from a direct effect of acetylcholine on smooth muscle cells (Figure 1-5) ^{123,331}. Thus, the aortic relaxation potential in response to accumulative doses of acetylcholine allows conclusions about the endothelial function. Similarly, endothelium-independent relaxation was measured in response to accumulative doses of nitroglycerin (NTG), an organic nitrate and \bullet NO donor, that leads to vasodilatation without the dependence on eNOS-derived \bullet NO formation ¹²².

Vascular reactivity studies were conducted as described in previous protocols ^{332,333}. In short, aortas were dissected, cleaned of perivascular fat and the thoracic part cut into 4 mm segments. Next, aortic rings were mounted on force transducers, that record the change in force (in grams [g] or milliNewtons [mN]) developed by muscle relaxation/contraction, within an organ bath chamber system ³³⁴. The rings were pre-constricted using prostaglandin F₂ α (2 μ M) to yield approximately 80 % of the maximal tone induced by the KCl bolus (80 mM). Finally, relaxation-response curves to acetylcholine (ACh, 1 nM to 3.2 μ M) and nitroglycerine (NTG, 1 nM to 32 μ M) were conducted. Organ bath chamber data was created with the technical assistance of Jörg Schreiner (Laboratory of Molecular Cardiology, University Medical Center Mainz).

4.2.7 Dihydroethidium (DHE)-dependent fluorescence oxidative microtopography in aortic and cardiac cryosections

Oxidative stress in aortic and cardiac cryosections was quantified by fluorescent microscopy employing dihydroethidium (DHE) as a fluorogenic probe. DHE is a lipophile, cell-permeable dye that is oxidized by superoxide ($O_2^{\bullet-}$) to give the highly specific product 2-hydroxyethidium (2-OH-E⁺ or 2-HE). 2-HE intercalates within the cell's DNA, which changes its fluorescent properties to give a red fluorescent product when excited with a wavelength at 488 nm. In biological systems, with other oxidants (hydrogen peroxide, peroxyxynitrite, or hydroxyl radical) present, DHE is simultaneously non-specifically oxidized to ethidium (E⁺) (Figure 4-7 A). Ethidium also intercalates into the DNA, exhibiting red fluorescence with a very similar emission spectrum as 2-HE (Figure 4-7 B). Thus, due to the overlapping fluorescence spectra, fluorescence-based microscopic assays cannot distinguish between fluorescent products 2-HE and E⁺ and are only indicative of all reactive oxygen species (ROS) found within the tissue. However, 2-HE and E⁺ can be detected and separated using an HPLC/fluorescence assay, allowing unambiguous quantitation of intracellular superoxide (see 4.2.8) ^{335,336}.

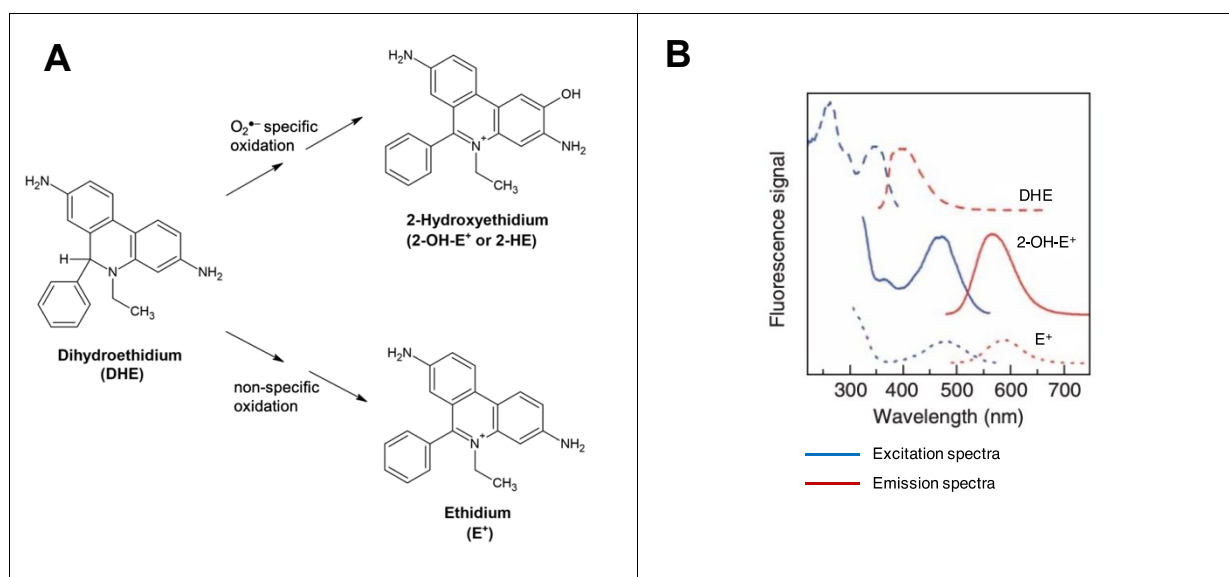


Figure 4-7: Oxidation products of dihydroethidium (DHE) with corresponding fluorescence spectra. (A) DHE is oxidized to 2-hydroxyethidium (2-OH-E⁺ or 2-HE) specifically by superoxide whereas ethidium (E⁺) is an unspecific oxidation product. Created with [ChemSketch](#). (B) The fluorescence spectrum of DHE does not interfere with the ones of 2-OH-E⁺ or E⁺, allowing use as a fluorogenic probe for ROS quantification. By contrast, the emission spectra of 2-OH-E⁺ and E⁺ exert significant spectral overlap, which cannot be resolved with common filters used in fluorescence microscopy, thus making the differentiation of the respective fluorescent products impossible. (The shown fluorescence spectra were taken in 10 mM Tris buffer/1 mM EDTA, pH 7.4. Fluorescence intensity increases upon binding to DNA.) Taken from ³³⁷ with permission. © 2007, Nature Publishing Group.

Isolated hearts (left ventricles only) and aortic ring segments (4 mm) were incubated in Krebs-Hepes buffer including protease inhibitors (see 3.6) for 10 min at 37°C, embedded in OCT (Optimal Cutting Temperature)-resin and frozen in liquid nitrogen. Frozen tissue sections of 8 μm were cut using a cryostat, mounted on microscope slides and either immediately processed or stored at -80°C until use. The object slides were created in a way that sections from all treatment groups were placed on the same slide, ensuring uniform staining and proceeding. The cryosections were incubated with DHE (1 μM in PBS) for 30 min at 37°C in the dark. The slides were coverslipped and ROS-derived red fluorescence was immediately measured by a fluorescence microscope (Zeiss) with rhodamine filter (excitation (Ex.) 510–560 nm; emission (Em.) ≥ 590 nm). Sequential to the DHE-derived signal, autofluorescence of the aortic collagen fibers was measured with a DAPI filter (Ex. 365 nm; Em. ≥ 420 nm). Images were quantified as IOD (integrated optical density) using the Gel-Pro Analyzer software. To investigate the involvement of eNOS uncoupling in ROS production and endothelial dysfunction, selected aortic rings were simultaneously pre-incubated with the NOS inhibitor L-NAME (0.5 mM) for 30 min at 37°C in the dark and ROS-derived red fluorescence in the endothelial layer was measured as described above.

4.2.8 Quantification of aortic superoxide formation by HPLC analysis

A high-performance liquid chromatography (HPLC)/fluorescence-based assay was used to quantify oxidative stress derived from aortic superoxide formation by analyzing 2-HE levels

after incubating aortic tissue with DHE. The method was conducted using previously published protocols^{336,338}. HPLC is an analytical method, which allows the separation, identification and quantification of different components within a complex mixture. It consists of a column with adsorbent material (stationary solid phase), through which the sample mixture, together with a liquid solvent (mobile phase), is pumped with high pressure. The individual components of the mixture interact differently with the stationary phase, thus leaving the column at different times (retention times) where they can be detected with an appropriate detector³³⁹. By running known substances with a specific concentration and comparing retention times and peak heights, it is possible to identify and quantify the samples' components.

Aortic tissue was incubated with 50 μ M DHE for 30 min at 37°C in PBS buffer. Afterwards, the tissue was pulverized in a mortar under liquid nitrogen, resuspended in homogenization buffer (acetonitrile/PBS, 1:1), and centrifuged at 20,000 g for 15 min at 4°C. The supernatant was removed and 50 μ l of it subjected to HPLC analysis. The system consisted of a control unit, two pumps, mixer, detectors, column oven, degasser, and an autosampler (AS-2057 plus) from Jasco and a C18-Nucleosil 100-3 (125x4) column from Macherey & Nagel. A high-pressure gradient was applied with acetonitrile and 50 mM citrate buffer pH 2.2 as mobile phases (flow = 1 ml/min). The percentages of the organic solvent were as follows: 0 min, 36 %; 7 min, 40 %; 8-12 min, 95 %; 13 min, 36 %. DHE was detected by its absorption at 355 nm whereas 2-HE was detected by fluorescence (Ex. 480 nm/Em. 580 nm). The signal was normalized to a 0.5 μ M 2-HE standard. HPLC analyses were performed with the cooperation of Sanela Kalinovic (PhD candidate, Laboratory of Molecular Cardiology, University Medical Center Mainz).

4.2.9 Quantification of NADPH oxidase activity in cardiac membrane fractions by lucigenin-enhanced chemiluminescence (ECL)

Besides the fluorescence detection of ROS in the presence of redox-sensitive probes (see 4.2.7–4.2.8), oxygen free radicals can also be detected using chemiluminescent probes, such as L-012 and lucigenin³⁴⁰⁻³⁴². On exposure to oxidative stress, the probe undergoes a chemical reaction with ROS, forming an energy-rich product that spontaneously decays into the ground state under emission of chemiluminescence light. The released photon can be measured by a scintillation counter or a luminometer³⁴¹. Even though the luminol analog L-012 (8-amino-5-chloro-7-phenylpyridol[3,4-d]pyridazine-1,4-(2H,3H)dione sodium salt) has been shown to be more sensitive than lucigenin, it does not exclusively react with superoxide. L-012-derived chemiluminescence (see 4.2.10) can be induced also by other reactive oxygen species such as hydrogen peroxide, hydroxyl radical, and peroxyxynitrite. Lucigenin (*N,N'*-dimethyl-9,9'-biacridinium dinitrate) on the other hand has been

demonstrated to be a superoxide-specific chemiluminescent probe³⁴⁰⁻³⁴². The reactions involved in lucigenin-enhanced chemiluminescence (ECL) are depicted in Figure 4-8.

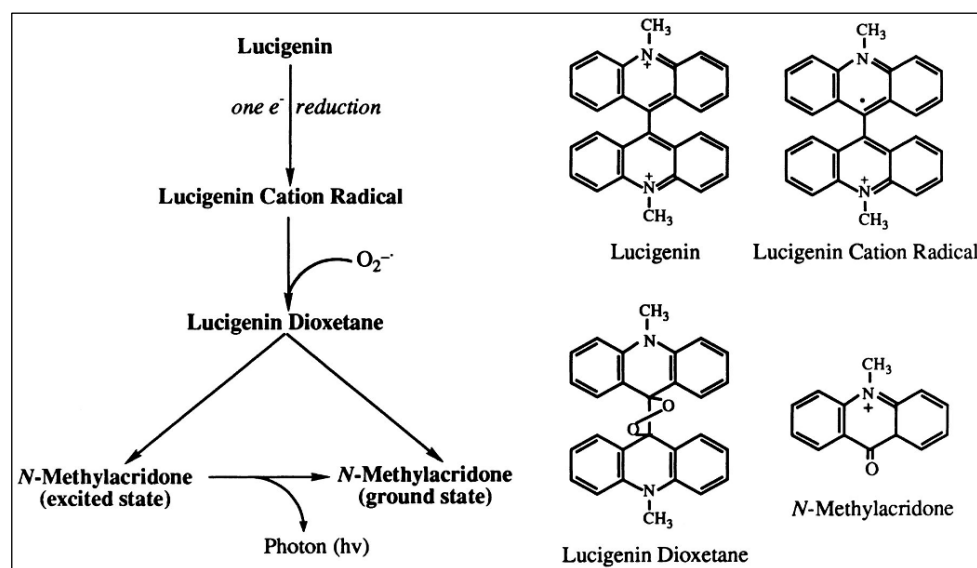


Figure 4-8: Lucigenin-enhanced chemiluminescence. In a first reaction, lucigenin is reduced to its cation radical in a one-electron transfer reaction (usually by $O_2^{\bullet-}$), which then reacts with a second $O_2^{\bullet-}$ to form an unstable lucigenin dioxetane intermediate, which decomposes into two molecules of *N*-methylacridone. One of the *N*-methylacridone molecules is in an electronically excited state, releasing a photon upon relaxation to the ground state. The respective chemical structures of the intermediates are depicted on the right side. In the case of high lucigenin concentrations ($> 10 \mu\text{M}$) and biological systems with low superoxide levels, lucigenin can be alternatively reduced by flavoenzymes, leading to the formation of the cation radical. The lucigenin cation radical subsequently reacts with molecular oxygen, thereby generating superoxide and reforming lucigenin. This initiates a process called 'redox cycling' (not shown). Chemiluminescence derived from lucigenin which entered redox cycling leads to incorrect assessment of superoxide levels from biological sources, as lucigenin becomes a source of superoxide itself. Taken from³⁴³ with permission. © 1998 ASBMB. Currently published by Elsevier Inc; originally published by American Society for Biochemistry and Molecular Biology.

Certain conditions (lucigenin concentrations $> 10 \mu\text{M}$, the absence of cells, the presence of oxidoreductases such as xanthine oxidase) have been associated with redox cycling of lucigenin³⁴². Redox cycling describes a process, in which a chemical, often through flavin-containing enzymes, is reduced to a free radical by a one-electron transfer, which then rapidly reacts with O_2 , thereby generating superoxide and reforming the parent molecule. Hence, with every cycle, O_2 and cellular reducing equivalents are consumed and $O_2^{\bullet-}$ is generated, which further fuels the formation of other ROS and RONS³⁴⁴. Thus, redox cycling of lucigenin can artificially overexpress superoxide production, impeding accurate measurement of superoxide production within the biological sample. However, this phenomenon has been shown not to occur at low concentrations ($\leq 5 \mu\text{M}$) of lucigenin³⁴¹⁻³⁴³. This method has been extensively used to measure NADPH oxidase-derived superoxide formation in cardiac membrane fractions (devoid of any mitochondrial constituents through differential centrifugation steps of 20,000g followed by 100,000g, see below)³⁴². As demonstrated by Oelze et al., ATII-infused hypertensive rats showed enhanced NADPH (200 μM)-stimulated lucigenin ECL signals, which correlated with increased membranous

content of the NADPH oxidase subunits Rac1 and p67^{phox}, both of which was inhibited by beta-blocker nebivolol treatment ³⁴⁵.

The method was conducted based on previously published protocols ^{75,345}. In short, cardiac membrane fractions were prepared by homogenization of the heart in 400 µl Tris DTT buffer (see 3.6) and subsequent differential centrifugation of the resulting homogenous liquid as follows: 2000 g, 10 min; supernatant 20,000 g, 20 min; supernatant 100,000 g, 60 min (all steps at 4°C), whereas the resulting pellet was resuspended in ca. 100 µl of Tris Mem buffer (see 3.6). NADPH oxidase activity of the membrane suspension (0.2 mg/ml protein) was measured by lucigenin (5 µM)-ECL in the presence of 200 µM NADPH. ECL was detected in a single vial luminometer Lumat LB9507. Results were expressed as counts/min after 5 min. The assay was performed with the technical assistance of Jessica Rudolph (Laboratory of Molecular Cardiology, University Medical Center Mainz).

4.2.10 Quantification of whole blood oxidative stress by L-012-enhanced chemiluminescence (ECL)

Whole blood oxidative burst mainly reflects leukocyte NADPH oxidase (Nox2) and myeloperoxidase activity and was used as a global readout of the pro-oxidant burden and activation of inflammatory pathways ^{209,346}.

The method was conducted according to previously published protocols. ^{347,348} Fresh citrate-anticoagulated blood (1:10) was kept at room temperature and diluted 1:50 in PBS buffer (containing Ca²⁺/Mg²⁺, 1 mM each). The endotoxin zymosan A (50µg/ml), a stimulator of NADPH oxidase activity ³⁴⁹, was added together with the chemiluminescent probe L-012 (100µM), and ROS formation was assessed by L-012-ECL using a Mithras² chemiluminescence plate reader (Berthold Technologies). Results were expressed as counts/s after 45 min.

4.2.11 Quantification of aortic nitric oxide by electron paramagnetic resonance spectroscopy (EPR)

Electron paramagnetic resonance spectrometry (EPR) was used to assess aortic •NO synthesis/bioavailability using colloid Fe(II)-diethyldithiocarbamate (Fe(DETC)₂) as spin trap. The method was conducted as described in general previously ^{350,351}.

Instead of measuring the "damage" that has been done by ROS, EPR directly detects the presence of unpaired electrons and has, thus, evolved as a powerful tool to measure free radical species. The principle of EPR is similar to the one of Nuclear Magnetic Resonance (NMR), with the difference that EPR detects electron spin transitions instead of nuclear

transitions when a magnetic field with additional microwave-frequency radiation is applied³⁵². Even though •NO itself is a paramagnetic compound, it cannot be directly detected by EPR due to its short half-life and relaxation time³⁴⁰. However, this problem can be overcome by addition of spin trapping agents, which form stable (paramagnetic) adducts detectable by EPR. One of such an EPR spin-trapping agents used for the unequivocal detection of •NO is Fe(DETC)₂, as it specifically reacts with •NO, giving a relatively stable complex with distinct EPR spectrum^{340,350}.

Aortic vessels were cleaned of perivascular fatty tissue and adventitia, cut into rings (3×5 mm), and placed in 1 ml Krebs-Hepes buffer on a 24-well plate on ice. For eNOS activation, samples were stimulated with 10 μM calcium ionophore (A23187) for 2 min on ice, followed by incubation with 1 ml of Fe(DETC)₂ colloid solution (400 μM in PBS with Ca²⁺/Mg²⁺) for 1 h at 37°C. After incubation, the aortic rings were placed at a fixed position in a 1 ml syringe with removed top in PBS buffer and immediately frozen in liquid nitrogen. The EPR measurements were carried out at 77 K using an X-band table-top spectrometer MS400 with the following settings: 10 mW microwave power; 7000 mG amplitude modulation; 100 kHz modulation frequency; 3300 G center field; 110 G sweep width; 30 s sweep time and 10 scans. The amplitude of the characteristic iron-nitrosyl triplet signal was measured to quantify total •NO production. EPR measurements were performed with the co-operation of Sanela Kalinovic (PhD candidate, Laboratory of Molecular Cardiology, University Medical Center Mainz).

4.2.12 Quantification of nitrite and nitrate from plasma by HPLC analysis

HPLC analysis to determine nitrite (NO₂⁻) and nitrate (NO₃⁻) concentrations in plasma was performed in collaboration with Prof. Dr. Stefan Chlopicki / Jagiellonian Centre for Experimental Therapeutics (JCET) / Jagiellonian University, Krakow, Poland according to published protocols (conducted by Dr. Kamil Kus)³⁵³.

Nitrite (NO₂⁻) is the autoxidation product of aqueous nitric oxide³⁵⁴ and has been demonstrated to be a marker for eNOS-derived •NO formation³⁵⁵. Nitrate (NO₃⁻) on the other hand is the oxidation product of •NO with O₂^{•-} and, thus, serves as a marker for peroxynitrite generation (see 1.4.3).

The concentrations of NO₂⁻ and NO₃⁻ were measured by ENO-20 NOx Analyzer (Eicom Corporation), based on the liquid chromatography method with post-column derivatization with Griess reagent. The plasma samples were precipitated with methanol at the ratio of 1:1 (v/v) and subsequently centrifuged at 10,000 × g for 10 min. The supernatant was removed and 10 mL of it injected into the HPLC system. NO₂⁻ and NO₃⁻ were separated on a NO-PAK column (4.6 μm × 50 mm; Eicom). NO₃⁻ was reduced to NO₂⁻ by a cadmium-copper column

(NO-RED; Eicom). NO_2^- was detected based on the Griess reaction, with sulfanilamide and naphthyl ethylenediamine (both from NO-EBP, Eicom) forming a purple diazo compound (tR = 4.9 min for nitrite and 7.8 min for nitrate) with UV/Vis detection at 540 nm.

4.2.13 Histological and immunohistochemical staining of aortic rings

The use of histological and immunohistological techniques allows to study the microscopic structure of biological tissue and, with the help of antibodies, to visualize the cell-specific distribution of antigens within tissue sections. Immunohistochemistry (IHC) was applied to aortic ring segments to characterize the immune cell infiltration to aortic tissue. Cellular components were visualized by an indirect detection method where the tissue is first incubated with a target-specific primary antibody, which is subsequently detected by a labeled secondary antibody. To increase IHC sensitivity, an additional amplification step was implemented using the ABC (Avidin-Biotin-Peroxidase Complex) method which relies on the high affinity of avidin for biotin³⁵⁶. Biotinylated secondary antibodies bind irreversibly to avidin which has been pre-incubated with biotin-coupled horseradish peroxidase (HRP), thus forming an avidin-biotin-reporter enzyme complex. Since avidin is tetravalent, it bridges multiple biotinylated reporter enzyme sites, resulting in increased IHC signal intensity³⁵⁶. By adding the peroxidase substrate DAB (3,3'-Diaminobenzidine) and hydrogen peroxide to the sample, an insoluble chromogenic product in form of a brown precipitate is formed at the sites of the antigen that can be observed under a light microscope (Figure 4-9).

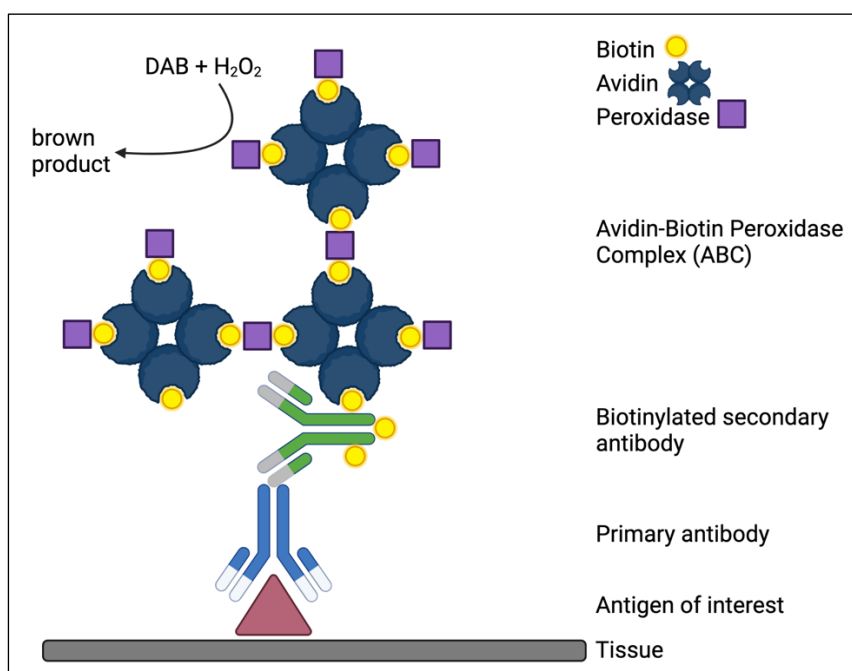


Figure 4-9: Molecular interactions of the ABC-based detection method. A biotinylated secondary antibody links the antigen-binding primary antibody to an avidin-biotin-peroxidase complex (ABC). Avidin possesses four binding sites for biotin, which is used for signal amplification. The peroxidase enzyme oxidizes DAB (3,3'-Diaminobenzidine) in the presence of hydrogen peroxide (H_2O_2) to a brown product, which can be visualized under a microscope. Created with BioRender.com.

Aortic ring segments (3–4 mm) with intact adventitia and perivascular fat were fixed in paraformaldehyde (4 %), paraffin-embedded and cut into sections of 5 µm using a rotary microtome. After deparaffinization, antibody epitopes were unmasked by immersing the sections in citrate buffer (0.01 M, pH 6.0) and boiling them for 20 min in a pressure cooker. This process called HIER (Heat-Induced Epitope Retrieval) breaks cross-links between proteins created during tissue fixation, enabling antibody binding to its target antigen³⁵⁷. The sections were washed with 1x wash buffer (Dako), followed by inactivation of endogenous peroxidase activity by incubating the dewaxed paraffin sections in 3 % H₂O₂ for 30 min at room temperature. By blocking the naturally occurring peroxidase enzyme in the tissue, false-positive results from oxidized DAB, not deriving from the antigen of interest, are avoided. The sections were washed with wash buffer (3 x 5 min) and then blocked with 2.5 % normal horse serum (NHS) blocking solution for 1 h at room temperature. Next, diluted primary antibodies were added to the tissue sections (see 3.8.1) and incubated at 4°C overnight. The next day, the slides were washed three times with wash buffer at 5 min each and incubated with appropriate biotinylated secondary antibodies (see 3.8.3) for 20 min at room temperature. After washing, freshly prepared ABC reagent (1:1 of avidin/biotinylated HRP) was added to the slides and incubated for 30 min at room temperature. The sections were washed with wash buffer (3 x 5 min), a suitable amount of DAB reagent added, and incubated in the dark until desired stain intensity developed (10–30 min). The latter was monitored under a bright-field microscope to prevent high background formation due to prolonged substrate incubation. Finally, the tissue sections were counterstained with hematoxylin for 5 min at room temperature to stain cell nuclei and enhance tissue morphology. The slides were rinsed in tap water for 10 min, causing the sections to change from brown to blue color ("bluing"). After dehydrating the sections, slides were mounted in Cytoseal mounting medium under a cover-slip, and images were taken with a bright-field microscope (Olympus) using a 20x objective.

Histological detection of collagen fibers in aortic tissue was assessed by picro-sirius red staining of paraffin-embedded aortic rings. Deparaffinized tissue sections were incubated for 5 min with hematoxylin to stain cell nuclei, washed with wash buffer, and stained in picro-sirius red solution (0.1 % with 1.2 % picric acid) for 1 h. Finally, specimens were dehydrated with ethanol, coverslipped with Cytoseal, and images taken as described above. (Immuno-) Histological analyses were performed with the co-operation of Konstantina Filippou (medical student) and technical assistance of Angelica Karpi (Laboratory of Molecular Cardiology, University Medical Center Mainz).

4.2.14 Flow cytometric quantification of aortic immune cell infiltration

Flow cytometry is a laser-based technique that helps to study the physical and chemical characteristics of particles or cells. It allows the simultaneous measurement of multiple parameters of individual cells (e.g., their size and granular content or the expression of intracellular and cell surface molecules) which enables the distinction of different cell types in a mixed cell population^{358,359}. A flow cytometric analysis involves several steps: the preparation of a single-cell suspension from cell culture or tissue samples, the staining with fluorescent-labeled antibodies (if additional parameters than just the cell size and granularity are desired to measure), and the acquisition on the instrument³⁵⁹. An overview of a typical flow cytometer is shown in Figure 4-10. In brief, the cell suspension is focused by sheath fluid (“hydrodynamic focusing”), causing the cells to pass the laser beams in a single file. Scattered light and fluorescence emission (from stained cells) give information about the cell’s nature. The physical characteristics of a cell are defined by light scattered in forward direction (forward scatter, FSC) and light scattered in $\sim 90^\circ$ direction (side scatter, SSC), correlating with cellular size and granular content, respectively. The chemical or immunological properties of a cell are characterized by light emitted from fluorochromes that are conjugated to antibodies for the detection of target proteins. Optical filters and dichroic mirrors split the emitted fluorescent light into specific wavelengths and guide them to detectors (photomultiplier tubes, PMTs) that convert and amplify the light signal (photons) into an electronic signal, a voltage. Finally, the signal is processed by analog-to-digital converters (ADC) that convert voltage into digital value^{358,359}. The process of not only phenotyping but actual separating of cells according to their physical and chemical properties is called ‘cell sorting’ or FACSTM (fluorescence-activated cell sorting). FACS requires a specialized type of flow cytometer where the cells of interest are separated by electrostatic flow sorting. If a cell matches the selection criteria, it becomes positively or negatively charged. Thus, when passing through an electrostatic field, the cell of interest gets deflected and can be collected³⁶⁰. With the use of several lasers as excitation sources, it is possible to enlarge the number of detectable fluorochromes. The *FACSCantoTM II* used within this study is a 3-laser flow cytometer (405 nm, 488 nm, and 633 nm; 4-2-2 configuration) allowing a simultaneous 8-color analysis.

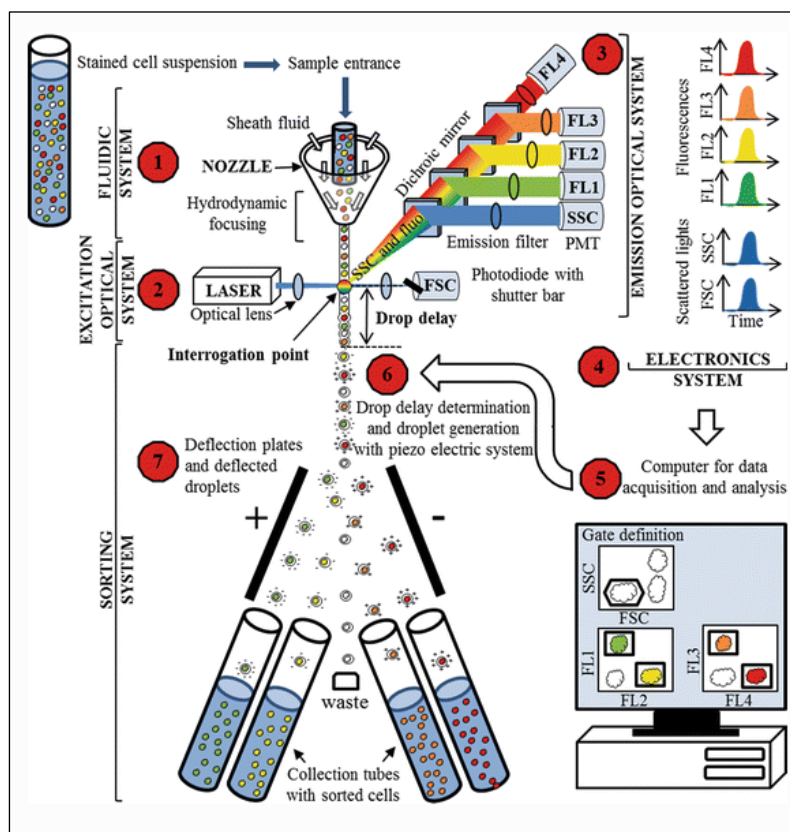


Figure 4-10: The principle of flow cytometry. A typical flow cytometer comprises of three parts, (a) hydrodynamic focusing through the fluidic system enables the cells in suspension to pass the laser beam one by one, (b) a focused laser beam hits individual cells in the optical system, leading to scattered and emitted fluorescence light that is filtered and collected, (c) the electronic system that digitalizes the signal. An additional cell sorting step is optional, a process called FACS (fluorescence-activated cell sorting). Taken from ³⁵⁸ with permission. © 2012, Springer Science Business Media B.V.

Flow Cytometry was used to quantify immune cell infiltration into aortic tissue from mice and to identify immune cell subtypes. The method was adapted from published protocols ^{209,211}. Aortic vessels were dissected, cleaned of fatty tissue, minced with a razor blade, and enzymatically digested with liberase (1 mg/ml in HBSS with calcium and magnesium) for 30 min at 37°C on a thermomixer (500 rpm). The digestion was stopped with serum-containing FACS buffer (see 3.6) and the aortic fragments passed through a 70 µm cell strainer to obtain a single-cell suspension. Cells were pelleted by 300 g for 6 min at 4°C, the supernatant removed and the aortic cells resuspended in 200 µl FACS buffer. For every single-cell suspended aorta, the cell count was determined and then plated onto one well of a 96 well-plate. The plate was centrifuged (300 g, 6 min, 4°C), the supernatant removed and the single-cell suspensions treated with anti-mouse CD16/CD32 (mouse Fc block, see 3.8.1) for 10 min at room temperature. The blocking reaction was stopped by adding 200 µl of FACS buffer and the supernatant removed after centrifugation. The aortic cells were surface-stained with a mixture of fluorescence-labeled antibodies and dyes (Table 4-1 and see 3.8.2) for immune cell phenotyping (30 min, 4°C in the dark). The cells were washed with FACS

buffer and finally analyzed on a *FACSCanto™ II* (equipped with *FACSDiva* software), with the whole stained single-cell suspended aorta being recorded.

To compensate for spectral overlap in multicolor fluorescence studies, single stainings with splenocytes were conducted (to spare aortic cells). For this purpose, the spleen was dissected and gently ground through a 40 µm using a 1 ml plunger. The filter was rinsed several times with FACS buffer. The cells were pelleted (300 g, 6 min, 4°C), the supernatant removed and erythrocytes lysed by resuspending the cell suspension in 3 ml of ACK lysis buffer (see 3.6) for 3 min. The reaction was stopped by adding 5 ml FACS buffer, cells pelleted, the supernatant removed and the splenocytes resuspended in 5 ml FACS buffer. The cells were counted and plated onto a 96 well plate at a density of 1.0×10^6 cells/well. For the single stainings, the same dilutions of antibodies as for the aortic cells were used (see 3.8.2), except for F4/80-APC, which was exchanged for CD8-APC (Table 4-1).

Table 4-1: Antibodies and dyes used for the assessment of aortic immune cell infiltration. (For antibody dilutions, see 3.8.2).

<u>Fluorochrome-labeled antibody / dye</u>	<u>Target antigen</u>
CD45-APC-efluor 780	Leukocytes
NK1.1-PE-Cy7	Natural killer (NK) cells
F4/80-APC CD8-APC (only single staining)	Macrophages, monocytes Cytotoxic T-cells
TCR-β V450	T-cells
CD11b-PE	Myeloid cells
Ly6G-FITC	(Neutrophil) Granulocytes
Ly6C-PerCP-Cy.5.5	Macrophages, monocytes (Neutrophil) Granulocytes
Fixable Viability Dye eFluor506	Live/dead cell distinction

The gating strategy used to differentiate immune cell subsets is shown in Figure 4-11. For quantitative evaluation, the number of immune cells for every subtype was normalized to the number of living cells (per cell count) in a sample and expressed as percentage of control.

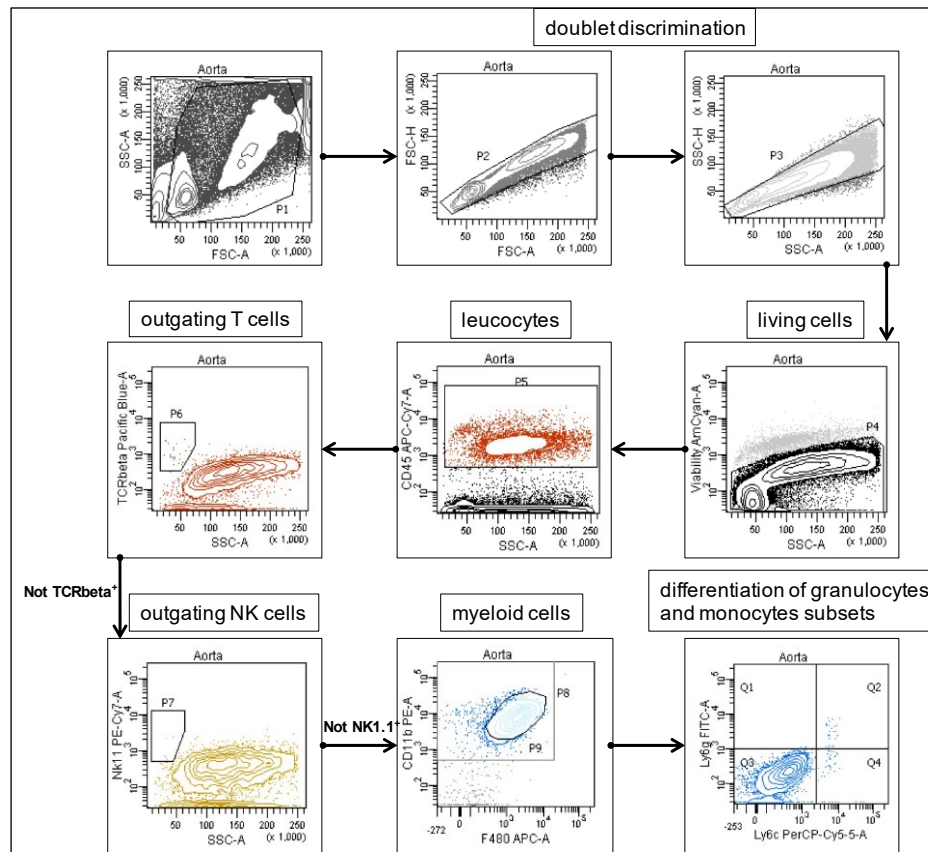


Figure 4-11: Gating strategy for identification of immune cell subtypes in aortic tissue. Debris (P1) and doublets (P2, P3) were excluded from the analysis. Only living cells that stained negatively for the viability dye (P4) were used for subsequent examination. Starting from leukocytes (CD45⁺, P5), lymphocytes subsets (T-cells, TCRβ⁺ (P6) and NK cells, NK1.1⁺ (P7)) were gated out and myeloid cells (CD11b⁺, P8) identified. F4/80⁺ cells immunophenotype tissue-residing monocytes and macrophages (P9). Proceeding from all myeloid cells (CD11b⁺), gating on Ly6c⁺Ly6g⁺ (Q2), Ly6c⁻Ly6g⁺ (Q3), and Ly6c⁺Ly6g⁻ (Q4) enables differentiation between neutrophils, resident and inflammatory monocytes, respectively³⁶¹. Taken from³⁰³ with permission. © 2019 Wolters Kluwer Health.

4.3 Molecular biological methods

4.3.1 DNA extraction from murine tissue

For genotyping of the transgenic mice, a tissue sample was collected by ear notching and genomic DNA extracted using the published 'HotSHOT' method³⁶². The tissue was transferred to 75 µl alkaline lysis reagent (see 3.6) and incubated for 45 min at 95°C and 500 rpm in a thermocycler. The samples were allowed to cool down to approximately 10°C before adding 75 µl neutralization buffer (see 3.6). After thoroughly mixing, the extracted DNA was ready for subsequent genotyping PCR analysis (see 4.3.2) without further purification.

4.3.2 Genotyping of transgenic mice by polymerase chain reaction (PCR)

The polymerase chain reaction (PCR) is a method used for the amplification of distinct DNA fragments. The principle is based on repeated cycles of heating and cooling for DNA

denaturing and enzymatic replication of certain DNA sections that lie in between the complementary binding sequence of the forward and reverse primer (single-stranded oligonucleotides). PCR was used to determine the genotype of transgenic mice (see 4.1.1). The extracted DNA from the ear punch preparations (see 4.3.1), 10x DreamTaq Green Buffer, DreamTaq Hot Start DNA Polymerase, dNTPs as well as distinct forward and reverse primers (see 3.9.2) were used according to the recipe and reaction profiles stated in tables 4-2–4-4.

Table 4-2: Reaction mix and program for the genotyping PCR of *Glp1rflox*.

PCR reaction mix (25 μ l)		PCR program		
10x DreamTaq Green Buffer	2.500 μ l	95°C	3 min	1 x
dNTPs (2 mM each)	2.500 μ l	95°C	30 sec	30 x
Primer forward (<i>Glp1rF2</i> , 10 pmol/ μ l)	1.000 μ l	60°C	30 sec	
Primer reverse (<i>Glp1rR2</i> , 10 pmol μ l)	1.000 μ l	72°C	30 sec	
DEPC treated water	15.875 μ l	4°C	∞	
DreamTaq Hot Start DNA Polymerase (5U/ μ l)	0.125 μ l			
Genomic DNA	2.000 μ l			

The PCR products were subsequently separated and analyzed via agarose gel electrophoresis (see 4.3.3). It was distinguished between homozygosity and heterozygosity for the floxed allele of the *Glp1r* gene as follows: *Glp1r^{flox/flox}* is homozygous for the floxed allele (transgene (tg): 456 bp), *Glp1r^{flox/wt}* is heterozygous for the floxed allele (tg: 456 bp and wt: 356 bp) and *Glp1r^{wt/wt}* is homozygous for the wild-type allele (wt: 356 bp).

Table 4-3: Reaction mix and program for the genotyping PCR of *Cdh5cre*.

PCR reaction mix (25 µl)		PCR program		
10x DreamTaq Green Buffer	2.500 µl	95°C	5 min	1 x
dNTPs (2 mM each)	2.500 µl	94°C	20 sec	10 x (-0.5°C/cycle)
Primer forward (Cdh5F, 10 pmol/µl)	2.000 µl	65°C	15 sec	
Primer reverse (Cdh5R, 10 pmol µl)	2.000 µl	68°C	10 sec	
DEPC treated water	13.875 µl	94°C	15 sec	28 x
DreamTaq Hot Start DNA Polymerase (5U/µl)	0.125 µl	60°C	15 sec	
Genomic DNA	2.000 µl	72°C	5 sec	
		72°C	1 min	
		4°C	∞	

This PCR protocol does not distinguish hemizygous from homozygous transgenic mice. Thus, the presence of the *Cre* transgene (tg: approx. 300 bp) was indicative of *Cdh5^{cre+}* and its absence of *Cdh5^{cre-}*.

Table 4-4: Reaction mix and program for the genotyping PCR of *LysMcre*.

PCR reaction mix (25 µl)		PCR program		
10x DreamTaq Green Buffer	2.500 µl	94°C	4 min	1 x
dNTPs (2 mM each)	2.500 µl	94°C	45 sec	34 x
Primer forward (MLys1, 10 pmol/µl)	2.000 µl	54°C	45 sec	
Primer reverse (MLys2, 10 pmol/µl for wild-type allele and Cre8, 10 pmol/µl for transgene allele)	2.000 µl	72°C	1 min	
DEPC treated water	13.875 µl	72°C	1 min	
DreamTaq Hot Start DNA Polymerase (5U/µl)	0.125 µl	12°C	∞	
Genomic DNA	2.000 µl			

It was distinguished between homozygosity and heterozygosity of the *LysMcre* genotype as follows: *LysM^{+/+}* is homozygous for the *Cre* transgene (tg: approx. 700 bp), *LysM^{+/-}* is heterozygous for the *Cre* transgene (tg: approx. 700 bp and wt: approx. 350 bp) and *LysM^{-/-}* is homozygous for the wild-type allele (wt: approx. 350 bp).

4.3.3 Agarose gel electrophoresis

Agarose gel electrophoresis is a method to analyze DNA fragments by separating them in an electric field according to their size. For verification of the PCR products (see 4.3.2), 2 % agarose gels were used with 1x TAE serving as solvent for the agarose and running buffer (see 3.6). The agarose/buffer mixture was heated to dissolve the agarose, allowed to cool down to approximately 50°C before adding the DNA-intercalating dye Midori Green (5 % v/v) and pouring the gel into a horizontal DNA gel electrophoresis chamber. Midori Green is a non-toxic, non-cancerogenic derivate of ethidium bromide that is able to intercalate into the DNA helix and that can be excited by UV light. The samples were loaded into the gel pockets and separated by 90 V for 35 min. The DNA-Midori Green dye complexes were visualized by fluorescence using a UV transilluminator and identified by comparison with DNA fragments of known sizes (100 bp DNA ladder).

4.3.4 RNA extraction from murine tissue and primary cells

RNA from tissue or cells was extracted using the acid guanidinium thiocyanate–phenol–chloroform extraction method by Chomczynski and Sacchi^{363,364}. A schematic overview of the RNA extraction steps is shown in Figure 4-12.

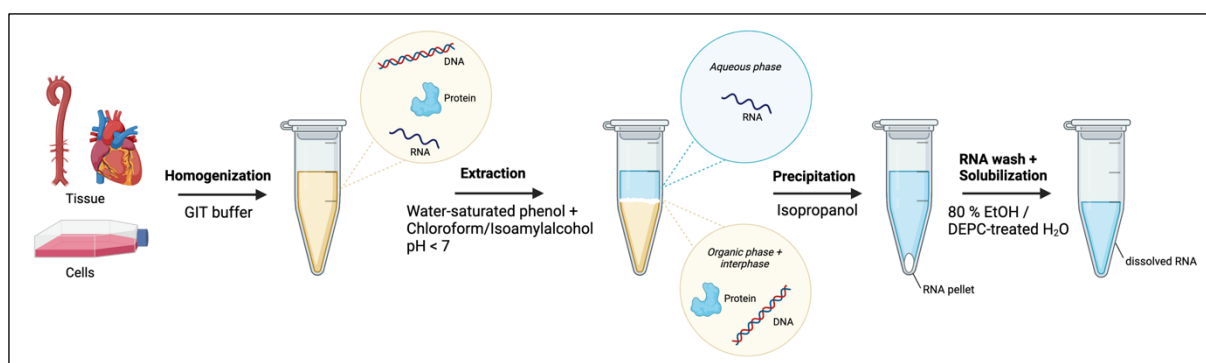


Figure 4-12: The principle of RNA isolation by acid guanidinium thiocyanate–phenol–chloroform extraction. Key step of the method is the separation of RNA from DNA (and proteins) via extraction with an acidic solution containing guanidinium thiocyanate, sodium acetate, phenol, and chloroform. After centrifugation, the upper RNA-containing aqueous phase is removed and total RNA precipitated with isopropanol. Created with BioRender.com.

For RNA isolation from MLECs (see 4.2.3) or BMDMs (see 4.2.4), cells were pelleted after harvest, vigorously resuspended in 600 µl GIT denaturing solution (see 3.6) to homogenize the samples and stored at -80°C until further RNA extraction. Tissue from snap-frozen murine aorta or heart was disrupted and homogenized by transferring it in 600 µl GIT buffer and subsequent high-speed shaking (6 min, 30 Hz) in 2 ml Eppendorf tubes with a 5 mm stainless steel bead using a TissueLyser II. The samples were allowed to lyse for 20 min at -20°C. Next, sodium acetate (60 µl, pH 4.0), water-saturated phenol (600 µl), and a mixture of chloroform/isoamylalcohol (49:1, 300 µl) were added, the solution thoroughly

mixed by shaking/vortexing and incubated for 15 min on ice. The phases were separated by centrifugation for 20 min at 12,500 g at 4°C. In this liquid-liquid extraction step, total RNA partitions into the upper acidic aqueous phase, while proteins and most DNA allocate in the interphase or lower organic phase. The upper RNA-containing phase (approx. 700 µl) was transferred into a fresh Eppendorf tube and RNA precipitated with 700 µl isopropanol at -20°C overnight. The sample was ultracentrifuged for 20 min at 12,500 g at 4°C, the supernatant removed and the nearly colorless RNA pellet resuspended in 80 % cold ethanol (300 µl). The washing step was repeated 2-3x. The RNA pellet was air-dried for 10 min at room temperature and finally resuspended in DEPC-treated water (aorta: 30 µl, heart: 50 µl). For complete solubilization, RNA was incubated for 10 min at 55°C at 600 rpm on a thermocycler. RNA was stored at -80°C.

4.3.5 RNA quantitation

Extracted RNA was quantified using a UV/VIS spectrophotometer. The device simultaneously performs absorbance readings at 260 nm (absorption maximum (A_{\max}) of nucleic acids), 280 nm (A_{\max} by proteins), and 230 nm (A_{\max} by phenols and residual guanidinium thiocyanate). The reading at 260 nm enables calculation of the RNA concentration in the sample since ~40 ng/µl of single-stranded RNA results in an optical density of 1:

$$\text{Concentration}_{\text{RNA}} [\text{ng}/\mu\text{l}] = A_{260} \times \text{dilution factor} \times 40^{365}$$

Absorbance readings at 230 nm and 280 nm were taken to evaluate the quality of the extracted RNA. Preparations of RNA with A_{260}/A_{280} ratios between 1.8–2.0 and A_{260}/A_{230} ratios ≥ 2.0 were considered pure. For subsequent qRT-PCR analyses, RNA concentrations were adjusted to 62.5 ng/µl with DEPC-treated water.

4.3.6 Quantitative real-time PCR (qRT-PCR)

Quantitative real-time PCR (qRT-PCR) is a tool for assessing gene expression by measuring the abundance of certain mRNAs. Beforehand, it is required to reverse-transcribe single-stranded RNA into double-stranded cDNA (complementary DNA), which serves as starting material for the qRT-PCR and can be recognized by the Taq polymerase with its DNA-dependent DNA polymerase activity.

The reverse transcription step depends on naturally occurring RNA-dependent DNA polymerases (“reverse transcriptases”) that convert RNA into complementary DNA. Reverse transcription and subsequent quantitative real-time PCR were conducted in a ‘one-step reverse transcription-quantitative PCR’, where cDNA synthesis and qRT-PCR are performed

in a single-tube reaction with a common buffer system. One gene-specific primer pair is used for both the cDNA synthesis and the amplification of a specific target (Figure 4-13).

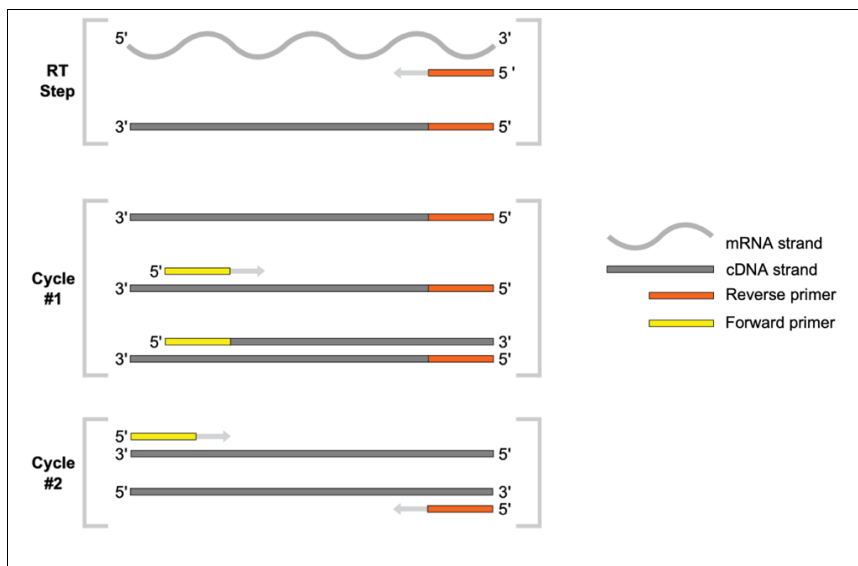


Figure 4-13: The principle of one-step reverse transcription-quantitative PCR. Reverse transcription (RT) is initiated by one of the target-specific PCR primers, thus allowing the reaction to directly proceed from RT to the quantitative real-time PCR step. Modified from ³⁶⁶.

Quantitative real-time PCRs are based upon the same principle as conventional PCRs (see 4.3.2) with additional allowance to quantitate newly synthesized cDNA ³⁶⁷. For all gene expression analyses within this study, TaqMan® assays were used as qRT-PCR system. Besides gene-specific forward and reverse primers, *TaqMan* chemistry makes use of a sequence-specific oligonucleotide probe (*TaqMan MGB probe*) that contains a fluorescent reporter (R) dye (6-carboxyfluorescein, 6-FAM) at its 5' end and a non-fluorescent quencher (NFQ) at its 3' end. The probe is complementary to a sequence that lies between the forward and reverse primer sites (Figure 4-14). Furthermore, a minor groove binder (MGB) is attached to the NFQ, which serves as a molecular clamp enhancing the melting temperature (T_m) of the probe, thus allowing to design shorter and more specific probes ^{366,368}.

As long as the probe is intact (i.e., reporter and quencher are in close proximity), there is no detectable fluorescence emitted by the reporter dye due to Förster resonance energy transfer (FRET) from FAM to the NFQ (Figure 4-14, Step 1 and 2). FRET describes a physical process of radiation-free transfer of energy between a donor chromophore in its electronic excited state to an acceptor chromophore ³⁶⁹. For efficient FRET, close proximity (1–10 nm) and spectral overlap of donor emission and acceptor excitation are required. In case of *TaqMan MGB probes*, the energy transferred to the acceptor is emitted as heat ("FRET-quenching") ³⁶⁷. During PCR, the probe hybridizes to the complementary target sequence and is cleaved by the 5'-3' exonuclease activity of the Taq polymerase in the extension phase (Figure 4-14, Step 3). This cleavage of the *TaqMan* probe separates the reporter from the quencher, preventing FRET from FAM to the NFQ, with resultant increased

reporter dye fluorescence (6-FAM; Ex_{max} : 518 nm), which can be detected by the qPCR-system by excitation with 488 nm. Due to the lack of a free 3'-hydroxyl group, the probe is not extended while the PCR process continues with completion of strand polymerization (Figure 4-14, Step 4). With each cycle, the Taq polymerase cleaves an additional reporter dye fluorophore. Hence, the detectable fluorescence signal is directly proportional to the amount of amplified target-specific cDNA during the reaction (and thus, original mRNA).

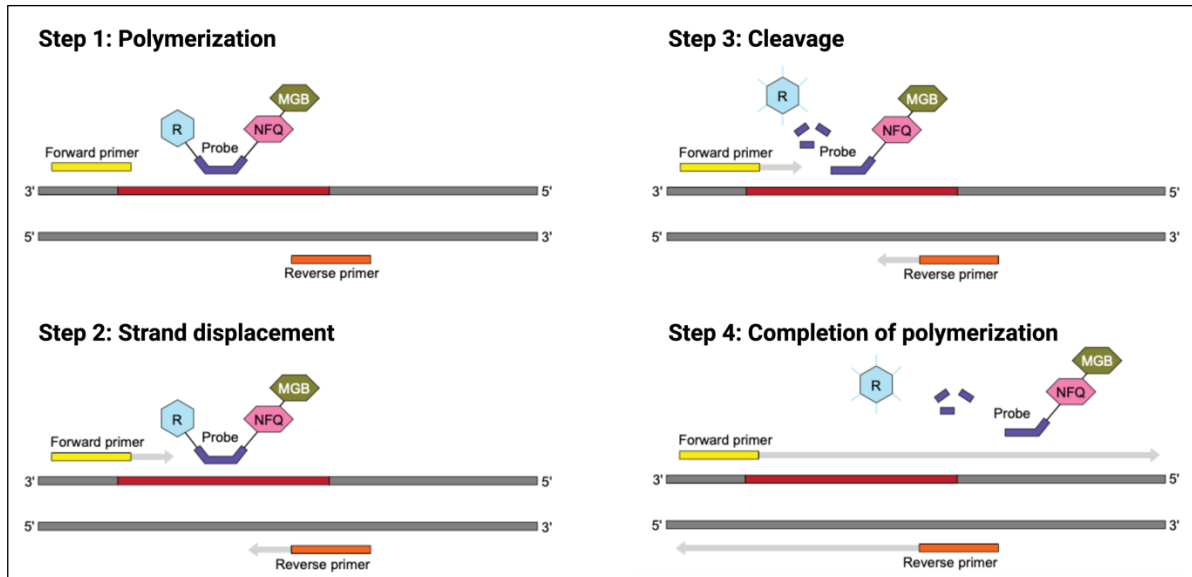


Figure 4-14: Principle of the *TaqMan* MGB probe-based assay chemistry. **Step 1:** The *TaqMan* probe anneals target-specifically to a sequence between the forward and reverse primer during the PCR process. (Unlike the diagram, the probe binds to single stranded DNA.) **Step 2:** In an intact probe, fluorescence from the reporter dye (R) is quenched due to Förster resonance energy transfer (FRET) to the non-fluorescent quencher (NFQ). A minor groove binder (MGB) attached to the 3'-end additionally stabilizes the binding of the probe to the template via van der Waals forces. **Step 3:** When reaching the annealed probe, the Taq polymerase causes strand displacement of the *TaqMan* probe and its 5'-3' exonuclease activity cleaves the probe, separating reporter and quencher. When excited with 488 nm, the reporter now fluoresces. With every extension cycle, the fluorescence increases. **Step 4:** Cleavage of the probe removes it from the template strand, enabling completion of strand polymerization. Modified from ³⁶⁶.

125 ng of total RNA was used for qRT-PCR analysis with the QuantiTect® Probe RT-PCR kit. TaqMan® gene expression assays were purchased as probe-and-primer sets (see 3.9.1). The *TaqMan* PCR-reaction mix and -profile are shown in Table 4-5 and measured in a StepOnePlus™ real-time PCR cyclor.

Table 4-5: Reaction mix and profile for the *TaqMan* qRT-PCR.

PCR reaction mix (20 μ l)		PCR program		
2x QuantiTect™ Probe RT-PCR Master Mix	10.0 μ l	50°C	30 min	Reverse transcription
RNase-free water	6.8 μ l	95°C	15 min	Initial activation
Primer/probe set	1.0 μ l	94°C	15 sec	40 x (Denaturing + annealing/elongation)
Template RNA	2.0 μ l	60°C	1 min	
QuantiTect™ Probe RT enzyme	0.2 μ l			

Quantification of mRNA gene expression levels was done using the $2^{-\Delta\Delta C_t}$ method which calculates the expression rate based on the C_t value (cycle threshold value of the exponential growth curve of the fluorescent signal) normalized to a constitutively expressed mRNA (housekeeping gene) of the same sample³⁷⁰. Within this study, the TATA-box binding protein (TBP) was used for normalization. Gene expression levels were expressed as percentage of control.

4.4 Protein biochemical methods

4.4.1 Total protein extraction from murine tissue

Protein from murine tissue/organs was extracted from samples that had been previously frozen in liquid nitrogen and stored at -80°C (see 4.2.1). Frozen tissue was pulverized in a liquid nitrogen pre-cooled ceramic mortar with a pestle. The powder was carefully transferred into Eppendorf tubes that were kept on liquid nitrogen, an equal volume of homogenization buffer (see 3.6) was added and the suspensions mixed vigorously by vortexing. Following a 1 h incubation of the homogenates on ice to enable complete membrane disruption, the tissue lysates were centrifuged for 10 min at 10,000 g at 4°C. The supernatants containing the whole protein extract were removed from the insoluble cell pellets, transferred to a fresh Eppendorf tube, and stored at -20°C. The protein content was quantified via Bradford assay (see 4.4.2) for further analyses.

4.4.2 Protein quantitation by Bradford assay

Protein concentrations were determined by a colorimetric assay that involves binding of the dye 'Coomassie Brilliant Blue G-250' (triphenylmethane derivative) to protein. When the dye is added to the protein, protein-dye complexes are formed causing an absorbance shift of the dye from 465 nm to 595 nm. The absorbance change is proportional to the amount of total

protein present in the sample. The principle was first described by Bradford in 1976, hence this method is also referred to as the *Bradford assay*³⁷¹. A standard curve consisting of protein samples of known concentrations (dilutions of bovine serum albumin of 0, 1, 5, 10, 20, and 30 µg/ml in ddH₂O) was used to compare and calculate the protein amount of the tissue lysates. The samples were diluted in ddH₂O (1:200 for aorta, 1:600 for heart) and 80 µl of each sample and respective standard pipetted onto a 96-well plate in quadruplicates. 200 µl of Roti[®]Quant reagent (containing Coomassie Brilliant Blue G-250) were added to each well, mixed and absorption readings immediately taken at 595 nm by a plate reader.

4.4.3 SDS polyacrylamide gel electrophoresis

One-dimensional SDS-polyacrylamide gel electrophoresis (SDS-PAGE) was applied for the separation and subsequent identification of proteins via Western blot (see 4.4.4). The technique was first described by Laemmli in 1970 and allows the separation of proteins according to their molecular weight³⁷². Previous to the separation within the gel, proteins are denatured with the detergent SDS (sodium dodecyl sulfate). Dodecyl sulfate is negatively charged and binds effectively to proteins due to its hydrophobic tail, thus masking the protein's intrinsic charge. Since SDS binds in proportion to the molecular weight of a protein, the SDS-proteins-complexes show a uniform charge-to-mass ratio (Figure 4-15 A). Consequently, when subjected to an electric field, the mobility of a protein is only proportional to its molecular weight and independent of its charge. The polyacrylamide matrix functions as a molecular sieve and separates the proteins according to their size (Figure 4-15 B)^{373,374}.

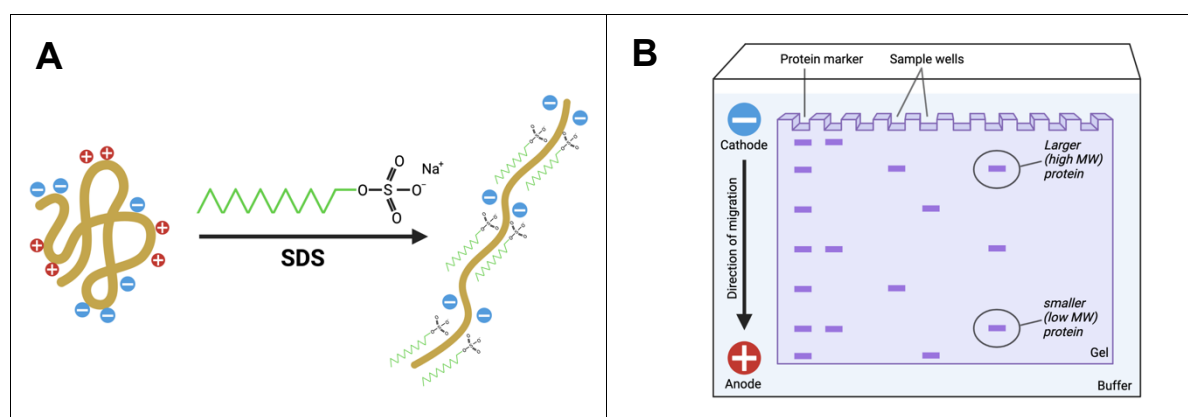


Figure 4-15: One-dimensional SDS-polyacrylamide gel electrophoresis (SDS-PAGE). (A) The negatively charged detergent sodium dodecyl sulfate (SDS) binds to proteins proportionally to their molecular weight (MW), thus providing them with a similar charge-to-mass ratio. (B) The latter enables protein separation only dependent on their size in a polyacrylamide gel when an electric field is applied. Created with [BioRender.com](https://www.biorender.com).

The SDS-PAGE was done using vertical gel electrophoresis chambers (*Mini-Protean 3 Cell*), which were loaded with the resolving gel. Depending on the molecular weight of the to-separating proteins, 7.5–10 % resolving gels were used. The higher the acrylamide

concentration in a gel, the smaller the pore size of the gel, which enables the resolution of lower molecular weight proteins. After complete polymerization of the resolving gel, the stacking gel (4 %) was poured on top of it and a comb inserted. The protein samples were adjusted to a uniform concentration (15–30 μg), mixed with Laemmli buffer (see 3.6) and denatured for 5 min at 95°C. If the gel electrophoresis was conducted under reducing conditions, the Laemmli buffer contained β -mercaptoethanol which reduces disulfide bonds within amino acid residues to free thiol groups. β -Mercaptoethanol was not added to the Laemmli buffer for an SDS-PAGE under non-reducing conditions (i.e., for the analysis of the S-glutathionylation state of eNOS). After cooling down to room temperature, the samples and protein markers were loaded into the pockets of the polyacrylamide gel and electrophoresis was conducted in SDS-PAGE running buffer (see 3.6) at 120 V (7.5 % gels) or 140 V (10 % gels) until an efficient separation of the desired proteins was reached. The protein markers herein served as calibrated molecular weight references.

Table 4-6: Recipes for stacking and resolving gels used in the SDS-PAGE.

	<u>7.5 % resolving gel</u>	<u>10 % resolving gel</u>	<u>4 % stacking gel</u>
ddH ₂ O	5.4 ml	4.8 ml	3.2 ml
40 % Acrylamide/bis (29:1)	1.88 ml	2.5 ml	0.5 ml
1.5 M Tris-HCl, pH 8.8	2.5 ml	2.5 ml	-
0.5 M Tris-HCl, pH 6.8	-	-	1.2 ml
10 % SDS	100 μl	100 μl	50 μl
10 % APS	100 μl	100 μl	50 μl
TEMED	10 μl	10 μl	5 μl

4.4.4 Immunological detection of proteins by Western blot

During Western blotting, proteins are moved by an electrophoretic transfer from the polyacrylamide gel onto a nitrocellulose membrane. While the proteins move onto the membrane, their spatial organization from the gel is preserved, enabling their individual immunological detection by specific antibodies³⁷⁵. Using a wet/tank blotting apparatus (*Mini Trans-Blot Electrophoretic Transfer Cell*) with an electric field transverse to the polyacrylamide gel, the via SDS-PAGE (see 4.4.3) separated proteins were transferred onto a nitrocellulose membrane (0.45 mm) in ice-cold transfer buffer (see 3.6). For this purpose, the gel holder cassette was assembled by placing the gel carefully on top of the nitrocellulose membrane and restraining the gel-membrane sandwich with in transfer buffer

pre-wetted foam pads and filter paper sheets on each side. The cassette was put into the blotting tank between the electrodes, minding the correct transfer direction from the cathode to the anode that allows the migration of the negatively charged proteins from the gel onto the membrane. The tank was filled with ice-cold transfer buffer, a stirring bar added and put in an ice box on top of a magnetic stir plate. An additional cooling unit was added to the blotting tank to prevent overheating during the transfer. The proteins were transferred for 150 min at 250 mA.

After blotting, protein loading and transfer efficiency were controlled by Ponceau S staining. Ponceau S is an anionic dye that binds to positively charged amino acid residues of proteins and is used for total protein staining. Since the staining can be reversed by washing the membrane with washing buffer (PBS-T or TBS-T, see 3.6), it does not interfere with subsequent immunological detection³⁷⁶. Washed membranes after Ponceau staining were blocked in an appropriate blocking solution (see 3.8.1) for 60 min at room temperature to saturate the membrane and prevent unspecific antibody binding. Afterwards, the membranes were incubated overnight at 4°C with primary antibody dilutions (in blocking solution, see 3.8.1) with gentle agitation. The next day, antigen-antibody complexes were detected using HRP-conjugated secondary antibodies. Membranes were washed three times at 5 min each with the corresponding washing buffers (PBS-T or TBS-T) and incubated with diluted secondary antibodies (in the same blocking buffer as the primary antibody, see 3.8.3) for 2 h at room temperature. Membranes were again washed three times before visualizing the HRP-conjugated protein complexes by adding a 1:1 mixture of luminol/hydrogen peroxide for 1 min (*Pierce™ ECL Western Blotting Substrat or SuperSignal™ West Femto Substrat*). HRP catalyzes the oxidation of luminol by hydrogen peroxide, which results in the formation of 3-aminophthalate in an excited state that releases light when transitioning into a lower energy state (chemiluminescence). The emitted light signal was captured with a digital imaging system (ChemiLux Imager) and densitometric quantification of the protein bands was performed using the Gel-Pro Analyzer software. The expression of each detected protein was normalized to at least one simultaneously analyzed housekeeping gene (β -actin).

4.4.5 Immunological detection of proteins by Dot blot

The total protein content of tissue samples was analyzed by Dot blotting. This technique allows the bulk transfer and detection of proteins in solution onto a membrane, without previously separating them by gel electrophoresis. Protein homogenates (see 4.4.1) were diluted with PBS to a final concentration that allowed loading of 50 μ g/well. The samples were loaded onto a PBS pre-wetted nitrocellulose membrane by vacuum-assisted filtration using a *Minifold I* vacuum dot-blot system device with a 96-well top frame. Each well was

washed twice with 200 μ l PBS after sample loading. The vacuum was removed, the membrane taken out of the *Minifold I* systems and dried for 1 h at 60°C to ensure complete protein immobilization on the surface. Ponceau S staining was performed to control and document the loaded protein amount/well. To immunologically detect the protein of interest, blocking and washing steps as well as incubation with primary and HRP-coupled secondary antibody was performed as described in the Western blot section (see 4.4.4). All used antibodies with appropriate dilutions and correspondent buffers are listed in 3.8.1 and 3.8.3. Visualization of the dots was achieved by enhanced chemiluminescence (ECL) after incubating the membrane for 1 min with HRP-substrate (*PierceTM ECL Western Blotting Substrat or SuperSignalTM West Femto Substrat*). Antibody-specific chemiluminescent dots were captured with a ChemiLux Imager and quantified using Gel-Pro Analyzer software. Protein-specific expression of each dot was normalized to its total protein count received in the Ponceau S staining.

4.4.6 Immunoprecipitation with magnetic beads

S-glutathionylation of the endothelial nitric oxide synthase (eNOS) serves as a readout for the coupling state of the enzyme (see 1.4.2)¹⁸⁷. For this purpose, eNOS protein from aortic tissue was first enriched by immunoprecipitation using magnetic beads and the precipitate subsequently immunoblotted for S-glutathionylation in Western blot analysis. Before the actual precipitating step, the magnetic beads (*Dynabeads M-280 Sheep anti-Mouse IgG*) were coated with monoclonal mouse eNOS antibody and covalently crosslinked to it. For this, the beads were vortexed and an appropriate volume of magnetic beads (15 μ l beads per 150 μ g protein sample at $c = 1 \mu\text{g}/\mu\text{l}$) transferred to a low-protein-binding 1.5 ml reaction tube. The supernatant was removed using a magnet and the beads washed three times with TBS/0.1 % BSA. Afterwards, the eNOS antibody was added (6 μ l/150 μ l beads) and the suspension incubated overnight at 4°C with gentle rotation to complete antibody-coating of the beads. The next day, the supernatant was removed by magnetic separation and the beads washed twice with 0.2 M TEA (triethanolamine, pH 8.2) to remove excess antibody. The beads were resuspended in 1 ml 20 mM DMP (dimethyl pimelimidate, diluted in TEA) and rotated for 30 min at room temperature to covalently crosslink the antibody to the magnetic beads. After removal of the supernatant, the beads were resuspended in 1 ml 50 mM Tris base (pH 7.5) and rotated for additional 15 min at room temperature. The supernatant was removed, followed by three washing steps with TBS/0.1 % BSA. Finally, the antibody-crosslinked beads (15 μ l) were added to the protein homogenates (150 μ g protein sample at $c = 1 \mu\text{g}/\mu\text{l}$) and the suspension incubated under rotation at 4°C overnight for eNOS precipitation. The next morning, the supernatant was removed by magnetic separation and the beads washed three times with TBS/0.2 % Triton-X and one time with pure TBS,

each wash for 5 min under rotation to remove unbound protein. The beads were resuspended in 1x Laemmli buffer (without β -mercaptoethanol) and incubated for 5 min at 95°C to denature the bead-target complex. The supernatant containing the precipitate was removed by magnetic separation, transferred into a fresh 1.5 ml Eppendorf tube, and stored at -20°C until eNOS glutathionylation was characterized by SDS-PAGE and subsequent Western blotting (see 4.4.3 and 4.4.4). The residual beads were discarded.

4.4.7 ELISA (enzyme-linked immunosorbent assay)

ELISA is an immunological method that was first described in 1971 and enables the antibody-based detection and quantification of a specific protein within a complex mixture³⁷⁷. Several ELISA systems exist. A very common format is the "sandwich ELISA", in which two primary antibodies are used to detect the antigen of interest by building an antibody-antigen-antibody complex. A first capturing antibody, pre-coated on a microtiter plate, immobilizes the target antigen, which is then bound by a second enzyme-labeled antibody in a subsequent step. Both the capturing and the enzyme-conjugated antibody are specific for the target antigen but detect a different epitope of the antigen. When a substrate solution is added to the plate, the enzyme catalyzes the conversion of the chromogenic substrate into a colored product that can be measured by a plate reader. By simultaneously running antigens of a known concentration, a standard curve can be created that allows the calculation of antigen concentration in an unknown sample.

For the quantification of insulin in plasma, a commercial ELISA kit (*Ultra Sensitive Mouse Insulin ELISA Kit*), based on a sandwich immunoassay, was used and the protocol followed according to the manufacturer's instructions applying the wide range (0.1–12.8 ng/ml) screening method. ELISA data was created with the technical assistance of Nicole Glas (Laboratory of Molecular Cardiology, University Medical Center Mainz).

4.4.8 Coating of *Dynabeads Sheep Anti-Rat IgG* with anti-mouse CD102 antibody from rat

Dynabeads Sheep anti-Rat IgG were vortexed and 40 μ l beads/treatment group transferred to a low-protein-binding 1.5 ml reaction tube. The supernatant was removed using magnetic separation. Next, the tube was removed from the magnet and the beads washed with 1 ml MACS buffer (see 3.6) by carefully pipetting up and down. The supernatant was discarded using the magnet and the beads resuspended in 150 μ l MACS buffer. 40 μ l of anti-mouse CD102 (see 3.8.1) was added and the beads incubated with the antibody overnight at 4°C under rotation. The next day, anti-CD102 coupled beads were washed at least three times

with MACS buffer and finally resuspended in 50 μ l MACS buffer for end use (see 4.2.3). The beads were coated fresh for every MLEC isolation.

4.5 Statistics

Results are expressed as means \pm standard error of the mean (SEM). Statistical calculations were performed with GraphPad Prism 8 (version 8.4.3). Shapiro-Wilk test was used to test for normality and equal variance of the data sets. If the data followed a normal distribution, unpaired Student t-test was applied to compare two groups and 1-way ANOVA (with Bonferroni post hoc test) to compare multiple groups. In case of failed normality, equivalent non-parametric tests (Mann-Whitney test (2 groups) or Kruskal-Wallis with Dunn's multiple comparisons (multiple groups)) were used. 2-way ANOVA (with Bonferroni correction for comparison of multiple means) was applied for data points received from relaxation studies in isometric tension recording experiments, the oral glucose tolerance test, and DHE staining in the presence of L-NAME (two factor analysis). $P < 0.05$ was considered statistically significant and marked as follows: * $P < 0.05$; ** $P < 0.01$; *** $P < 0.001$; **** $P < 0.0001$.

5 Results

The obtained results are – whenever possible and reasonable – displayed as scatter bar plots, which show individual readings of analyzed animals or tissue samples, as well as the corresponding mean (\bar{x}) and SEM. Furthermore, written explanations of the results are given following the recommendations of David S Small who suggests expressing changes in the magnitude of numbers as percentages or ratios and not as 'fold increase' or 'fold decrease' due to the ambiguity of the latter ³⁷⁸. Parts of this thesis have previously been published in Helmstädter et al., *Arterioscler Thromb Vasc Biol.* 2020 Jan;40(1):145-158 (doi: 10.1161/atv.0000615456.97862.30).

5.1 Liraglutide exerts cardio- and vasoprotective properties in experimental arterial hypertension without altering glucose and insulin metabolism

GLP-1RAs like liraglutide reduce the risk for cardiovascular death in diabetic patients (see 1.6.2) and possess potent anti-atherogenic actions as proven in numerous pre-clinical studies (see 1.6.3). Since high blood pressure is one of the main risk factors for atherosclerosis, a regulatory role of liraglutide in arterial hypertension seems likely and was therefore assessed in a murine model of chronic angiotensin (ATII) infusion. To investigate cardiovascular protection, it was analyzed how liraglutide modifies hypertensive heart disease (see 5.1.1) and vascular function in relaxation studies (see 5.1.2). As systemic GLP-1R activation is associated with glucose-lowering effects that could contribute to cardioprotection of GLP-1RAs, it was further analyzed how liraglutide affects glucose and insulin metabolism in non-diabetic hypertensive mice (see 5.1.3).

5.1.1 Liraglutide improves ATII-induced arterial hypertension and hypertensive heart disease

Blood pressure was measured non-invasively via tail-cuff plethysmography (see 4.1.4) in control and ATII-infused mice with additional vehicle- or liraglutide treatment (see 4.1.3).

Liraglutide treatment (+Lira) significantly reduced elevated systolic blood pressure (SBP) levels caused by ATII infusion (Figure 5-1 A). Control mice (B6) had a mean SBP of 103 mmHg, which was significantly increased by 20 mm Hg with ATII (\bar{x} 123 mmHg). Upon liraglutide treatment, SBP levels were normalized to nearly control levels with a mean SBP of 104 mmHg.

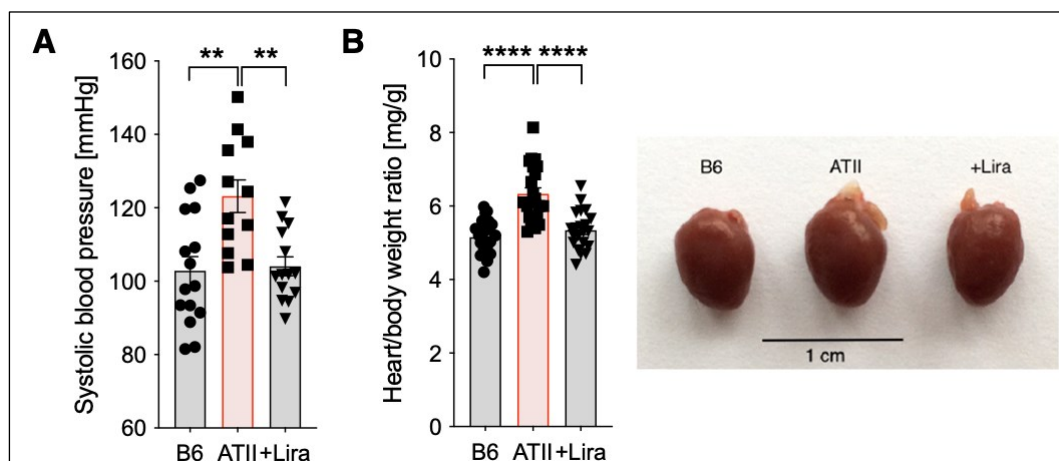


Figure 5-1: Liraglutide (Lira) normalizes elevated blood pressure levels and cardiac hypertrophy caused by angiotensin II (ATII) in wild-type (C57BL/6J) mice. (A) Systolic blood pressure was measured non-invasively by the tail-cuff method 6 days after the start of ATII infusion (n=12-15). ** P<0.01; 1-way ANOVA with Bonferroni's multiple comparison test. **(B)** Mice and isolated hearts (post-transection) were weighed on day 7 of treatment and the heart/body weight ratio was determined as an indicator of cardiac hypertrophy (n=21-22). A representative picture of isolated mouse hearts is shown next to the quantification bar graph (scale bar 1 cm). **** P<0.0001; 1-way ANOVA with Bonferroni's multiple comparison test. Data are means \pm SEM.

A common complication of chronic arterial hypertension is left ventricular hypertrophy (LVH), an enlargement and thickening of the left ventricle that develops as a result of the increased effort of the heart to pump blood against the higher pressure in the vessels³⁷⁹. Cardiac hypertrophy can eventually lead to heart failure or ischemic heart disease. LVH causes an increase in cardiac mass and is, hence, indicated by elevated heart/body ratios (see 4.2.5). ATII infusion caused a marked increase in volume and weight of hearts compared to control, with a mean heart/body weight ratio of 6.3 mg/g. Liraglutide protected from cardiac hypertrophy as the heart/body weight ratio averaged to 5.3 mg/g, which was similar to the one of controls with 5.2 mg/g (Figure 5-1 B).

5.1.2 Liraglutide ameliorates ATII-induced endothelial dysfunction and vascular fibrosis

Endothelial dysfunction represents the first indicator for vascular damage and possesses prognostic value for the development of atherosclerosis and future adverse cardiovascular events (see 1.3.3). To investigate how liraglutide modulates vascular tone in arterial hypertension, isometric tension recordings of isolated aortic rings were conducted, in which their relaxation potential in response to ACh (endothelium-dependent vasodilation) and NTG (endothelium-independent vasodilation) was studied (see 4.2.6).

Plotting the percentage of relaxation against cumulative doses of acetylcholine revealed a significant right-shift of the curve for ATII-infused aortic rings relative to controls, denotive of a strongly deteriorated endothelial function (Figure 5-2 A). The mean maximal relaxation potential (ACh dose of $10^{-5.5}$ M) of control rings amounted to 76 % whereas it was only 53 %

in aortic rings from hypertensive mice, representing an impairment by approximately one third compared to controls. This extent of endothelial dysfunction is in line with other reports of ATII application in C57BL/6J mice, considering the dose and interval used (0.5 mg/kg for 7 d)³⁸⁰. Liraglutide markedly improved the vasorelaxation potential of aortic rings upon ATII infusion, as no significant right-shift of the relaxation curve in response to ACh occurred. Furthermore, the mean maximal relaxation potential was with 72 % almost at control levels (Figure 5-2 A). This indicates that liraglutide potently rescues an ATII-induced endothelial dysfunction. Notably, liraglutide did not affect the endothelial-dependent vasorelaxation potential in healthy animals (Figure 5-2 B). ATII infusion also worsened endothelium-independent (NTG-response) vasodilation relative to controls, which was not positively impacted by liraglutide treatment (Figure 5-2 C). Hence, further vascular tonus studies focused on the modulation of endothelium-dependent relaxation by liraglutide (see 5.4–5.6).

During vascular fibrosis, extracellular matrix components, particularly collagen, are excessively deposited in the vessel wall causing a decreased lumen diameter and arterial wall thickening³⁸¹. These fibrotic changes accelerate stiffening of the arteries, which exacerbates the progression of CVD³⁸². Compared to controls, ATII infusion caused collagen accumulation in aortic rings as revealed by sirius red staining (Figure 5-2 D), in line with its established role in deleterious vascular remodeling as the main bioactive peptide of the renin-angiotensin system (see 1.2.1)^{32,383}. In contrast, the collagen accumulation in the tunica adventitia of aortas of liraglutide-treated mice was visibly blunted, thus demonstrating reduced vascular fibrosis (Figure 5-2 D). Concomitantly, aortic expression of *Glp1r* mRNA was not affected by ATII but was significantly elevated in response to additional liraglutide treatment (Figure 5-2 E).

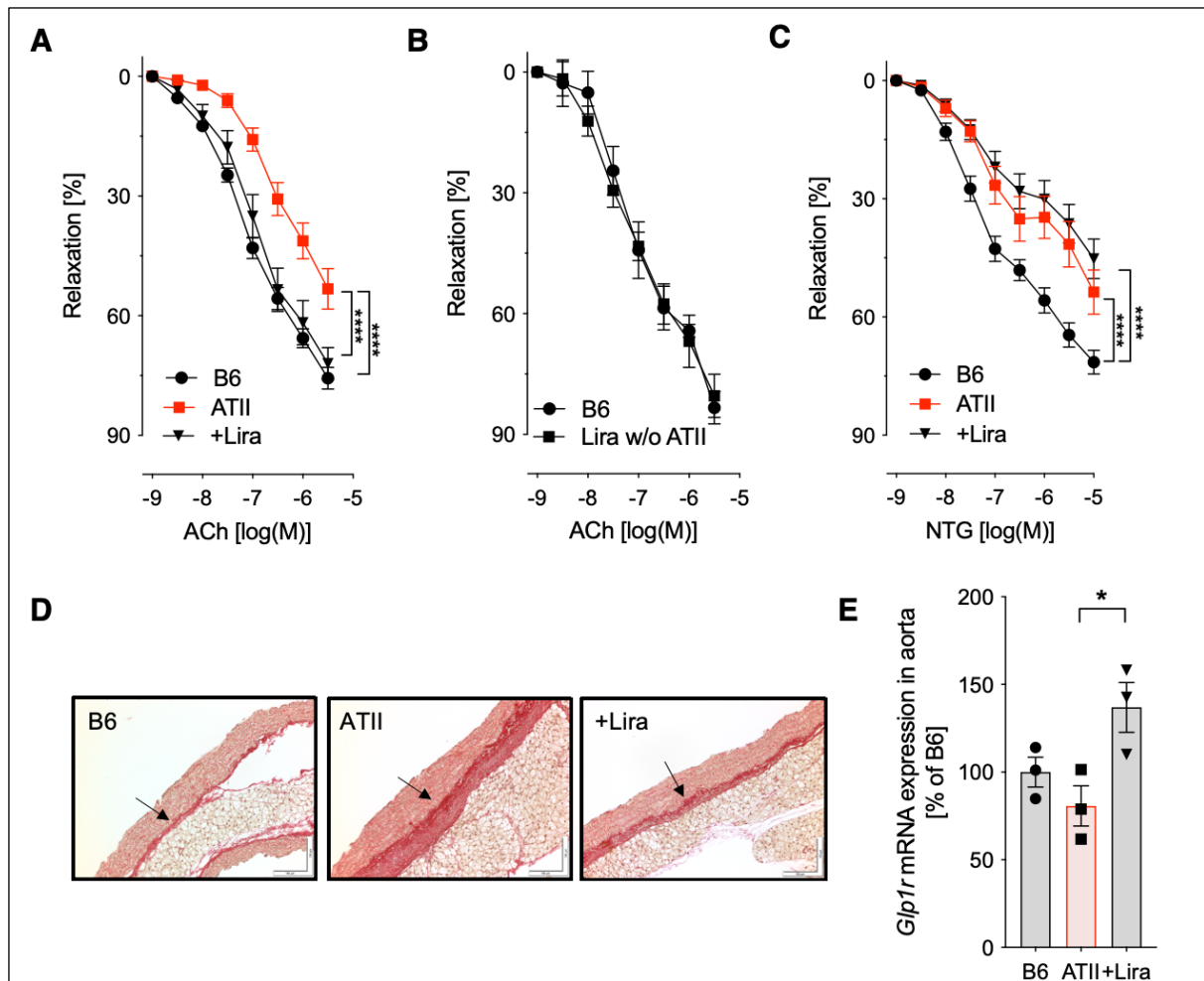


Figure 5-2: Liraglutide (Lira) improves angiotensin II (ATII)-induced endothelial dysfunction and vascular fibrosis in wild-type (C57BL/6J) mice. Freshly isolated aorta was cut into rings and pre-constricted using KCl to induce maximal tone and prostaglandin F₂ α for 80 % submaximal tone induction. **(A)** Accumulative doses of acetylcholine (ACh) were administered to induce endothelium-dependent vasodilatation of the aortic rings, which was recorded in an organ bath chamber system (n=16-28). **** P<0.0001; 2-way ANOVA with Bonferroni's multiple comparison test. **(B)** Endothelium-dependent relaxation was evaluated in non-hypertensive C57BL/6J mice treated with liraglutide (Lira) only [w/o=without ATII] (n=4-6). Not significant; 2-way ANOVA with Bonferroni's multiple comparison test. **(C)** Accumulative doses of nitroglycerine (NTG) were administered to induce endothelium-independent vasodilatation of the aortic rings (n=15-17). **** P<0.0001; 2-way ANOVA with Bonferroni's multiple comparison test. **(D)** Paraffin-embedded aortic rings were stained with picro-sirius red to detect collagen fiber accumulation as a manifestation of vascular fibrosis (n=3-4). The figure shows one representative staining. Magnification 20x (scale bar 100 μ m). **(E)** Gene expression level of *Glp1r* (Glucagon-like peptide-1 receptor) was measured in aortic tissue by qRT-PCR (n=3). * P<0.05; 1-way ANOVA with Bonferroni's multiple comparison test. Data are means \pm SEM.

5.1.3 Liraglutide does not affect glucose and insulin metabolism in murine arterial hypertension

GLP-1 plays an important role in the control of metabolism (see 1.6.1). Thus, changes in body weight, non-fasting blood glucose, and non-fasting plasma insulin arising from 7 d ATII-infusion and concomitant liraglutide treatment were analyzed. To elucidate the differences in blood glucose homeostasis between the experimental groups in more detail, an oral glucose tolerance test (OGTT) was performed. The OGTT enables the identification of alterations in glucose tolerance and insulin sensitivity³²¹. After 6 h of starvation, mice were administered a

defined amount of glucose by gavage and blood glucose monitored over time up to 120 minutes (see 4.1.5). In parallel, insulin levels in plasma were measured at time points 0 and 120 min of the OGTT.

Control mice gained on average +0.8 g in body weight over the course of 7 d. Liraglutide treatment led to a significant reduction in body weight with a mean loss of ca. -0.9 g (Figure 5-3 A). ATII infusion alone showed no significant effect on body weight and was only reduced by trend compared to controls (\emptyset -0.3 g). Yet, neither non-fasting blood glucose nor non-fasting plasma insulin was altered by ATII or liraglutide (Figure 5-3 B-C). Likewise, the OGTT revealed no significant effect on glucose homeostasis by either ATII infusion or liraglutide treatment (Figure 5-3 D-E). Basal blood glucose in fasting mice amounted to (on average) 7.3 mM in controls (B6), 6.7 mM in ATII-infused mice, and 7.8 mM in liraglutide-treated mice, which was non-significantly increased between the groups 15 min after glucose stimulus (\emptyset 16.9 mM, \emptyset 18.4 mM, and \emptyset 19.7 mM for B6, ATII, and liraglutide, respectively). 2 h after gavage, the administered glucose was almost cleared from the blood and was again not altered between groups accounting for (on average) 9.3 mM for B6, 7.9 mM for ATII, and 10.5 mM with liraglutide treatment (Figure 5-3 D). Similarly, basal plasma insulin (t=0 min) and plasma insulin levels 2 h after OGTT (t=120 min) non-significantly differed between the experimental groups, however, were by trend even lower in the liraglutide-treated mice (t=0 min: B6: \emptyset 0.73 ng/ml, ATII: \emptyset 0.68 ng/ml, +Lira: \emptyset 0.48 ng/ml and t=120 min: B6: \emptyset 0.70 ng/ml, ATII: \emptyset 0.58 ng/ml, +Lira: \emptyset 0.37 ng/ml, Figure 5-3 E). Thus, liraglutide did not affect glucose metabolism in this non-diabetic hypertension model.

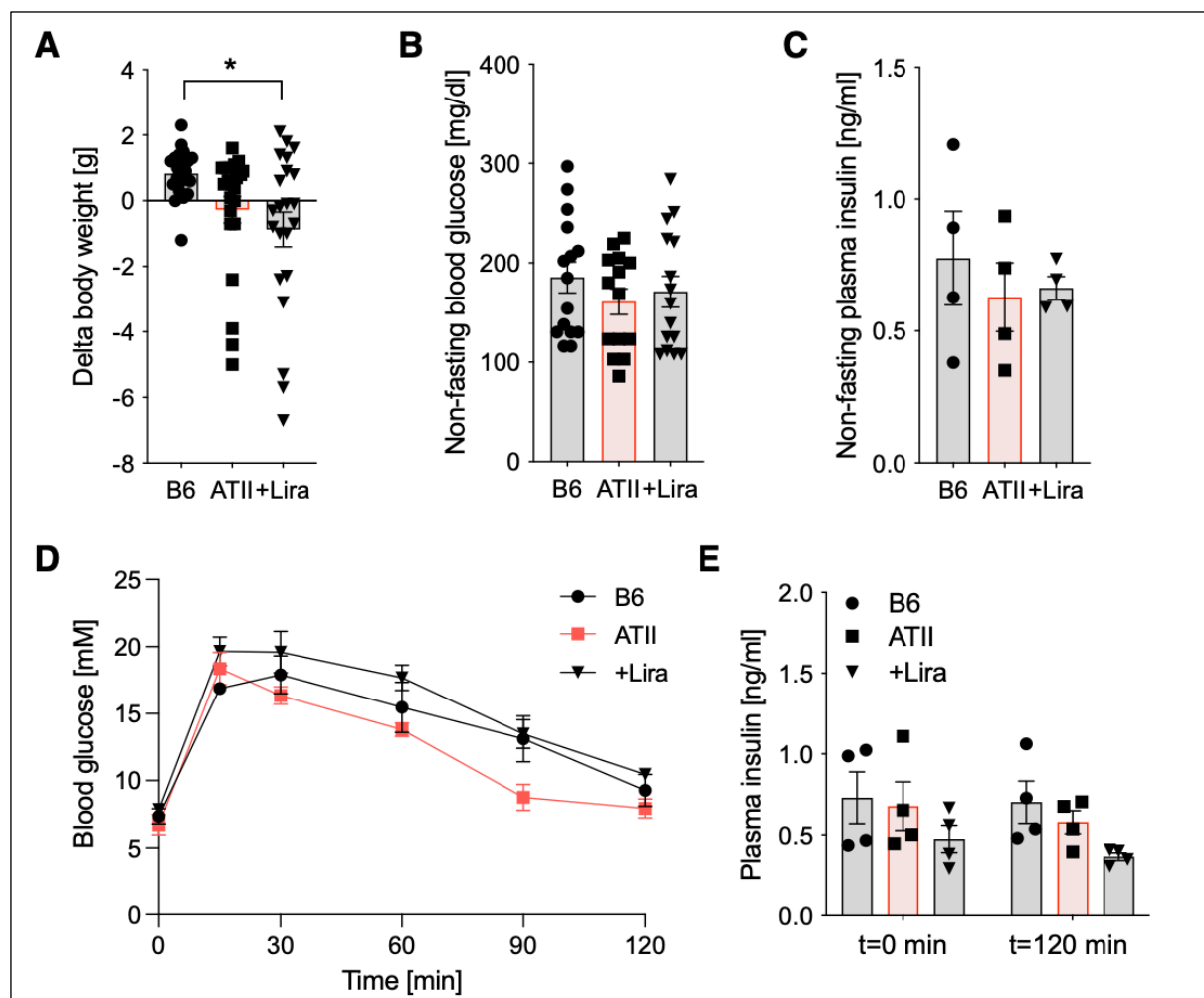


Figure 5-3: Liraglutide (Lira) does not alter glucose and insulin metabolism of wild-type (C57BL/6J) mice with arterial hypertension. (A) Mice were weighed before (day 0) and on day 7 of treatment and the delta body weight was calculated (n=21-22). * P<0.05; 1-way ANOVA with Bonferroni's multiple comparison test. (B) Blood glucose levels were measured from whole blood of non-fasted mice using a glucometer after 7 d of treatment (n=15). Not significant; 1-way ANOVA with Bonferroni's multiple comparison test. (C) Insulin levels were measured from plasma of non-fasted mice by ELISA after 7 d of treatment (n=4). Not significant; 1-way ANOVA with Bonferroni's multiple comparison test. (D) Blood glucose progression of mice challenged with 1.5 g/kg glucose administered by gavage after 6 h of starvation (oral glucose tolerance test, OGTT) after 7 d of treatment. At the indicated time points, blood glucose was measured from tail vein blood samples using a glucometer (n=4). Not significant; 2-way ANOVA with Bonferroni's multiple comparison test. (E) Basal (t=0 min) and final (t=120 min) plasma insulin levels during the OGTT were measured by ELISA (n=4). Not significant; 1-way ANOVA with Bonferroni's multiple comparison test (for each time point). Data are means \pm SEM.

5.2 Liraglutide diminishes oxidative stress and inflammation in murine arterial hypertension

Vascular inflammation and oxidative stress are major drivers for CVD including arterial hypertension and constitute the main determinants of endothelial dysfunction (see 1.3.3–1.5.2). Hence, it was analyzed how liraglutide modulates the amount of ROS in whole blood and the heart (see 5.2.1) as well as in the vasculature (see 5.2.2) of hypertensive mice. Primary sources of endogenous ROS in the vasculature are NADPH oxidases (Nox), with Nox2 being the predominant isoform in phagocytes (neutrophils, monocytes, and

macrophages)¹⁴⁵ (see 1.4.1). As previous findings identified the importance of functional Nox2 activity in monocytes for mediating the inflammatory and oxidative signaling cascade in ATII-induced arterial hypertension (see 1.5.1)²⁰⁹, the influence of liraglutide on the activity and expression of Nox2 in heart and aorta was measured, respectively. Simultaneously, the effect of liraglutide on immune cell infiltration in cardiac tissue (see 5.2.1) and aorta (see 5.2.2) was investigated as a possible source of oxidative stress.

5.2.1 Liraglutide reduces ATII-induced oxidative stress and inflammation of whole blood and the heart

Oxidative stress in whole blood and NADPH oxidase activity in heart membrane fractions were measured with L-012- and lucigenin-enhanced chemiluminescence (ECL), respectively (see 4.2.9 and 4.2.10). ROS formation in the left ventricle of the heart was determined using dihydroethidium (DHE)-dependent fluorescence oxidative microtopography in cardiac cryosections (see 4.2.7). Furthermore, the Dot blot technique (see 4.4.5) was employed to investigate 3-nitrotyrosin (3-NT), asymmetric dimethylarginine (ADMA) and F4/80 levels in heart tissue as biomarkers for nitro-oxidative stress (see 1.4.3), systemic manifestation of endothelial dysfunction³⁸⁴ and macrophage infiltration³⁸⁵, respectively.

Leukocyte-dependent oxidative burst was significantly elevated with ATII infusion as count/s more than doubled from (on average) 565 to 1257 count/s relative to controls. Liraglutide treatment strongly alleviated the global pro-oxidant burden caused by hypertension and was with (on average) 785 counts/s non-significantly changed compared to control (Figure 5-4 A). Likewise, ATII-induced arterial hypertension caused a significant increase in ROS in the left ventricle of the heart compared to control (arbitrarily set to Ø 100 %), whereas liraglutide mitigated oxidative stress in cardiac cryosections (Figure 5-4 B). A similar pattern was found for the NADPH oxidase activity in cardiac membranous fractions. The NADPH activity in the heart, and thus oxidative stress, was massively increased with ATII but abrogated with additional liraglutide treatment (Figure 5-4 C).

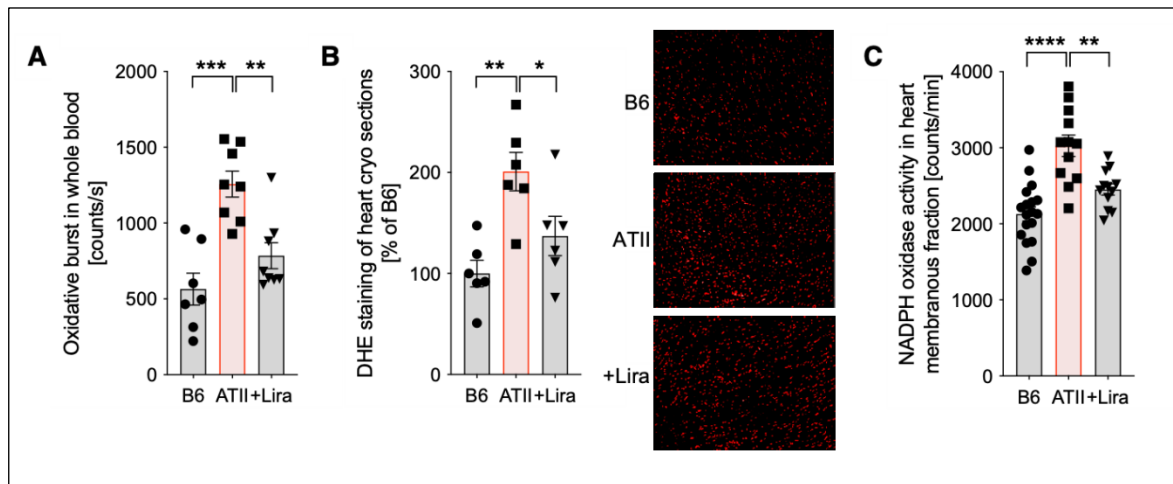


Figure 5-4: Liraglutide (Lira) lowers the angiotensin II (ATII)-induced oxidative burden of whole blood and heart in wild-type (C57BL/6J) mice. (A) Whole blood oxidative burst was measured by L-012-enhanced chemiluminescence in the presence of 50 $\mu\text{g/ml}$ zymosan A and the results expressed as counts per second after 45 min ($n=7-8$). ** $P<0.01$, *** $P<0.001$; 1-way ANOVA with Bonferroni's multiple comparison test. (B) Cardiac cryosections (8 μm) were incubated with dihydroethidium (DHE) and reactive oxygen species (ROS)-derived fluorescence measured by fluorescence microscopy ($n=6$). Representative photomicrographs are shown next to the densitometric analysis. (Red: fluorescence from ROS). * $P<0.05$, ** $P<0.01$; 1-way ANOVA with Bonferroni's multiple comparison test. (C) The activity of NADPH oxidase in isolated cardiac membrane fractions was measured by lucigenin-enhanced chemiluminescence in the presence of 200 μM NADPH and the results expressed as counts per minute after 5 min ($n=12-18$). ** $P<0.01$, **** $P<0.0001$; 1-way ANOVA with Bonferroni's multiple comparison test. Data are means \pm SEM.

Furthermore, ATII infusion more than tripled 3-NT-, ADMA-, and F4/80-positive proteins in the whole heart, indicative of enhanced production of peroxynitrite, dysregulation of eNOS, and infiltration of immune cells into the heart, respectively. Liraglutide treatment was able to significantly attenuate all of these detrimental factors (Figure 5-5 A-C).

Thus, three methodic independent approaches confirmed that liraglutide potently reduces cardiac oxidative stress in ATII-induced hypertensive heart disease, whereof NADPH oxidase is a major contributor. Additionally, reductions in cardiac ROS by liraglutide were accompanied by diminished cardiac macrophage infiltration and improved eNOS function.

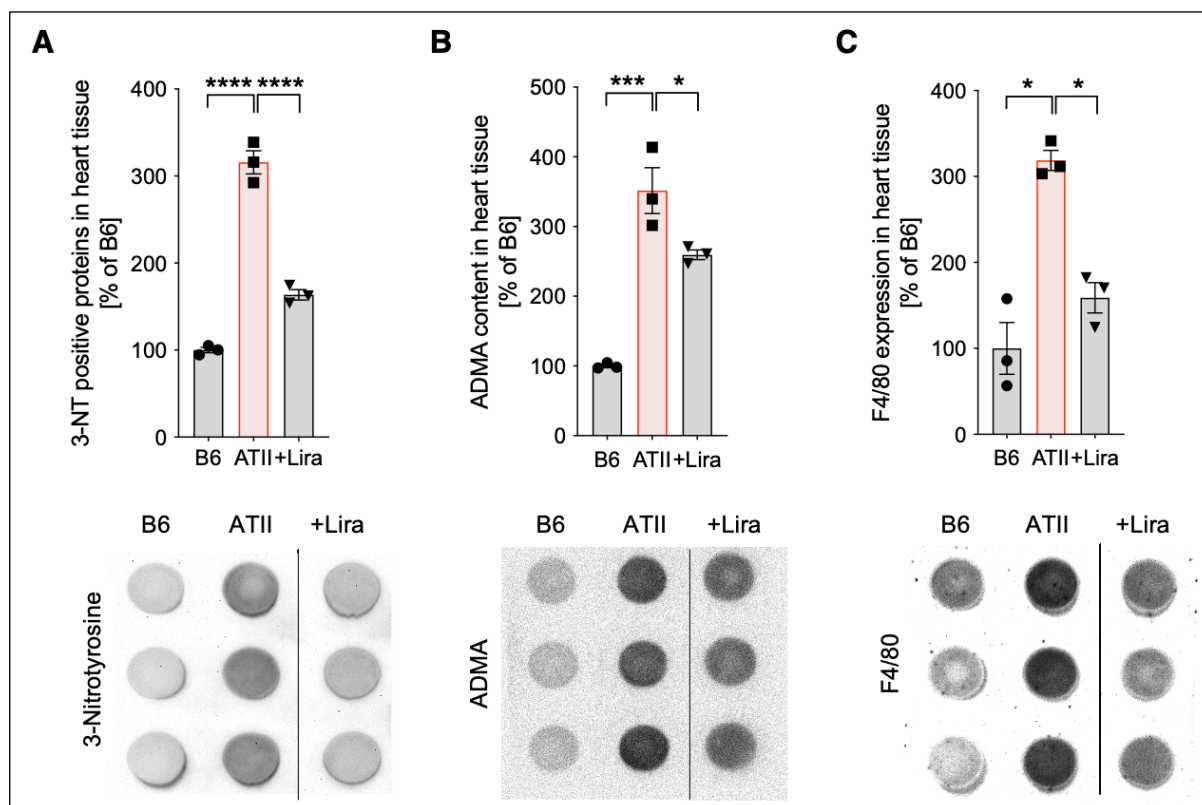


Figure 5-5: Liraglutide (Lira) reduces angiotensin II (ATII)-induced oxidative stress, dysregulation of eNOS, and immune cell infiltration in cardiac tissue of wild-type (C57BL/6J) mice. (A) Total 3-Nitrotyrosine (3-NT) positive proteins were measured in cardiac tissue by Dot blot (n=3). A representative blot is shown below the quantification bar graph. **** P<0.0001; 1-way ANOVA with Bonferroni's multiple comparison test. (B) Total ADMA (asymmetric dimethylarginine) levels were measured in cardiac tissue by Dot blot (n=3). A representative blot is shown below the quantification bar graph. * P<0.05, *** P<0.001; 1-way ANOVA with Bonferroni's multiple comparison test. (C) Total F4/80 (macrophage marker) levels were measured in cardiac tissue by Dot blot (n=3). A representative blot is shown below the quantification bar graph. * P<0.05; 1-way ANOVA with Bonferroni's multiple comparison test. Data are means \pm SEM.

5.2.2 Liraglutide attenuates ATII-induced oxidative stress and inflammation of the vasculature

Parallel to measuring ROS-derived fluorescence of DHE-stained aortic cryosections, the amount of aortic superoxide was quantified in an HPLC-based method. The latter allows separation of the DHE oxidation products 2-hydroxyethidium (2-HE, superoxide-specific) and ethidium (E^+ , non-specific) (see 4.2.7 and 4.2.8). Furthermore, aortic Nox2 expression was determined on mRNA level by qRT-PCR analysis (see 4.3.6) as well as on protein level via immunohistochemistry (see 4.2.13). Plasma nitrate (NO_3^-), as a marker for global peroxynitrite formation, was quantified via HPLC (see 4.2.12). In this regard, the expression of possible $\bullet NO$ sources within the aorta was analyzed, i.e., iNOS activity on mRNA level (*Nos2* gene) and eNOS protein levels. Lastly, immune cell infiltration into aorta as a source of oxidative stress was investigated by immunohistochemical and flow cytometric (see 4.2.14) methods.

DHE stainings in aortic cryosections revealed that liraglutide protected from a significantly enhanced oxidative stress burden caused by ATII infusion. The mean amount of aortic ROS was with 184 % in the ATII group nearly twice as high as in the control group (100 %), whereas liraglutide treatment normalized ROS levels with an average of 110 % (Figure 5-6 A). A similar result was obtained by quantitative HPLC analysis of the superoxide-specific DHE product, 2-hydroxyethidium (retention time: approx. 3 min). Higher levels of superoxide were detected in aortic tissue of ATII-infused mice relative to control (\bar{x} 56 $\mu\text{M}/\mu\text{g}$ for B6 vs. \bar{x} 456 $\mu\text{M}/\mu\text{g}$ for ATII) that were diminished with liraglutide (\bar{x} 86 $\mu\text{M}/\mu\text{g}$) (Figure 5-6 B, note: no statistical test was performed due to the limited n number of n=2). The *Nox2* gene expression pattern in aorta was in line with the detected superoxide levels between experimental groups. Hypertensive mice showed a more than 300 % increased aortic NADPH oxidase 2 levels compared to control (\bar{x} expression of 453 % for ATII vs. \bar{x} 100 % for B6), which was notably mitigated with liraglutide (\bar{x} expression of 233 %) (Figure 5-6 C). Additional immunohistochemical stainings confirmed that liraglutide markedly attenuated an ATII-induced oxidative stress burden in aorta which was caused by *Nox2* (Figure 5-6 D).

ATII infusion nearly doubled plasma nitrate levels (NO_3^-) compared to control (B6: \bar{x} 26.8 μM vs. ATII: \bar{x} 47.3 μM), whereas liraglutide significantly reduced plasma NO_3^- (\bar{x} 22.7 μM , retention time of NO_3^- : approx. 7.7 min) (Figure 5-6 E). As nitrate levels reflect the oxidative break-down of $\bullet\text{NO}$ by superoxide, $\bullet\text{NO}$ synthase levels of major $\bullet\text{NO}$ sources were analyzed. *Nos2* gene expression was significantly upregulated by ATII but normalized to control levels with liraglutide (Figure 5-6 F). In contrast, eNOS protein levels by quantitative Western blot analysis were, despite a weak trend of increase with ATII, non-significantly changed between groups (Figure 5-6 G). Thus, the increase in plasma nitrate by ATII infusion originates from an induction of iNOS/*Nos2* and *Nox2*, whereas liraglutide attenuates both factors leading to reduced plasma nitrate levels.

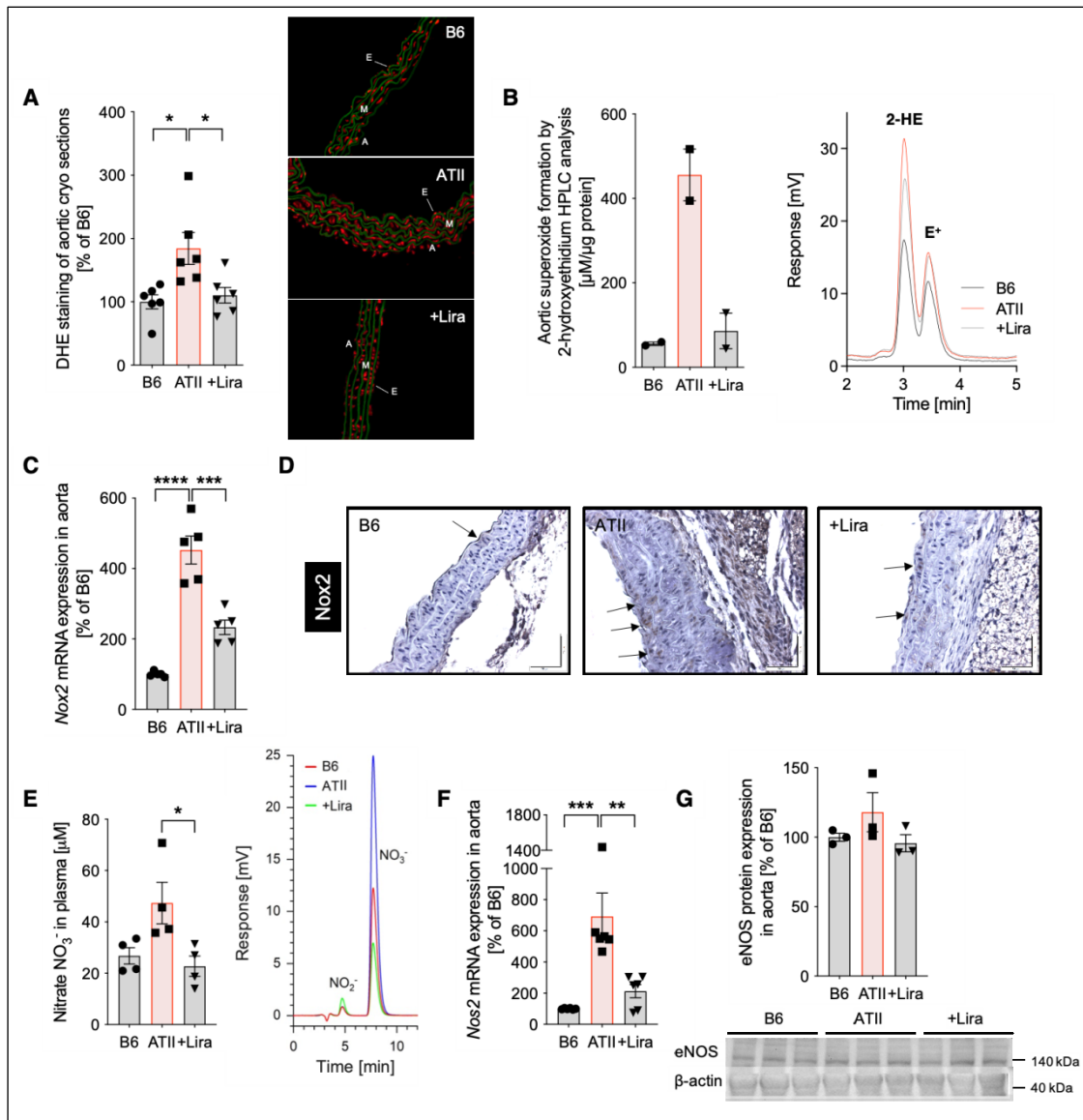


Figure 5-6: Liraglutide (Lira) reduces angiotensin II (ATII)-induced vascular oxidative stress in wild-type (C57BL/6J) mice. (A) Aortic cryosections (8 μm) were incubated with dihydroethidium (DHE) and reactive oxygen species (ROS)-derived fluorescence measured by fluorescence microscopy (n=6). Representative photomicrographs are shown next to the densitometric analysis. (Green: autofluorescence of aortic laminae; red: fluorescence from ROS; E=endothelium, M=media, A=adventitia). * $P < 0.05$; 1-way ANOVA with Bonferroni's multiple comparison test. (B) Aortic tissue was incubated with DHE and the supernatant subjected to HPLC analysis to separate the superoxide-specific oxidation product of DHE, 2-hydroxyethidium (2-HE), from the unspecific oxidation product of DHE, ethidium (E⁺). The bar graph left to the chromatogram shows the quantification of aortic superoxide formation derived from the 2-HE signal (n=2). Due to the limited n number, no statistical test was performed. (C) Gene expression level of *Nox2* (NADPH oxidase 2) was measured in aortic tissue by qRT-PCR (n=5). *** $P < 0.001$, **** $P < 0.0001$; 1-way ANOVA with Bonferroni's multiple comparison test. (D) Paraffin-embedded aortic rings were stained with Nox2 antibody for gp91phox detection (n=3). The figure shows one representative staining. Magnification 40x (scale bar 50 μm). (E) Nitrate (NO₃⁻) concentrations in plasma were determined in an HPLC-based assay (n=4). A representative chromatogram is shown next to the quantification bar graph. * $P < 0.05$; 1-way ANOVA with Bonferroni's multiple comparison test. Data generated in collaboration with Prof. Dr. Stefan Chlopicki / Jagiellonian Centre for Experimental Therapeutics (JCET) / Jagiellonian University, Krakow, Poland (conducted by Dr. Kamil Kus). (F) Gene expression level of *Nos2* (inducible $\bullet\text{NO}$ synthase) was measured in aortic tissue by qRT-PCR (n=6). ** $P < 0.01$, *** $P < 0.001$; 1-way ANOVA with Bonferroni's multiple comparison test. (G) Protein expression level of endothelial $\bullet\text{NO}$ synthase (eNOS) was measured in aortic tissue by Western blot (n=3). A representative blot is shown below the quantification bar graph. Not significant; 1-way ANOVA with Bonferroni's multiple comparison test. Data are means \pm SEM.

As *Nos2* and *Nox2* gene expression was increased in hypertensive mice, for both of which immune cells are a main source (see 1.3.1 and 1.4.1), immune cell infiltration into aortic tissue was investigated and its modulation by liraglutide. With the use of immunohistochemical techniques, aortic rings were stained with Mac-2 antibody for macrophage detection. Compared to controls, ATII infusion caused a strong macrophage infiltration in aorta as revealed by the DAB staining. In contrast, liraglutide-treated aortic rings showed visibly reduced macrophage accumulation (Figure 5-7 A). To further characterize and quantify immune cell subtypes of aortic inflammatory infiltration, aortic cells were surface-stained with a mixture of cell-type specific antibodies (Table 4-1, see 4.2.14) and analyzed via flow cytometry. The immune cell phenotyping revealed that liraglutide mitigated an ATII-induced infiltration of inflammatory monocytes ($\text{Ly6G}^- \text{Ly6C}^+$) and neutrophils ($\text{Ly6G}^+ \text{Ly6C}^+$) in aortic tissue (Figure 5-7 B-C). Aortas of hypertensive mice exhibited a more than 400 % increase of both cell subtypes compared to controls (ATII: \emptyset 560 % and 506 % vs. B6: \emptyset 100 % for both $\text{Ly6G}^- \text{Ly6C}^+$ and $\text{Ly6G}^+ \text{Ly6C}^+$, respectively), whereas aortic inflammatory monocytes and neutrophils infiltration was reduced by more than half upon liraglutide treatment (\emptyset 248 % $\text{Ly6G}^- \text{Ly6C}^+$ and \emptyset 225 % for $\text{Ly6G}^+ \text{Ly6C}^+$).

Thus, liraglutide potently attenuates ATII-induced oxidative stress and inflammation of the vasculature by prevention of $\text{Ly6G}^- \text{Ly6C}^+$ - inflammatory monocyte and $\text{Ly6G}^+ \text{Ly6C}^+$ neutrophil infiltration into the vascular wall.

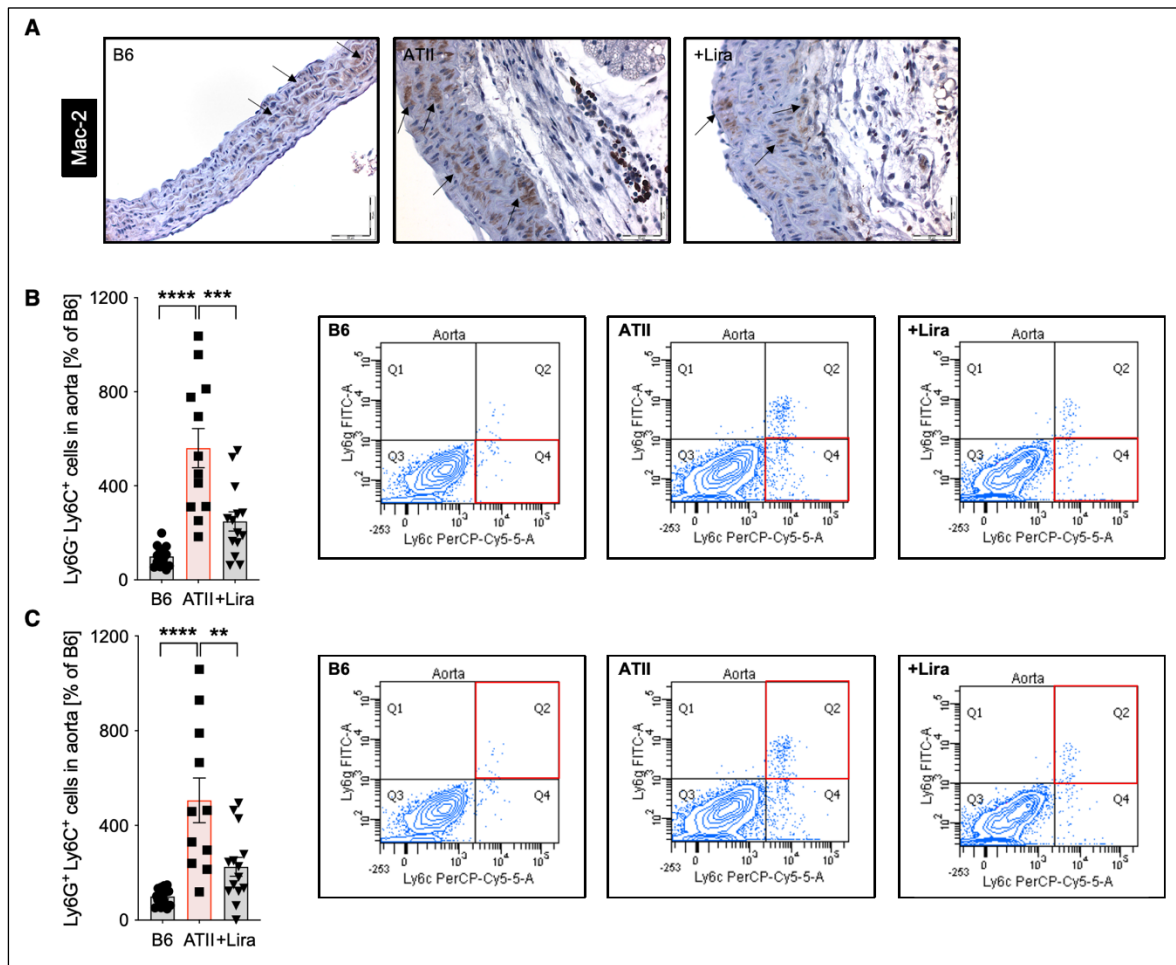


Figure 5-7: Liraglutide (Lira) mitigates angiotensin II (ATII)-induced infiltration of inflammatory cells into the vasculature of wild-type (C57BL/6J) mice. (A) Paraffin-embedded aortic rings were stained with Mac-2 antibody for macrophage detection (n=3). The figure shows one representative staining. Magnification 40x (scale bar 50 μ m). (B,C) Immune cell subtypes infiltrated into the aorta were identified and quantified using a combination of different fluorescence-labeled antibodies in flow cytometric analyses. Ly6G and Ly6C antibodies were used to differentiate inflammatory monocytes (Ly6G⁺Ly6C⁺, (B); n=12-15) and neutrophils (Ly6G⁺Ly6C⁺, (C); n=11-15). Representative contour plots are depicted next to the quantification bar graphs. ** P<0.01, *** P<0.001, **** P<0.0001; 1-way ANOVA with Bonferroni's multiple comparison test. Data are means \pm SEM.

5.3 Liraglutide modulates the interplay of inflammation, oxidative stress, and eNOS uncoupling in murine arterial hypertension

As the main producer of vasoprotective nitric oxide, an intact functional eNOS activity is crucial for vascular integrity. However, eNOS is a redox-sensitive enzyme which becomes uncoupled under oxidative stress conditions. In this regard, eNOS S-glutathionylation is an established marker for eNOS dysfunction (see 1.4.2). NF- κ B is a key regulator of inflammation which is known to be inducible by ATII³⁸⁶⁻³⁸⁸. To gain a more detailed mechanistic understanding of cardioprotection by liraglutide, the effect of liraglutide on parts of the NF- κ B signaling cascade in hypertensive mice (see 5.3.1) as well as the outcome on eNOS integrity (see 5.3.2) was investigated.

5.3.1 Liraglutide suppresses an NF- κ B-mediated proinflammatory cascade responsible for leukocyte adhesion and migration in murine arterial hypertension

As liraglutide strongly mitigated inflammatory monocyte and neutrophil infiltration in aortic tissue (see 5.2.2), the leukocyte adhesion cascade was investigated in more detail. During leukocyte extravasation, leukocytes, initiated by proinflammatory mediators such as NF- κ B, IL-1 β , and TNF- α , migrate out of the vascular lumen into inflamed tissue. This process comprises several sequential steps of leukocyte-vessel wall interactions, including initial chemoattraction and capturing, leukocyte rolling, followed by firm attachment to the vascular wall, and finally endothelial transmigration³⁸⁹. A prerequisite for inflammatory cell migration through the vascular wall is the expression of adhesion molecules on the surface of endothelial cells and leukocytes, enabling successful cell-cell interactions^{389,390}. Using *in vivo* intravital microscopy (IVM), it was investigated whether liraglutide modulates leukocyte rolling at the inner vascular wall of hypertensive mice. For this purpose, the fluorescent dye acridine orange was injected in anesthetized mice, allowing leukocyte visualization. Leukocyte rolling was measured under flow conditions using a fluorescence microscope with real-time imaging software (see 4.1.6). Furthermore, a possible favorable intervention of liraglutide in the NF- κ B-mediated proinflammatory cascade caused by ATII infusion was analyzed by gene and protein expression analyses.

As visualized by IVM, ATII infusion led to a trend of increased rolling of leukocytes at the inner vascular wall compared to controls, whereas liraglutide treatment significantly suppressed leukocyte rolling in hypertensive mice (Figure 5-8 A). Additionally, *Icam1*, *Vcam1*, and *Selp* genes coding for the adhesion molecules ICAM-1, VCAM-1, and P-selectin were strongly upregulated in aortas of ATII-infused mice, 50 % for *Icam1* and more than 200 % for *Vcam1* and *Selp*. Liraglutide significantly lowered the gene expression of these adhesion molecules (Figure 5-8 B-D). A pro-inflammatory phenotype in the aorta of hypertensive mice was further confirmed by a marked increase in *Nfkb2* and *Tnfa* mRNA transcripts as well as upregulated IL-1 β protein expression. Liraglutide significantly reduced this inflammatory phenotype as it downregulated all key inflammatory mediators in arterial hypertension (Figure 5-8 E-G).

Hence, liraglutide counteracted an NF- κ B-mediated inflammatory cascade in the hypertensive vasculature responsible for vascular inflammatory cell rolling, adhesion, and infiltration into the vascular wall.

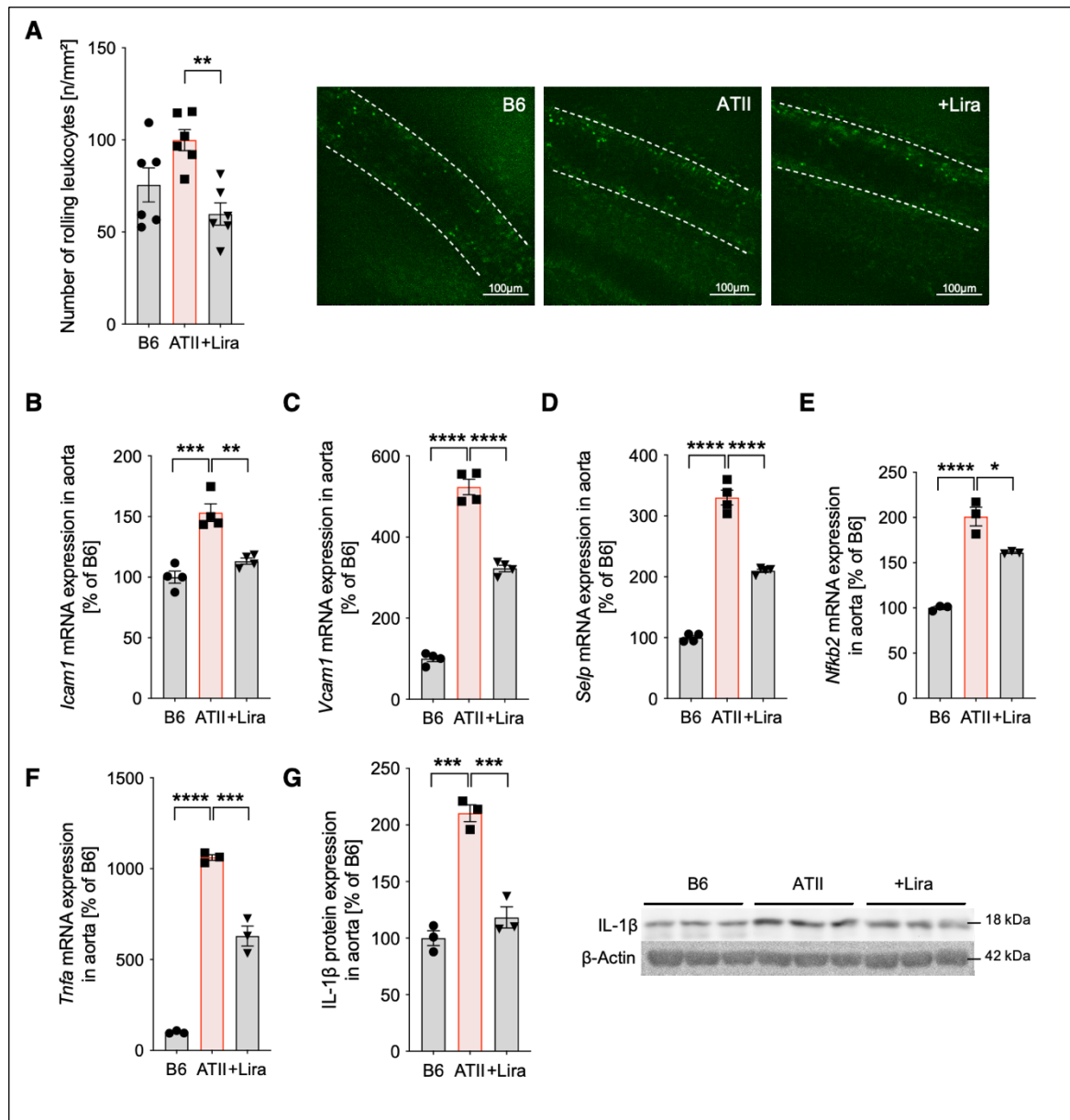


Figure 5-8: Liraglutide (Lira) attenuates angiotensin II (ATII)-triggered leukocyte migration (rolling, adhesion) and moderates proinflammatory signals in the vasculature of wild-type (C57BL/6J) mice with arterial hypertension. (A) After 7 d of treatment, leukocytes were stained with acridine orange and their rolling at the vascular wall (*V. femoralis*) visualized by intravital microscopy (IVM) (n=6). Representative images are shown next to the quantification bar graph. Magnification 25x (scale bar 100 μ m). ** P<0.01; 1-way ANOVA with Bonferroni's multiple comparison test. Data generated in collaboration with Jun. Prof. Dr. Christoph Reinhardt / Platform Intravital Microscopy / Center for Thrombosis and Hemostasis (CTH), University Medical Center Mainz (conducted by Dr. Alexandra Grill). (B-D) Gene expression levels of adhesion molecules (*Icam1*: intercellular adhesion molecule 1, *Vcam1*: vascular cell adhesion molecule 1, and *Selp*: P-selectin) were measured in aortic tissue by qRT-PCR (n=4). ** P<0.01, *** P<0.001, **** P<0.0001; 1-way ANOVA with Bonferroni's multiple comparison test. (E,F) Gene expression levels of inflammatory mediators (*Nfkb2*: nuclear factor kappa b subunit 2, *Tnfa*: tumor necrosis factor alpha) were measured in aortic tissue by qRT-PCR (n=3). * P<0.05, *** P<0.001, **** P<0.0001; 1-way ANOVA with Bonferroni's multiple comparison test. (G) Protein expression level of Interleukin 1 beta (IL-1 β) was measured in aortic tissue by Western blot (n=3). A representative blot is shown below the quantification bar graph. *** P<0.001; 1-way ANOVA with Bonferroni's multiple comparison test. Data are means \pm SEM.

5.3.2 Liraglutide avoids uncoupling of eNOS and maintains •NO bioavailability in murine arterial hypertension

Liraglutide significantly attenuated the amount of aortic ROS in hypertensive mice by reducing leukocyte infiltration into the vascular wall (see 5.2.2). Hence, a potential implication on eNOS function by liraglutide was investigated. Two complementary methods were applied to study eNOS uncoupling, on the one hand via DHE staining of aortic cryosections in the presence of the NOS inhibitor L-NAME (L-N^G- nitroarginine methyl ester, see 4.2.7) and on the other hand by quantifying the extent of eNOS S-glutathionylation in Western blot analyses (see 4.4.4). Moreover, the amount of bioavailable nitric oxide in aorta was measured by EPR spectroscopy. This technique allows the direct detection of unpaired electrons in a biological sample, in the present case of eNOS-derived •NO using an established protocol (see 4.2.11).

Endothelial DHE staining of aortic cryosection in the absence of L-NAME revealed a pattern already known from Figure 5-6 (see 5.2.2). ATII infusion caused an increase in oxidative stress in the aortic endothelium compared to controls, whereas liraglutide normalized the amount of ROS (Figure 5-9 A). Upon treatment with L-NAME, the DHE signal in the endothelial layer increased in the control and liraglutide group, whereas a previous increased DHE signal caused by ATII infusion was suppressed by L-NAME. Thus, DHE signals were non-significantly changed in between groups in the presence of L-NAME (Figure 5-9 A). This inhibitable endothelial DHE staining for ATII indicates an uncoupled eNOS since blocking the dysfunctional enzyme reduces its superoxide formation. On the contrary, inhibiting functional eNOS (B6, Lira) with L-NAME increases superoxide to the suspense of •NO production. In parallel, analysis of eNOS S-glutathionylation by Western blot analysis revealed significant enhanced eNOS glutathionylation in hypertensive aorta compared to controls (Figure 5-9 B), indicative of an uncoupled enzyme. Liraglutide treatment prevented eNOS uncoupling, as the extent of eNOS glutathionylation was strongly mitigated (Figure 5-9 B). To verify eNOS output, aortic •NO formation was measured by EPR spectroscopy. The measurements confirmed that the amount of bioavailable •NO was significantly impaired in the hypertensive vasculature. ATII infusion reduced aortic •NO production by more than 80 % relative to control (B6: Ø 100 % vs. ATII: Ø 19 %), whereas aortas of liraglutide-treated mice exhibited only mildly reduced •NO levels (Ø 71 %) compared to control but strongly increased levels compared to ATII (Figure 5-9 C).

Hence, two complementary methods confirmed that liraglutide avoids eNOS uncoupling in arterial hypertension, thereby preserving •NO bioavailability.

Relaxation studies in aortic rings revealed that *Glp1r^{-/-}* mice exhibit a per se deteriorated endothelial function compared to their genetic background strain C57BL/6J (B6). The mean maximal relaxation potential of *Glp1r^{-/-}* aortic rings was with 70 % markedly impaired relative to B6 with 79 % (Figure 5-10 A). ATII infusion worsened acetylcholine-dependent vasodilation in *Glp1r^{-/-}* mice and was not improved by liraglutide treatment, as indicated by a further right-shift of the relaxation curve (Figure 5-10 A). DHE stainings of aortic cryosections demonstrated increased ROS production in the vasculature of hypertensive *Glp1r^{-/-}* mice. Liraglutide did not alleviate this oxidative stress burden in aorta (Figure 5-10 B). In line with that, aortic *Nox2* gene expression was upregulated in ATII-infused *Glp1r^{-/-}* mice, which liraglutide not only failed to normalize but even enhanced (Figure 5-10 C). A similar pattern was observed for cardiac *Nox2* activity, which was significantly increased with ATII and (by trend) further deteriorated with liraglutide (Figure 5-10 D). Moreover, liraglutide failed to downregulate increased inflammatory gene expression of *Nos2* and *Tnfa* in aortas of hypertensive *Glp1r^{-/-}* mice (Figure 5-10 E-F).

Hence, the cardiovascular protective effects of liraglutide in arterial hypertension are abrogated in the absence of a functional canonical GLP-1R.

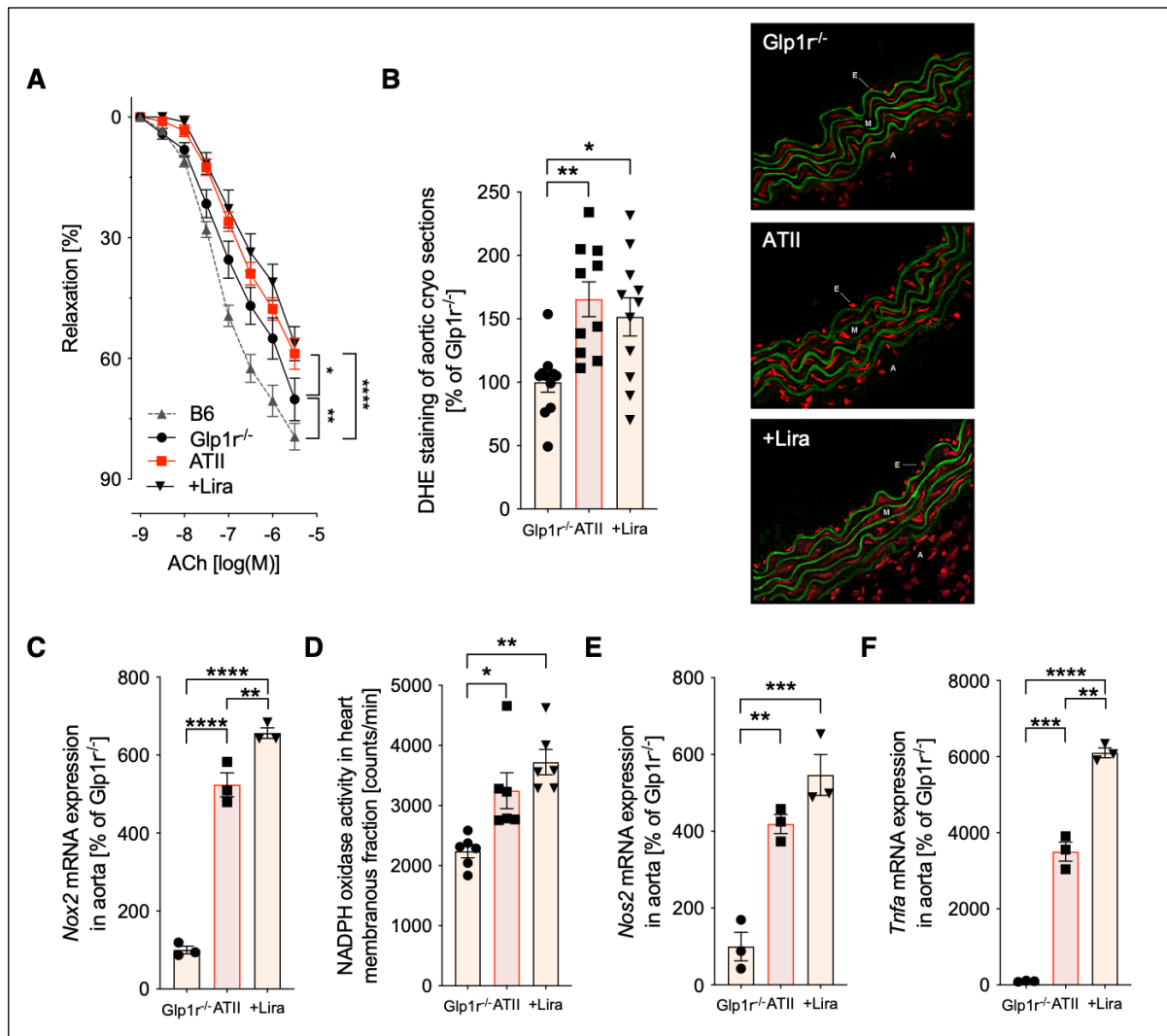


Figure 5-10: Liraglutide (Lira) causes increased vascular inflammation and oxidative stress in hypertensive *Glp1r^{-/-}* mice and fails to prevent endothelial dysfunction. Freshly isolated aorta was cut into rings and pre-constricted using KCl to induce maximal tone and prostaglandin F₂ α for 80 % submaximal tone induction. **(A)** Accumulative doses of acetylcholine (ACh) were administered to induce endothelium-dependent vasodilatation of the aortic rings, which was recorded in an organ bath chamber system (n=8-10). The aortic relaxation potential from C57BL/6J (B6) mice was measured in parallel and is depicted in grey for comparison. * P<0.05, ** P<0.01, **** P<0.0001; 2-way ANOVA with Bonferroni's multiple comparison test. **(B)** Aortic cryosections (8 μ m) were incubated with dihydroethidium (DHE) and reactive oxygen species (ROS)-derived fluorescence measured by fluorescence microscopy (n=10-11). Representative photomicrographs are shown next to the densitometric analysis. (Green: autofluorescence of aortic laminae; red: fluorescence from ROS; E=endothelium, M=media, A=adventitia). * P<0.05, ** P<0.01; 1-way ANOVA with Bonferroni's multiple comparison test. **(C)** Gene expression level of *Nox2* (NADPH oxidase 2) was measured in aortic tissue by qRT-PCR (n=3). ** P<0.01, **** P<0.0001; 1-way ANOVA with Bonferroni's multiple comparison test. **(D)** The activity of NADPH oxidase in isolated cardiac membrane fractions was measured by lucigenin-enhanced chemiluminescence in the presence of 200 μ M NADPH and the results expressed as counts per minute after 5 min (n=6). * P<0.05, ** P<0.01; 1-way ANOVA with Bonferroni's multiple comparison test. **(E,F)** Gene expression levels of *Nos2* (inducible \bullet NO synthase) and *Tnfa* (tumor necrosis factor alpha) were measured in aortic tissue by qRT-PCR (n=3). ** P<0.01, *** P<0.001, **** P<0.0001; 1-way ANOVA with Bonferroni's multiple comparison test. Data are means \pm SEM.

5.5 The cardiovascular protective effects of liraglutide persist in ATII-infused *Glp1r my^{-/-}* mice

The cardiovascular protective actions of liraglutide in arterial hypertension were removed in the absence of a functional GLP-1R (see 5.4), suggesting a GLP-1R dependent mechanism. However, it remains unclear which particular cell type is responsible for the favorable effects. Since liraglutide reduced inflammatory cell adhesion and infiltration, in particular inflammatory monocytes and neutrophils, into the vasculature of ATII-infused B6 mice (see 5.2.2 and 5.3.1), it was first analyzed how the myeloid GLP-1R contributes to cardiovascular protection in arterial hypertension.

Exploiting the Cre/loxP system, myelomonocytic cell-specific *Glp1r* knockout mice (*Glp1r^{fllox/fllox}LysM^{cre+/-}*, *Glp1r my^{-/-}*) were generated by crossing *Glp1r^{fllox/fllox}* with *LysM^{cre+}* mice (see 4.1.1). The latter express Cre under control of the lysozyme c type M (LysM) promoter, which is specific to the murine myeloid lineage (monocytes, macrophages, and neutrophils)^{307,399}. To verify the cell-type efficiency of Cre-mediated deletion, *Glp1r* gene expression was analyzed in bone marrow-derived macrophages (BMDMs) from *LysM^{cre+/-}* vs. *Glp1r my^{-/-}* mice (see 5.5.1). Furthermore, *Glp1r my^{-/-}* mice were characterized regarding metabolic (see 5.5.1) and cardiovascular (see 5.5.2) parameters. Finally, it was investigated how liraglutide modulates ATII-induced aortic inflammatory cell infiltration in these mice (see 5.5.3).

5.5.1 Verification of GLP-1R deficiency in *Glp1r my^{-/-}* mice and determination of metabolic parameters

GLP-1R knockdown in myeloid cells was assessed by *Glp1r* gene expression analysis in cells known to express the LysM protein, i.e., BMDMs, mature macrophages that are differentiated of bone marrow cells with the use of macrophage colony-stimulating factor (M-CSF) (see 4.2.4). To exclude the presence of a vascular phenotype in the newly generated *Glp1r my^{-/-}* line, the vascular response of sham- or ATII-infused *Glp1r my^{-/-}* vs. *LysM^{cre+/-}* mice was tested in relaxation studies. Furthermore, liraglutide-induced changes in body weight, non-fasting blood glucose and non-fasting plasma insulin were analyzed in hypertensive *Glp1r my^{-/-}* mice.

In contrast to *LysM^{cre+/-}* mice, no *Glp1r* gene expression could be observed in *Glp1r^{fllox/fllox}LysM^{cre+/-}* (*Glp1r my^{-/-}*) mice, as the number of mRNA transcripts was under the detectable limit (Figure 5-11 A). This indicates a successful selective disruption of GLP-1R expression in myeloid cells of *Glp1r my^{-/-}* mice. In head-to-head experiments of aortic rings from *LysM^{cre+/-}* and *Glp1r my^{-/-}* mice, acetylcholine responses (after the respective sham- or ATII-treatment) did not differ between the two mouse lines. Endothelium-dependent

relaxation of aortic rings from sham-treated *LysM^{cre+/+}* and *Glp1r my^{-/-}* mice was nearly identical, with a mean maximal relaxation potential of 92 % and 93 % for *LysM^{cre+/+}* and *Glp1r my^{-/-}*, respectively. ATII infusion in both strains led to an impairment of endothelial function at a similar extent, as indicated by non-significantly different right-shifted relaxation curves with a mean maximal relaxation potential of 72 % and 73 % for *LysM^{cre+/+}* and *Glp1r my^{-/-}* (Figure 5-11 B).

Seven days of ATII infusion (+ vehicle treatment) in *Glp1r my^{-/-}* mice led to a mean weight loss of -0.7 g whereas controls (*Glp1r my^{-/-}*) gained weight with an average of +0.6 g. ATII-infused *Glp1r my^{-/-}* mice treated with liraglutide significantly lost body weight compared to control but not to hypertensive mice, with a mean loss of -1.0 g (Figure 5-11 C). Both non-fasting blood glucose and non-fasting plasma insulin were non-significantly changed between the treatment groups in *Glp1r my^{-/-}* mice (Figure 5-11 D-E). Thus, liraglutide had no effect on glucose metabolism in non-diabetic hypertensive *Glp1r my^{-/-}* mice.

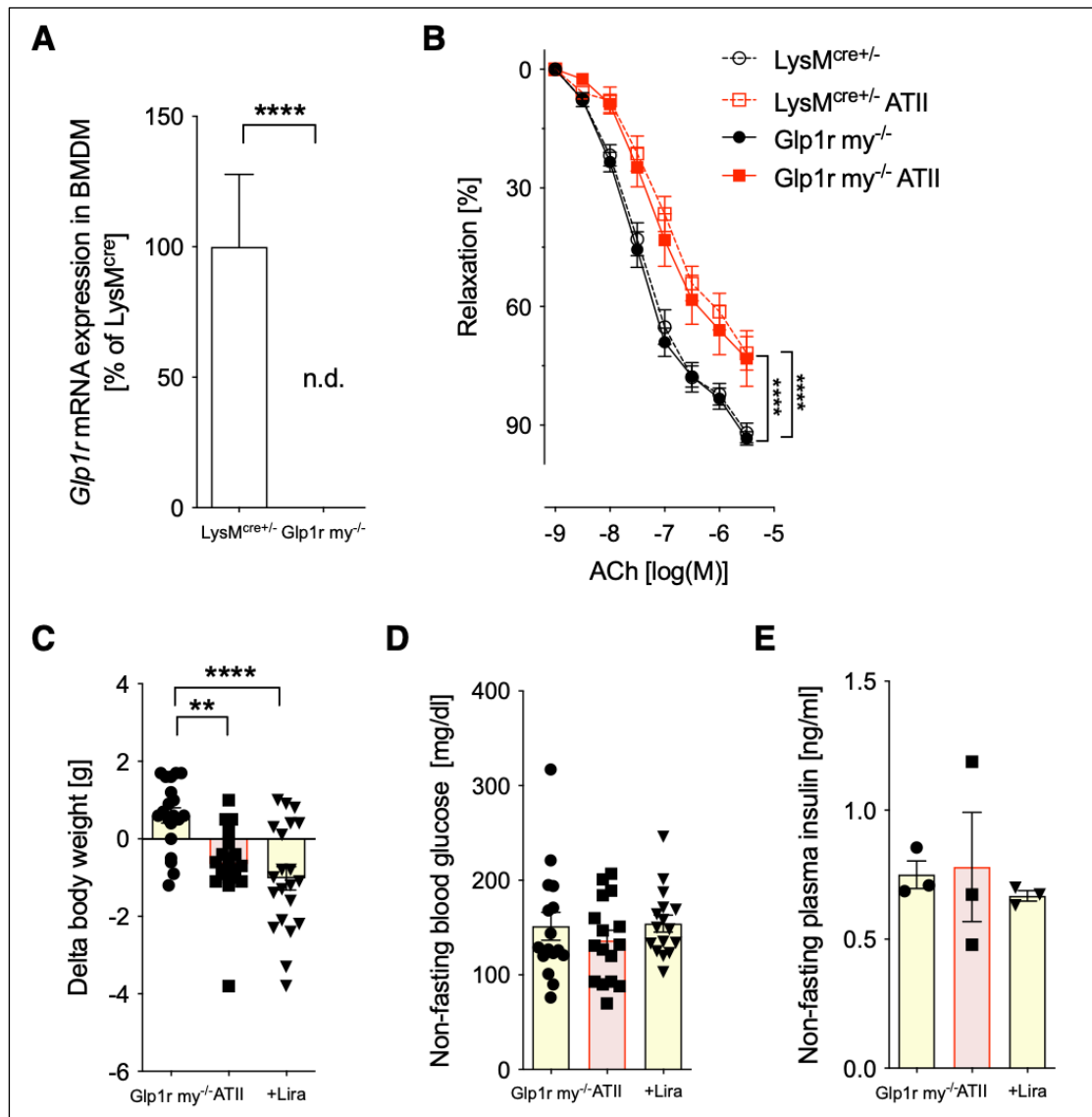


Figure 5-11: *Glp1r* gene deficiency in bone marrow-derived macrophages (BMDMs), vascular and metabolic phenotyping of myelomonocytic cell-specific *Glp1r* knockout mice (*Glp1r my^{-/-}*). (A) BMDMs derived from femur and tibia of *LysM^{cre/+}* vs. *Glp1r my^{-/-}* mice were tested for gene expression levels of *Glp1r* (Glucagon-like peptide-1 receptor) by qRT-PCR (n=3). **** P<0.0001; unpaired t-test. (B) Freshly isolated aorta from non-hypertensive *LysM^{cre/+}* vs. non-hypertensive *Glp1r my^{-/-}* mice was cut into rings and pre-constricted using KCl to induce maximal tone and prostaglandin F_{2α} for 80 % submaximal tone induction. Accumulative doses of acetylcholine (ACh) were administered to induce endothelium-dependent vasodilatation of the aortic rings, which was recorded in an organ bath chamber system (n=8). **** P<0.0001; 2-way ANOVA with Bonferroni's multiple comparison test. (C) Mice were weighed before (day 0) and on day 7 of treatment and the delta body weight was calculated (n=20-21). ** P<0.01, **** P<0.0001; 1-way ANOVA with Bonferroni's multiple comparison test. (D) Blood glucose levels were measured from whole blood of non-fasted mice using a glucometer (n=16). Not significant; 1-way ANOVA with Bonferroni's multiple comparison test. (E) Insulin levels were measured from plasma of non-fasted mice by ELISA (n=3). Not significant; 1-way ANOVA with Bonferroni's multiple comparison test. Data are means ± SEM.

5.5.2 Liraglutide alleviates endothelial dysfunction, vascular fibrosis, and cardiac hypertrophy in ATII-infused *Glp1r my^{-/-}* mice

To analyze whether the cardiovascular protective effects of liraglutide are altered in hypertensive *Glp1r my^{-/-}* mice, vascular function was determined in aortic relaxation studies. Besides, cardiovascular remodeling was investigated by sirius red stainings, indicative of vascular fibrosis, and by measuring heart body weight ratios denotive of cardiac hypertrophy.

Liraglutide potently improved an ATII-triggered endothelial dysfunction in *Glp1r my^{-/-}* mice. ATII infusion markedly deteriorated endothelial function compared to control, as shown by a right-shift of the acetylcholine-dependent relaxation curve. The mean maximal aortic relaxation potential was 82 % in control mice which was impaired by nearly one fifth to 69 % upon ATII infusion. Additional liraglutide treatment significantly attenuated the endothelial dysfunction caused by ATII and restored endothelium-dependent vasodilation to control levels with a mean maximal relaxation potential of 80 % (Figure 5-12 A). Aortas from hypertensive *Glp1r my^{-/-}* mice showed strong collagen accumulation in the sirius red staining which was visibly mitigated by liraglutide, to an extent similar to the *Glp1r my^{-/-}* control vasculature (Figure 5-12 B). Furthermore, hearts of ATII-infused *Glp1r my^{-/-}* mice were hypertrophic, indicated by an increased heart body weight ratio of 5.6 mg/g. Liraglutide protected from cardiac hypertrophy as the heart/body weight ratio averaged to 5.0 mg/g which was similar to the one of controls with 4.9 mg/g. (Figure 5-12 C).

Thus, liraglutide amends ATII-induced endothelial dysfunction, vascular fibrosis, and cardiac hypertrophy in myelomonocytic cell-specific *Glp1r* knockout mice (*Glp1r my^{-/-}*) mice.

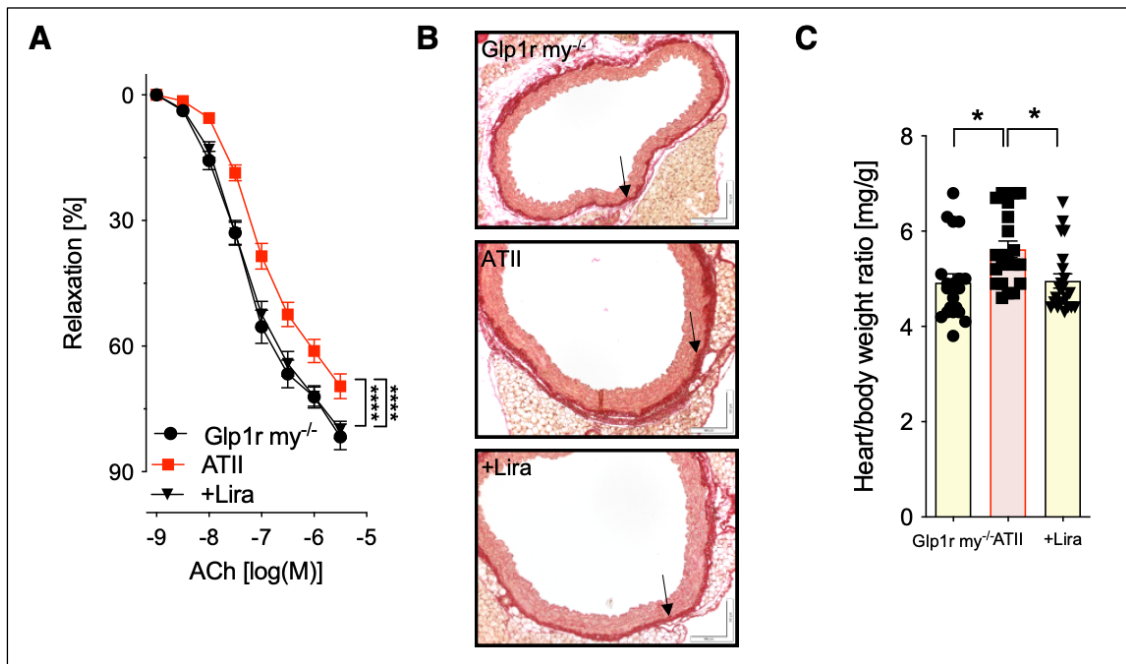


Figure 5-12: Liraglutide (Lira) amends angiotensin II (ATII)-induced endothelial dysfunction, vascular fibrosis and cardiac hypertrophy in myelomonocytic cell-specific *Gp1r* knockout mice (*Gp1r* $my^{-/-}$) mice. Freshly isolated aorta was cut into rings and pre-constricted using KCl to induce maximal tone and prostaglandin F₂ α for 80 % submaximal tone induction. **(A)** Accumulative doses of acetylcholine (ACh) were administered to induce endothelium-dependent vasodilatation of the aortic rings, which was recorded in an organ bath chamber system (n=16-22). **** P<0.0001; 2-way ANOVA with Bonferroni's multiple comparison test. **(B)** Paraffin-embedded aortic rings were stained with picro-sirius red to detect collagen fiber accumulation as a manifestation of vascular fibrosis (n=3-4). The figure shows one representative staining. Magnification 20x (scale bar 100 μ m). **(C)** Mice and isolated hearts (post-transection) were weighed on day 7 of treatment and the heart/body weight ratio was determined as an indicator of cardiac hypertrophy (n=20-21). * P<0.05; 1-way ANOVA with Bonferroni's multiple comparison test. Data are means \pm SEM.

5.5.3 Liraglutide diminishes vascular inflammation in ATII-infused *Gp1r* $my^{-/-}$ mice

The reduction of ATII-induced infiltration of inflammatory monocytes and neutrophils into the vasculature of B6 mice (see 5.2.2) was central to the cardiovascular protective properties of liraglutide in arterial hypertension. Hence, it was tested how liraglutide modulates the migration of blood-derived inflammatory cells into hypertensive aortas of *Gp1r* $my^{-/-}$ mice.

Qualitative analysis of immunohistochemical stainings for Mac-2 demonstrated a distinct accumulation of tissue-resident macrophages in ATII-infused mice, whereas liraglutide visibly mitigated macrophage infiltration (Figure 5-13 A).

Complementary flow cytometric measurements for inflammatory monocytes (Ly6G⁻Ly6C⁺) and neutrophils (Ly6G⁺Ly6C⁺) revealed a similar trend. Aortas of hypertensive *Gp1r* $my^{-/-}$ mice exhibited a strong burden with both cell subtypes compared to controls (ATII: \emptyset 3388 % and 1265 % vs. *Gp1r* $my^{-/-}$: \emptyset 100 % for Ly6G⁻Ly6C⁺ and Ly6G⁺Ly6C⁺, respectively), whereas liraglutide significantly reduced aortic inflammatory monocytes infiltration to nearly a

fifth (\emptyset 706 %, Ly6G⁻Ly6C⁺) and decreased aortic neutrophil infiltration to nearly a third (\emptyset 433 %, Ly6G⁺Ly6C⁺) (Figure 5-13 B-C) compared to ATII.

Thus, liraglutide attenuates inflammatory monocytes and neutrophils immune cell infiltration in aortic tissue of ATII-infused mice even when the GLP-1R is absent in myeloid cells.

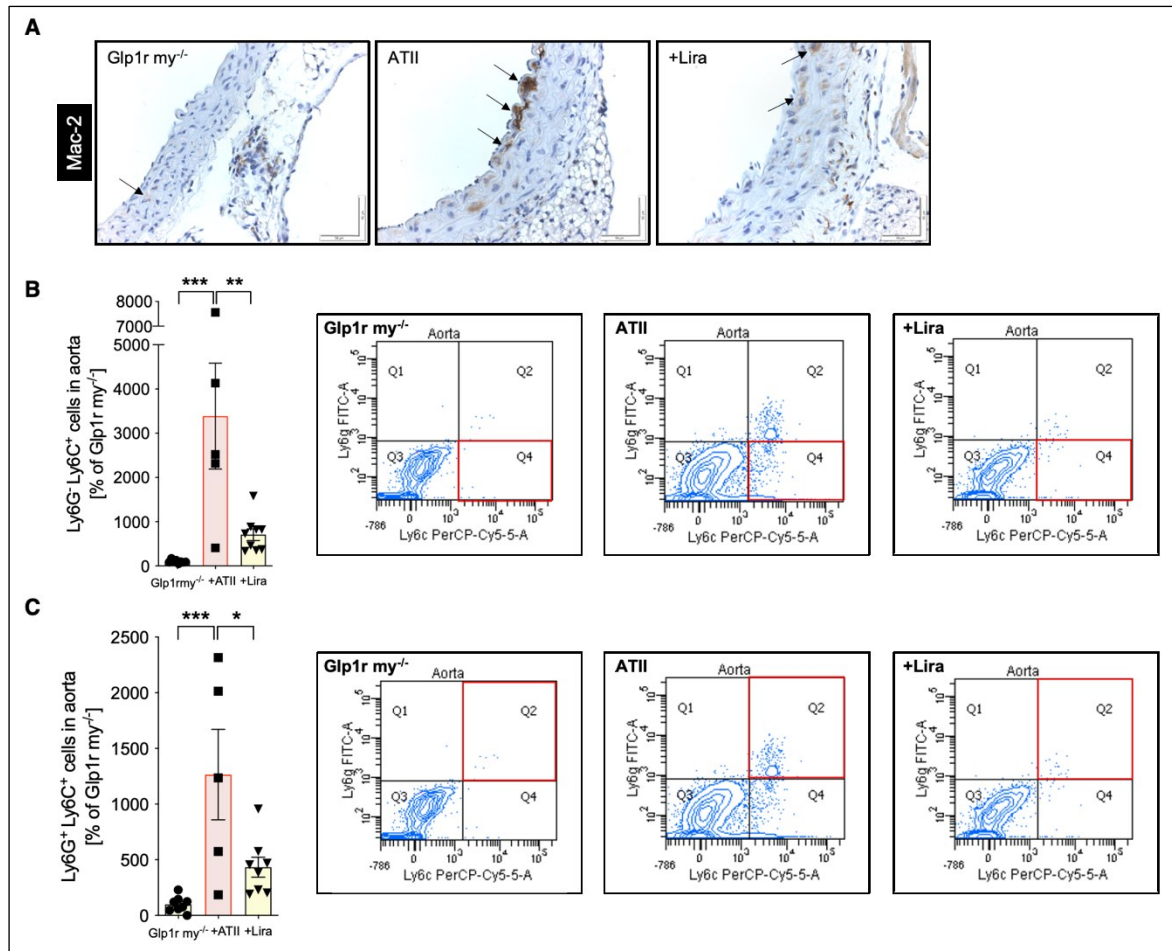


Figure 5-13: Liraglutide (Lira) mitigates angiotensin II (ATII)-induced infiltration of inflammatory cells into the vasculature of myelomonocytic cell-specific *Glp1r* knockout mice (*Glp1r* my^{-/-}) mice. (A) Paraffin-embedded aortic rings were stained with Mac-2 antibody for macrophage detection (n=3). The figure shows one representative staining. Magnification 40x (scale bar 50 μ m). **(B,C)** Immune cell subtypes infiltrated into the aorta were identified and quantified using a combination of different fluorescence-labeled antibodies in flow cytometric analyses. Ly6G and Ly6C antibodies were used to differentiate inflammatory monocytes (Ly6G⁻Ly6C⁺, **(B)**; n=5-9) and neutrophils (Ly6G⁺Ly6C⁺, **(C)**; n=5-8). Representative contour plots are depicted next to the quantification bar graphs. * P<0.05, ** P<0.01, *** P<0.001; 1-way ANOVA with Bonferroni's multiple comparison test. Data are means \pm SEM.

5.6 The cardiovascular protective effects of liraglutide are abolished in ATII-infused *Glp1r* $ec^{-/-}$ mice

Oxidative injury of the endothelium is a major catalyst for the development of endothelial dysfunction and subsequent CVD (see 1.3.3). As liraglutide improved endothelial function (see 5.1.2) and reduced the vascular recruitment of immune cells (see 5.2.2 and 5.3.1) in ATII-infused B6 mice, the contribution of the endothelial GLP-1R for cardiovascular benefits of liraglutide in arterial hypertension was investigated.

For this purpose, endothelial cell-specific *Glp1r* knockout mice (*Glp1r*^{fllox/fllox}*Cdh5*^{cre+}, *Glp1r* $ec^{-/-}$) were generated by crossing *Glp1r*^{fllox/fllox} with *Cdh5*^{cre+} mice using Cre-loxP-mediated recombination (see 4.1.1). Cadherin-5 (*Cdh5*, also VE-Cadherin or CD144) is a transmembrane protein located in adherens junctions of endothelial cells, enabling endothelial cell-cell adhesion. The endothelium of both developing and quiescent vessels uniformly express *Cdh5*, making Cadherin-Cre transgenic mice suitable for generating endothelial-specific mouse lines³⁰⁶. However, during early development, *Cdh5* has been shown to label a population of progenitor cells that can differentiate not only into endothelial but also into hematopoietic cells^{306,400,401}. Hence, Cadherin-Cre-mediated recombination can also lead to gene deletion in cells of the hematopoietic lineage^{306,312}.

To verify the cell-type efficiency of Cre-mediated deletion, *Glp1r* gene expression was analyzed in primary mouse lung endothelial cells (MLECs) from *Cdh5*^{cre+} vs. *Glp1r* $ec^{-/-}$ mice (see 5.6.1). To assess a possible non-endothelial deletion of the *Glp1r* in the hematopoietic cell lineage, *Glp1r* mRNA expression was also measured in CD45⁺ cells of *Glp1r*^{fllox/fllox}*Cdh5*^{cre+} in comparison to C57BL/6J mice. Subsequently, metabolic (see 5.6.1) and cardiovascular (see 5.6.2) actions of liraglutide were characterized in hypertensive *Glp1r* $ec^{-/-}$ mice. For this purpose, it was further investigated how liraglutide modulates ATII-induced aortic inflammatory cell infiltration and vascular oxidative stress parameters in these mice (see 5.6.3).

5.6.1 Verification of GLP-1R deficiency in *Glp1r* $ec^{-/-}$ mice and determination of metabolic parameters

MLECs are microvascular endothelial cells which were isolated by CD31⁺/CD102⁺-double selection of enzymatically disrupted lung tissue (see 4.2.3). Pan CD45⁺-leukocytes were enriched from EDTA-blood samples collected from B6 and *Glp1r* $ec^{-/-}$ mice through ACK lysis of erythrocytes and thrombocytes (see 4.2.2). To check for a normal physiological response of the *Glp1r* $ec^{-/-}$ vasculature, *Glp1r* $ec^{-/-}$ and *Cdh5*^{cre+} mice were sham- or ATII-infused and their endothelium-dependent aortic relaxation potential investigated in head-to-head

experiments. Besides, the effect of liraglutide on body weight, non-fasting blood glucose and non-fasting plasma insulin was analyzed in hypertensive *Glp1r ec^{-/-}*.

Glp1r gene expression was significantly reduced in endothelial cells of *Glp1r ec^{-/-}* in comparison to *Cdh5^{cre+}* mice (Figure 5-14 A). The number of *Glp1r* mRNA transcripts was decreased by 85 % (*Cdh5^{cre+}*: Ø 100% vs. *Glp1r ec^{-/-}*: Ø 15 %), demonstrating an efficient disruption of endogenous GLP-1R expression in endothelial cells of *Glp1r ec^{-/-}* mice. Concomitantly, *Glp1r* mRNA expression in CD45⁺ hematopoietic cells was non-significantly changed between *Glp1r ec^{-/-}* and B6 mice (Figure 5-14 B). The latter indicates that the Cre-mediated deletion in *Glp1r ec^{-/-}* mice was endothelial cell-type specific. The acetylcholine responses of aortic rings from sham- or ATII-treated *Cdh5^{cre+}* vs. *Glp1r ec^{-/-}* mice did not differ between the two mouse lines (Figure 5-14 C). The aortic relaxation potential of sham-treated *Cdh5^{cre+}* and *Glp1r ec^{-/-}* was similar, with a mean maximal relaxation potential of 78 % and 76 % for *Cdh5^{cre+}* and *Glp1r ec^{-/-}*, respectively. ATII infusion in both strains deteriorated endothelial function to a similar extent, causing a right-shift of the relaxation curve with a mean maximal relaxation potential of 58 % (*Cdh5^{cre+}*) and 62 % (*Glp1r ec^{-/-}*). Hence, selective knockdown of the endothelial GLP-1R does not cause a vascular phenotype that per se deviates from *Cdh5^{cre+}* mice.

Over the course of one week, hypertensive *Glp1r ec^{-/-}* mice (on average) neither lost or gained weight (Ø ±0.0 g) in contrast to controls (*Glp1r ec^{-/-}*) which gained weight (Ø +0.7 g). Liraglutide treatment led to a mean weight loss of ca. -0.8 g, which represents a significant reduction relative to controls but only a loss by trend compared to ATII-infused mice (Figure 5-14 D). Both non-fasting blood glucose and non-fasting plasma insulin were non-significantly changed between the treatment groups in *Glp1r ec^{-/-}* mice (Figure 5-14 E-F).

Thus, liraglutide does not alter glucose metabolism in ATII-infused *Glp1r ec^{-/-}* mice.

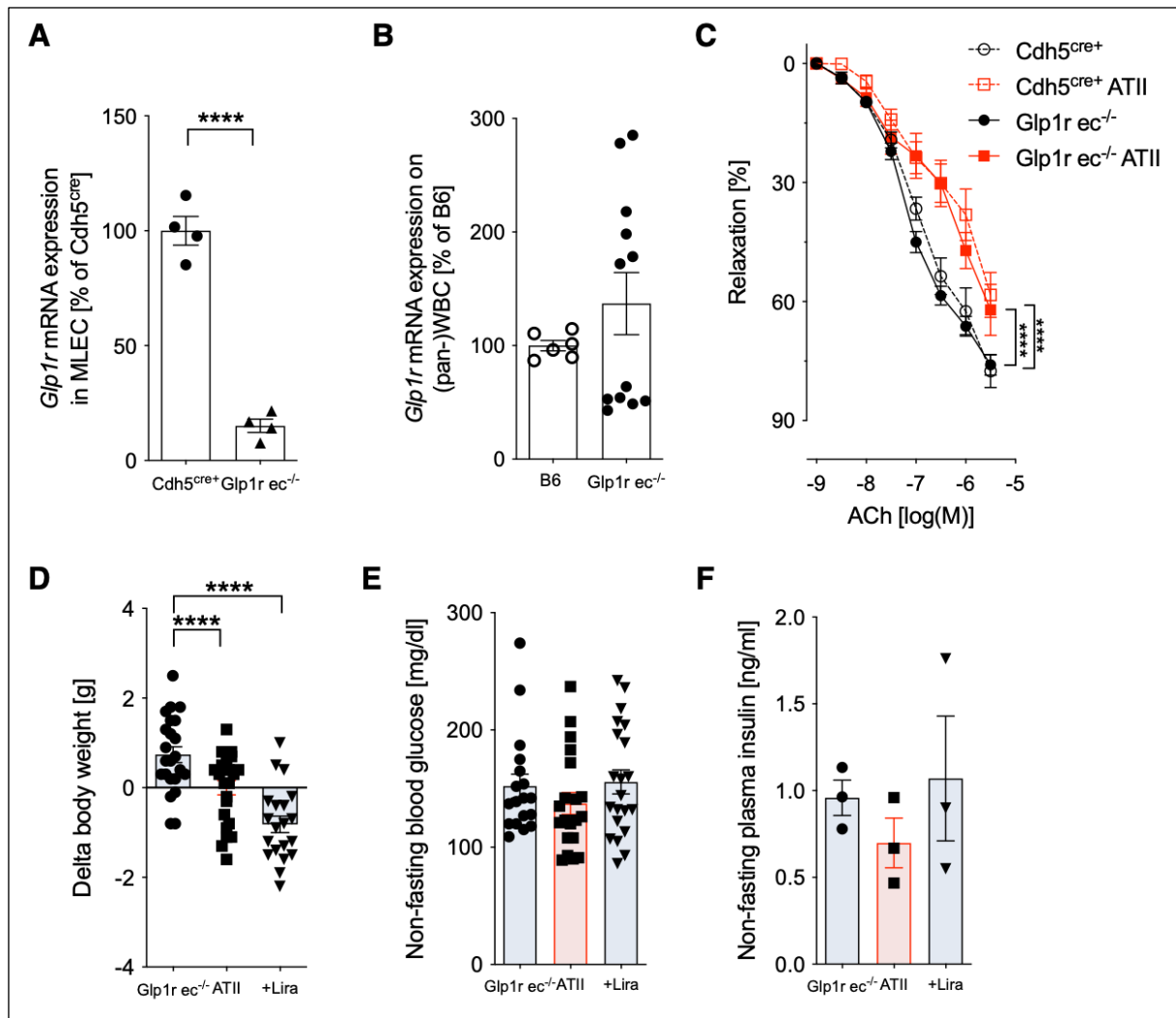


Figure 5-14: *Glp1r* gene deficiency in mouse lung endothelial cells (MLECs), vascular and metabolic phenotyping of endothelial cell-specific *Glp1r* knockout mice (*Glp1r ec^{-/-}*). (A) MLECs of *Cdh5^{cre+}* vs. *Glp1r ec^{-/-}* mice were tested for gene expression levels of *Glp1r* (Glucagon-like peptide-1 receptor) by qRT-PCR (n=4). **** P<0.0001; unpaired t-test. (B) White blood cells (WBCs) were isolated from EDTA blood samples from C57BL/6J (B6) vs. *Glp1r ec^{-/-}* mice and tested for gene expression levels of *Glp1r* by qRT-PCR (B6: n=6, *Glp1r ec^{-/-}*: n=12). Not significant; Mann-Whitney test. (C) Freshly isolated aorta from (non-) hypertensive *Cdh5^{cre+}* vs. (non-) hypertensive *Glp1r ec^{-/-}* mice was cut into rings and pre-constricted using KCl to induce maximal tone and prostaglandin F2 α for 80 % submaximal tone induction. Accumulative doses of acetylcholine were administered to induce endothelium-dependent vasodilatation of the aortic rings, which was recorded in an organ bath chamber system (n=7-8). **** P<0.0001; 2-way ANOVA with Bonferroni's multiple comparison test. (D) Mice were weighed before (day 0) and on day 7 of treatment and the delta body weight was calculated (n=20-24). **** P<0.0001; 1-way ANOVA with Bonferroni's multiple comparison test. (E) Blood glucose levels were measured from whole blood of non-fasted mice using a glucometer (n=3). Not significant; 1-way ANOVA with Bonferroni's multiple comparison test. (F) Insulin levels were measured from plasma of non-fasted mice by ELISA (n=18-21). Not significant; 1-way ANOVA with Bonferroni's multiple comparison test. Data are means \pm SEM.

5.6.2 Liraglutide does not protect from endothelial dysfunction, vascular fibrosis, cardiac hypertrophy, and hypertension in ATII-infused *Glp1r ec^{-/-}* mice

To assess whether a selective disruption of the GLP-1R in endothelial cells alters the cardiovascular protective effects of liraglutide in arterial hypertension, liraglutide-treated hypertensive *Glp1r ec^{-/-}* mice were examined regarding their endothelial function, cardiac and vascular structure, and blood pressure levels.

ATII infusion in *Glp1r ec^{-/-}* mice caused endothelial dysfunction, as shown by a significant right-shift of the aortic relaxation curve in response to acetylcholine. Liraglutide treatment did not improve endothelial function in hypertensive *Glp1r ec^{-/-}* mice (Figure 5-15 B). The mean maximal relaxation potential of vehicle-treated hypertensive aortic rings was with 66 % worsened by approximately one fifth relative to controls (Ø 81 %) and impaired to a similar extent with liraglutide treatment (69 %). Besides, liraglutide did not alleviate the fibrotic phenotype in hypertensive *Glp1r ec^{-/-}* aortas. As shown by sirius red staining for collagen, ATII infusion and additional liraglutide treatment both caused a similar extent of collagen accumulation in aortic tissue, which was visibly enhanced relative to controls (Figure 5-15 A). Likewise, *Glp1r ec^{-/-}* hearts were hypertrophic upon ATII infusion, as indicated by increased heart/body weight ratios (Ø 4.6 mg/g in *Glp1r ec^{-/-}* vs. Ø 5.1 mg/g upon ATII), whereas liraglutide non-significantly reduced cardiac hypertrophy with a mean heart/body weight ratio of 4.8 mg/g (Figure 5-15 C). Finally, liraglutide did not restore normal SBP levels in *Glp1r ec^{-/-}* mice. ATII infusion significantly increased blood pressure levels by 28 mmHg, from (on average) 129 mmHg in controls to 157 mmHg with ATII, and high blood pressure levels (Ø 149 mmHg) persisted with additional liraglutide treatment (Figure 5-15 D).

Thus, liraglutide does not protect hypertensive *Glp1r ec^{-/-}* mice from impaired endothelial function, vascular fibrosis, cardiac hypertrophy and elevated blood pressure levels.

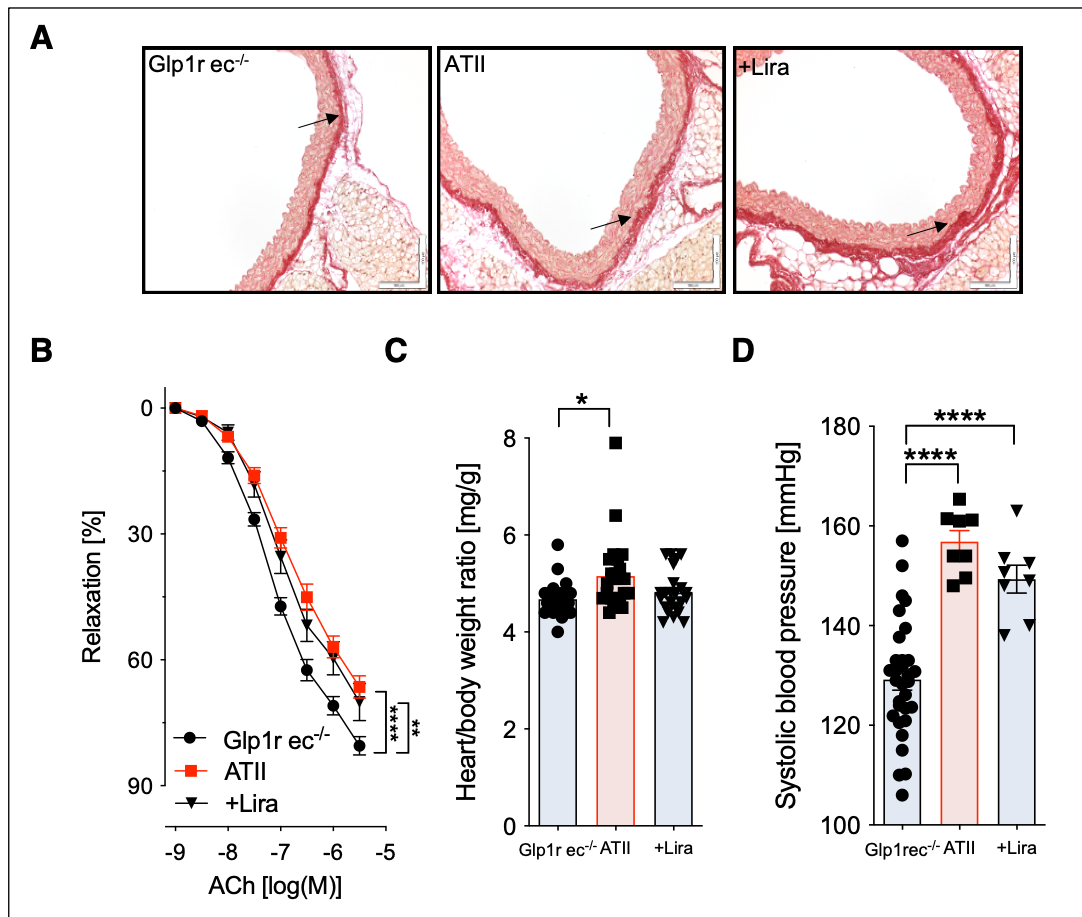


Figure 5-15: Liraglutide (Lira) does not eradicate angiotensin II (ATII)-induced endothelial dysfunction, vascular fibrosis, cardiac hypertrophy, and hypertension in endothelial cell-specific *Glp1r* knockout mice (*Glp1r ec^{-/-}*) mice. (A) Paraffin-embedded aortic rings were stained with picro-sirius red to detect collagen fiber accumulation as a manifestation of vascular fibrosis (n=3-4). The figure shows one representative staining. Magnification 20x (scale bar 100 μm). (B) Freshly isolated aorta was cut into rings and pre-constricted using KCl to induce maximal tone and prostaglandin F₂α for 80% submaximal tone induction. Accumulative doses of acetylcholine (ACh) were administered to induce endothelium-dependent vasodilatation of the aortic rings, which was recorded in an organ bath chamber system (n=20-30). ** P<0.01, **** P<0.0001; 2-way ANOVA with Bonferroni's multiple comparison test. (C) Mice and isolated hearts (post-transection) were weighed on day 7 of treatment and the heart/body weight ratio was determined as an indicator of cardiac hypertrophy (n=23-25). * P<0.05; 1-way ANOVA with Bonferroni's multiple comparison test. (D) Systolic blood pressure was measured non-invasively by the tail-cuff method 6 days after start of ATII infusion (n=8-31). **** P<0.0001; 1-way ANOVA with Bonferroni's multiple comparison test. Data are means ± SEM.

5.6.3 Liraglutide fails to prevent aortic inflammatory infiltration and vascular oxidative stress in ATII-infused *Glp1r ec^{-/-}* mice

Liraglutide reduced ATII-induced infiltration of inflammatory monocytes and neutrophils into the vasculature of both B6 and *Glp1r my^{-/-}* mice (see 5.2.2 and 5.5.3), thereby preventing vascular oxidative injury in these mouse lines. In hypertensive *Glp1r ec^{-/-}* mice, liraglutide failed to improve impaired endothelial function (see 5.6.2). Hence, the effect of liraglutide on vascular recruitment of immune cells into the hypertensive vasculature of *Glp1r ec^{-/-}* mice was analyzed.

ATII infusion augmented the amount of tissue-resident macrophages in aorta of *Glp1r ec^{-/-}* mice, as revealed by qualitative immunohistochemical stainings for Mac-2. Liraglutide did not

visibly attenuate aortic macrophage accumulation (Figure 5-16 A). A more detailed analysis of immune cell subtypes in flow cytometry experiments confirmed that liraglutide did not abrogate increased aortic inflammatory monocytes (Ly6G⁻Ly6C⁺) and neutrophils (Ly6G⁺Ly6C⁺) infiltration caused by ATII. Aortas of hypertensive *Glp1r ec^{-/-}* mice exhibited a strong burden with both cell subtypes. Upon ATII treatment, inflammatory monocytes significantly increased by more than 400 % and neutrophils by trend more than 200 % compared to controls (ATII: Ø 506 % and 310 % vs. *Glp1r ec^{-/-}*: Ø 100 % for Ly6G⁻Ly6C⁺ and Ly6G⁺Ly6C⁺, respectively). Liraglutide in both cases non-significantly reduced aortic inflammatory cell infiltration compared to ATII, with only a small decrease by trend for inflammatory monocytes (Ø 293 %, Ly6G⁻Ly6C⁺) and even an increase by trend for neutrophils (Ø 412 %, Ly6G⁺Ly6C⁺) (Figure 5-16 B-C). However, neutrophils were significantly increased in aortas of hypertensive liraglutide-treated *Glp1r ec^{-/-}* mice compared to control.

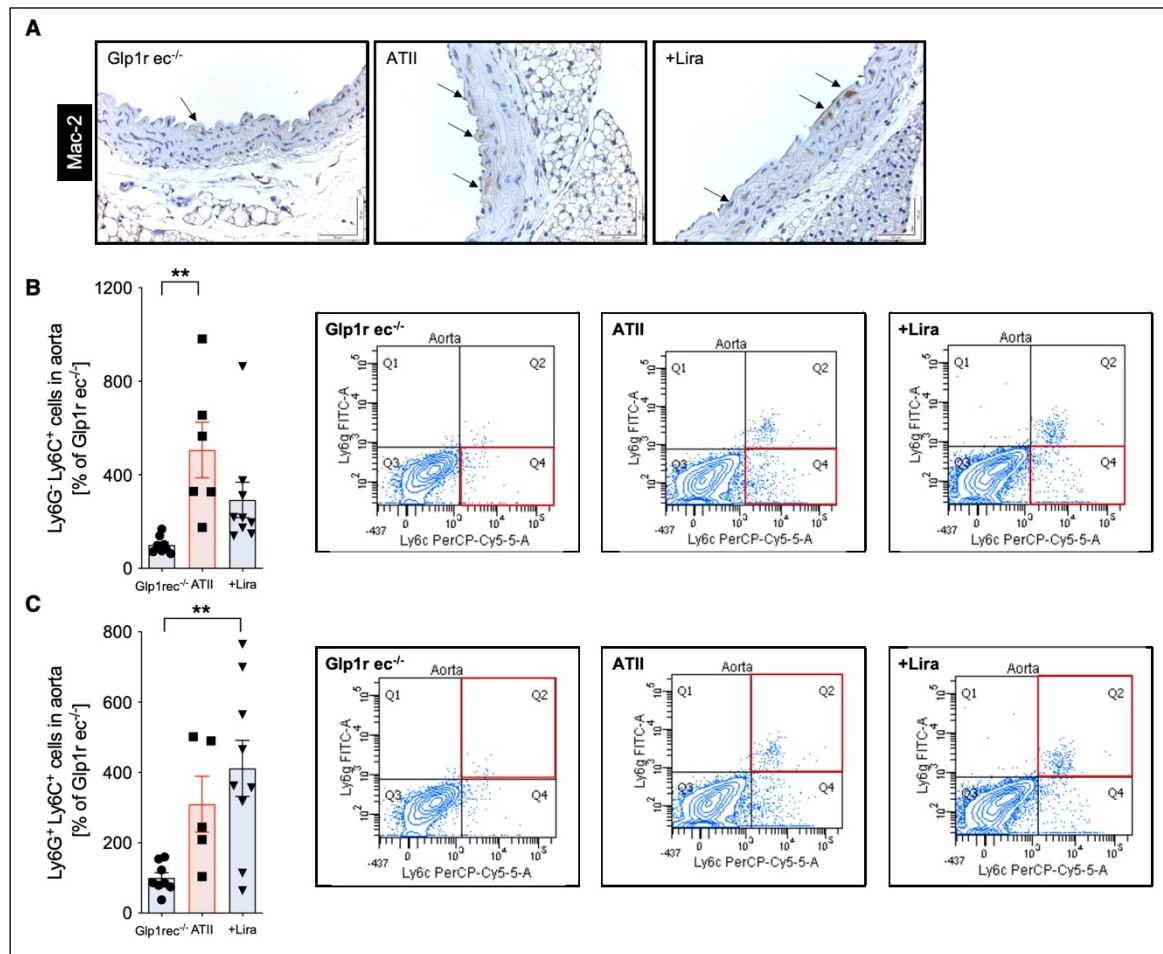


Figure 5-16: Liraglutide (Lira) fails to mitigate angiotensin II (ATII)-induced infiltration of inflammatory cells into the vasculature of endothelial cell-specific *Glp1r* knockout mice (*Glp1r ec^{-/-}*) mice. (A) Paraffin-embedded aortic rings were stained with Mac-2 antibody for macrophage detection (n=3). The figure shows one representative staining. Magnification 40x (scale bar 50 μ m). **(B,C)** Immune cell subtypes infiltrated into the aorta were identified and quantified using a combination of different fluorescence-labeled antibodies in flow cytometric analyses. Ly6G and Ly6C antibodies were used to differentiate inflammatory monocytes (Ly6G⁺Ly6C⁺, **(B)**; n=6-9) and neutrophils (Ly6G⁺Ly6C⁺, **(C)**; n=5-9). Representative contour plots are depicted next to the quantification bar graphs. ** P<0.01; 1-way ANOVA with Bonferroni's multiple comparison test. Data are means \pm SEM.

As further proof that a lack of the endothelial GLP-1R in hypertensive mice fails to prevent aortic phagocyte infiltration with liraglutide, *Nox2* gene expression in aorta, and plasma nitrate levels were analyzed as vascular oxidative stress parameters. Additionally, cytokine *Tnfa* and vascular adhesion molecule *Vcam1* gene expression was measured in aorta of hypertensive *Glp1r ec^{-/-}* mice.

Liraglutide failed to reduce an ATII-induced *Nox2* upregulation in aorta of *Glp1r ec^{-/-}* mice, thus retaining the superoxide burden caused by arterial hypertension (Figure 5-17 A). Plasma nitrate levels increased by trend upon ATII infusion and were significantly augmented with liraglutide treatment compared to controls, reflecting an enhanced oxidative break-down of \bullet NO by superoxide (Figure 5-17 B). Furthermore, both aortic *Vcam1* and *Tnfa* gene

expression were significantly enhanced upon ATII infusion in *Glp1r ec^{-/-}* mice and not mitigated by additional liraglutide treatment (Figure 5-17 C-D).

Thus, in the absence of the endothelial GLP-1R, liraglutide no longer contains vascular inflammatory cell recruitment into hypertensive aorta, thereby increasing the vascular oxidative stress burden.

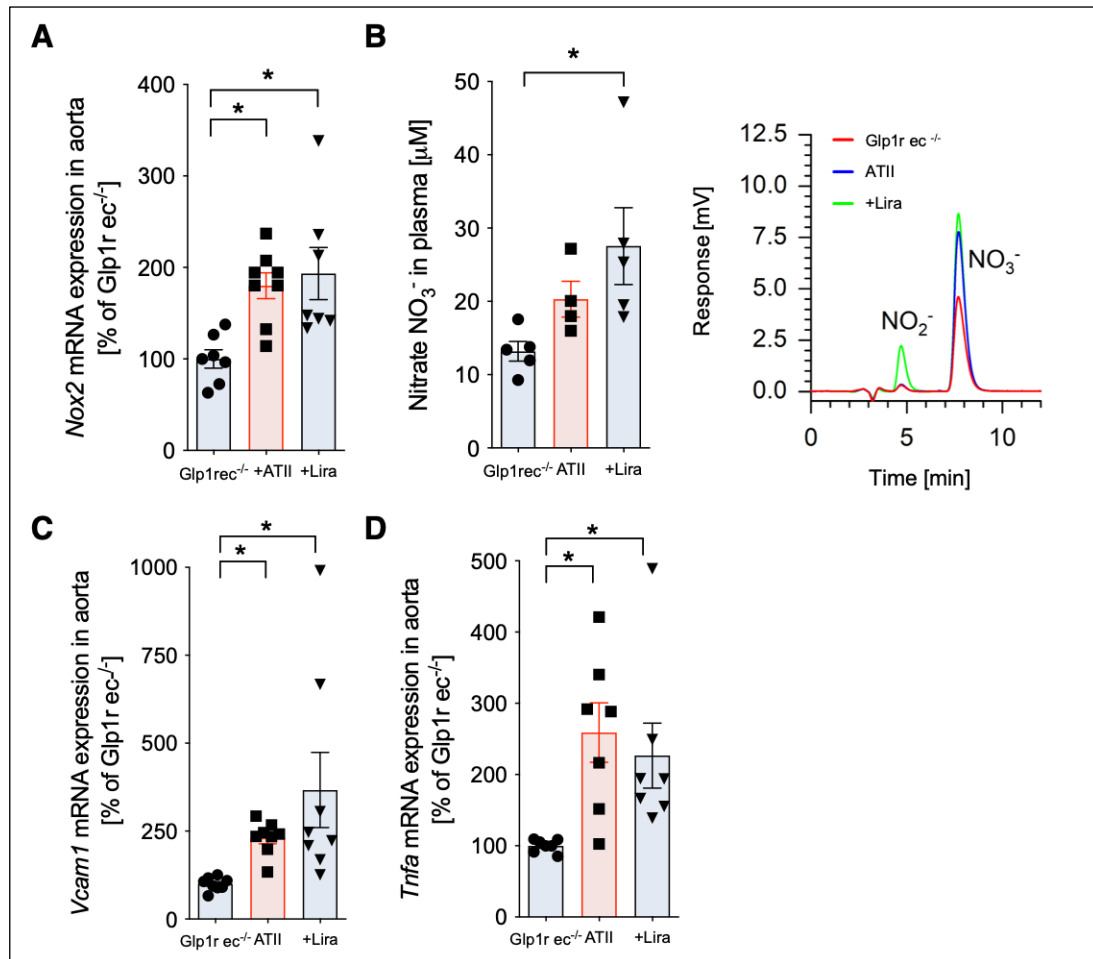


Figure 5-17: Liraglutide (Lira) fails to reduce angiotensin II (ATII)-induced oxidative stress and proinflammatory mediators in the vasculature of endothelial cell-specific *Glp1r* knockout mice (*Glp1r ec^{-/-}*) mice. (A) Gene expression level of *Nox2* (NADPH oxidase 2) was measured in aortic tissue by qRT-PCR (n=7-8). * P<0.05; 1-way ANOVA with Bonferroni's multiple comparison test. (B) Nitrate (NO₃⁻) concentrations in plasma were determined in an HPLC-based assay (n=4-5). A representative chromatogram is shown next to the quantification bar graph. * P<0.05; 1-way ANOVA with Bonferroni's multiple comparison test. Data generated in collaboration with Prof. Dr. Stefan Chlopicki / Jagiellonian Centre for Experimental Therapeutics (JCET) / Jagiellonian University, Krakow, Poland (conducted by Dr. Kamil Kus). (C) Gene expression level of *Vcam1* (vascular cell adhesion molecule 1) was measured in aortic tissue by qRT-PCR (n=8). * P<0.05; Kruskal-Wallis with Dunn's multiple comparisons test. (D) Gene expression level of *Tnfa* (tumor necrosis factor alpha) was measured in aortic tissue by qRT-PCR (n=7). * P<0.05; Kruskal-Wallis with Dunn's multiple comparisons test. Data are means ± SEM.

6 Discussion

This PhD thesis characterizes for the first time the cardio- and vasoprotective mechanisms of GLP-1 analog liraglutide in experimental arterial hypertension at the cellular level. Numerous (pre-clinical) studies have previously reported cardiovascular benefits of GLP-1 and GLP-1RAs including reductions in infarct size and blood pressure, or the improvement of left-ventricular function (see 1.6.3). Furthermore, CVOTs revealed a significant risk reduction of MACE such as myocardial infarction or stroke in T2DM patients with established CVD (see 1.6.2). However, the precise mechanisms and cellular origin of cardiovascular protection by liraglutide have remained incompletely understood. The results of this work demonstrate that selective activation of the endothelial but not the myeloid GLP-1R reduces the cardiovascular complications of arterial hypertension by controlling vascular recruitment of inflammatory leukocytes, major sources of vascular oxidative stress which cause eNOS uncoupling. Figure 6-1 gives a visual overview of the proposed mechanism for cardiovascular protection by liraglutide, which will be discussed in more detail in the following sections.

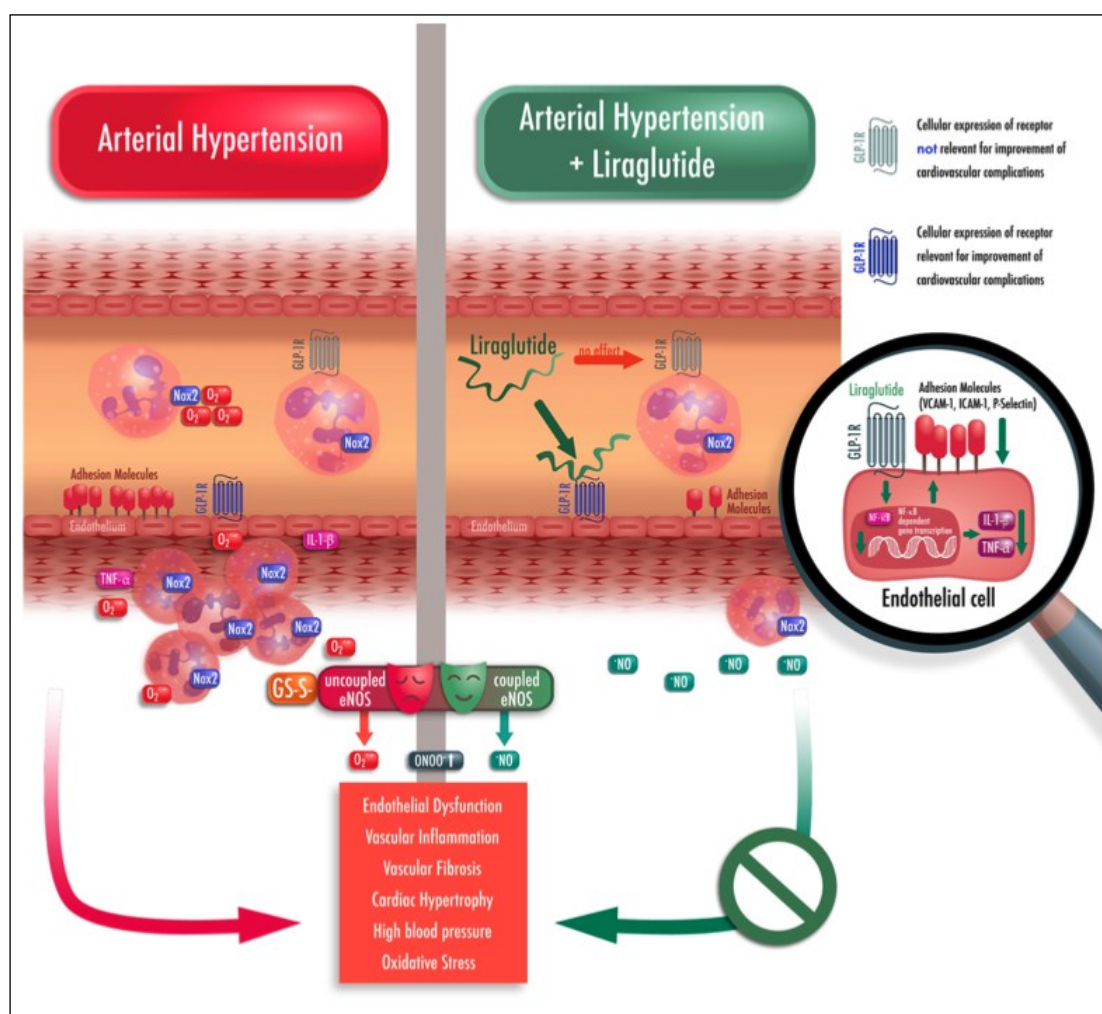


Figure 6-1: Schematic illustration of the proposed mechanism of cardiovascular protection by GLP-1RA liraglutide in experimental arterial hypertension. Arterial hypertension (*left side*) induces the expression of adhesion molecules (VCAM-1, ICAM-1, P-selectin) on the surface of endothelial cells, which causes activated immune cells (inflammatory monocytes and neutrophil granulocytes) to infiltrate into the vascular wall, resulting in enhanced vascular inflammation and oxidative stress. Under prolonged oxidative stress conditions, endothelial eNOS thiols get S-glutathionylated (eNOS-SSG), which uncouples the enzyme, switching it from eNOS to superoxide ($\text{O}_2^{\bullet-}$) production. Reduced eNO bioavailability causes impaired endothelium-mediated vasorelaxation (endothelial dysfunction), leading to vascular remodeling, fibrosis, and finally high blood pressure. The activation of the endothelial GLP-1R by liraglutide (*right side*) counteracts an NF- κ B-mediated inflammatory cascade in the hypertensive endothelium, reducing vascular inflammatory cell infiltration. Thus, NADPH oxidase 2 (Nox2)-derived oxidative stress from inflammatory cells is strongly decreased, thereby keeping eNOS in its coupled state. Hence, eNO bioavailability is restored and vascular integrity preserved. On the contrary, the GLP-1R on myeloid cells does not mediate cardiovascular protection by liraglutide in experimental arterial hypertension and is thus dispensable for GLP-1RA's antioxidative and anti-inflammatory actions. Taken from ³⁰³ with permission. © 2019 Wolters Kluwer Health.

6.1 GLP-1RA liraglutide controls cardiovascular function in experimental arterial hypertension through anti-inflammatory and antioxidative actions

This study provides significant new insight into the cardiovascular protective mechanism by GLP-1RA liraglutide in experimental arterial hypertension. With the use of several *ex vivo* and *in vivo* approaches, it was shown that eNOS uncoupling was prevented by the antioxidative and anti-inflammatory action of liraglutide in the vasculature and heart (Figure 5-4–5-7) of ATII-infused mice, which was crucial for its cardiovascular benefits. The endothelial $\bullet\text{NO}$ synthase is a redox-sensitive enzyme, which possesses several enzyme-specific regulatory pathways determining the activity of the enzyme (see 1.4.1). S-glutathionylation of eNOS is considered a “redox master switch” because it controls the production of $\bullet\text{NO}$ over superoxide¹⁷⁵. Triggered by oxidative stress conditions, an uncoupled eNOS in the hypertensive endothelium not only abolishes the formation of vasodilatory $\bullet\text{NO}$ but constitutes an important ROS source itself. Liraglutide treatment in ATII-infused C57BL/6J mice prevented eNOS glutathionylation and suspended eNOS-derived L-NAME-sensitive superoxide formation in the endothelial layer (Figure 5-9) as well as reduced cardiac ADMA levels (Figure 5-5). Thus, liraglutide avoided uncoupling of eNOS in arterial hypertension, which markedly improved aortic $\bullet\text{NO}$ levels (Figure 5-9). The maintained $\bullet\text{NO}$ bioavailability was responsible for the preserved endothelium-mediated vasorelaxation, prevention of vascular remodeling and fibrosis (Figure 5-2), and contributed to reduced SBP levels (Figure 5-1).

As mentioned, the cascade of eNOS uncoupling is initiated by excess production of superoxide ($\text{O}_2^{\bullet-}$), yet in turn, fuels further vascular oxidative stress because of eNOS-derived $\text{O}_2^{\bullet-}$ formation. Moreover, superoxide reacts readily with $\bullet\text{NO}$ to form peroxynitrite (ONOO^-), which not only further consumes $\bullet\text{NO}$ but uncouples eNOS itself. Besides, ONOO^- is a highly potent oxidant that easily modifies other cellular structures such as lipids or nucleic acids, which can ultimately lead to cell death (see 1.4.3). Thus, superoxide functions as a “kindling radical”, whose initial formation triggers the formation of additional ROS (and RONS), initiating a vicious cycle of ROS-induced ROS-formation (“bonfire” hypothesis)^{136,176}. Consequently, the identification and elimination of the source of superoxide is an important target for combating oxidative stress-induced CVD. A multitude of studies has shown that NADPH oxidase-derived $\text{O}_2^{\bullet-}$ is a major source of vascular oxidative stress in ATII-dependent arterial hypertension^{74,75,174,402,403}. Yet, the relevance of the different Nox isoforms as well as their cell-specific action activated by ATII is still not fully elucidated⁷⁷. Previous studies have proposed an implication of Nox1 in the pathology of ATII-induced arterial hypertension, mainly attributed to its detrimental role in VSMC from large arteries. For example, ATII-induced SBP levels and aortic hypertrophy were worsened in transgenic mice overexpressing *Nox1* in smooth muscle cells¹⁶² and transfection of VSMCs with an

adenovirus expressing antisense *Nox1* mRNA inhibited ATII-induced superoxide production¹⁶¹. Similarly in the present study, NADPH oxidase was found to be the main contributor to ATII-induced vascular oxidative stress, subsequently targeted by liraglutide. In respiratory burst of whole blood and membranous fraction of heart, NADPH-oxidase activity was increased by ATII but strongly diminished upon liraglutide treatment (Figure 5-4). However, Nox2-derived oxidative stress was found to be one of the major targets for the antioxidative actions of liraglutide. In the aorta of ATII-infused B6 mice, increased superoxide levels were paralleled by upregulated *Nox2* gene expression and Nox2 immunostaining, both of which were strongly mitigated with liraglutide treatment (Figure 5-6).

Even though immune cells are known to be a main source of Nox2¹⁴⁵, the importance of the phagocytic vs. the vascular NADPH oxidase 2 in arterial hypertension, and in CVD in general, is to date still debated. In a study from 2011, Wenzel et al. were able to attribute a causative role for Nox2, Agtr1 (ATII receptor type 1)-competent inflammatory monocytes in mediating oxidative stress, vascular dysfunction, and high blood pressure in ATII-induced arterial hypertension²⁰⁹. Mice with a selective ablation of LysM⁺ monocytes and macrophages displayed a significantly reduced hypertensive response to ATII, which could be reestablished by reconstitution of depleted mice with proinflammatory CD11b⁺Gr-1⁺ monocytes. However, aside from the role of the myeloid cells, ATII-induced arterial hypertension has also been associated with the infiltration of Nox2-expressing T lymphocytes^{213,404}. Besides Nox2-containing inflammatory cells, this Nox isoform has also been shown to be expressed in several other cell types involved in blood regulation, including microglia, cardiomyocytes, fibroblasts, and endothelial cells, even though at much lower levels than in phagocytes^{159,405,406}. Indeed, increases in Nox2 endothelial levels were demonstrated to significantly worsen ATII-dependent arterial hypertension, vascular remodeling, and endothelial dysfunction¹⁶⁵. In 2017, Sag et al. aimed to dissect the contribution of the myelomonocytic vs. endothelial Nox2 for blood regulation using endothelial (Cdh5-CreERT-Nox2KO)- and myeloid (LysM-Cre-Nox2KO)-specific *Nox2* knockout mice. They proposed myeloid cell Nox2 to regulate basal blood pressure levels, whereas endothelial cell Nox2 modulates ATII-induced hypertension⁴⁰⁷. Cdh5-CreERT-Nox2KO mice showed unaltered basal aortic •NO and blood pressure levels but exhibited reduced blood pressure levels upon ATII-treatment compared to their floxed-control mice. In contrast, LysM-Cre-Nox2KO mice had lower basal blood pressure compared to floxed-controls, simultaneous to higher eNOS-derived aortic •NO levels. The blood pressure increased upon ATII infusion, however, was comparable to controls, indicating that LysM-Cre-Nox2KO mice are not protected from ATII-induced hypertension. The authors explain this discrepancy to the study of Wenzel et al. with LysM⁺ cell ablation *before* ATII infusion in the latter study. However, even though they claim Nox2 in myeloid cells not to modulate ATII-

dependent hypertension, they admit that the vasculature is the site of action of myelomonocytic cells with a disrupted Nox2 and that this effect might be increased in inflammatory conditions⁴⁰⁷. Within this study, with the use of complementary methods like intravital microscopy, immunohistochemical, and flow cytometric analyses, the main source of vascular oxidative stress in arterial hypertension – modulated by liraglutide – was identified as the one from Nox2-bearing phagocytes, consistent with the findings from Wenzel et al.. Leukocyte rolling at the vascular wall was increased upon ATII infusion, together with an enhanced vascular mRNA expression of adhesion molecules *Vcam1*, *Icam1*, and *Selp* (Figure 5-8), facilitating the recruitment of inflammatory cells to the vessel wall. Furthermore, ATII infusion induced aortic Mac-2 and cardiac F4/80 expression (Figure 5-5 and 5-7). A flow cytometric-based immune cell phenotyping identified the accumulated cells as Ly6G⁻Ly6C⁺ inflammatory monocytes and Ly6G⁺Ly6C⁺ neutrophils (Figure 5-7). All of the mentioned parameters were strongly attenuated with liraglutide treatment, suggesting that the antioxidative action of liraglutide can be attributed to an anti-inflammatory effect in ATII-induced arterial hypertension by limiting the infiltration of phagocytic cells into the vasculature.

As a signature enzyme of inflammatory cells, it was also comprehensible that liraglutide strongly reduced an ATII-induced upregulation of iNOS/*Nos2* mRNA expression in aorta (Figure 5-6). Together with their endogenous Nox2 activity, inflammatory cells are a main source of toxic nitro-oxidative stress (see 1.4.3). Indeed, iNOS-derived peroxynitrite generation from LysM⁺ monocytes has been previously shown to be responsible for eNOS uncoupling and endothelial dysfunction in an ATII model of arterial hypertension²¹¹. Liraglutide strongly abolished nitro-oxidative stress caused by ATII, as revealed by reduced 3-NT protein levels in cardiac tissue (Figure 5-5) and normalized plasma nitrate levels (Figure 5-6). Even though EPR revealed lowered •NO levels with ATII (Figure 5-9), this measurement mainly reflects eNOS activity, as the •NO-EPR measurement was conducted after Ca-ionophore incubation known to stimulate eNOS (see 4.2.11)^{342,408}. This finding is thus in line with an uncoupled eNOS, no longer producing •NO (but O₂^{•-}). Furthermore, despite a weak trend of increase, there was no significant overall change in eNOS protein expression (Figure 5-6). Hence, the increase in nitrate by ATII can be explained by an induction of iNOS-derived •NO and Nox2 activation. Liraglutide treatment significantly reduced the inflammatory burden reflected by lowered aortic Nox2 and *Nos2* gene expression and consequently mitigated plasma nitrate levels.

Furthermore, the data presented here suggest that the contained vascular recruitment of inflammatory monocytes and neutrophils by liraglutide is caused by a downregulated NF-κB-mediated inflammatory cascade in arterial hypertension. ATII is known, mainly via its AT₁R, to activate NF-κB, which promotes vascular inflammation by upregulation of cytokine and adhesion protein expression^{72,73,388,409}. For example, in the rodent vasculature, ATII was

shown to induce VCAM-1 expression in both endothelial and smooth muscle cells through NF- κ B transcriptional mechanisms^{386,410}. Within this study, liraglutide was able to contain the ATII-activated upregulation of NF- κ B, which led to reduced cytokine (TNF- α , IL-1 β)-mediated gene expression of adhesion molecules (VCAM-1, ICAM-1, P-selectin) (Figure 5-8).

Ventricular cardiomyocytes do not express the GLP-1R and the cardioprotective effects of liraglutide persists in mice with a genetic deletion in the atrial cardiomyocyte GLP-1R (*Glp1r^{CM-/-}*) (see 1.6.3), both indicating that cardiac-independent/indirect actions of GLP-1RAs may constitute for their cardioprotective actions²⁸¹. It is therefore plausible to suggest that the reduced cardiac hypertrophy observed within this study is not due to direct effects of liraglutide on cardiomyocytes but rather due to the normalized \bullet NO levels and antihypertensive effect of liraglutide described here. Indeed, improvements of oxidative stress, inflammation, dysregulation of eNOS, and peroxynitrite by liraglutide were also found in cardiac tissue (Figure 5-4 and 5-5). Another potential mechanism for the blood pressure lowering effect of liraglutide was proposed by Kim et al.. In their study, liraglutide treatment in ATII-infused male C57/BL6 mice was shown to promote atrial natriuretic peptide (ANP) release via activation of the GLP-1R on atrial cardiomyocytes⁴¹¹. ANP is well known for its renal and cardiovascular actions, causing increased glomerular filtration, inhibited renal sodium and water reabsorption as well as systemic vasodilation due to cGMP-mediated smooth muscle relaxation^{412,413}. Yet, treatment with liraglutide does not consistently increase ANP levels in T2DM patients^{414,415} despite reproducible antihypertensive actions in this population^{416,417}, justifying the involvement of an additional vascular mechanism presented herein. Nevertheless, albeit endothelial dysfunction adds to increased systemic vascular resistance and thus to the development of hypertension⁴¹⁸, blood pressure regulation is complex and involves multiple organ systems. Hence, it cannot be excluded that mechanisms additional to an improved endothelial function and normalized \bullet NO bioavailability contribute to the antihypertensive actions of liraglutide, e.g., renal^{419,420} or neurogenic actions^{421,422}. Sympathetic hyperactivity is well known to be associated with both the development and maintenance of arterial hypertension^{423,424}. In this regard, lateral cerebroventricular injection of liraglutide was shown to activate central GLP-1R signaling in brainstem catecholamine neurons of spontaneous hypertensive rats (SHRs), which counteracted hypertension by suppression of sympathetic nerve activity⁴²². As ATII is a known stimulator of the SNS^{425,426} and GLP-1RA are able to pass the blood brain barrier⁴²⁷, this mechanism might also be of relevance for peripherally administered liraglutide in the present study. Furthermore, even though the here presented magnitude of blood pressure lowering is in line with previous studies⁴¹¹, the antihypertensive effect of liraglutide seems to be higher in mice compared to humans, in which reductions of 2 to 4 mmHg are reported²⁴⁶. The latter represents a limitation of this study regarding translation to clinical data³⁰³.

Based on the experiments conducted in C57BL/6J mice within this study and considering the mentioned literature, the following mechanism of cardiovascular protection by liraglutide in arterial hypertension is proposed: liraglutide treatment in ATII-induced arterial hypertension downregulates vascular NF- κ B, which strongly abolished the chemoattraction and infiltration of inflammatory cells (in particular Ly6G⁻Ly6C⁺ inflammatory monocytes and Ly6G⁺Ly6C⁺ neutrophils) into the vascular wall. All of this leads to reduced vascular oxidative stress in liraglutide-treated mice, finally preventing eNOS uncoupling, restoring •NO bioavailability, and maintaining cardiovascular integrity/function (Figure 6-1).

It is to emphasize, that this study demonstrated cardiovascular benefits for the antidiabetic agent liraglutide in a non-diabetic model of CVD. The lower rates of cardiovascular events in the LEADER trial were, however, revealed in T2DM patients at high risk or with established CVD. Hence, the suggested anti-atherogenic actions for cardiovascular protection in the LEADER trial (see 1.6.2) cannot directly be translated into a non-diabetic model. Yet, there are several indications that the mechanism of cardiovascular protection cannot (solely) be explained by improved glycemic control. After 36 months of the LEADER trial, (i) glycated hemoglobin (HbA_{1c}) was only mildly reduced compared to control therapy (mean difference of -0.40 percentage points, Table 1-3) and (ii) the effect of glycemic control was comparable to other CVOTs for antidiabetic drugs such as insulin⁴²⁸, thiazolidinediones^{429,430}, and DPP-4Is⁴³¹⁻⁴³³ for which, however, adequate cardiovascular benefits were not found²⁶⁰. Conversely, a meta-analysis of four Intensive Glycemic Control Trials (IGCTs) demonstrated a risk reduction of MACE by 9 % (HR 0.91, 95 % CI 0.84–0.99) using combinations of 'classical' antidiabetics (sulfonylurea, metformin, thiazolidinedione, acarbose, glinide, and insulin), which was associated with a HbA_{1c} reduction of -0.88 %⁴³⁴. Newer antidiabetic medications lower the MACE risk in the same magnitude (by 8 %; HR 0.92, 95 % CI 0.87–0.96) yet achieve this result already with a HbA_{1c} reduction of -0.42 %ⁱⁱ, as revealed in a meta-analysis of five different GLP-1RAs, four DPP-4Is and three sodium-glucose cotransporter-2 inhibitors (SGLT-2Is, see 6.4)⁴³⁵. In general, the importance of glycemic control for reducing microvascular disease (such as diabetic retino- or nephropathy) is nowadays recognized, whereas it is less defined for the protection against macrovascular disease (i.e., myocardial infarction, stroke)⁴³⁶⁻⁴³⁸. Furthermore, even if the latter effect exists, it is agreed that it takes many years of treatment (> 10 years) to show it⁴³⁹. In the present study, GLP-1 analog liraglutide was confirmed to exert cardioprotective effects in a murine model of arterial hypertension without affecting blood glucose and insulin levels in plasma (Figure 5-3). Despite inducing moderate body weight loss, likely due to central GLP-1R

ⁱⁱ Even when the MACE risk reduction was extrapolated to an HbA_{1c} decrease equal to that obtained in IGCTs (-0.90 %), the calculated HR of 0.67 (95 % CI 0.49–0.93) was markedly lower compared to the one of IGCTs with 0.91, indicating that the same level of glycemic control correlates with a higher cardiovascular risk reduction in the newer antidiabetic drugs.

activation²³², an OGTT conducted in C57BL/6J mice revealed that liraglutide did not alter both glucose and insulin tolerance in hypertensive mice (Figure 5-3). Thus, liraglutide exerts cardiovascular effects in arterial hypertension beyond glycemic control. However, a limitation of the present study is the intervention duration of only one week, with the long-term treatment effects of liraglutide in an ATII model being also worthy to investigate in a subsequent study.

Another technical limitation of this study is the use of male mice only. The effect of sexual hormones on vascular function is known⁴⁴⁰, and increasing evidence points at a role of the female sex hormone 17 β -estradiol for the protection of premenopausal women from CVD⁴⁴¹. In experimental models of arterial hypertension, chronic ATII infusion was shown to increase blood pressure to a higher extent in adult male mice compared to adult females^{442,443}. Hence, it would be of interest to investigate how liraglutide impacts arterial hypertension in female mice and how this relates to vascular GLP-1R expression. However, the focus of the present study was not to study sex-specific differences of liraglutide in arterial hypertension. Nevertheless, this question is worth addressing in a following study.

6.2 Cardiovascular protection by liraglutide in experimental arterial hypertension depends on canonical GLP-1R signaling

Experiments in *Glp1r*^{-/-} mice revealed that the cardiovascular protective effects of liraglutide in arterial hypertension were abrogated in the absence of a functional canonical GLP-1R. Liraglutide failed to prevent ATII-induced cardiac as well as aortic oxidative stress and did not reduce inflammatory parameters in the vasculature of hypertensive *Glp1r*^{-/-} mice. Consequently, liraglutide did not improve an endothelial dysfunction caused by ATII (Figure 5-10) in this mouse strain. Interestingly, *Glp1r*^{-/-} mice already showed a deteriorated basal endothelium-dependent vasodilation compared to B6 mice, indicating that the endogenous GLP-1R causally contributes to vascular integrity. Furthermore, several parameters were not only no longer attenuated by liraglutide but even worsened (cardiac Nox-activity as well as *Nos2* gene expression by trend and aortic *Nox2* and *Tnfa* gene expression significantly). The reason for these observations remains unclear and it can only be speculated that GLP-1RA liraglutide – in the absence of its main receptor – may exert adverse effects through (other) low-affinity targets. Collectively, these findings strongly suggest the cardiovascular protective mechanism of liraglutide to be dependent on canonical GLP-1R signaling.

The ongoing question of whether GLP-1 and GLP-1RAs exert their salutary actions dependently or independently of the canonical GLP-1R is a result of studies showing GLP-1 actions in tissue with low or yet to be demonstrated endogenous GLP-1R expression^{444,445}, as well as reports on GLP-1 effects through mechanisms insensitive to exendin(9-39), a

known GLP-1R antagonist⁴⁴⁶. Some of these actions can be explained by GLP-1 metabolites whose beneficiary effects are partially overlapping but also partially distinct from those of known GLP-1R-dependent effects²⁸¹. Their mode of action has not been revealed yet but suggested to involve mitochondrial pathways (see 1.6.3) or non-receptor-mediated effects on adenylate cyclase²⁴⁶. Furthermore, the possibility of a second, still unknown GLP-1 receptor has been raised^{246,281}. Liraglutide is a GLP-1RA whose structural modification with a C-16 fatty acid was designed to protect from DPP-4 degradation, owing to reversible binding to albumin and/or direct steric hindrance (see 1.6.2)^{232,248}. Therefore, liraglutide is thought to exert its salutary actions dependent on the GLP-1R. However, liraglutide, as a "true" GLP-1 homologue, shares 97 % structural homology with native GLP-1, including the N-terminal His-Ala sequence, the recognition site of DPP-4 (Figure 1-13)^{232,248}. Indeed, liraglutide was shown to be degraded by DPP-4 and NEP *in vivo* and *in vitro*, even though at much slower rates, and this route contributes to its elimination²⁴⁷. Therefore, within the present study, a potential contribution of GLP-1 metabolites to the observed effects in C57/BL6 mice, independent of the canonical GLP-1R, cannot be fully excluded and represents a limitation of the study³⁰³. In contrast, exenatide (exendin-4), discovered from Glia monster venom, shares only 53 % structural homology with native GLP-1 and bears a changed His-Gly N-terminal, making it truly resistant to degradation by DPP-4²³². Yet, unexpectedly, some GLP-1R-independent cardioprotective activity has been also demonstrated for exendin-4²⁸². Hence, the cardiovascular mechanisms of GLP-1RAs and GLP-1-derived metabolites are complex and future studies are needed to unravel their particular actions on distinct receptors and intracellular pathways in more detail²⁸¹.

Nevertheless, the revoked key effects in *Glp1r*^{-/-} mice presented within this study clearly indicate the necessity of GLP-1R activity for cardiovascular protection in arterial hypertension.

6.3 The GLP-1R on endothelial cells mediates cardiovascular protection in experimental arterial hypertension

Interestingly, studies in *Glp1r my^{-/-}* and *Glp1r ec^{-/-}* mice showed that the cardiovascular benefits of liraglutide in arterial hypertension persisted in the absence of the myeloid GLP-1R, whereas they were abolished without a functional endothelial GLP-1R.

The results in *Glp1r my^{-/-}* mice excluded that the GLP-1R on myeloid cells is needed to confer the anti-inflammatory and antioxidative actions of liraglutide, which were shown to be essential for its protective mechanism in the ATII model. Even with the GLP-1R missing on LysM⁺ cells, liraglutide still potently prevented infiltration of Ly6G⁻Ly6C⁺ inflammatory monocytes and Ly6G⁺Ly6C⁺ neutrophils into the aorta of *Glp1r my^{-/-}* mice (Figure 5-13), cells that had been previously identified to cause Nox2-derived vascular oxidative stress and eNOS uncoupling in arterial hypertension. Accordingly, treatment with liraglutide persisted to protect from an ATII-caused endothelial dysfunction, vascular fibrosis, and cardiac hypertrophy in *Glp1r my^{-/-}* mice (Figure 5-12). This finding was at first surprising as an inflammatory target of liraglutide was expected, considering that the reduction of MACE reported in the LEADER trial has been associated with anti-atherosclerotic and anti-inflammatory mechanisms, actions that have been corroborated in numerous pre-clinical studies, for liraglutide and GLP-1RAs in general (see 1.6.2. and 1.6.3). Furthermore, Nox2-competent LysM⁺ inflammatory cells were shown to be causal for vascular oxidative stress and inflammation in arterial hypertension, so that a direct effect of liraglutide on those cells seemed likely.

To date, GLP-1R expression on circulating immune cells from mice has been limited to very low levels in lymphocytes from thymus, spleen, and bone marrow from C57BL/6J mice (see 1.6.3). Furthermore, reports on GLP-1R presence in monocytes and macrophages *in vivo* are inconsistent^{447,448}. In this study, the GLP-1R was shown for the first time to be successfully downregulated in bone marrow-derived macrophages (BMDMs) from *Glp1r my^{-/-}* mice (Figure 5-11). Yet, depletion of the myeloid GLP-1R did not translate into altered beneficiary cardiovascular functions of liraglutide in arterial hypertension. In contrast, the GLP-1R is abundantly expressed in duodenal Brunner glands and intestinal intraepithelial lymphocytes (IELs), and GLP-1RA treatment, in both cases, has been associated with improved gut barrier (see 1.6.3). This 'gut defense mechanism' has been proposed to contribute to the systemic anti-inflammatory actions of liraglutide²⁹⁰, as disturbances of intestinal integrity and intestinal inflammation are nowadays recognized to be involved in the genesis of arterial hypertension and CVD in general^{449,450}. However, the physiological importance of both axes remains to be explored, and, so far, direct activation of the GLP-1R on gut immune cells has not been shown to translate into reductions of cardiac or vascular

inflammation^{237,238}. In a recent study from He et al., mice lacking natural IELs in the small intestine (integrin $\beta 7^{-/-}$) were protected from HFSSD (diet high in fat, sugar, and sodium)-induced hypertension and atherosclerosis due to increased GLP-1 levels. The authors were able to credit this finding to the high GLP-1R expression of IELs that enables them to capture secreted GLP-1 from neighboring L-cells, thus acting as critical gatekeepers of dietary metabolism and GLP-1 bioavailability⁴⁵¹. This finding is hence in line with the present results that do not suggest a direct involvement of the GLP-1R on inflammatory/immune cells for the systemic and vascular anti-inflammatory effects of GLP-1RAs, but rather points to an indirect GLP-1R activation on other tissues²⁸¹.

The results in *Glp1r ec^{-/-}* mice, on the contrary, indicated that the GLP-1R on endothelial cells is indispensable for cardiovascular protection of liraglutide in arterial hypertension. With a disrupted GLP-1R on endothelial cells, liraglutide failed to normalize an ATII-mediated induction of the inflammatory parameters TNF- α and VCAM-1 in the hypertensive vasculature, which accordingly led to an infiltration of Nox2-bearing Ly6G⁻Ly6C⁺ inflammatory monocytes and Ly6G⁺Ly6C⁺ neutrophils into the aorta of *Glp1r ec^{-/-}* mice, even under liraglutide treatment (Figure 5-16 and 5-17). (Although both immune cell subtypes were non-significantly reduced with liraglutide treatment in ATII-infused *Glp1r ec^{-/-}* mice, the effect was more prominent on neutrophils, which were significantly increased compared to control and worsened by trend relative to ATII). Indicative of an enhanced oxidative breakdown of •NO, peroxynitrite/nitrate plasma levels were increased in liraglutide-treated hypertensive *Glp1r ec^{-/-}* mice (Figure 5-17). Consequently, liraglutide did not protect from an ATII-induced endothelial dysfunction, did not restore normal blood pressure levels and no longer attenuated vascular fibrosis and cardiac hypertrophy in hypertensive *Glp1r ec^{-/-}* mice (Figure 5-15). Thus, these results suggest that an endothelial target of liraglutide in arterial hypertension indirectly mediates its anti-inflammatory actions.

The findings presented here are in line with a large number of *in vitro* studies that reported direct protective effects of native GLP-1 and GLP-1RAs on cultured endothelial cells (mainly HUVECs and HAECs), through anti-inflammatory and antioxidative mechanisms (see 1.6.3). Furthermore, several *in vivo* studies in atherosclerosis models using *Apoe^{-/-}* mice support the mechanism presented here. In a study from Arakawa et al., DPP-4 resistant GLP-1RA exendin-4 reduced Mac-2⁺ monocyte adhesion to the aortic endothelium of *Apoe^{-/-}* mice, which led to a reduction in atherosclerotic lesion size. These effects were accompanied by reduced aortic levels of *Vcam1* and *Icam1* mRNA transcripts²⁹¹. Moreover, Gaspari et al. reported liraglutide treatment to improve endothelium-dependent vasorelaxation of isolated aortic segments from 12 weeks HFD-(high-fat diet)-fed *Apoe^{-/-}* mice, which was abrogated by co-infusion with exendin(9-39), indicating a GLP-1R dependent effect. The inhibited endothelial dysfunction by liraglutide in atherosclerotic *Apoe^{-/-}* mice correlated with increased

eNOS expression and reduced ICAM-1 expression in the aortic endothelium⁴⁵². The endothelial mechanism presented here may also help explain the reports of improved LV function and blood flow with GLP-1RA treatment (see 1.6.3), considering that liraglutide possesses no direct vasodilatory effect in isolated aortic preparations *ex vivo*⁴¹¹ and that the cardiomyocyte GLP-1R is limited to the cardiac atrium²⁷⁷. However, blood pressure levels trended a bit lower upon liraglutide treatment in hypertensive *Glp1r ec^{-/-}* mice (Figure 5-15), indicating that – at least in rodents – the ANP mechanism presented above (see 6.1) might also play a role³⁰³.

To date, little is known about the GLP-1R expression in specific vascular beds, with continuous debates about its existence within major blood vessels (see 1.6.3). Despite unambiguously highlighting the importance of the endothelial GLP-1R for cardiovascular protection in arterial hypertension by employing a (pan-) EC knockout model, a limitation of the present study is that *Glp1r* knockdown was only verified in CD31⁺CD102⁺ primary lung endothelial cells (Figure 5-14). Even though the used MLEC preparation protocol (see 4.2.3) has been demonstrated to result in ≥ 85 % pure (micro-) endothelial cells³²⁷, *Glp1r* knockdown was not examined in macro- vs. microvascular endothelial cells from different vascular sites, e.g., aorta, heart, kidney, or resistance vessels, while the latter are known to be primarily involved in blood pressure regulation⁴⁵³. Thus, further scrutiny in subsequent analyses is needed to delineate the GLP-1R expression from different vascular beds. Furthermore, the *Tg(Cdh5-cre)7Mlia* line was used in this study to generate *Glp1r ec^{-/-}* mice (see 3.10), for which *Cdh5* Cre-mediated recombination can also occur in cells of the hematopoietic lineage (see 4.1.1). An optimized system could have been utilized with *Cdh-Cre/ERT2ⁱⁱⁱ*-driven endothelial Cre recombinase, in which Cre-activity can not only be spatially but also temporally controlled, through active induction by tamoxifen administration^{310,312}. There are currently two available *Cdh-Cre/ERT2* mouse lines, for which none non-endothelial recombinase activity has been detected (Mouse Genome Informatics ID: 5705396 & 3848982)^{312,454}. However, *Glp1r* expression on CD45⁺ cells of *Glp1r ec^{-/-}* mice was tested (Figure 5-14) and found to be present, thus excluding a non-endothelial specific *Glp1r* knockdown in this study. Even in the case of a non-specific/residual Cre activity in hematopoietic cells, the results in *Glp1r my^{-/-}* mice demonstrated that (at least) the GLP-1R on myeloid cells is anyway dispensable for cardiovascular protection of liraglutide in ATII-induced arterial hypertension.

Thus, to summarize, the results from *Glp1r^{-/-}*, *Glp1r my^{-/-}* and *Glp1r ec^{-/-}* mice presented within this study support the conclusion that GLP-1RA liraglutide controls the cardiovascular

ⁱⁱⁱ Cre-ERT: Tamoxifen (T) inducible Cre recombinase due to fusion of the Cre protein to a mutated ligand-binding domain of the human estrogen receptor (ER)

complications of ATII-induced arterial hypertension selectively through the endothelial cell GLP-1R (Figure 6-1).

A general limitation of this study is that tissue-specific *Glp1r* expression and/or *Glp1r* knockdown was only detected on mRNA and not complementary verified on protein level. Even though several commercially available GLP-1R exist (14 search results for 'GLP-1R' using the filters "primary antibodies", "unconjugated", "mouse" reactivity, "Western Blotting" and "Immunohistochemistry" application at <https://www.antibodies-online.com>, accessed on 2021-01-27), many of the antibodies used to detect GLP-1R protein in published paper have proven to be non-specific afterwards²⁹⁵. Thus, it is generally accepted to provide *Glp1r* mRNA data for the understanding of GLP-1 action, and it has been performed like that by other (reputable) researchers in the GLP-1 field^{278,279,411}. Yet, the lack of specificity and sensitivity of GLP-1R antibodies^{313,448} has certainly hampered the identification of precise GLP-1R tissue and cell type localization, as well as complicated the interpretation of already published results due to the use of non-validated GLP-1R antibodies. The reasons for the unspecificity and insensitivity of GLP-1R antibodies are various but can be ascribed, among others, to the insufficient material for immunization due to the in general low expression of GPCRs *in vivo*, destruction of the epitopes upon removal of the cellular membrane, and cross-reactivities between GPCRs owing to their highly conserved transmembrane regions³¹⁴. From the available GLP-1 antibodies, only two (non-fluorescent) monoclonal antibodies have been validated for detection specificity of the mouse/rat and human/primate GLP-1R (Mab 7F38 and 3F52, respectively; source: [Iowa Developmental Studies Hybridoma Bank](#))^{238,276,455}. Nevertheless, albeit showing improved specificity, these new antibodies are still associated with vulnerability to experimental pitfalls due to low-level expression of class B GPCRs²⁸⁰. Thus, the highest care for optimal technical conditions and the use of multiple complementary techniques including the analysis of appropriate negative (e.g., from *Glp1r*^{-/-} mice) and positive tissues (e.g., pancreatic islets) are necessary^{238,280}. The mentioned Mab 3F38 antibody was recently acquired in our laboratory and appropriate staining conditions are currently attempted to be established.

6.4 Relevance of the results and implication for further use/strategy of GLP-1 therapeutics

The significance of CVOTs demonstrating cardiovascular benefits for diabetic patients by treatment with long-acting GLP-1RAs (see 1.6.2) is highlighted by a paradigm shift in the recommendations for glucose-lowering treatment. The 2019 ESC (European Society of Cardiology) guidelines on diabetes include, for the first time, that T2DM patients at high/very high risk for or with established CVD should be either treated with an SGLT-2i^{iv} or GLP-1RA monotherapy in case of drug naivety or, if they are already on metformin medication, an SGLT-2i or GLP-1RA with proven CVD benefit (liraglutide, semaglutide, or dulaglutide; Table 1-3) should be added ⁴⁵⁸. Similar recommendations have been issued by the ADA/EASD (American Diabetes Association and European Association for the Study of Diabetes) who endorses the use of liraglutide as the preferential GLP-1RA in T2DM patients with established atherosclerotic CVD ⁴⁵⁹. Given that diabetics are frequently high-risk cardiovascular patients, with CVD the predominant cause of their premature death ⁴⁶⁰, the clinical dispensation of GLP-1RAs is likely to strongly increase within the next years. Moreover, the latest results from the REWIND trial for the GLP-1RA dulaglutide indicate a cardiovascular benefit in T2DM patients even without established CVD ²⁶⁹, albeit the longer duration of this trial suggests that reduction of cardiovascular events may need more time to establish in patients without/low risk for CVD ²⁶².

Considering the highly conserved actions of GLP-1 among rodents, primates, and humans (see 1.6.1), the findings presented within this study might contribute to a better molecular understanding of the clinical evidence linking GLP-1RAs to the reduction of MACE ³⁰³. The here presented vascular/endothelial mechanism helps to explain the blood pressure lowering

^{iv} Sodium-glucose cotransporter-2 inhibitors (SGLT-2Is) are another class of relatively new antidiabetic drugs, exerting their glucose-lowering actions by blocking the SGLT-2-mediated glucose reabsorption in the proximal tubules of the kidney (456. Thrasher, J. Pharmacologic Management of Type 2 Diabetes Mellitus: Available Therapies. *Am J Cardiol* **120**, S4-S16 (2017).).

CVOTs have been also conducted for this drug class and they reported reduced MACE in diabetic patients with known CVD in a similar magnitude as GLP-1RAs (262. Zelniker et al. Comparison of the Effects of Glucagon-Like Peptide Receptor Agonists and Sodium-Glucose Cotransporter 2 Inhibitors for Prevention of Major Adverse Cardiovascular and Renal Outcomes in Type 2 Diabetes Mellitus. *Circulation* **139**, 2022-2031 (2019).), e.g., EMPA-REG OUTCOME=Empagliflozin Cardiovascular Outcome Event Trial in Type 2 Diabetes Mellitus Patients: HR 0.86, 95 % CI 0.74–0.99, P<0.001 for noninferiority, P=0.05 for superiority (457. Zinman et al. & Investigators, E.-R.O. Empagliflozin, Cardiovascular Outcomes, and Mortality in Type 2 Diabetes. *N Engl J Med* **373**, 2117-2128 (2015).). Similar to GLP-1RAs, it is incompletely understood how they exert a cardiovascular benefit, independently of glucose control. However, in contrast to GLP-1RAs, for which reduction of MACE has been linked to a decrease in atherosclerosis-driven events, SGLT-2Is seem to have a more pronounced effect on the prevention of heart-failure-related events (261. Marx, N. & Libby, P. Cardiovascular Benefits of GLP-1 Receptor Agonism: Is Inflammation a Key? *JACC Basic Transl Sci* **3**, 858-860 (2018), 263. Khan et al. Glucagon-Like Peptide 1 Receptor Agonists and Heart Failure: The Need for Further Evidence Generation and Practice Guidelines Optimization. *Circulation* **142**, 1205-1218 (2020).). A detailed comparison of SGLT-2Is with GLP-1RAs is beyond the scope of this thesis.

and anti-atherogenic of GLP-1RAs including liraglutide, which have been suggested to be causal for their cardiovascular benefit independently of glycemic control. In fact, arterial hypertension, which has been used as a model in the present study, is a main risk factor for the development of atherosclerosis and RAAS activation majorly adds to the formation of vascular complications in diabetic patients ^{461,462}.

Furthermore, the current findings may also have implications for the potential therapeutic use of GLP-1RAs independently of T2DM. For example, it is conceivable that they will be employed for the prevention and/or treatment of cardio- and neurovascular diseases associated with low-grade inflammation and oxidative stress. Indeed, GLP-1RAs were demonstrated to exert neuroprotective properties in the setting of acute ischemic stroke by reducing the infarct volume and improving functional outcome ⁴⁶³⁻⁴⁶⁵. These effects have been associated with increased blood flow and/or vascular anti-inflammatory actions of GLP-1RAs, for which the here presented mechanisms could give mechanistic explanations.

In addition, GLP-1RAs showed salutary actions in the treatment of NASH (Nonalcoholic steatohepatitis). NASH is a severe form of nonalcoholic fatty liver disease and is characterized by liver inflammation, steatosis (accumulation of fat), hepatocyte apoptosis, and fibrosis ⁴⁶⁶. In two clinical trials, treatment with either liraglutide or semaglutide led to significantly NASH resolution and no worsening of liver fibrosis compared to placebo treatment ^{467,468}. Aside from weight loss and reduced hepatocyte lipid synthesis, these salutary actions have been attributed to antioxidative, anti-inflammatory, and anti-fibrotic actions of GLP-1RAs. As shown in a murine model of NASH, proinflammatory monocytes/macrophages are crucially implicated in the formation of hepatic oxidative stress and fibrosis ⁴⁶⁹. Since hepatocytes do not seem to express a functional GLP-1R ^{238,448}, the herein demonstrated mechanism of a vascular target for GLP-1R activation, to reduce inflammation and improve endothelial function, could help explain this knowledge gap. Intriguingly, despite having a significantly increased risk for liver cirrhosis and hepatocellular carcinoma, the primary cause of death in NASH patients is CVD, independent of other metabolic comorbidities ⁴⁷⁰. Here, too, GLP-1RAs could possibly prove useful in the secondary prevention of cardiovascular complications, as demonstrated in a pre-clinical model of NASH ⁴⁶⁹.

Nevertheless, to understand the cardioprotective properties of GLP-1 and GLP-1RAs in its entirety, future investigations need to more intensively aim at delineating GLP-1R-dependent from GLP-1R-independent pathways and to differentiate direct (primary) from indirect (secondary) actions of GLP-1 in multiple organs, both of which has been impeded in the past by the lack of sensitive and specific antibodies (see 6.3). It is possible that, besides the here demonstrated endothelial GLP-1R-mediated effect, other cell types might additionally contribute to cardiovascular protection exerted by GLP-1RAs, e.g., VSMCs or platelets.

Indeed, for both of them, a beneficial effect of GLP-1RAs has been described and suggested to involve antiproliferative³⁰¹ and anti-aggregatory⁴⁷¹ effects, respectively. Yet, their GLP-1R expression has been incompletely characterized²⁸¹. The use of new validated antibodies and recent technological advances (such as RNAscope® in situ hybridization⁴⁷²) promise considerably progress of GLP-1R localization, especially in tissue with low GLP-1R abundance, and will likely allow further mechanistic interpretations²³⁸.

Additionally, further scrutiny is needed to define the drug-specific differences within the class of GLP-1RAs. The results of CVOTs from various GLP-1RAs suggest that one cannot necessarily speak of a generalized drug-class effect, as lixisenatide and exenatide did not show improved cardiovascular outcome but only neutral effects on the reduction of MACE ($P > 0.05$ for superiority, Table 1-3). Leaving aside the trial-specific differences, this might suggest that only GLP-1RAs based on the structure of endogenous GLP-1 exert an additional cardiovascular benefit. It is yet to be revealed whether these differences can be ascribed to their particular molecular structure, which, in the case of 'true' GLP-1 homologues, possibly allows the formation of bioactive GLP-1 metabolites, whereas GLP-1RA lixisenatide and exenatide share structural similarity to exendin-4, excluding the proteolytic cleavage by DPP-4 (see 6.2). Yet, on the other hand, albiglutide, dulaglutide, semaglutide, and liraglutide are long-acting GLP-1RAs and their administration correlates with a prolonged duration of GLP-1R activation, whereas lixisenatide has only a mean half-life of 3 hours (short-acting GLP-1RA, Table 1-3)^{280,281}. For a better understanding of these drug-specific differences, future (pre- and) clinical studies should therefore include head-to-head comparisons of structurally distinct GLP-1RAs²⁴⁶.

Taken together, this study provides significant new evidence that the anti-hypertensive and anti-atherosclerotic actions of long-acting GLP-1RA liraglutide revealed in CVOTs may be credited to their activation of the vascular/endothelial GLP-1R and contributes to a molecular understanding for the therapeutic benefit of GLP-1RAs in non-diabetic patients at cardiovascular risk.

7 Summary

Glucagon-like peptide-1 (GLP-1) receptor agonists (GLP-1RAs) are a relatively new class of drugs that are approved for the treatment of type 2 diabetes mellitus. Additional to their blood glucose-lowering effect, cardiovascular outcome trials (CVOTs) revealed that long-acting GLP-1RAs including liraglutide significantly reduce the risk for cardiovascular events in diabetic patients with established cardiovascular disease. Until today, the mechanism and cellular components underlying the cardiovascular benefit of liraglutide, as well as its dependence on glycemic control, have only been incompletely understood.

Herein it was shown that liraglutide confers vaso- and cardioprotective effects in a non-diabetic murine model of Angiotensin II (ATII)-induced arterial hypertension, which rely on the antioxidant and anti-inflammatory actions of liraglutide and require the endothelial GLP-1 receptor (GLP-1R).

Using C57BL/6J wild-type mice, it was demonstrated that liraglutide effectively protects from an ATII-mediated increase in blood pressure, cardiac hypertrophy, vascular fibrosis, and endothelial dysfunction – independently of alterations in insulin and glucose metabolism. Mechanistic analyses revealed that liraglutide downregulates central pro-inflammatory mediators such as nuclear factor- κ B (NF- κ B) and adhesion molecules (VCAM-1, *vascular cell adhesion molecule 1*; ICAM-1, *intercellular adhesion molecule 1*; P-selectin) in the vessel wall, which reduces the vascular adhesion and infiltration of inflammatory monocytes and neutrophils. As they are a main source of reactive oxygen species (ROS) with their endogenous NADPH oxidase 2 (Nox2) activity, liraglutide significantly attenuated ATII-induced vascular oxidative stress. As a result, S-glutathionylation and thus endothelial nitric oxide synthase (eNOS) uncoupling was prevented, which in turn markedly improved \bullet NO bioavailability and explains liraglutide's protection against hypertension-associated damage. Importantly, all of these effects were dependent on the canonical GLP-1R, as liraglutide no longer protected global *Glp1r* knockout mice (*Glp1r*^{-/-}) from vascular oxidative stress, inflammation, and endothelial dysfunction.

As another central aspect of this study, it was shown that liraglutide alleviates cardiovascular complications of arterial hypertension through selective action on the endothelial GLP-1R. With the use of myelomonocytic (*Glp1r* *my*^{-/-}) and endothelial cell (*Glp1r* *ec*^{-/-})-specific *Glp1r* knockout mice, it was demonstrated that the beneficial effects of liraglutide persist upon GLP-1R deletion in inflammatory cells but are abrogated in the absence of the endothelial GLP-1R. Hence, this work revealed that the immunomodulating effect of liraglutide is not mediated by direct activation of the GLP-1R on myeloid cells but indirectly through stimulation of the endothelial GLP-1R.

The here presented vascular/endothelial mechanism contributes to a better molecular understanding of the cardioprotective effects of long-acting GLP-1RAs like liraglutide reported in clinical trials and provides first evidence for a potential use of GLP-1RAs in the prevention and treatment of (cardio-)vascular disease beyond diabetes mellitus that are characterized by oxidative stress and inflammation.

8 Zusammenfassung

Glucagon-like peptide-1 (GLP-1)-Rezeptor-Agonisten (GLP-1RAs) sind eine relativ neue Wirkstoffklasse, die zur Behandlung des Typ 2 Diabetes Mellitus zugelassen ist. Neben blutzuckersenkenden Wirkungen wurden für einige langwirkende Vertreter, darunter Liraglutid, in kardiovaskulären Endpunktstudien nachgewiesen, dass sie die Anzahl an kardiovaskulären Todesfällen in Typ 2-Diabetikern mit erhöhtem Risiko für Herz-Kreislauf-Erkrankungen signifikant reduzieren. Bislang waren der Mechanismus und die zellulären Komponenten, die dem kardiovaskulären Nutzen von Liraglutid zugrunde liegen, sowie dessen Abhängigkeit von glykämischen Effekten, nur unvollständig geklärt.

Mit der vorliegenden Arbeit konnte gezeigt werden, dass Liraglutid vaso- und kardioprotektive Eigenschaften im nicht-diabetischen Mausmodell der Angiotensin II (ATII)-induzierten arteriellen Hypertonie besitzt, die auf antioxidativen und anti-inflammatorischen Effekten von Liraglutid basieren und durch den endothelialen GLP-1 Rezeptor (GLP-1R) vermittelt werden.

Hierzu wurde zunächst in C57BL/6J Wildtyp Mäusen gezeigt, dass Liraglutid wirkungsvoll vor einem ATII-vermittelten Blutdruckanstieg, kardialer Hypertrophie, vaskulärer Fibrose sowie endothelialer Dysfunktion schützt – unabhängig von Änderungen im Insulin und Glukose Metabolismus. Mechanistische Untersuchungen ergaben, dass Liraglutid zentral proinflammatorische Mediatoren wie den Nuclear factor- κ B (NF- κ B) und Adhäsionsmoleküle (VCAM-1, *vascular cell adhesion molecule 1*; ICAM-1, *intercellular adhesion molecule 1*; P-selectin) in der Gefäßwand herunterreguliert, und damit insbesondere die vaskuläre Adhäsion und Infiltration inflammatorischer Monozyten und Neutrophile reduziert. Da diese mit ihrer endogenen NADPH Oxidase 2 (Nox2) Aktivität eine Hauptquelle für reaktive Sauerstoffspezies sind, verringerte Liraglutid somit deutlich den ATII-induzierten vaskulären oxidativen Stress. Dies wiederum wirkte einer S-Glutathionylierung und somit Entkopplung der endothelialen Stickstoffmonoxid-Synthase (eNOS) entgegen, was in einer merklichen Verbesserung der •NO Bioverfügbarkeit resultierte und den Schutz von Liraglutid vor oben erwähnten Hypertonie-assoziierten Schäden erklärt. Wichtigerweise waren all diese Effekte abhängig vom kanonischen GLP-1R, da Liraglutid Mäuse mit globalem *Glp1r* knockout

(*Glp1r^{-/-}*) nicht mehr vor vaskulärem oxidativem Stress, Inflammation und endothelialer Dysfunktion schützt.

Als weiterer zentraler Aspekt dieser Studie wurde gezeigt, dass Liraglutid kardiovaskuläre Komplikationen der arteriellen Hypertonie speziell über den GLP-1R auf Endothelzellen verringert. Mit Hilfe von myelomonocytyären (*Glp1r my^{-/-}*) und Endothelzell-spezifischen (*Glp1r ec^{-/-}*) *Glp1r* knockout Mäusen konnte nachgewiesen werden, dass der protektive Effekt von Liraglutid weiterbesteht, wenn der GLP-1R auf inflammatorischen Zellen deletiert ist, jedoch bei Fehlen des endothelialen GLP-1R aufgehoben ist. Somit konnte im Rahmen dieser Arbeit zum ersten Mal gezeigt werden, dass der immun-modulierende Effekt von Liraglutid nicht direkt durch Aktivierung des GLP-1R auf myeloiden Zellen vermittelt wird, sondern indirekt durch Stimulation des endothelialen GLP-1R.

Der hier vorgestellte vaskuläre/endotheliale Mechanismus trägt dazu bei, die klinische Evidenz des kardiovaskulären Nutzens von langwirkenden GLP-1RAs wie Liraglutid auf molekularer Ebene besser zu verstehen und liefert erste Indizien für einen etwaigen Einsatz von GLP-1RAs in der Prävention und Behandlung (kardio-)vaskulärer Krankheiten jenseits des Diabetes Mellitus, die durch oxidativen Stress und Inflammation gekennzeichnet sind.

9 Literature

1. WorldHealthOrganization. The top 10 causes of death <https://www.who.int/news-room/fact-sheets/detail/the-top-10-causes-of-death>. (2020; accessed on 2021-03-05).
2. Diseases, G.B.D. & Injuries, C. Global burden of 369 diseases and injuries in 204 countries and territories, 1990-2019: a systematic analysis for the Global Burden of Disease Study 2019. *Lancet* **396**, 1204-1222 (2020).
3. Roth, G.A., *et al.* Global Burden of Cardiovascular Diseases and Risk Factors, 1990-2019: Update From the GBD 2019 Study. *J Am Coll Cardiol* **76**, 2982-3021 (2020).
4. Collaborators, G.B.D.R.F. Global burden of 87 risk factors in 204 countries and territories, 1990-2019: a systematic analysis for the Global Burden of Disease Study 2019. *Lancet* **396**, 1223-1249 (2020).
5. Libby, P., *et al.* Atherosclerosis. *Nat Rev Dis Primers* **5**, 56 (2019).
6. Collaboration, N.C.D.R.F. Worldwide trends in diabetes since 1980: a pooled analysis of 751 population-based studies with 4.4 million participants. *Lancet* **387**, 1513-1530 (2016).
7. International Diabetes Federation. IDF Diabetes Atlas, 9th Edition <https://www.diabetesatlas.org/en/resources/>. (2019).
8. Saeedi, P., *et al.* Global and regional diabetes prevalence estimates for 2019 and projections for 2030 and 2045: Results from the International Diabetes Federation Diabetes Atlas, 9(th) edition. *Diabetes Res Clin Pract* **157**, 107843 (2019).
9. Leon, B.M. & Maddox, T.M. Diabetes and cardiovascular disease: Epidemiology, biological mechanisms, treatment recommendations and future research. *World J Diabetes* **6**, 1246-1258 (2015).
10. Drucker, D.J. The Cardiovascular Biology of Glucagon-like Peptide-1. *Cell Metab* **24**, 15-30 (2016).
11. Mutschler, E., Schaible, H.G. & Vaupel, P. Anatomie, Physiologie, Pathophysiologie des Menschen. *Wissenschaftliche Verlagsgesellschaft mbH Stuttgart* **6**(2007).
12. Ross, R. Atherosclerosis--an inflammatory disease. *N Engl J Med* **340**, 115-126 (1999).
13. Maiolino, G., *et al.* The role of oxidized low-density lipoproteins in atherosclerosis: the myths and the facts. *Mediators Inflamm* **2013**, 714653 (2013).
14. Ross, R. & Glomset, J.A. Atherosclerosis and the arterial smooth muscle cell: Proliferation of smooth muscle is a key event in the genesis of the lesions of atherosclerosis. *Science* **180**, 1332-1339 (1973).
15. Ross, R. & Glomset, J.A. The pathogenesis of atherosclerosis (first of two parts). *N Engl J Med* **295**, 369-377 (1976).
16. Ross, R. & Glomset, J.A. The pathogenesis of atherosclerosis (second of two parts). *N Engl J Med* **295**, 420-425 (1976).
17. Bonetti, P.O., Lerman, L.O. & Lerman, A. Endothelial dysfunction: a marker of atherosclerotic risk. *Arterioscler Thromb Vasc Biol* **23**, 168-175 (2003).
18. Anderson, T.J. Assessment and treatment of endothelial dysfunction in humans. *J Am Coll Cardiol* **34**, 631-638 (1999).
19. Forouzanfar, M.H., *et al.* Global Burden of Hypertension and Systolic Blood Pressure of at Least 110 to 115 mm Hg, 1990-2015. *JAMA* **317**, 165-182 (2017).
20. Mills, K.T., *et al.* Global Disparities of Hypertension Prevalence and Control: A Systematic Analysis of Population-Based Studies From 90 Countries. *Circulation* **134**, 441-450 (2016).
21. Sharma, G., Ram, C.V.S. & Yang, E. Comparison of the ACC/AHA and ESC/ESH Hypertension Guidelines <https://www.acc.org/latest-in-cardiology/articles/2019/11/25/08/57/comparison-of-the-acc-aha-and-esc-esh-hypertension-guidelines>. (2019; accessed on 2021-03-07).
22. Williams, B., *et al.* 2018 ESC/ESH Guidelines for the management of arterial hypertension. *Eur Heart J* **39**, 3021-3104 (2018).

23. Whelton, P.K., et al. 2017 ACC/AHA/AAPA/ABC/ACPM/AGS/APhA/ASH/ASPC/NMA/PCNA Guideline for the Prevention, Detection, Evaluation, and Management of High Blood Pressure in Adults: A Report of the American College of Cardiology/American Heart Association Task Force on Clinical Practice Guidelines. *Hypertension* **71**, e13-e115 (2018).
24. Bakris, G., Ali, W. & Parati, G. ACC/AHA Versus ESC/ESH on Hypertension Guidelines: JACC Guideline Comparison. *J Am Coll Cardiol* **73**, 3018-3026 (2019).
25. Group, S.R., et al. A Randomized Trial of Intensive versus Standard Blood-Pressure Control. *N Engl J Med* **373**, 2103-2116 (2015).
26. Lewington, S., et al. Age-specific relevance of usual blood pressure to vascular mortality: a meta-analysis of individual data for one million adults in 61 prospective studies. *Lancet* **360**, 1903-1913 (2002).
27. Hall, M.E. & Hall, J.E. Pathogenesis of Hypertension, published in Hypertension: A Companion to Braunwald's Heart Disease 3rd edn (eds Bakris, G. L. & Sorrentino, M.) Elsevier, 33-51 (2018).
28. Oparil, S., et al. Hypertension. *Nat Rev Dis Primers* **4**, 18014 (2018).
29. Munzel, T., et al. Environmental Noise and the Cardiovascular System. *J Am Coll Cardiol* **71**, 688-697 (2018).
30. Munzel, T., et al. Reduction of environmental pollutants for prevention of cardiovascular disease: it's time to act. *Eur Heart J* (2020).
31. Lavoie, J.L. & Sigmund, C.D. Minireview: overview of the renin-angiotensin system--an endocrine and paracrine system. *Endocrinology* **144**, 2179-2183 (2003).
32. Wu, C.H., et al. Renin-Angiotensin System and Cardiovascular Functions. *Arterioscler Thromb Vasc Biol* **38**, e108-e116 (2018).
33. Fleming, I. Signaling by the angiotensin-converting enzyme. *Circ Res* **98**, 887-896 (2006).
34. Ng, K.K. & Vane, J.R. The conversion of angiotensin I to angiotensin II in vivo. *Naunyn Schmiedebergs Arch Exp Pathol Pharmacol* **259**, 188-189 (1968).
35. Carey, R.M., Wang, Z.Q. & Siragy, H.M. Role of the angiotensin type 2 receptor in the regulation of blood pressure and renal function. *Hypertension* **35**, 155-163 (2000).
36. Ito, M., et al. Regulation of blood pressure by the type 1A angiotensin II receptor gene. *Proc Natl Acad Sci U S A* **92**, 3521-3525 (1995).
37. Hall, J.E. Control of sodium excretion by angiotensin II: intrarenal mechanisms and blood pressure regulation. *Am J Physiol* **250**, R960-972 (1986).
38. Cogan, M.G. Angiotensin II: a powerful controller of sodium transport in the early proximal tubule. *Hypertension* **15**, 451-458 (1990).
39. Horisberger, J.D. & Rossier, B.C. Aldosterone regulation of gene transcription leading to control of ion transport. *Hypertension* **19**, 221-227 (1992).
40. Harris, H.W., Jr., Strange, K. & Zeidel, M.L. Current understanding of the cellular biology and molecular structure of the antidiuretic hormone-stimulated water transport pathway. *J Clin Invest* **88**, 1-8 (1991).
41. Mukoyama, M., et al. Expression cloning of type 2 angiotensin II receptor reveals a unique class of seven-transmembrane receptors. *J Biol Chem* **268**, 24539-24542 (1993).
42. Steckelings, U.M., Kaschina, E. & Unger, T. The AT2 receptor--a matter of love and hate. *Peptides* **26**, 1401-1409 (2005).
43. Donoghue, M., et al. A novel angiotensin-converting enzyme-related carboxypeptidase (ACE2) converts angiotensin I to angiotensin 1-9. *Circ Res* **87**, E1-9 (2000).
44. Santos, R.A., et al. Angiotensin-(1-7) is an endogenous ligand for the G protein-coupled receptor Mas. *Proc Natl Acad Sci U S A* **100**, 8258-8263 (2003).
45. Atkinson, A.B. & Robertson, J.I. Captopril in the treatment of clinical hypertension and cardiac failure. *Lancet* **2**, 836-839 (1979).
46. Stock, P., Liefeldt, L., Paul, M. & Ganten, D. Local renin-angiotensin systems in cardiovascular tissues: localization and functional role. *Cardiology* **86 Suppl 1**, 2-8 (1995).

47. van Kats, J.P., *et al.* Angiotensin production by the heart: a quantitative study in pigs with the use of radiolabeled angiotensin infusions. *Circulation* **98**, 73-81 (1998).
48. Hilgers, K.F., *et al.* Renin uptake by the endothelium mediates vascular angiotensin formation. *Hypertension* **38**, 243-248 (2001).
49. Moulik, S., Speth, R.C., Turner, B.B. & Rowe, B.P. Angiotensin II receptor subtype distribution in the rabbit brain. *Exp Brain Res* **142**, 275-283 (2002).
50. Kobori, H., Prieto-Carrasquero, M.C., Ozawa, Y. & Navar, L.G. AT1 receptor mediated augmentation of intrarenal angiotensinogen in angiotensin II-dependent hypertension. *Hypertension* **43**, 1126-1132 (2004).
51. Iwai, N., Inagami, T., Ohmichi, N. & Kinoshita, M. Renin is expressed in rat macrophage/monocyte cells. *Hypertension* **27**, 399-403 (1996).
52. Karlsson, C., *et al.* Human adipose tissue expresses angiotensinogen and enzymes required for its conversion to angiotensin II. *J Clin Endocrinol Metab* **83**, 3925-3929 (1998).
53. Thomas, W.G. & Sernia, C. The immunocytochemical localization of angiotensinogen in the rat ovary. *Cell Tissue Res* **261**, 367-373 (1990).
54. Benigni, A., Cassis, P. & Remuzzi, G. Angiotensin II revisited: new roles in inflammation, immunology and aging. *EMBO Mol Med* **2**, 247-257 (2010).
55. de Gasparo, M., Catt, K.J., Inagami, T., Wright, J.W. & Unger, T. International union of pharmacology. XXIII. The angiotensin II receptors. *Pharmacol Rev* **52**, 415-472 (2000).
56. Iwai, N. & Inagami, T. Identification of two subtypes in the rat type I angiotensin II receptor. *FEBS Lett* **298**, 257-260 (1992).
57. Sandberg, K., Ji, H., Clark, A.J., Shapira, H. & Catt, K.J. Cloning and expression of a novel angiotensin II receptor subtype. *J Biol Chem* **267**, 9455-9458 (1992).
58. Burson, J.M., Aguilera, G., Gross, K.W. & Sigmund, C.D. Differential expression of angiotensin receptor 1A and 1B in mouse. *Am J Physiol* **267**, E260-267 (1994).
59. Oliverio, M.I. & Coffman, T.M. Angiotensin II Receptor Physiology Using Gene Targeting. *News Physiol Sci* **15**, 171-175 (2000).
60. Daugherty, A., Rateri, D.L., Lu, H., Inagami, T. & Cassis, L.A. Hypercholesterolemia stimulates angiotensin peptide synthesis and contributes to atherosclerosis through the AT1A receptor. *Circulation* **110**, 3849-3857 (2004).
61. Rateri, D.L., *et al.* Endothelial cell-specific deficiency of Ang II type 1a receptors attenuates Ang II-induced ascending aortic aneurysms in LDL receptor^{-/-} mice. *Circ Res* **108**, 574-581 (2011).
62. Vukelic, S. & Griendling, K.K. Angiotensin II, from vasoconstrictor to growth factor: a paradigm shift. *Circ Res* **114**, 754-757 (2014).
63. Te Riet, L., van Esch, J.H., Roks, A.J., van den Meiracker, A.H. & Danser, A.H. Hypertension: renin-angiotensin-aldosterone system alterations. *Circ Res* **116**, 960-975 (2015).
64. Alexander, R.W., Brock, T.A., Gimbrone, M.A., Jr. & Rittenhouse, S.E. Angiotensin increases inositol trisphosphate and calcium in vascular smooth muscle. *Hypertension* **7**, 447-451 (1985).
65. Griendling, K.K., *et al.* Sustained diacylglycerol formation from inositol phospholipids in angiotensin II-stimulated vascular smooth muscle cells. *J Biol Chem* **261**, 5901-5906 (1986).
66. Balla, T., Varnai, P., Tian, Y. & Smith, R.D. Signaling events activated by angiotensin II receptors: what goes before and after the calcium signals. *Endocr Res* **24**, 335-344 (1998).
67. Kawai, T., *et al.* AT1 receptor signaling pathways in the cardiovascular system. *Pharmacol Res* **125**, 4-13 (2017).
68. Schmidt-Ott, K.M., Kagiya, S. & Phillips, M.I. The multiple actions of angiotensin II in atherosclerosis. *Regul Pept* **93**, 65-77 (2000).
69. Rodriguez-Vita, J., *et al.* Angiotensin II activates the Smad pathway in vascular smooth muscle cells by a transforming growth factor-beta-independent mechanism. *Circulation* **111**, 2509-2517 (2005).

70. Marrero, M.B., *et al.* Role of Janus kinase/signal transducer and activator of transcription and mitogen-activated protein kinase cascades in angiotensin II- and platelet-derived growth factor-induced vascular smooth muscle cell proliferation. *J Biol Chem* **272**, 24684-24690 (1997).
71. Marrero, M.B., *et al.* Direct stimulation of Jak/STAT pathway by the angiotensin II AT1 receptor. *Nature* **375**, 247-250 (1995).
72. Ruiz-Ortega, M., *et al.* Angiotensin II activates nuclear transcription factor kappaB through AT(1) and AT(2) in vascular smooth muscle cells: molecular mechanisms. *Circ Res* **86**, 1266-1272 (2000).
73. Brasier, A.R., Jamaluddin, M., Han, Y., Patterson, C. & Runge, M.S. Angiotensin II induces gene transcription through cell-type-dependent effects on the nuclear factor-kappaB (NF-kappaB) transcription factor. *Mol Cell Biochem* **212**, 155-169 (2000).
74. Griendling, K.K., Minieri, C.A., Ollerenshaw, J.D. & Alexander, R.W. Angiotensin II stimulates NADH and NADPH oxidase activity in cultured vascular smooth muscle cells. *Circ Res* **74**, 1141-1148 (1994).
75. Rajagopalan, S., *et al.* Angiotensin II-mediated hypertension in the rat increases vascular superoxide production via membrane NADH/NADPH oxidase activation. Contribution to alterations of vasomotor tone. *J Clin Invest* **97**, 1916-1923 (1996).
76. Zhang, H., *et al.* Angiotensin II-induced superoxide anion generation in human vascular endothelial cells: role of membrane-bound NADH/NADPH-oxidases. *Cardiovasc Res* **44**, 215-222 (1999).
77. Nguyen Dinh Cat, A., Montezano, A.C., Burger, D. & Touyz, R.M. Angiotensin II, NADPH oxidase, and redox signaling in the vasculature. *Antioxid Redox Signal* **19**, 1110-1120 (2013).
78. Yayama, K., Hiyoshi, H., Imazu, D. & Okamoto, H. Angiotensin II stimulates endothelial NO synthase phosphorylation in thoracic aorta of mice with abdominal aortic banding via type 2 receptor. *Hypertension* **48**, 958-964 (2006).
79. Sandoo, A., van Zanten, J.J., Metsios, G.S., Carroll, D. & Kitas, G.D. The endothelium and its role in regulating vascular tone. *Open Cardiovasc Med J* **4**, 302-312 (2010).
80. Munzel, T., Sinning, C., Post, F., Warnholtz, A. & Schulz, E. Pathophysiology, diagnosis and prognostic implications of endothelial dysfunction. *Ann Med* **40**, 180-196 (2008).
81. Vane, J.R. & Botting, R.M. Secretory functions of the vascular endothelium. *J Physiol Pharmacol* **43**, 195-207 (1992).
82. Thomas, G.D. Neural control of the circulation. *Adv Physiol Educ* **35**, 28-32 (2011).
83. Auger, F.A., D'Orleans-Juste, P. & Germain, L. Adventitia contribution to vascular contraction: hints provided by tissue-engineered substitutes. *Cardiovasc Res* **75**, 669-678 (2007).
84. Bruno, R.M., *et al.* Sympathetic regulation of vascular function in health and disease. *Front Physiol* **3**, 284 (2012).
85. Gordan, R., Gwathmey, J.K. & Xie, L.H. Autonomic and endocrine control of cardiovascular function. *World J Cardiol* **7**, 204-214 (2015).
86. Rees, D.D., Palmer, R.M. & Moncada, S. Role of endothelium-derived nitric oxide in the regulation of blood pressure. *Proc Natl Acad Sci U S A* **86**, 3375-3378 (1989).
87. Vallance, P., Collier, J. & Moncada, S. Effects of endothelium-derived nitric oxide on peripheral arteriolar tone in man. *Lancet* **2**, 997-1000 (1989).
88. Furchgott, R.F. & Zawadzki, J.V. The obligatory role of endothelial cells in the relaxation of arterial smooth muscle by acetylcholine. *Nature* **288**, 373-376 (1980).
89. Palmer, R.M., Ferrige, A.G. & Moncada, S. Nitric oxide release accounts for the biological activity of endothelium-derived relaxing factor. *Nature* **327**, 524-526 (1987).
90. Ignarro, L.J., Buga, G.M., Wood, K.S., Byrns, R.E. & Chaudhuri, G. Endothelium-derived relaxing factor produced and released from artery and vein is nitric oxide. *Proc Natl Acad Sci U S A* **84**, 9265-9269 (1987).
91. Smith, O. Nobel Prize for NO research. *Nat Med* **4**, 1215 (1998).

92. Palmer, R.M., Ashton, D.S. & Moncada, S. Vascular endothelial cells synthesize nitric oxide from L-arginine. *Nature* **333**, 664-666 (1988).
93. Panza, J.A., Quyyumi, A.A., Brush, J.E., Jr. & Epstein, S.E. Abnormal endothelium-dependent vascular relaxation in patients with essential hypertension. *N Engl J Med* **323**, 22-27 (1990).
94. Panza, J.A., Casino, P.R., Kilcoyne, C.M. & Quyyumi, A.A. Role of endothelium-derived nitric oxide in the abnormal endothelium-dependent vascular relaxation of patients with essential hypertension. *Circulation* **87**, 1468-1474 (1993).
95. Garg, U.C. & Hassid, A. Nitric oxide-generating vasodilators and 8-bromo-cyclic guanosine monophosphate inhibit mitogenesis and proliferation of cultured rat vascular smooth muscle cells. *J Clin Invest* **83**, 1774-1777 (1989).
96. Sneddon, J.M. & Vane, J.R. Endothelium-derived relaxing factor reduces platelet adhesion to bovine endothelial cells. *Proc Natl Acad Sci U S A* **85**, 2800-2804 (1988).
97. Radomski, M.W., Vallance, P., Whitley, G., Foxwell, N. & Moncada, S. Platelet adhesion to human vascular endothelium is modulated by constitutive and cytokine induced nitric oxide. *Cardiovasc Res* **27**, 1380-1382 (1993).
98. Kubes, P., Suzuki, M. & Granger, D.N. Nitric oxide: an endogenous modulator of leukocyte adhesion. *Proc Natl Acad Sci U S A* **88**, 4651-4655 (1991).
99. De Caterina, R., *et al.* Nitric oxide decreases cytokine-induced endothelial activation. Nitric oxide selectively reduces endothelial expression of adhesion molecules and proinflammatory cytokines. *J Clin Invest* **96**, 60-68 (1995).
100. Hogg, N., Kalyanaraman, B., Joseph, J., Struck, A. & Parthasarathy, S. Inhibition of low-density lipoprotein oxidation by nitric oxide. Potential role in atherogenesis. *FEBS Lett* **334**, 170-174 (1993).
101. Forstermann, U., *et al.* Nitric oxide synthase isozymes. Characterization, purification, molecular cloning, and functions. *Hypertension* **23**, 1121-1131 (1994).
102. Forstermann, U. & Sessa, W.C. Nitric oxide synthases: regulation and function. *Eur Heart J* **33**, 829-837, 837a-837d (2012).
103. Fleming, I. Brain in the brawn: the neuronal nitric oxide synthase as a regulator of myogenic tone. *Circ Res* **93**, 586-588 (2003).
104. Kleinert, H., Pautz, A., Linker, K. & Schwarz, P.M. Regulation of the expression of inducible nitric oxide synthase. *Eur J Pharmacol* **500**, 255-266 (2004).
105. Steinert, J.R., Chernova, T. & Forsythe, I.D. Nitric oxide signaling in brain function, dysfunction, and dementia. *Neuroscientist* **16**, 435-452 (2010).
106. Nathan, C.F. & Hibbs, J.B., Jr. Role of nitric oxide synthesis in macrophage antimicrobial activity. *Curr Opin Immunol* **3**, 65-70 (1991).
107. MacMicking, J., Xie, Q.W. & Nathan, C. Nitric oxide and macrophage function. *Annu Rev Immunol* **15**, 323-350 (1997).
108. Pacher, P., Beckman, J.S. & Liaudet, L. Nitric oxide and peroxynitrite in health and disease. *Physiol Rev* **87**, 315-424 (2007).
109. Forstermann, U. & Munzel, T. Endothelial nitric oxide synthase in vascular disease: from marvel to menace. *Circulation* **113**, 1708-1714 (2006).
110. Fleming, I. & Busse, R. Signal transduction of eNOS activation. *Cardiovasc Res* **43**, 532-541 (1999).
111. Zhao, Y., Vanhoutte, P.M. & Leung, S.W. Vascular nitric oxide: Beyond eNOS. *J Pharmacol Sci* **129**, 83-94 (2015).
112. Attina, T.M., Oliver, J.J., Malatino, L.S. & Webb, D.J. Contribution of the M3 muscarinic receptors to the vasodilator response to acetylcholine in the human forearm vascular bed. *Br J Clin Pharmacol* **66**, 300-303 (2008).
113. Saternos, H.C., *et al.* Distribution and function of the muscarinic receptor subtypes in the cardiovascular system. *Physiol Genomics* **50**, 1-9 (2018).
114. Dimmeler, S., *et al.* Activation of nitric oxide synthase in endothelial cells by Akt-dependent phosphorylation. *Nature* **399**, 601-605 (1999).
115. Fleming, I., Fisslthaler, B., Dimmeler, S., Kemp, B.E. & Busse, R. Phosphorylation of Thr(495) regulates Ca(2+)/calmodulin-dependent endothelial nitric oxide synthase activity. *Circ Res* **88**, E68-75 (2001).

116. Daiber, A. & Ullrich, V. Stickstoffmonoxid, Superoxid und Peroxynitrit: Radikalchemie im Organismus. *Chemie in unserer Zeit*, 366-375 (2002).
117. Radi, R. Oxygen radicals, nitric oxide, and peroxynitrite: Redox pathways in molecular medicine. *Proc Natl Acad Sci U S A* **115**, 5839-5848 (2018).
118. Denninger, J.W. & Marletta, M.A. Guanylate cyclase and the .NO/cGMP signaling pathway. *Biochim Biophys Acta* **1411**, 334-350 (1999).
119. Munzel, T., *et al.* Physiology and pathophysiology of vascular signaling controlled by guanosine 3',5'-cyclic monophosphate-dependent protein kinase [corrected]. *Circulation* **108**, 2172-2183 (2003).
120. Oelze, M., *et al.* Vasodilator-stimulated phosphoprotein serine 239 phosphorylation as a sensitive monitor of defective nitric oxide/cGMP signaling and endothelial dysfunction. *Circ Res* **87**, 999-1005 (2000).
121. Tzoumas, N., Farrah, T.E., Dhaun, N. & Webb, D.J. Established and emerging therapeutic uses of PDE type 5 inhibitors in cardiovascular disease. *Br J Pharmacol* **177**, 5467-5488 (2020).
122. Munzel, T., Daiber, A. & Mulsch, A. Explaining the phenomenon of nitrate tolerance. *Circ Res* **97**, 618-628 (2005).
123. Ludmer, P.L., *et al.* Paradoxical vasoconstriction induced by acetylcholine in atherosclerotic coronary arteries. *N Engl J Med* **315**, 1046-1051 (1986).
124. Daiber, A., *et al.* Targeting vascular (endothelial) dysfunction. *Br J Pharmacol* **174**, 1591-1619 (2017).
125. Anderson, T.J., *et al.* Close relation of endothelial function in the human coronary and peripheral circulations. *J Am Coll Cardiol* **26**, 1235-1241 (1995).
126. Munzel, T., Gori, T., Bruno, R.M. & Taddei, S. Is oxidative stress a therapeutic target in cardiovascular disease? *Eur Heart J* **31**, 2741-2748 (2010).
127. Gryglewski, R.J., Palmer, R.M. & Moncada, S. Superoxide anion is involved in the breakdown of endothelium-derived vascular relaxing factor. *Nature* **320**, 454-456 (1986).
128. Ohara, Y., Peterson, T.E. & Harrison, D.G. Hypercholesterolemia increases endothelial superoxide anion production. *J Clin Invest* **91**, 2546-2551 (1993).
129. McIntyre, M., Bohr, D.F. & Dominiczak, A.F. Endothelial function in hypertension: the role of superoxide anion. *Hypertension* **34**, 539-545 (1999).
130. Bauersachs, J., *et al.* Endothelial dysfunction in chronic myocardial infarction despite increased vascular endothelial nitric oxide synthase and soluble guanylate cyclase expression: role of enhanced vascular superoxide production. *Circulation* **100**, 292-298 (1999).
131. Heitzer, T., Just, H. & Munzel, T. Antioxidant vitamin C improves endothelial dysfunction in chronic smokers. *Circulation* **94**, 6-9 (1996).
132. Taddei, S., Virdis, A., Ghiadoni, L., Magagna, A. & Salvetti, A. Vitamin C improves endothelium-dependent vasodilation by restoring nitric oxide activity in essential hypertension. *Circulation* **97**, 2222-2229 (1998).
133. Ting, H.H., *et al.* Vitamin C improves endothelium-dependent vasodilation in patients with non-insulin-dependent diabetes mellitus. *J Clin Invest* **97**, 22-28 (1996).
134. Heitzer, T., Schlinzig, T., Krohn, K., Meinertz, T. & Munzel, T. Endothelial dysfunction, oxidative stress, and risk of cardiovascular events in patients with coronary artery disease. *Circulation* **104**, 2673-2678 (2001).
135. Munzel, T.G., T. Endotheliale Dysfunktion: Ursachen und prognostische Bedeutung. *Kardiologie up2date* **5**(2009).
136. Daiber, A., *et al.* Vascular Redox Signaling, Redox Switches in Endothelial Nitric Oxide Synthase (eNOS Uncoupling), and Endothelial Dysfunction. *In: Laher I. (eds) Systems Biology of Free Radicals and Antioxidants. Springer, Berlin, Heidelberg*, pp. 1177-1211 (2014).
137. Martinez, M.C. & Andriantsitohaina, R. Reactive nitrogen species: molecular mechanisms and potential significance in health and disease. *Antioxid Redox Signal* **11**, 669-702 (2009).

138. Tullio, F., Angotti, C., Perrelli, M.G., Penna, C. & Pagliaro, P. Redox balance and cardioprotection. *Basic Res Cardiol* **108**, 392 (2013).
139. Ursini, F., Maiorino, M. & Forman, H.J. Redox homeostasis: The Golden Mean of healthy living. *Redox Biol* **8**, 205-215 (2016).
140. Sies, H. Oxidative stress: a concept in redox biology and medicine. *Redox Biol* **4**, 180-183 (2015).
141. Halliwell, B. Antioxidant defence mechanisms: from the beginning to the end (of the beginning). *Free Radic Res* **31**, 261-272 (1999).
142. Ischiropoulos, H. & Beckman, J.S. Oxidative stress and nitration in neurodegeneration: cause, effect, or association? *J Clin Invest* **111**, 163-169 (2003).
143. Steven, S., *et al.* Vascular Inflammation and Oxidative Stress: Major Triggers for Cardiovascular Disease. *Oxid Med Cell Longev* **2019**, 7092151 (2019).
144. Cai, H. & Harrison, D.G. Endothelial dysfunction in cardiovascular diseases: the role of oxidant stress. *Circ Res* **87**, 840-844 (2000).
145. Bedard, K. & Krause, K.H. The NOX family of ROS-generating NADPH oxidases: physiology and pathophysiology. *Physiol Rev* **87**, 245-313 (2007).
146. Babior, B.M., Kipnes, R.S. & Curnutte, J.T. Biological defense mechanisms. The production by leukocytes of superoxide, a potential bactericidal agent. *J Clin Invest* **52**, 741-744 (1973).
147. Segal, A.W. & Jones, O.T. Novel cytochrome b system in phagocytic vacuoles of human granulocytes. *Nature* **276**, 515-517 (1978).
148. Lassegue, B. & Griendling, K.K. NADPH oxidases: functions and pathologies in the vasculature. *Arterioscler Thromb Vasc Biol* **30**, 653-661 (2010).
149. Guzik, T.J., *et al.* Calcium-dependent NOX5 nicotinamide adenine dinucleotide phosphate oxidase contributes to vascular oxidative stress in human coronary artery disease. *J Am Coll Cardiol* **52**, 1803-1809 (2008).
150. Schulz, E. & Munzel, T. NOX5, a new "radical" player in human atherosclerosis? *J Am Coll Cardiol* **52**, 1810-1812 (2008).
151. Brandes, R.P., Weissmann, N. & Schroder, K. Nox family NADPH oxidases: Molecular mechanisms of activation. *Free Radic Biol Med* **76**, 208-226 (2014).
152. el Benna, J., Faust, L.P. & Babior, B.M. The phosphorylation of the respiratory burst oxidase component p47phox during neutrophil activation. Phosphorylation of sites recognized by protein kinase C and by proline-directed kinases. *J Biol Chem* **269**, 23431-23436 (1994).
153. Ago, T., Nunoi, H., Ito, T. & Sumimoto, H. Mechanism for phosphorylation-induced activation of the phagocyte NADPH oxidase protein p47(phox). Triple replacement of serines 303, 304, and 328 with aspartates disrupts the SH3 domain-mediated intramolecular interaction in p47(phox), thereby activating the oxidase. *J Biol Chem* **274**, 33644-33653 (1999).
154. Han, C.H., Freeman, J.L., Lee, T., Motalebi, S.A. & Lambeth, J.D. Regulation of the neutrophil respiratory burst oxidase. Identification of an activation domain in p67(phox). *J Biol Chem* **273**, 16663-16668 (1998).
155. Diekmann, D., Abo, A., Johnston, C., Segal, A.W. & Hall, A. Interaction of Rac with p67phox and regulation of phagocytic NADPH oxidase activity. *Science* **265**, 531-533 (1994).
156. Gorzalczany, Y., Sigal, N., Itan, M., Lotan, O. & Pick, E. Targeting of Rac1 to the phagocyte membrane is sufficient for the induction of NADPH oxidase assembly. *J Biol Chem* **275**, 40073-40081 (2000).
157. Serrander, L., *et al.* NOX4 activity is determined by mRNA levels and reveals a unique pattern of ROS generation. *Biochem J* **406**, 105-114 (2007).
158. Kawahara, T., Jackson, H.M., Smith, S.M., Simpson, P.D. & Lambeth, J.D. Nox5 forms a functional oligomer mediated by self-association of its dehydrogenase domain. *Biochemistry* **50**, 2013-2025 (2011).
159. Lassegue, B., San Martin, A. & Griendling, K.K. Biochemistry, physiology, and pathophysiology of NADPH oxidases in the cardiovascular system. *Circ Res* **110**, 1364-1390 (2012).

160. Schulz, E., Gori, T. & Munzel, T. Oxidative stress and endothelial dysfunction in hypertension. *Hypertens Res* **34**, 665-673 (2011).
161. Lassegue, B., *et al.* Novel gp91(phox) homologues in vascular smooth muscle cells : nox1 mediates angiotensin II-induced superoxide formation and redox-sensitive signaling pathways. *Circ Res* **88**, 888-894 (2001).
162. Dikalova, A., *et al.* Nox1 overexpression potentiates angiotensin II-induced hypertension and vascular smooth muscle hypertrophy in transgenic mice. *Circulation* **112**, 2668-2676 (2005).
163. Matsuno, K., *et al.* Nox1 is involved in angiotensin II-mediated hypertension: a study in Nox1-deficient mice. *Circulation* **112**, 2677-2685 (2005).
164. Bendall, J.K., Cave, A.C., Heymes, C., Gall, N. & Shah, A.M. Pivotal role of a gp91(phox)-containing NADPH oxidase in angiotensin II-induced cardiac hypertrophy in mice. *Circulation* **105**, 293-296 (2002).
165. Murdoch, C.E., *et al.* Role of endothelial Nox2 NADPH oxidase in angiotensin II-induced hypertension and vasomotor dysfunction. *Basic Res Cardiol* **106**, 527-538 (2011).
166. Dikalov, S.I., *et al.* Distinct roles of Nox1 and Nox4 in basal and angiotensin II-stimulated superoxide and hydrogen peroxide production. *Free Radic Biol Med* **45**, 1340-1351 (2008).
167. Montezano, A.C., *et al.* Nicotinamide adenine dinucleotide phosphate reduced oxidase 5 (Nox5) regulation by angiotensin II and endothelin-1 is mediated via calcium/calmodulin-dependent, rac-1-independent pathways in human endothelial cells. *Circ Res* **106**, 1363-1373 (2010).
168. Heitzer, T., Krohn, K., Albers, S. & Meinertz, T. Tetrahydrobiopterin improves endothelium-dependent vasodilation by increasing nitric oxide activity in patients with Type II diabetes mellitus. *Diabetologia* **43**, 1435-1438 (2000).
169. Stroes, E., *et al.* Tetrahydrobiopterin restores endothelial function in hypercholesterolemia. *J Clin Invest* **99**, 41-46 (1997).
170. Heitzer, T., *et al.* Tetrahydrobiopterin improves endothelium-dependent vasodilation in chronic smokers : evidence for a dysfunctional nitric oxide synthase. *Circ Res* **86**, E36-41 (2000).
171. Higashi, Y., *et al.* Tetrahydrobiopterin enhances forearm vascular response to acetylcholine in both normotensive and hypertensive individuals. *Am J Hypertens* **15**, 326-332 (2002).
172. Kerr, S., *et al.* Superoxide anion production is increased in a model of genetic hypertension: role of the endothelium. *Hypertension* **33**, 1353-1358 (1999).
173. Landmesser, U., *et al.* Oxidation of tetrahydrobiopterin leads to uncoupling of endothelial cell nitric oxide synthase in hypertension. *J Clin Invest* **111**, 1201-1209 (2003).
174. Mollnau, H., *et al.* Effects of angiotensin II infusion on the expression and function of NAD(P)H oxidase and components of nitric oxide/cGMP signaling. *Circ Res* **90**, E58-65 (2002).
175. Schulz, E., Wenzel, P., Munzel, T. & Daiber, A. Mitochondrial redox signaling: Interaction of mitochondrial reactive oxygen species with other sources of oxidative stress. *Antioxid Redox Signal* **20**, 308-324 (2014).
176. Karbach, S., Wenzel, P., Waisman, A., Munzel, T. & Daiber, A. eNOS uncoupling in cardiovascular diseases--the role of oxidative stress and inflammation. *Curr Pharm Des* **20**, 3579-3594 (2014).
177. Milstien, S. & Katusic, Z. Oxidation of tetrahydrobiopterin by peroxynitrite: implications for vascular endothelial function. *Biochem Biophys Res Commun* **263**, 681-684 (1999).
178. Kuzkaya, N., Weissmann, N., Harrison, D.G. & Dikalov, S. Interactions of peroxynitrite, tetrahydrobiopterin, ascorbic acid, and thiols: implications for uncoupling endothelial nitric-oxide synthase. *J Biol Chem* **278**, 22546-22554 (2003).
179. Vasquez-Vivar, J., Martasek, P., Whitsett, J., Joseph, J. & Kalyanaraman, B. The ratio between tetrahydrobiopterin and oxidized tetrahydrobiopterin analogues controls

- superoxide release from endothelial nitric oxide synthase: an EPR spin trapping study. *Biochem J* **362**, 733-739 (2002).
180. d'Uscio, L.V., Milstien, S., Richardson, D., Smith, L. & Katusic, Z.S. Long-term vitamin C treatment increases vascular tetrahydrobiopterin levels and nitric oxide synthase activity. *Circ Res* **92**, 88-95 (2003).
 181. Alp, N.J. & Channon, K.M. Regulation of endothelial nitric oxide synthase by tetrahydrobiopterin in vascular disease. *Arterioscler Thromb Vasc Biol* **24**, 413-420 (2004).
 182. Chalupsky, K. & Cai, H. Endothelial dihydrofolate reductase: critical for nitric oxide bioavailability and role in angiotensin II uncoupling of endothelial nitric oxide synthase. *Proc Natl Acad Sci U S A* **102**, 9056-9061 (2005).
 183. Zou, M.H., Shi, C. & Cohen, R.A. Oxidation of the zinc-thiolate complex and uncoupling of endothelial nitric oxide synthase by peroxynitrite. *J Clin Invest* **109**, 817-826 (2002).
 184. Sydow, K. & Munzel, T. ADMA and oxidative stress. *Atheroscler Suppl* **4**, 41-51 (2003).
 185. Jia, S.J., *et al.* Lysophosphatidylcholine-induced elevation of asymmetric dimethylarginine level by the NADPH oxidase pathway in endothelial cells. *Vascul Pharmacol* **44**, 143-148 (2006).
 186. Leiper, J., Murray-Rust, J., McDonald, N. & Vallance, P. S-nitrosylation of dimethylarginine dimethylaminohydrolase regulates enzyme activity: further interactions between nitric oxide synthase and dimethylarginine dimethylaminohydrolase. *Proc Natl Acad Sci U S A* **99**, 13527-13532 (2002).
 187. Chen, C.A., *et al.* S-glutathionylation uncouples eNOS and regulates its cellular and vascular function. *Nature* **468**, 1115-1118 (2010).
 188. Loot, A.E., Schreiber, J.G., Fisslthaler, B. & Fleming, I. Angiotensin II impairs endothelial function via tyrosine phosphorylation of the endothelial nitric oxide synthase. *J Exp Med* **206**, 2889-2896 (2009).
 189. Lin, M.I., *et al.* Phosphorylation of threonine 497 in endothelial nitric-oxide synthase coordinates the coupling of L-arginine metabolism to efficient nitric oxide production. *J Biol Chem* **278**, 44719-44726 (2003).
 190. Xu, J., Xie, Z., Reece, R., Pimental, D. & Zou, M.H. Uncoupling of endothelial nitric oxidase synthase by hypochlorous acid: role of NAD(P)H oxidase-derived superoxide and peroxynitrite. *Arterioscler Thromb Vasc Biol* **26**, 2688-2695 (2006).
 191. Zhang, M., Song, P., Xu, J. & Zou, M.H. Activation of NAD(P)H oxidases by thromboxane A2 receptor uncouples endothelial nitric oxide synthase. *Arterioscler Thromb Vasc Biol* **31**, 125-132 (2011).
 192. Li, H., *et al.* Reversal of endothelial nitric oxide synthase uncoupling and up-regulation of endothelial nitric oxide synthase expression lowers blood pressure in hypertensive rats. *J Am Coll Cardiol* **47**, 2536-2544 (2006).
 193. Guzik, T.J., *et al.* Mechanisms of increased vascular superoxide production in human diabetes mellitus: role of NAD(P)H oxidase and endothelial nitric oxide synthase. *Circulation* **105**, 1656-1662 (2002).
 194. Wenzel, P., *et al.* AT1-receptor blockade by telmisartan upregulates GTP-cyclohydrolase I and protects eNOS in diabetic rats. *Free Radic Biol Med* **45**, 619-626 (2008).
 195. Ferrer-Sueta, G., *et al.* Biochemistry of Peroxynitrite and Protein Tyrosine Nitration. *Chem Rev* **118**, 1338-1408 (2018).
 196. Beckman, J.S., Beckman, T.W., Chen, J., Marshall, P.A. & Freeman, B.A. Apparent hydroxyl radical production by peroxynitrite: implications for endothelial injury from nitric oxide and superoxide. *Proc Natl Acad Sci U S A* **87**, 1620-1624 (1990).
 197. Daiber, A. & Munzel, T. Increased circulating levels of 3-nitrotyrosine autoantibodies: marker for or maker of cardiovascular disease? *Circulation* **126**, 2371-2373 (2012).
 198. Kaur, H. & Halliwell, B. Evidence for nitric oxide-mediated oxidative damage in chronic inflammation. Nitrotyrosine in serum and synovial fluid from rheumatoid patients. *FEBS Lett* **350**, 9-12 (1994).

199. Khan, M.A., Dixit, K., Moinuddin, Arif, Z. & Alam, K. Studies on peroxynitrite-modified H1 histone: implications in systemic lupus erythematosus. *Biochimie* **97**, 104-113 (2014).
200. Turko, I.V. & Murad, F. Protein nitration in cardiovascular diseases. *Pharmacol Rev* **54**, 619-634 (2002).
201. Soltesz, P., *et al.* Comparative assessment of vascular function in autoimmune rheumatic diseases: considerations of prevention and treatment. *Autoimmun Rev* **10**, 416-425 (2011).
202. Murdaca, G., *et al.* Endothelial dysfunction in rheumatic autoimmune diseases. *Atherosclerosis* **224**, 309-317 (2012).
203. Vena, G.A., Vestita, M. & Cassano, N. Psoriasis and cardiovascular disease. *Dermatol Ther* **23**, 144-151 (2010).
204. Hak, A.E., Karlson, E.W., Feskanich, D., Stampfer, M.J. & Costenbader, K.H. Systemic lupus erythematosus and the risk of cardiovascular disease: results from the nurses' health study. *Arthritis Rheum* **61**, 1396-1402 (2009).
205. Mehta, N.N., *et al.* Patients with severe psoriasis are at increased risk of cardiovascular mortality: cohort study using the General Practice Research Database. *Eur Heart J* **31**, 1000-1006 (2010).
206. Herrera, J., Ferrebuz, A., MacGregor, E.G. & Rodriguez-Iturbe, B. Mycophenolate mofetil treatment improves hypertension in patients with psoriasis and rheumatoid arthritis. *J Am Soc Nephrol* **17**, S218-225 (2006).
207. Harrison, D.G. & Bernstein, K.E. Inflammation and Immunity in Hypertension, published in Hypertension: A Companion to Braunwald's Heart Disease 3rd edn (eds Bakris, G. L. & Sorrentino, M.) Elsevier, 60-69 (2018).
208. McMaster, W.G., Kirabo, A., Madhur, M.S. & Harrison, D.G. Inflammation, immunity, and hypertensive end-organ damage. *Circ Res* **116**, 1022-1033 (2015).
209. Wenzel, P., *et al.* Lysozyme M-positive monocytes mediate angiotensin II-induced arterial hypertension and vascular dysfunction. *Circulation* **124**, 1370-1381 (2011).
210. Chatterjee, M., *et al.* Augmented nitric oxide generation in neutrophils: oxidative and pro-inflammatory implications in hypertension. *Free Radic Res* **43**, 1195-1204 (2009).
211. Kossmann, S., *et al.* Angiotensin II-induced vascular dysfunction depends on interferon-gamma-driven immune cell recruitment and mutual activation of monocytes and NK-cells. *Arterioscler Thromb Vasc Biol* **33**, 1313-1319 (2013).
212. Kirabo, A., *et al.* DC isoketal-modified proteins activate T cells and promote hypertension. *J Clin Invest* **124**, 4642-4656 (2014).
213. Guzik, T.J., *et al.* Role of the T cell in the genesis of angiotensin II induced hypertension and vascular dysfunction. *J Exp Med* **204**, 2449-2460 (2007).
214. Chan, C.T., *et al.* Obligatory Role for B Cells in the Development of Angiotensin II-Dependent Hypertension. *Hypertension* **66**, 1023-1033 (2015).
215. Jackson, S.H., Devadas, S., Kwon, J., Pinto, L.A. & Williams, M.S. T cells express a phagocyte-type NADPH oxidase that is activated after T cell receptor stimulation. *Nat Immunol* **5**, 818-827 (2004).
216. Mantegazza, A.R., *et al.* NADPH oxidase controls phagosomal pH and antigen cross-presentation in human dendritic cells. *Blood* **112**, 4712-4722 (2008).
217. Krstic, J. & Santibanez, J.F. Transforming growth factor-beta and matrix metalloproteinases: functional interactions in tumor stroma-infiltrating myeloid cells. *ScientificWorldJournal* **2014**, 521754 (2014).
218. Cassatella, M.A., *et al.* Molecular basis of interferon-gamma and lipopolysaccharide enhancement of phagocyte respiratory burst capability. Studies on the gene expression of several NADPH oxidase components. *J Biol Chem* **265**, 20241-20246 (1990).
219. De Keulenaer, G.W., Alexander, R.W., Ushio-Fukai, M., Ishizaka, N. & Griendling, K.K. Tumour necrosis factor alpha activates a p22phox-based NADH oxidase in vascular smooth muscle. *Biochem J* **329** (Pt 3), 653-657 (1998).

220. Pietrowski, E., *et al.* Pro-inflammatory effects of interleukin-17A on vascular smooth muscle cells involve NAD(P)H- oxidase derived reactive oxygen species. *J Vasc Res* **48**, 52-58 (2011).
221. Madhur, M.S., *et al.* Interleukin 17 promotes angiotensin II-induced hypertension and vascular dysfunction. *Hypertension* **55**, 500-507 (2010).
222. Schrader, L.I., Kinzenbaw, D.A., Johnson, A.W., Faraci, F.M. & Didion, S.P. IL-6 deficiency protects against angiotensin II induced endothelial dysfunction and hypertrophy. *Arterioscler Thromb Vasc Biol* **27**, 2576-2581 (2007).
223. Rodriguez-Iturbe, B., Pons, H. & Johnson, R.J. Role of the Immune System in Hypertension. *Physiol Rev* **97**, 1127-1164 (2017).
224. Liu, T., Zhang, L., Joo, D. & Sun, S.C. NF-kappaB signaling in inflammation. *Signal Transduct Target Ther* **2**(2017).
225. Monaco, C., *et al.* Canonical pathway of nuclear factor kappa B activation selectively regulates proinflammatory and prothrombotic responses in human atherosclerosis. *Proc Natl Acad Sci U S A* **101**, 5634-5639 (2004).
226. Kempe, S., Kestler, H., Lasar, A. & Wirth, T. NF-kappaB controls the global pro-inflammatory response in endothelial cells: evidence for the regulation of a pro-atherogenic program. *Nucleic Acids Res* **33**, 5308-5319 (2005).
227. Gareus, R., *et al.* Endothelial cell-specific NF-kappaB inhibition protects mice from atherosclerosis. *Cell Metab* **8**, 372-383 (2008).
228. Zhou, Z., Connell, M.C. & MacEwan, D.J. TNFR1-induced NF-kappaB, but not ERK, p38MAPK or JNK activation, mediates TNF-induced ICAM-1 and VCAM-1 expression on endothelial cells. *Cell Signal* **19**, 1238-1248 (2007).
229. Wenzel, P., Kossmann, S., Munzel, T. & Daiber, A. Redox regulation of cardiovascular inflammation - Immunomodulatory function of mitochondrial and Nox-derived reactive oxygen and nitrogen species. *Free Radic Biol Med* **109**, 48-60 (2017).
230. Baggio, L.L. & Drucker, D.J. Biology of incretins: GLP-1 and GIP. *Gastroenterology* **132**, 2131-2157 (2007).
231. Campbell, J.E. & Drucker, D.J. Pharmacology, physiology, and mechanisms of incretin hormone action. *Cell Metab* **17**, 819-837 (2013).
232. Andersen, A., Lund, A., Knop, F.K. & Vilsboll, T. Glucagon-like peptide 1 in health and disease. *Nat Rev Endocrinol* **14**, 390-403 (2018).
233. Drucker, D.J., Habener, J.F. & Holst, J.J. Discovery, characterization, and clinical development of the glucagon-like peptides. *J Clin Invest* **127**, 4217-4227 (2017).
234. Sandoval, D.A. & D'Alessio, D.A. Physiology of proglucagon peptides: role of glucagon and GLP-1 in health and disease. *Physiol Rev* **95**, 513-548 (2015).
235. Holst, J.J. The physiology of glucagon-like peptide 1. *Physiol Rev* **87**, 1409-1439 (2007).
236. Deacon, C.F. Circulation and degradation of GIP and GLP-1. *Horm Metab Res* **36**, 761-765 (2004).
237. Drucker, D.J. Mechanisms of Action and Therapeutic Application of Glucagon-like Peptide-1. *Cell Metab* **27**, 740-756 (2018).
238. McLean, B.A., *et al.* Revisiting the complexity of GLP-1 action-from sites of synthesis to receptor activation. *Endocr Rev* (2020).
239. Knudsen, L.B., Hastrup, S., Underwood, C.R., Wulff, B.S. & Fleckner, J. Functional importance of GLP-1 receptor species and expression levels in cell lines. *Regul Pept* **175**, 21-29 (2012).
240. Donnelly, D. The structure and function of the glucagon-like peptide-1 receptor and its ligands. *Br J Pharmacol* **166**, 27-41 (2012).
241. Graaf, C., *et al.* Glucagon-Like Peptide-1 and Its Class B G Protein-Coupled Receptors: A Long March to Therapeutic Successes. *Pharmacol Rev* **68**, 954-1013 (2016).
242. Carlessi, R., *et al.* GLP-1 receptor signalling promotes beta-cell glucose metabolism via mTOR-dependent HIF-1alpha activation. *Sci Rep* **7**, 2661 (2017).
243. Muller, T.D., *et al.* Glucagon-like peptide 1 (GLP-1). *Mol Metab* **30**, 72-130 (2019).

244. Knudsen, L.B. & Pridal, L. Glucagon-like peptide-1-(9-36) amide is a major metabolite of glucagon-like peptide-1-(7-36) amide after in vivo administration to dogs, and it acts as an antagonist on the pancreatic receptor. *Eur J Pharmacol* **318**, 429-435 (1996).
245. Ussher, J.R. & Drucker, D.J. Cardiovascular actions of incretin-based therapies. *Circ Res* **114**, 1788-1803 (2014).
246. Nauck, M.A., Meier, J.J., Cavender, M.A., Abd El Aziz, M. & Drucker, D.J. Cardiovascular Actions and Clinical Outcomes With Glucagon-Like Peptide-1 Receptor Agonists and Dipeptidyl Peptidase-4 Inhibitors. *Circulation* **136**, 849-870 (2017).
247. Malm-Erfjelt, M., *et al.* Metabolism and excretion of the once-daily human glucagon-like peptide-1 analog liraglutide in healthy male subjects and its in vitro degradation by dipeptidyl peptidase IV and neutral endopeptidase. *Drug Metab Dispos* **38**, 1944-1953 (2010).
248. Knudsen, L.B. & Lau, J. The Discovery and Development of Liraglutide and Semaglutide. *Front Endocrinol (Lausanne)* **10**, 155 (2019).
249. Sorli, C., *et al.* Efficacy and safety of once-weekly semaglutide monotherapy versus placebo in patients with type 2 diabetes (SUSTAIN 1): a double-blind, randomised, placebo-controlled, parallel-group, multinational, multicentre phase 3a trial. *Lancet Diabetes Endocrinol* **5**, 251-260 (2017).
250. Aroda, V.R., *et al.* PIONEER 1: Randomized Clinical Trial of the Efficacy and Safety of Oral Semaglutide Monotherapy in Comparison With Placebo in Patients With Type 2 Diabetes. *Diabetes Care* **42**, 1724-1732 (2019).
251. Pi-Sunyer, X., *et al.* A Randomized, Controlled Trial of 3.0 mg of Liraglutide in Weight Management. *N Engl J Med* **373**, 11-22 (2015).
252. Wilding, J.P.H., *et al.* Once-Weekly Semaglutide in Adults with Overweight or Obesity. *N Engl J Med* **384**, 989 (2021).
253. European Medicines Agency. Saxenda <https://www.ema.europa.eu/en/medicines/human/EPAR/saxenda>. (accessed on 2021-07-23).
254. FDA News Release. FDA Approves New Drug Treatment for Chronic Weight Management, First Since 2014 <https://www.fda.gov/news-events/press-announcements/fda-approves-new-drug-treatment-chronic-weight-management-first-2014>. (2021; accessed on 2021-07-23).
255. Kelly, A.S., *et al.* A Randomized, Controlled Trial of Liraglutide for Adolescents with Obesity. *N Engl J Med* **382**, 2117-2128 (2020).
256. FDA News Release. FDA approves weight management drug for patients aged 12 and older <https://www.fda.gov/drugs/drug-safety-and-availability/fda-approves-weight-management-drug-patients-aged-12-and-older>. (2020; accessed on 2021-07-23).
257. Smith, R.J., Goldfine, A.B. & Hiatt, W.R. Evaluating the Cardiovascular Safety of New Medications for Type 2 Diabetes: Time to Reassess? *Diabetes Care* **39**, 738-742 (2016).
258. FDA. Guidance for Industry: Diabetes Mellitus — Evaluating Cardiovascular Risk in New Antidiabetic Therapies to Treat Type 2 Diabetes <https://www.fda.gov/media/71297/download>. (2008; accessed on 2021-03-20).
259. Holman, R.R., Sourij, H. & Califf, R.M. Cardiovascular outcome trials of glucose-lowering drugs or strategies in type 2 diabetes. *Lancet* **383**, 2008-2017 (2014).
260. Marso, S.P., *et al.* Liraglutide and Cardiovascular Outcomes in Type 2 Diabetes. *N Engl J Med* **375**, 311-322 (2016).
261. Marx, N. & Libby, P. Cardiovascular Benefits of GLP-1 Receptor Agonism: Is Inflammation a Key? *JACC Basic Transl Sci* **3**, 858-860 (2018).
262. Zelniker *et al.* Comparison of the Effects of Glucagon-Like Peptide Receptor Agonists and Sodium-Glucose Cotransporter 2 Inhibitors for Prevention of Major Adverse Cardiovascular and Renal Outcomes in Type 2 Diabetes Mellitus. *Circulation* **139**, 2022-2031 (2019).

263. Khan et al. Glucagon-Like Peptide 1 Receptor Agonists and Heart Failure: The Need for Further Evidence Generation and Practice Guidelines Optimization. *Circulation* **142**, 1205-1218 (2020).
264. Heuvelman, V.D., Van Raalte, D.H. & Smits, M.M. Cardiovascular effects of glucagon-like peptide 1 receptor agonists: from mechanistic studies in humans to clinical outcomes. *Cardiovasc Res* **116**, 916-930 (2020).
265. Pfeffer, M.A., et al. Lixisenatide in Patients with Type 2 Diabetes and Acute Coronary Syndrome. *N Engl J Med* **373**, 2247-2257 (2015).
266. Marso, S.P., et al. Semaglutide and Cardiovascular Outcomes in Patients with Type 2 Diabetes. *N Engl J Med* **375**, 1834-1844 (2016).
267. Holman, R.R., et al. Effects of Once-Weekly Exenatide on Cardiovascular Outcomes in Type 2 Diabetes. *N Engl J Med* **377**, 1228-1239 (2017).
268. Hernandez, A.F., et al. Albiglutide and cardiovascular outcomes in patients with type 2 diabetes and cardiovascular disease (Harmony Outcomes): a double-blind, randomised placebo-controlled trial. *Lancet* (2018).
269. Gerstein, H.C., et al. Dulaglutide and cardiovascular outcomes in type 2 diabetes (REWIND): a double-blind, randomised placebo-controlled trial. *Lancet* **394**, 121-130 (2019).
270. Husain, M., et al. Oral Semaglutide and Cardiovascular Outcomes in Patients with Type 2 Diabetes. *N Engl J Med* **381**, 841-851 (2019).
271. Ryan, D.H., et al. Semaglutide Effects on Cardiovascular Outcomes in People With Overweight or Obesity (SELECT) rationale and design. *Am Heart J* **229**, 61-69 (2020).
272. Bose, A.K., Mocanu, M.M., Carr, R.D., Brand, C.L. & Yellon, D.M. Glucagon-like peptide 1 can directly protect the heart against ischemia/reperfusion injury. *Diabetes* **54**, 146-151 (2005).
273. Noyan-Ashraf, M.H., et al. GLP-1R agonist liraglutide activates cytoprotective pathways and improves outcomes after experimental myocardial infarction in mice. *Diabetes* **58**, 975-983 (2009).
274. Poornima, I., et al. Chronic glucagon-like peptide-1 infusion sustains left ventricular systolic function and prolongs survival in the spontaneously hypertensive, heart failure-prone rat. *Circ Heart Fail* **1**, 153-160 (2008).
275. Withaar, C., et al. The effects of liraglutide and dapagliflozin on cardiac function and structure in a multi-hit mouse model of Heart Failure with Preserved Ejection Fraction. *Cardiovasc Res* (2020).
276. Pyke, C., et al. GLP-1 receptor localization in monkey and human tissue: novel distribution revealed with extensively validated monoclonal antibody. *Endocrinology* **155**, 1280-1290 (2014).
277. Richards, P., et al. Identification and characterization of GLP-1 receptor-expressing cells using a new transgenic mouse model. *Diabetes* **63**, 1224-1233 (2014).
278. Ussher, J.R., et al. Inactivation of the cardiomyocyte glucagon-like peptide-1 receptor (GLP-1R) unmasks cardiomyocyte-independent GLP-1R-mediated cardioprotection. *Mol Metab* **3**, 507-517 (2014).
279. Baggio, L.L., et al. The autonomic nervous system and cardiac GLP-1 receptors control heart rate in mice. *Mol Metab* **6**, 1339-1349 (2017).
280. Drucker, D.J. The Ascending GLP-1 Road From Clinical Safety to Reduction of Cardiovascular Complications. *Diabetes* **67**, 1710-1719 (2018).
281. Helmstadter, J., et al. GLP-1 receptor agonists and their cardiovascular benefits - the role of the GLP-1 receptor. *Br J Pharmacol* (2021).
282. Ban, K., et al. Cardioprotective and vasodilatory actions of glucagon-like peptide 1 receptor are mediated through both glucagon-like peptide 1 receptor-dependent and -independent pathways. *Circulation* **117**, 2340-2350 (2008).
283. Nikolaidis, L.A., Elahi, D., Shen, Y.T. & Shannon, R.P. Active metabolite of GLP-1 mediates myocardial glucose uptake and improves left ventricular performance in conscious dogs with dilated cardiomyopathy. *Am J Physiol Heart Circ Physiol* **289**, H2401-2408 (2005).

284. Burgmaier, M., *et al.* Glucagon-like peptide-1 (GLP-1) and its split products GLP-1(9-37) and GLP-1(28-37) stabilize atherosclerotic lesions in apoe(-)/(-) mice. *Atherosclerosis* **231**, 427-435 (2013).
285. Siraj, M.A., *et al.* Cardioprotective GLP-1 metabolite prevents ischemic cardiac injury by inhibiting mitochondrial trifunctional protein- α . *J Clin Invest* (2020).
286. Hogan, A.E., *et al.* Glucagon-like peptide 1 analogue therapy directly modulates innate immune-mediated inflammation in individuals with type 2 diabetes mellitus. *Diabetologia* **57**, 781-784 (2014).
287. Chaudhuri, A., *et al.* Exenatide exerts a potent antiinflammatory effect. *J Clin Endocrinol Metab* **97**, 198-207 (2012).
288. Steven, S., *et al.* Gliptin and GLP-1 analog treatment improves survival and vascular inflammation/dysfunction in animals with lipopolysaccharide-induced endotoxemia. *Basic Res Cardiol* **110**, 6 (2015).
289. Steven, S., *et al.* Glucagon-like peptide-1 receptor signalling reduces microvascular thrombosis, nitro-oxidative stress and platelet activation in endotoxaemic mice. *Br J Pharmacol* **174**, 1620-1632 (2017).
290. Rakipovski, G., *et al.* The GLP-1 Analogs Liraglutide and Semaglutide Reduce Atherosclerosis in ApoE(-/-) and LDLr(-/-) Mice by a Mechanism That Includes Inflammatory Pathways. *JACC Basic Transl Sci* **3**, 844-857 (2018).
291. Arakawa, M., *et al.* Inhibition of monocyte adhesion to endothelial cells and attenuation of atherosclerotic lesion by a glucagon-like peptide-1 receptor agonist, exendin-4. *Diabetes* **59**, 1030-1037 (2010).
292. Hadjiyanni, I., Siminovitch, K.A., Danska, J.S. & Drucker, D.J. Glucagon-like peptide-1 receptor signalling selectively regulates murine lymphocyte proliferation and maintenance of peripheral regulatory T cells. *Diabetologia* **53**, 730-740 (2010).
293. Yusta, B., *et al.* GLP-1R Agonists Modulate Enteric Immune Responses Through the Intestinal Intraepithelial Lymphocyte GLP-1R. *Diabetes* **64**, 2537-2549 (2015).
294. Bang-Berthelsen, C.H., *et al.* GLP-1 Induces Barrier Protective Expression in Brunner's Glands and Regulates Colonic Inflammation. *Inflamm Bowel Dis* **22**, 2078-2097 (2016).
295. Pujadas, G. & Drucker, D.J. Vascular Biology of Glucagon Receptor Superfamily Peptides: Mechanistic and Clinical Relevance. *Endocr Rev* **37**, 554-583 (2016).
296. Ishibashi, Y., Matsui, T., Takeuchi, M. & Yamagishi, S. Glucagon-like peptide-1 (GLP-1) inhibits advanced glycation end product (AGE)-induced up-regulation of VCAM-1 mRNA levels in endothelial cells by suppressing AGE receptor (RAGE) expression. *Biochem Biophys Res Commun* **391**, 1405-1408 (2010).
297. Wang, R., *et al.* Effect of Glucagon-like Peptide-1 on High-Glucose-induced Oxidative Stress and Cell Apoptosis in Human Endothelial Cells and Its Underlying Mechanism. *J Cardiovasc Pharmacol* **66**, 135-140 (2015).
298. Krasner, N.M., Ido, Y., Ruderman, N.B. & Cacicedo, J.M. Glucagon-like peptide-1 (GLP-1) analog liraglutide inhibits endothelial cell inflammation through a calcium and AMPK dependent mechanism. *PLoS One* **9**, e97554 (2014).
299. Wei, R., *et al.* Exenatide exerts direct protective effects on endothelial cells through the AMPK/Akt/eNOS pathway in a GLP-1 receptor-dependent manner. *Am J Physiol Endocrinol Metab* **310**, E947-957 (2016).
300. Hirata, Y., *et al.* Exendin-4, a glucagon-like peptide-1 receptor agonist, attenuates neointimal hyperplasia after vascular injury. *Eur J Pharmacol* **699**, 106-111 (2013).
301. Jojima, T., *et al.* Liraglutide, a GLP-1 receptor agonist, inhibits vascular smooth muscle cell proliferation by enhancing AMP-activated protein kinase and cell cycle regulation, and delays atherosclerosis in ApoE deficient mice. *Atherosclerosis* **261**, 44-51 (2017).
302. Ridker, P.M., *et al.* Antiinflammatory Therapy with Canakinumab for Atherosclerotic Disease. *N Engl J Med* **377**, 1119-1131 (2017).
303. Helmstadter, J., *et al.* Endothelial GLP-1 (Glucagon-Like Peptide-1) Receptor Mediates Cardiovascular Protection by Liraglutide In Mice With Experimental Arterial Hypertension. *Arterioscler Thromb Vasc Biol* **40**, 145-158 (2020).

304. Scrocchi, L.A., *et al.* Glucose intolerance but normal satiety in mice with a null mutation in the glucagon-like peptide 1 receptor gene. *Nat Med* **2**, 1254-1258 (1996).
305. Wilson-Perez, H.E., *et al.* Vertical sleeve gastrectomy is effective in two genetic mouse models of glucagon-like Peptide 1 receptor deficiency. *Diabetes* **62**, 2380-2385 (2013).
306. Alva, J.A., *et al.* VE-Cadherin-Cre-recombinase transgenic mouse: a tool for lineage analysis and gene deletion in endothelial cells. *Dev Dyn* **235**, 759-767 (2006).
307. Clausen, B.E., Burkhardt, C., Reith, W., Renkawitz, R. & Forster, I. Conditional gene targeting in macrophages and granulocytes using LysMcre mice. *Transgenic Res* **8**, 265-277 (1999).
308. Metzger, D. & Feil, R. Engineering the mouse genome by site-specific recombination. *Curr Opin Biotechnol* **10**, 470-476 (1999).
309. Nagy, A. Cre recombinase: the universal reagent for genome tailoring. *Genesis* **26**, 99-109 (2000).
310. Feil, R., *et al.* Ligand-activated site-specific recombination in mice. *Proc Natl Acad Sci U S A* **93**, 10887-10890 (1996).
311. Bouabe, H. & Okkenhaug, K. Gene targeting in mice: a review. *Methods Mol Biol* **1064**, 315-336 (2013).
312. Payne, S., De Val, S. & Neal, A. Endothelial-Specific Cre Mouse Models. *Arterioscler Thromb Vasc Biol* **38**, 2550-2561 (2018).
313. Pyke, C. & Knudsen, L.B. The glucagon-like peptide-1 receptor--or not? *Endocrinology* **154**, 4-8 (2013).
314. Aroor, A. & Nistala, R. Tissue-specific expression of GLP1R in mice: is the problem of antibody nonspecificity solved? *Diabetes* **63**, 1182-1184 (2014).
315. Theeuwes, F. & Yum, S.I. Principles of the design and operation of generic osmotic pumps for the delivery of semisolid or liquid drug formulations. *Ann Biomed Eng* **4**, 343-353 (1976).
316. Alzet. Osmotic Pumps Mechanism of Operation https://www.alzet.com/products/alzet_pumps/how-does-it-work/. (accessed on 2021-04-29).
317. Daugherty, A., Rateri, D., Hong, L. & Balakrishnan, A. Measuring blood pressure in mice using volume pressure recording, a tail-cuff method. *J Vis Exp* (2009).
318. Feng, M., *et al.* Validation of volume-pressure recording tail-cuff blood pressure measurements. *Am J Hypertens* **21**, 1288-1291 (2008).
319. Wang, Y., Thatcher, S.E. & Cassis, L.A. Measuring Blood Pressure Using a Noninvasive Tail Cuff Method in Mice. *Methods Mol Biol* **1614**, 69-73 (2017).
320. Andrikopoulos, S., Blair, A.R., Deluca, N., Fam, B.C. & Proietto, J. Evaluating the glucose tolerance test in mice. *Am J Physiol Endocrinol Metab* **295**, E1323-1332 (2008).
321. Vinue, A. & Gonzalez-Navarro, H. Glucose and Insulin Tolerance Tests in the Mouse. *Methods Mol Biol* **1339**, 247-254 (2015).
322. Jackel, S., *et al.* Gut microbiota regulate hepatic von Willebrand factor synthesis and arterial thrombus formation via Toll-like receptor-2. *Blood* **130**, 542-553 (2017).
323. Lagrange, J., Kossmann, S., Kiouptsi, K. & Wenzel, P. Visualizing Leukocyte Rolling and Adhesion in Angiotensin II-Infused Mice: Techniques and Pitfalls. *J Vis Exp* (2018).
324. Schmidt, S., Moser, M. & Sperandio, M. The molecular basis of leukocyte recruitment and its deficiencies. *Mol Immunol* **55**, 49-58 (2013).
325. Sobczak, M., Dargatz, J. & Chrzanowska-Wodnicka, M. Isolation and culture of pulmonary endothelial cells from neonatal mice. *J Vis Exp* (2010).
326. Wang, J., Niu, N., Xu, S. & Jin, Z.G. A simple protocol for isolating mouse lung endothelial cells. *Sci Rep* **9**, 1458 (2019).
327. Ebert, J., *et al.* Paraoxonase-2 regulates coagulation activation through endothelial tissue factor. *Blood* **131**, 2161-2172 (2018).
328. Bosmann, M., *et al.* Interruption of macrophage-derived IL-27(p28) production by IL-10 during sepsis requires STAT3 but not SOCS3. *J Immunol* **193**, 5668-5677 (2014).

329. Ying, W., Cheruku, P.S., Bazer, F.W., Safe, S.H. & Zhou, B. Investigation of macrophage polarization using bone marrow derived macrophages. *J Vis Exp* (2013).
330. Stanley, E.R. & Heard, P.M. Factors regulating macrophage production and growth. Purification and some properties of the colony stimulating factor from medium conditioned by mouse L cells. *J Biol Chem* **252**, 4305-4312 (1977).
331. del Campo, L. & Ferrer, M. Wire Myography to Study Vascular Tone and Vascular Structure of Isolated Mouse Arteries. *Methods Mol Biol* **1339**, 255-276 (2015).
332. Munzel, T., Giaid, A., Kurz, S., Stewart, D.J. & Harrison, D.G. Evidence for a role of endothelin 1 and protein kinase C in nitroglycerin tolerance. *Proc Natl Acad Sci U S A* **92**, 5244-5248 (1995).
333. Munzel, T., *et al.* Hydralazine prevents nitroglycerin tolerance by inhibiting activation of a membrane-bound NADH oxidase. A new action for an old drug. *J Clin Invest* **98**, 1465-1470 (1996).
334. ADInstruments. Organ Bath Systems http://cdn.adinstruments.com/adi-web/techniques/tn-Organ_Bath_Systems.pdf. (accessed on 2021-04-29).
335. Zhao, H., *et al.* Superoxide reacts with hydroethidine but forms a fluorescent product that is distinctly different from ethidium: potential implications in intracellular fluorescence detection of superoxide. *Free Radic Biol Med* **34**, 1359-1368 (2003).
336. Zhao, H., *et al.* Detection and characterization of the product of hydroethidine and intracellular superoxide by HPLC and limitations of fluorescence. *Proc Natl Acad Sci U S A* **102**, 5727-5732 (2005).
337. Zielonka, J., Vasquez-Vivar, J. & Kalyanaraman, B. Detection of 2-hydroxyethidium in cellular systems: a unique marker product of superoxide and hydroethidine. *Nat Protoc* **3**, 8-21 (2008).
338. Wenzel, P., *et al.* First evidence for a crosstalk between mitochondrial and NADPH oxidase-derived reactive oxygen species in nitroglycerin-triggered vascular dysfunction. *Antioxid Redox Signal* **10**, 1435-1447 (2008).
339. JoVE Science Education Database. Analytical Chemistry. *High-Performance Liquid Chromatography (HPLC)*. JoVE, Cambridge, MA (2021).
340. Griendling, K.K., *et al.* Measurement of Reactive Oxygen Species, Reactive Nitrogen Species, and Redox-Dependent Signaling in the Cardiovascular System: A Scientific Statement From the American Heart Association. *Circ Res* **119**, e39-75 (2016).
341. Munzel, T., Afanas'ev, I.B., Kleschyov, A.L. & Harrison, D.G. Detection of superoxide in vascular tissue. *Arterioscler Thromb Vasc Biol* **22**, 1761-1768 (2002).
342. Daiber, A., Oelze, M., Steven, S., Kroller-Schon, S. & Munzel, T. Taking up the cudgels for the traditional reactive oxygen and nitrogen species detection assays and their use in the cardiovascular system. *Redox Biol* **12**, 35-49 (2017).
343. Li, Y., *et al.* Validation of lucigenin (bis-N-methylacridinium) as a chemilumigenic probe for detecting superoxide anion radical production by enzymatic and cellular systems. *J Biol Chem* **273**, 2015-2023 (1998).
344. Cohen, G.M. & d'Arcy Doherty, M. Free radical mediated cell toxicity by redox cycling chemicals. *Br J Cancer Suppl* **8**, 46-52 (1987).
345. Oelze, M., *et al.* Nebivolol inhibits superoxide formation by NADPH oxidase and endothelial dysfunction in angiotensin II-treated rats. *Hypertension* **48**, 677-684 (2006).
346. Kroller-Schon, S., *et al.* Molecular mechanisms of the crosstalk between mitochondria and NADPH oxidase through reactive oxygen species-studies in white blood cells and in animal models. *Antioxid Redox Signal* **20**, 247-266 (2014).
347. Daiber, A., *et al.* Measurement of NAD(P)H oxidase-derived superoxide with the luminol analogue L-012. *Free Radic Biol Med* **36**, 101-111 (2004).
348. Kalinovic, S., *et al.* Comparison of Mitochondrial Superoxide Detection Ex Vivo/In Vivo by mitoSOX HPLC Method with Classical Assays in Three Different Animal Models of Oxidative Stress. *Antioxidants (Basel)* **8**(2019).
349. Moreland, J.G., *et al.* Endotoxin priming of neutrophils requires NADPH oxidase-generated oxidants and is regulated by the anion transporter CIC-3. *J Biol Chem* **282**, 33958-33967 (2007).

350. Kleschyov, A.L., *et al.* Spin trapping of vascular nitric oxide using colloid Fe(II)-diethyldithiocarbamate. *Biochem Biophys Res Commun* **275**, 672-677 (2000).
351. Kossmann, S., *et al.* Inflammatory monocytes determine endothelial nitric-oxide synthase uncoupling and nitro-oxidative stress induced by angiotensin II. *J Biol Chem* **289**, 27540-27550 (2014).
352. Bruker. How does EPR work? <https://www.bruker.com/en/products-and-solutions/mr/epr-instruments/what-is-epr/What-Is-EPR.html>. (accessed on 2021-04-29).
353. Kus, K., *et al.* Hepatoselective Nitric Oxide (NO) Donors, V-PYRRO/NO and V-PROLI/NO, in Nonalcoholic Fatty Liver Disease: A Comparison of Antisteatotic Effects with the Biotransformation and Pharmacokinetics. *Drug Metab Dispos* **43**, 1028-1036 (2015).
354. Kharitonov, V.G., Sundquist, A.R. & Sharma, V.S. Kinetics of nitric oxide autoxidation in aqueous solution. *J Biol Chem* **269**, 5881-5883 (1994).
355. Lauer, T., *et al.* Plasma nitrite rather than nitrate reflects regional endothelial nitric oxide synthase activity but lacks intrinsic vasodilator action. *Proc Natl Acad Sci U S A* **98**, 12814-12819 (2001).
356. Bratthauer, G.L. The avidin-biotin complex (ABC) method and other avidin-biotin binding methods. *Methods Mol Biol* **115**, 203-214 (1999).
357. Krenacs, L., Krenacs, T., Stelkovich, E. & Raffeld, M. Heat-induced antigen retrieval for immunohistochemical reactions in routinely processed paraffin sections. *Methods Mol Biol* **588**, 103-119 (2010).
358. Picot, J., Guerin, C.L., Le Van Kim, C. & Boulanger, C.M. Flow cytometry: retrospective, fundamentals and recent instrumentation. *Cytotechnology* **64**, 109-130 (2012).
359. Abcam. Introduction to flow cytometry http://docs.abcam.com/pdf/protocols/flow-cytometry-introduction.pdf?utm_source=Eloqua&utm_medium=Email&utm_campaign=%7C%7C%7C%7C%7C&mi_u=1240186. (accessed on 2021-05-03).
360. Rahman, M. Introduction to Flow Cytometry [https://smhs.gwu.edu/flow-cytometry/sites/flow-cytometry/files/Introduction%20Flow%20Cytometry-AbD%20Serotec\(1\).pdf](https://smhs.gwu.edu/flow-cytometry/sites/flow-cytometry/files/Introduction%20Flow%20Cytometry-AbD%20Serotec(1).pdf). (2009, accessed on 2021-05-03).
361. Rose, S., Misharin, A. & Perlman, H. A novel Ly6C/Ly6G-based strategy to analyze the mouse splenic myeloid compartment. *Cytometry A* **81**, 343-350 (2012).
362. Truett, G.E., *et al.* Preparation of PCR-quality mouse genomic DNA with hot sodium hydroxide and tris (HotSHOT). *Biotechniques* **29**, 52, 54 (2000).
363. Chomczynski, P. & Sacchi, N. Single-step method of RNA isolation by acid guanidinium thiocyanate-phenol-chloroform extraction. *Anal Biochem* **162**, 156-159 (1987).
364. Chomczynski, P. & Sacchi, N. The single-step method of RNA isolation by acid guanidinium thiocyanate-phenol-chloroform extraction: twenty-something years on. *Nat Protoc* **1**, 581-585 (2006).
365. Arnemann, J. DNA-/RNA-Konzentrationsbestimmung. In: Gressner A.M., Arndt T. (eds) *Lexikon der Medizinischen Laboratoriumsdiagnostik*. Springer Reference Medizin. Springer, Berlin, Heidelberg https://doi.org/10.1007/978-3-662-48986-4_3464. (2019).
366. Thermo Fisher. Introduction to Gene Expression. Publication Number 4454239. (2018).
367. Navarro, E., Serrano-Heras, G., Castano, M.J. & Solera, J. Real-time PCR detection chemistry. *Clin Chim Acta* **439**, 231-250 (2015).
368. Thermo Fisher. How TaqMan Works - Ask TaqMan® Ep. 13 by Life Technologies <https://www.thermofisher.com/de/de/home/life-science/pcr/real-time-pcr/real-time-pcr-learning-center/real-time-pcr-basics/ask-taqman-video-series.html>. (2013; accessed on 2021-04-29).
369. Kedziora, K.M. & Jalink, K. Fluorescence resonance energy transfer microscopy (FRET). *Methods Mol Biol* **1251**, 67-82 (2015).

370. Livak, K.J. & Schmittgen, T.D. Analysis of relative gene expression data using real-time quantitative PCR and the 2(-Delta Delta C(T)) Method. *Methods* **25**, 402-408 (2001).
371. Bradford, M.M. A rapid and sensitive method for the quantitation of microgram quantities of protein utilizing the principle of protein-dye binding. *Anal Biochem* **72**, 248-254 (1976).
372. Laemmli, U.K. Cleavage of structural proteins during the assembly of the head of bacteriophage T4. *Nature* **227**, 680-685 (1970).
373. Gallagher, S.R. One-dimensional SDS gel electrophoresis of proteins. *Curr Protoc Cell Biol* **Chapter 6**, Unit 6 1 (2007).
374. Bio-Rad. A Guide to Polyacrylamide Gel Electrophoresis and Detection http://www.bio-rad.com/webroot/web/pdf/lsr/literature/Bulletin_6040.pdf. (accessed on 2021-04-29).
375. Towbin, H., Staehelin, T. & Gordon, J. Electrophoretic transfer of proteins from polyacrylamide gels to nitrocellulose sheets: procedure and some applications. *Proc Natl Acad Sci U S A* **76**, 4350-4354 (1979).
376. Stochaj, W.R., Berkelman, T. & Laird, N. Staining membrane-bound proteins with ponceau s. *CSH Protoc* **2006**(2006).
377. Engvall, E. & Perlmann, P. Enzyme-linked immunosorbent assay (ELISA). Quantitative assay of immunoglobulin G. *Immunochemistry* **8**, 871-874 (1971).
378. Small, D.S. Let's abolish 'fold higher' and 'fold increase' from our lexicon <https://doi.org/10.4155/ipk-2016-0007>. *Int. J. Pharmacokinet* **1(1)**, 13-15 (2016).
379. Yildiz, M., *et al.* Left ventricular hypertrophy and hypertension. *Prog Cardiovasc Dis* **63**, 10-21 (2020).
380. Steven, S., *et al.* Exacerbation of adverse cardiovascular effects of aircraft noise in an animal model of arterial hypertension. *Redox Biol*, 101515 (2020).
381. Lan, T.H., Huang, X.Q. & Tan, H.M. Vascular fibrosis in atherosclerosis. *Cardiovasc Pathol* **22**, 401-407 (2013).
382. Shirwany, N.A. & Zou, M.H. Arterial stiffness: a brief review. *Acta Pharmacol Sin* **31**, 1267-1276 (2010).
383. Intengan, H.D. & Schiffrin, E.L. Vascular remodeling in hypertension: roles of apoptosis, inflammation, and fibrosis. *Hypertension* **38**, 581-587 (2001).
384. Sibal, L., Agarwal, S.C., Home, P.D. & Boger, R.H. The Role of Asymmetric Dimethylarginine (ADMA) in Endothelial Dysfunction and Cardiovascular Disease. *Curr Cardiol Rev* **6**, 82-90 (2010).
385. McKnight, A.J., *et al.* Molecular cloning of F4/80, a murine macrophage-restricted cell surface glycoprotein with homology to the G-protein-linked transmembrane 7 hormone receptor family. *J Biol Chem* **271**, 486-489 (1996).
386. Tummala, P.E., *et al.* Angiotensin II induces vascular cell adhesion molecule-1 expression in rat vasculature: A potential link between the renin-angiotensin system and atherosclerosis. *Circulation* **100**, 1223-1229 (1999).
387. Luft, F.C. Angiotensin, inflammation, hypertension, and cardiovascular disease. *Curr Hypertens Rep* **3**, 61-67 (2001).
388. Tham, D.M., *et al.* Angiotensin II is associated with activation of NF-kappaB-mediated genes and downregulation of PPARs. *Physiol Genomics* **11**, 21-30 (2002).
389. Nourshargh, S. & Alon, R. Leukocyte migration into inflamed tissues. *Immunity* **41**, 694-707 (2014).
390. Gonzalez-Amaro, R. & Sanchez-Madrid, F. Cell adhesion molecules: selectins and integrins. *Crit Rev Immunol* **19**, 389-429 (1999).
391. Scrocchi, L.A. & Drucker, D.J. Effects of aging and a high fat diet on body weight and glucose tolerance in glucagon-like peptide-1 receptor *-/-* mice. *Endocrinology* **139**, 3127-3132 (1998).
392. Scrocchi, L.A., Marshall, B.A., Cook, S.M., Brubaker, P.L. & Drucker, D.J. Identification of glucagon-like peptide 1 (GLP-1) actions essential for glucose homeostasis in mice with disruption of GLP-1 receptor signaling. *Diabetes* **47**, 632-639 (1998).

393. Flamez, D., *et al.* Altered cAMP and Ca²⁺ signaling in mouse pancreatic islets with glucagon-like peptide-1 receptor null phenotype. *Diabetes* **48**, 1979-1986 (1999).
394. Hsieh, J., *et al.* The glucagon-like peptide 1 receptor is essential for postprandial lipoprotein synthesis and secretion in hamsters and mice. *Diabetologia* **53**, 552-561 (2010).
395. MacLusky, N.J., *et al.* Neuroendocrine function and response to stress in mice with complete disruption of glucagon-like peptide-1 receptor signaling. *Endocrinology* **141**, 752-762 (2000).
396. During, M.J., *et al.* Glucagon-like peptide-1 receptor is involved in learning and neuroprotection. *Nat Med* **9**, 1173-1179 (2003).
397. Ayala, J.E., *et al.* Glucagon-like peptide-1 receptor knockout mice are protected from high-fat diet-induced insulin resistance. *Endocrinology* **151**, 4678-4687 (2010).
398. Gros, R., *et al.* Cardiac function in mice lacking the glucagon-like peptide-1 receptor. *Endocrinology* **144**, 2242-2252 (2003).
399. Cross, M., Mangelsdorf, I., Wedel, A. & Renkawitz, R. Mouse lysozyme M gene: isolation, characterization, and expression studies. *Proc Natl Acad Sci U S A* **85**, 6232-6236 (1988).
400. Nishikawa, S.I., *et al.* In vitro generation of lymphohematopoietic cells from endothelial cells purified from murine embryos. *Immunity* **8**, 761-769 (1998).
401. Hirashima, M., Kataoka, H., Nishikawa, S., Matsuyoshi, N. & Nishikawa, S. Maturation of embryonic stem cells into endothelial cells in an in vitro model of vasculogenesis. *Blood* **93**, 1253-1263 (1999).
402. Landmesser, U., *et al.* Role of p47(phox) in vascular oxidative stress and hypertension caused by angiotensin II. *Hypertension* **40**, 511-515 (2002).
403. Li, J.M., Wheatcroft, S., Fan, L.M., Kearney, M.T. & Shah, A.M. Opposing roles of p47phox in basal versus angiotensin II-stimulated alterations in vascular O₂-production, vascular tone, and mitogen-activated protein kinase activation. *Circulation* **109**, 1307-1313 (2004).
404. Emmerson, A., *et al.* Nox2 in regulatory T cells promotes angiotensin II-induced cardiovascular remodeling. *J Clin Invest* **128**, 3088-3101 (2018).
405. Kim, D., *et al.* NADPH oxidase 2-derived reactive oxygen species in spinal cord microglia contribute to peripheral nerve injury-induced neuropathic pain. *Proc Natl Acad Sci U S A* **107**, 14851-14856 (2010).
406. Zhang, M., Perino, A., Ghigo, A., Hirsch, E. & Shah, A.M. NADPH oxidases in heart failure: poachers or gamekeepers? *Antioxid Redox Signal* **18**, 1024-1041 (2013).
407. Sag, C.M., *et al.* Distinct Regulatory Effects of Myeloid Cell and Endothelial Cell NAPDH Oxidase 2 on Blood Pressure. *Circulation* **135**, 2163-2177 (2017).
408. Prabhakar, P., *et al.* Receptor-regulated translocation of endothelial nitric-oxide synthase. *J Biol Chem* **273**, 27383-27388 (1998).
409. Hernandez-Presa, M., *et al.* Angiotensin-converting enzyme inhibition prevents arterial nuclear factor-kappa B activation, monocyte chemoattractant protein-1 expression, and macrophage infiltration in a rabbit model of early accelerated atherosclerosis. *Circulation* **95**, 1532-1541 (1997).
410. Pueyo, M.E., *et al.* Angiotensin II stimulates endothelial vascular cell adhesion molecule-1 via nuclear factor-kappaB activation induced by intracellular oxidative stress. *Arterioscler Thromb Vasc Biol* **20**, 645-651 (2000).
411. Kim, M., *et al.* GLP-1 receptor activation and Epac2 link atrial natriuretic peptide secretion to control of blood pressure. *Nat Med* **19**, 567-575 (2013).
412. Marin-Grez, M., Fleming, J.T. & Steinhausen, M. Atrial natriuretic peptide causes pre-glomerular vasodilatation and post-glomerular vasoconstriction in rat kidney. *Nature* **324**, 473-476 (1986).
413. Brenner, B.M., Ballermann, B.J., Gunning, M.E. & Zeidel, M.L. Diverse biological actions of atrial natriuretic peptide. *Physiol Rev* **70**, 665-699 (1990).
414. Li, C.J., *et al.* Changes in liraglutide-induced body composition are related to modifications in plasma cardiac natriuretic peptides levels in obese type 2 diabetic patients. *Cardiovasc Diabetol* **13**, 36 (2014).

415. Lovshin, J.A., *et al.* Liraglutide promotes natriuresis but does not increase circulating levels of atrial natriuretic peptide in hypertensive subjects with type 2 diabetes. *Diabetes Care* **38**, 132-139 (2015).
416. Robinson, L.E., Holt, T.A., Rees, K., Randevara, H.S. & O'Hare, J.P. Effects of exenatide and liraglutide on heart rate, blood pressure and body weight: systematic review and meta-analysis. *BMJ Open* **3**(2013).
417. Sun, F., *et al.* Impact of GLP-1 receptor agonists on blood pressure, heart rate and hypertension among patients with type 2 diabetes: A systematic review and network meta-analysis. *Diabetes Res Clin Pract* **110**, 26-37 (2015).
418. Dinh, Q.N., Drummond, G.R., Sobey, C.G. & Chrissobolis, S. Roles of inflammation, oxidative stress, and vascular dysfunction in hypertension. *Biomed Res Int* **2014**, 406960 (2014).
419. Hirata, K., *et al.* Exendin-4 has an anti-hypertensive effect in salt-sensitive mice model. *Biochem Biophys Res Commun* **380**, 44-49 (2009).
420. Jensen, E.P., *et al.* Activation of GLP-1 receptors on vascular smooth muscle cells reduces the autoregulatory response in afferent arterioles and increases renal blood flow. *Am J Physiol Renal Physiol* **308**, F867-877 (2015).
421. Oshima, N., *et al.* Direct effects of glucose, insulin, GLP-1, and GIP on bulbospinal neurons in the rostral ventrolateral medulla in neonatal wistar rats. *Neuroscience* **344**, 74-88 (2017).
422. Katsurada, K., *et al.* Central Glucagon-like Peptide-1 Receptor Signaling via Brainstem Catecholamine Neurons Counteracts Hypertension in Spontaneously Hypertensive Rats. *Sci Rep* **9**, 12986 (2019).
423. Fisher, J.P. & Paton, J.F. The sympathetic nervous system and blood pressure in humans: implications for hypertension. *J Hum Hypertens* **26**, 463-475 (2012).
424. Grassi, G., Mark, A. & Esler, M. The sympathetic nervous system alterations in human hypertension. *Circ Res* **116**, 976-990 (2015).
425. Bickerton, R. & Buckley, J.P. Evidence for a central mechanism in angiotensin induced hypertension. *Proc Soc Exp Biol Med* **106**, 834-836 (1961).
426. Ferrario, C.M. Neurogenic actions of angiotensin II. *Hypertension* **5**, V73-79 (1983).
427. Hunter, K. & Holscher, C. Drugs developed to treat diabetes, liraglutide and lixisenatide, cross the blood brain barrier and enhance neurogenesis. *BMC Neurosci* **13**, 33 (2012).
428. Investigators, O.T., *et al.* Basal insulin and cardiovascular and other outcomes in dysglycemia. *N Engl J Med* **367**, 319-328 (2012).
429. Home, P.D., *et al.* Rosiglitazone evaluated for cardiovascular outcomes in oral agent combination therapy for type 2 diabetes (RECORD): a multicentre, randomised, open-label trial. *Lancet* **373**, 2125-2135 (2009).
430. Dormandy, J.A., *et al.* Secondary prevention of macrovascular events in patients with type 2 diabetes in the PROactive Study (PROspective pioglitAzone Clinical Trial In macroVascular Events): a randomised controlled trial. *Lancet* **366**, 1279-1289 (2005).
431. Scirica, B.M., *et al.* Saxagliptin and cardiovascular outcomes in patients with type 2 diabetes mellitus. *N Engl J Med* **369**, 1317-1326 (2013).
432. Green, J.B., *et al.* Effect of Sitagliptin on Cardiovascular Outcomes in Type 2 Diabetes. *N Engl J Med* **373**, 232-242 (2015).
433. White, W.B., *et al.* Alogliptin after acute coronary syndrome in patients with type 2 diabetes. *N Engl J Med* **369**, 1327-1335 (2013).
434. Control, G., *et al.* Intensive glucose control and macrovascular outcomes in type 2 diabetes. *Diabetologia* **52**, 2288-2298 (2009).
435. Giugliano, D., Maiorino, M.I., Bellastella, G., Chiodini, P. & Esposito, K. Glycemic Control, Preexisting Cardiovascular Disease, and Risk of Major Cardiovascular Events in Patients with Type 2 Diabetes Mellitus: Systematic Review With Meta-Analysis of Cardiovascular Outcome Trials and Intensive Glucose Control Trials. *J Am Heart Assoc* **8**, e012356 (2019).
436. Terry, T., Ravivakar, K., Chokrungravanon, N. & Reaven, P.D. Does aggressive glycemic control benefit macrovascular and microvascular disease in type 2

- diabetes? Insights from ACCORD, ADVANCE, and VADT. *Curr Cardiol Rep* **14**, 79-88 (2012).
437. Hemmingsen, B., *et al.* Intensive glycaemic control for patients with type 2 diabetes: systematic review with meta-analysis and trial sequential analysis of randomised clinical trials. *BMJ* **343**, d6898 (2011).
438. Barer, Y., Cohen, O. & Cukierman-Yaffe, T. Effect of glycaemic control on cardiovascular disease in individuals with type 2 diabetes with pre-existing cardiovascular disease: A systematic review and meta-analysis. *Diabetes Obes Metab* **21**, 732-735 (2019).
439. Holman, R.R., Paul, S.K., Bethel, M.A., Matthews, D.R. & Neil, H.A. 10-year follow-up of intensive glucose control in type 2 diabetes. *N Engl J Med* **359**, 1577-1589 (2008).
440. Orshal, J.M. & Khalil, R.A. Gender, sex hormones, and vascular tone. *Am J Physiol Regul Integr Comp Physiol* **286**, R233-249 (2004).
441. Pabbidi, M.R., *et al.* Sex differences in the vascular function and related mechanisms: role of 17beta-estradiol. *Am J Physiol Heart Circ Physiol* **315**, H1499-H1518 (2018).
442. Xue, B., Pamidimukkala, J. & Hay, M. Sex differences in the development of angiotensin II-induced hypertension in conscious mice. *Am J Physiol Heart Circ Physiol* **288**, H2177-2184 (2005).
443. Ji, H., *et al.* Sex chromosome effects unmasked in angiotensin II-induced hypertension. *Hypertension* **55**, 1275-1282 (2010).
444. Tomas, E., Stanojevic, V. & Habener, J.F. GLP-1 (9-36) amide metabolite suppression of glucose production in isolated mouse hepatocytes. *Horm Metab Res* **42**, 657-662 (2010).
445. Abu-Hamdah, R., *et al.* Clinical review: The extrapancreatic effects of glucagon-like peptide-1 and related peptides. *J Clin Endocrinol Metab* **94**, 1843-1852 (2009).
446. Sonne, D.P., Engstrom, T. & Treiman, M. Protective effects of GLP-1 analogues exendin-4 and GLP-1(9-36) amide against ischemia-reperfusion injury in rat heart. *Regul Pept* **146**, 243-249 (2008).
447. Kodera, R., *et al.* Glucagon-like peptide-1 receptor agonist ameliorates renal injury through its anti-inflammatory action without lowering blood glucose level in a rat model of type 1 diabetes. *Diabetologia* **54**, 965-978 (2011).
448. Panjwani, N., *et al.* GLP-1 receptor activation indirectly reduces hepatic lipid accumulation but does not attenuate development of atherosclerosis in diabetic male ApoE(-/-) mice. *Endocrinology* **154**, 127-139 (2013).
449. Karbach, S.H., *et al.* Gut Microbiota Promote Angiotensin II-Induced Arterial Hypertension and Vascular Dysfunction. *J Am Heart Assoc* **5**(2016).
450. Witkowski, M., Weeks, T.L. & Hazen, S.L. Gut Microbiota and Cardiovascular Disease. *Circ Res* **127**, 553-570 (2020).
451. He, S., *et al.* Gut intraepithelial T cells calibrate metabolism and accelerate cardiovascular disease. *Nature* **566**, 115-119 (2019).
452. Gaspari, T., *et al.* A GLP-1 receptor agonist liraglutide inhibits endothelial cell dysfunction and vascular adhesion molecule expression in an ApoE-/- mouse model. *Diab Vasc Dis Res* **8**, 117-124 (2011).
453. Intengan, H.D. & Schiffrin, E.L. Structure and mechanical properties of resistance arteries in hypertension: role of adhesion molecules and extracellular matrix determinants. *Hypertension* **36**, 312-318 (2000).
454. The Jackson Laboratory, B.H., Maine. Mouse Genome Database (MGD) at the Mouse Genome Informatics website <http://www.informatics.jax.org/allele>. (accessed on 2021-04-29).
455. Jensen, C.B., *et al.* Characterization of the Glucagonlike Peptide-1 Receptor in Male Mouse Brain Using a Novel Antibody and In Situ Hybridization. *Endocrinology* **159**, 665-675 (2018).
456. Thrasher, J. Pharmacologic Management of Type 2 Diabetes Mellitus: Available Therapies. *Am J Cardiol* **120**, S4-S16 (2017).
457. Zinman *et al.* & Investigators, E.-R.O. Empagliflozin, Cardiovascular Outcomes, and Mortality in Type 2 Diabetes. *N Engl J Med* **373**, 2117-2128 (2015).

458. Cosentino, F., *et al.* 2019 ESC Guidelines on diabetes, pre-diabetes, and cardiovascular diseases developed in collaboration with the EASD. *Eur Heart J* **41**, 255-323 (2020).
459. Davies, M.J., *et al.* Management of Hyperglycemia in Type 2 Diabetes, 2018. A Consensus Report by the American Diabetes Association (ADA) and the European Association for the Study of Diabetes (EASD). *Diabetes Care* **41**, 2669-2701 (2018).
460. Baena-Diez, J.M., *et al.* Risk of Cause-Specific Death in Individuals With Diabetes: A Competing Risks Analysis. *Diabetes Care* **39**, 1987-1995 (2016).
461. Cooper, M.E. The role of the renin-angiotensin-aldosterone system in diabetes and its vascular complications. *Am J Hypertens* **17**, 16S-20S; quiz A12-14 (2004).
462. Barnett, A.H., *et al.* Angiotensin-receptor blockade versus converting-enzyme inhibition in type 2 diabetes and nephropathy. *N Engl J Med* **351**, 1952-1961 (2004).
463. Marlet, I.R., Olmestig, J.N.E., Vilsboll, T., Rungby, J. & Kruuse, C. Neuroprotective Mechanisms of Glucagon-like Peptide-1-based Therapies in Ischaemic Stroke: A Systematic Review based on Pre-Clinical Studies. *Basic Clin Pharmacol Toxicol* **122**, 559-569 (2018).
464. Basalay, M.V., Davidson, S.M. & Yellon, D.M. Can glucagon-like peptide-1 (GLP-1) analogues make neuroprotection a reality? *Neural Regen Res* **15**, 1852-1853 (2020).
465. Maskery, M.P., *et al.* Glucagon-like peptide-1 receptor agonists as neuroprotective agents for ischemic stroke: a systematic scoping review. *J Cereb Blood Flow Metab* **41**, 14-30 (2021).
466. Chalasani, N., *et al.* The diagnosis and management of nonalcoholic fatty liver disease: Practice guidance from the American Association for the Study of Liver Diseases. *Hepatology* **67**, 328-357 (2018).
467. Armstrong, M.J., *et al.* Liraglutide safety and efficacy in patients with non-alcoholic steatohepatitis (LEAN): a multicentre, double-blind, randomised, placebo-controlled phase 2 study. *Lancet* **387**, 679-690 (2016).
468. Newsome, P.N., *et al.* A Placebo-Controlled Trial of Subcutaneous Semaglutide in Nonalcoholic Steatohepatitis. *N Engl J Med* (2020).
469. Wang, X., *et al.* Gliptins Suppress Inflammatory Macrophage Activation to Mitigate Inflammation, Fibrosis, Oxidative Stress, and Vascular Dysfunction in Models of Nonalcoholic Steatohepatitis and Liver Fibrosis. *Antioxid Redox Signal* **28**, 87-109 (2018).
470. Sheka, A.C., *et al.* Nonalcoholic Steatohepatitis: A Review. *JAMA* **323**, 1175-1183 (2020).
471. Cameron-Vendrig, A., *et al.* Glucagon-Like Peptide 1 Receptor Activation Attenuates Platelet Aggregation and Thrombosis. *Diabetes* **65**, 1714-1723 (2016).
472. Kersigo, J., *et al.* A RNAscope whole mount approach that can be combined with immunofluorescence to quantify differential distribution of mRNA. *Cell Tissue Res* **374**, 251-262 (2018).

Appendix

Representative videos of intravital microscopy (Figure 5-8 A, see 5.3.1) are available in the online-only Data Supplement of Helmstädter et al. ATVB, 2020: <https://www.ahajournals.org/doi/suppl/10.1161/atv.0000615456.97862.30> (accessed on 2021-04-29).

Publications

The publication originating as part of this doctoral thesis is marked in bold.

Original publications:

Helmstädter J, Keppeler K, Aust F, Küster L, Frenis K, Filippou K, Vujacic-Mirski K, Tsohataridis S, Kalinovic S, Kröller-Schön S, Oelze M, Bosmann M, Münzel T, Daiber A, Steven S. GLP-1R analog liraglutide improves vascular function in polymicrobial sepsis by reduction of oxidative stress and inflammation. 2021, *Antioxidants*, doi: 10.3390/antiox10081175.

Birk M, Baum E, Zadeh JK, Manicam C, Pfeiffer N, Patzak A, Helmstädter J, Steven S, Kuntic M, Daiber A, Gericke A. Angiotensin II Induces Oxidative Stress and Endothelial Dysfunction in Mouse Ophthalmic Arteries via Involvement of AT1 Receptors and NOX2. 2021, *Antioxidants*, doi: 10.3390/antiox10081238

Frenis K, Helmstädter J, Ruan Y, Schramm E, Kalinovic S, Kröller-Schön S, Bayo Jimenez MT, Hahad O, Oelze M, Jiang S, Wenzel P, Sommer CJ, Frauenknecht KBM, Waisman A, Gericke A, Daiber A, Münzel T, Steven S. Ablation of lysozyme M-positive cells prevents aircraft noise-induced vascular damage without improving cerebral side effects. 2021, *Basic Research in Cardiology*, doi: 10.1007/s00395-021-00869-5.

Helmstädter J, Keppeler K, Küster L, Münzel T, Daiber A, Steven S. GLP-1 receptor agonists and their cardiovascular benefits—The role of the GLP-1 receptor. 2021, *British Journal of Pharmacology*, doi: 10.1111/bph.15462.

Steven S, Frenis K, Kalinovic S, Kvandova M, Oelze M, Helmstädter J, Hahad O, Filippou K, Kus K, Trevisan C, Schlüter KD, Boengler K, Chlopicki S, Frauenknecht K, Schulz R, Sorensen M, Daiber A, Kröller-Schön S, Münzel T. Exacerbation of adverse cardiovascular effects of aircraft noise in an animal model of arterial hypertension. 2020, *Redox Biology*, doi: 10.1016/j.redox.2020.101515.

Helmstädter J, Frenis K, Filippou K, Grill A, Dib M, Kalinovic S, Pawelke F, Kus K, Kröller-Schön S, Oelze M, Chlopicki S, Schuppan D, Wenzel P, Ruf W, Drucker DJ, Münzel T, Daiber A, Steven S. **Endothelial GLP-1 (Glucagon-Like Peptide-1) Receptor Mediates Cardiovascular Protection by Liraglutide In Mice With Experimental Arterial Hypertension.** 2020, *Arteriosclerosis, Thrombosis, and Vascular Biology*, doi: 10.1161/atv.0000615456.97862.30.

Daiber A, Kröller-Schön S, Frenis K, Oelze M, Kalinovic S, Vujacic-Mirski K, Kuntic M, Bayo Jimenez MT, Helmstädter J, Steven S, Korac B, Münzel T. Environmental noise induces the release of stress hormones and inflammatory signaling molecules leading to oxidative stress and vascular dysfunction-Signatures of the internal exposome. 2019, *Biofactors*, doi: 10.1002/biof.1506.

Steven S, Frenis K, Oelze M, Kalinovic S, Kuntic M, Bayo Jimenez MT, Vujacic-Mirski K, Helmstädter J, Kröller-Schön S, Münzel T, Daiber A. Vascular Inflammation and Oxidative Stress: Major Triggers for Cardiovascular Disease. 2019, *Oxidative Medicine and Cellular Longevity*, doi: 10.1155/2019/7092151.

Steven S, Oelze M, Hausding M, Roohani S, Kashani F, Kröller-Schön S, Helmstädter J, Jansen T, Baum C, Iglarz M, Schulz E, Münzel T, Daiber A. The endothelin receptor antagonist macitentan improves isosorbide-5-mononitrate (ISMN) and isosorbide dinitrate (ISDN) induced endothelial dysfunction, oxidative stress and vascular inflammation. 2018, *Oxidative Medicine and Cellular Longevity*, doi: 10.1155/2018/7845629.

Agarwal N, Helmstädter J, Rojas DR, Bali KK, Gangadharan V, Kuner R. Evoked hypoalgesia is accompanied by tonic pain and immune cell infiltration in the dorsal root ganglia at late stages of diabetic neuropathy in mice. 2018, *Molecular Pain*, doi: 10.1177/1744806918817975.

Krueger M, Amort J, Wilgenbus P, Helmstädter JP, Grechowa I, Ebert J, Tenzer S, Moergel M, Witte I, Horke S. The anti-apoptotic PON2 protein is Wnt/ β -catenin-regulated and correlates with radiotherapy resistance in OSCC patients. 2016, *Oncotarget*, doi: 10.18632/oncotarget.9013.

Presentations:

Helmstädter J, Frenis K, Filippou K, Grill A, Dib M, Kalinovic S, Pawelke F, Kus K, Kröller-Schön S, Oelze M, Chlopicki S, Schuppan D, Wenzel P, Ruf W, Drucker DJ, Münzel T, Daiber A, Steven S. The endothelial GLP-1 receptor confers cardiovascular protection in experimental arterial hypertension. 6th Science Day by the TransMed Graduate School of the Johannes Gutenberg University Mainz, 2019. (Best Presentation Award)

Helmstädter J, Kalinovic S, Vujacic-Mirski K, Münzel T, Daiber A, Steven S. The glucagon-like peptide-1 receptor (GLP-1r) agonist liraglutide improves angiotensin II (ATII)-induced vascular inflammation, oxidative stress and endothelial dysfunction. FEBS Advanced Lecture Course Redox-omic Technologies, Spetses, Greek, 2018.

Abstracts:

Helmstädter J, Filippou K, Pawelke F, Frenis K, Vujacic-Mirski K, Kalinovic S, Kröller-Schön S, Oelze M, Münzel T, Daiber A, Steven S. The Endothelial GLP-1 Receptor is Critical for the Cardiovascular Protective Effects of GLP-1 (Liraglutide) Treatment in Experimental Arterial Hypertension. Vascular Discovery (formerly ATVB) Scientific Sessions, Boston, MA, USA, 2019.

Helmstädter J, Pawelke F, Filippou K, Frenis K, Vujacic-Mirski K, Kalinovic S, Kröller-Schön S, Oelze M, Münzel T, Daiber A, Steven S. Anti-Inflammatory and Vascular Protective Effects of Glucagon-like Peptide 1 (GLP-1) in Polymicrobial Septic Mice Induced by Cecal Ligation and Puncture (CLP). Vascular Discovery (formerly ATVB) Scientific Sessions, Boston, MA, USA, 2019.

Curriculum Vitae

xxx

Danksagung

xxx

